Novel Approaches to PET Imaging Neuroinflammation

by

Lindsey Drake

A dissertation submitted in partial fulfillment
of the requirements for the degree of
Doctor of Philosophy
(Medicinal Chemistry)
in the University of Michigan
2019

Doctoral Committee:

Associate Professor Peter J. H. Scott, Chair
Professor Robert A. Koeppe
Professor Scott D. Larsen
Professor Emily E. Scott
Professor Duxin Sun

Lindsey Drake

lrdrake@umich.edu

ORCID id: 0000-0001-8594-8922

ACKNOWLEDGEMENTS

"Take chances, make mistakes, get messy!" -Ms. Frizzle, "The Magic School Bus"

It took four and a half years to get through this, and it wouldn't have been possible without an incredibly supportive group of family and friends. My parents, Vicki and Jeff, always encouraged me to be curious and I think that helped lead me to science. In addition to that, I had amazing teachers, including an exceptional high school chemistry teacher Kathy Hallett, who inspired me to continue studying chemistry at Butler. In college, I continued to benefit from dedicated teachers: Geoff Hoops, Stacy O'Reilly, Paul Morgan, Anne Wilson, and Todd Hopkins. During this time I also worked as an intern at Lilly Research Labs with Jeff Cramer, Will Higgins, and Maria Posada. This experience showed me what possibilities were available to PhD scientists, and ultimately led me to Michigan.

Joining Peter Scott's lab was one of the easiest decisions I have ever made. The research was exciting and I knew the field of PET imaging was where I wanted to be. In lab, I worked with some amazing postdocs and staff scientists: Allen Brooks, Xia Shao, Missy Rodnick, Tim Desmond, Ginny Rogers, Carole Quesada, Guie Gui, So Jeong Lee, Andy Mossine, Stephen Thompson, and Stefan Verhoog. I thought of this lab as a kind of dysfunctional family, with two older sisters Allie Sowa and Megan Stewart showing me the ropes- and many younger brothers, Sean Tanzey, Isaac Jackson, Dale Mallette, Tony Mufarreh, Jonathan Pham, Austin Zao, and Wade Winton. Jonathan was the best undergrad of them all, there, it is on record! My research would not have been possible without the small animal team Jenelle Stauff, Janna Arteaga, and Phil Sherman. And of course a big thanks to Peter Scott, Bob Koeppe, and Mike Kilbourn for their mentorship.

TABLE OF CONTENTS

LIST OF FIGURES

FIGURE

LIST OF TABLES

TABLE

LIST OF SCHEMES

LIST OF APPENDICES

ABSTRACT

The number of individuals with neurodegenerative disorders, particularly Alzheimer's disease (AD), is growing and is projected to continue increasing. Despite this reality, there are no available treatments for AD. Positron emission tomography (PET) imaging has been a valuable tool for drug discovery in the AD space, and has been used to improve our understanding of the pathology of AD. PET imaging strategies in AD have followed the biomarkers used in the drug discovery pipeline, with an early focus on misfolded proteins (amyloid-β (Aβ) and tau neurofibrillary tangles (NFTs)), neurotransmitters, and neuroinflammation. The focus of this thesis has been on using PET imaging to investigate novel aspects of AD pathology. The widely used tau ligand [^{18}F]AV-1451 was investigated for its off-target binding effects to monoamine oxidase (MAO). MAO is also a marker of microgliosis, the activation of microglia, and we have investigated it as an imaging biomarker of neuroinflammation. We developed substrates for imaging MAO-B activity, using a trapped metabolite approach. Inspired by this principle, we used one of these substrates, [^{11}C]AZ, to demonstrate that the feasibility of using an enzyme substrate for dual PET-magnetic resonance (MR) imaging. PET-MR with a single agent has typically been considered impossible because PET imaging would not work at the concentrations required for MRI (i.e. low specific activity). However, we demonstrated that MAO was not saturable *in vivo* at the necessary MR concentration, and that the PET whole brain time activity curves did not suffer. Finally, we evaluated ligands for the receptor for advanced glycation end-products (RAGE), a potential new biomarker of neuroinflammation, using an extracellular and

intracellular approach. We evaluated RAGE as a biomarker using the standard lipopolysaccharide (LPS) murine model of neuroinflammation.

CHAPTER 1

Introduction

Neurodegenerative disorders encompass a broad group of diseases that describe individuals whom experience progressive loss of neurons and brain function deficits.[1] These disorders include Alzheimer's disease (AD), Parkinson's disease (PD), Dementia with Lewy bodies (DLB), fronto-temporal lobar degeneration (FTD), amyotrophic lateral sclerosis (ALS), Huntington's disease (HD), and multiple sclerosis (MS). Brain functions affected by neuronal loss are specific to certain brain regions. PD, HD, and ALS are characterized by the loss of movement and gait control, among other symptoms. In regards to prevalence, most sufferers of neurodegeneration fall into the 'dementia' umbrella of disorders, with AD and Lewy Body Disease (LBD; including pure autonomic failure, DLB, and Parkinson's disease with dementia) being the top diseases in the United States. AD is the most common form of dementia, affecting 5.7 million Americans and 10% of adults over 65 with over two thirds of those individuals being women (figure 1.1).[2] These patients are mostly receiving unpaid care by family members, an estimated $232 billion worth of care per year. There is no cure for dementia of any type, nor are there any effective treatments to ameliorate the burden. Throughout this chapter, the current state of understanding, drug options, and imaging efforts will be reviewed for AD. The focus on protein aggregates (figure 1.2) has dominated the field of dementia and through trials and tribulations, it is apparent that an alternative strategy is necessary for understanding the process of neurodegeneration. Recently, neuroinflammation has been identified as a cause of neuronal

death in AD.[3] The involvement of inflammation in the CNS will be explored throughout this chapter for its use in studying AD pathology.

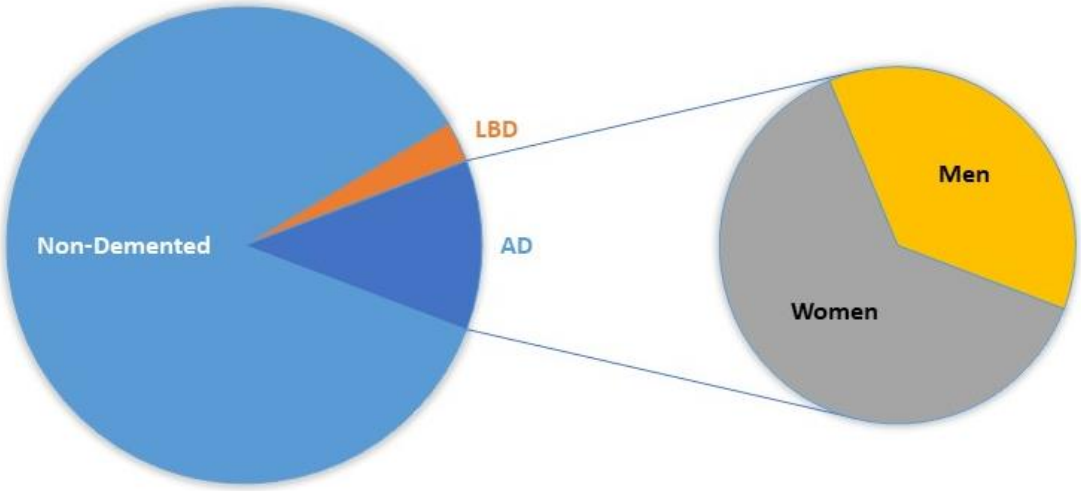

Figure 1.1. Dementia in the American population 65 and older.

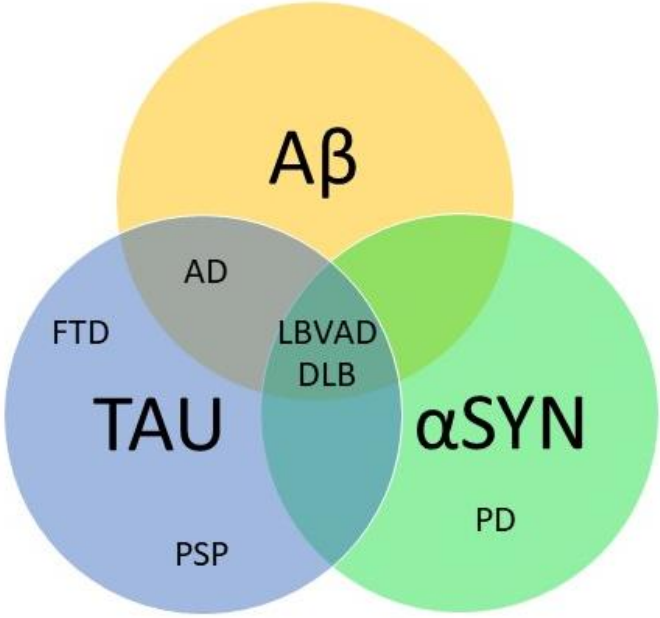

Figure 1.2. Protein aggregates shared between neurodegenerative diseases. AD is marked by the presence of Aβ plaques and tau NFTs. The main component of Lewy bodies is α- synuclein (αsyn), found in PD. Lewy body vascular AD (LBVAD) and DLB contain all three protein aggregates. FTD and progressive supranuclear palsy (PSP) only contain tau NFTs.

Alzheimer's disease and the Amyloid Hypothesis

AD has been characterized for over a century by the symptoms of impaired cognition and memory decline, in addition to the amyloid-beta (Aβ) plaques present extracellularly and

intracellular neurofibrillary tangles (NFTs) in the brain tissue.[4] Definitive diagnosis of AD can only be given post-mortem based on the presence of protein aggregates. Symptomatically, AD can present similarly to other dementias, like vascular dementia or FTD, and diagnosis based on behavioral and psychological symptoms of dementia (BPSD) and cognitive testing is required.[5] BPSD represents the non-cognitive symptoms and behaviors associated with dementia subjects. For example, it has been shown that depression and anxiety symptoms are more frequent in vascular dementia than AD.[5] Cognitive function is often measured by the mini-mental state examination (MMSE).[6] MMSE and similar tests are frequently used as the primary outcome measure for cognition in clinical drug trials. Advances in diagnosis and treatment technology for AD rely on the continuing research efforts into the causes of AD and their relation to these symptoms. Much of the knowledge surrounding AD pathology has been focused on the extracellular Aβ plaques and their origin.

Aβ was first isolated in 1984 from fibrils,[7] but cloning and gene mapping in 1987 revealed that the peptide was synthesized from a larger protein then named β–amyloid precursor protein (APP).[8] The amyloid hypothesis centers on the formation of Aβ fibrils from cleaving a peptide from APP (figure 1.3). This cleavage can occur by two different proteases and results in different outcomes. The non-amyloidogenic pathway is controlled by α-secretase which first cleaves and releases the extracellular amino-terminus of APP; then γ-secretase digests an 83-amino acid residue carboxy-terminal fragment. The amyloidogenic pathway combines the sequential actions of β- and γ-secretases, which generate Aβ peptides that can misfold and form extracellular fibrils.[9] The amyloid hypothesis claims that the generation of Aβ peptides and the eventual formation of plaques is the cause of neuronal cell death.[10]

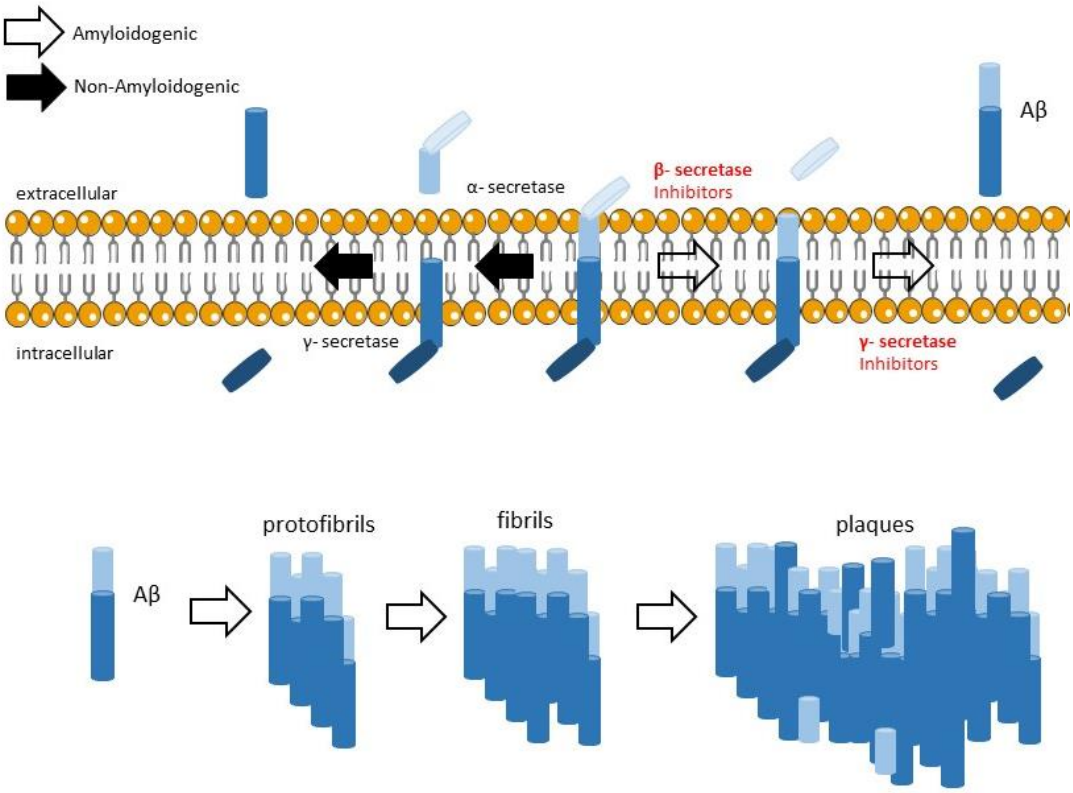

Figure 1.3. Pathway of Aβ plaque formation from amyloid precursor protein (APP). Filled arrows represent non-amyloidogenic pathway of α-secretase cleavage being the primary step. Open arrows follow the amyloidogenic pathway beginning with β-secretase cleavage. This cleavage results in the Aβ peptide which can form protofibrils, fibrils, and plaques.

Classic Approaches to Drugging Alzheimer's Disease

γ- and β-secretase (BACE) were identified early as druggable enzyme targets for AD treatment because of their direct role in processing APP in the amyloidogenic pathway (figure 1.3). Despite an abundance of work toward protease inhibitors for AD; this strategy has demonstrated little success clinically (structures in figure 1.4).[11] γ secretase inhibitors (GSI) have been abandoned in clinical trials because of Notch-related toxicity. Notch is another substrate of gamma secretase. The GSI semagacestat (LY-450139) was well tolerated and appeared to have selection against Notch; however, it failed to show cognitive improvement and exhibited severe skin toxicity.[12] In light of the GSI strategy failure and safety concerns, use of γ-secretase modulators (GSM) was also explored. Utilizing an allosteric binding site, these drugs were able

to avoid Notch-related toxicity and, *in vitro*, increase non-amyloidogenic peptide production. However, poor blood-brain barrier permeability and unpredicted eye side effects (cataracts) have halted this strategy.[13] Inhibition of BACE1 has also proven difficult, with failures like LY2811376 and Verubecestat (MK-8931) (figure 1.4).[14] For example, verubecestat was abandoned in a phase III clinical trial because of no improved cognition (primary end point) despite having improved Aβ peptide clearance in cerebral spinal fluid (CSF).[15]

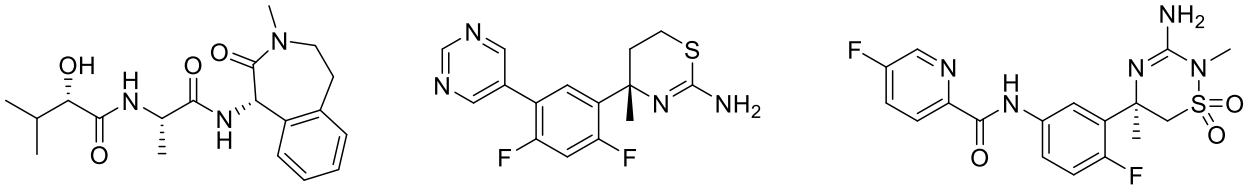

Figure 1.4 Structures of γ secretase inhibitor and BACE1 inhibitors.

The main non-secretase strategy has been antibodies and antibody drug fragments for the removal of peptide before fibrils (and plaques) can form. Humanized murine monoclonal antibodies which targeted linear epitopes of the primary Aβ monomer sequence advanced the furthest in clinical trial. Two versions, bapineuzumab (N-terminal region targeting)[16] and solanezumab (central region targeting)[17] have been evaluated through phase III clinical trial. Although amyloid burden was decreased, based on positron emission tomography (PET) imaging, both of these antibodies failed to meet their primary endpoint.[18] The primary outcome measure was the AD assessment scale- cognition (ADAS-Cog).[19] Aducanumab,[20] another antibody being developed by Biogen is in phase III now and results of the trial have not been announced yet. The high profile failures of bapinuezumab and solanezumab are causing the AD community to consider the need to move away from the amyloid hypothesis. They demonstrated that although the amyloid burden was lowered, cognition did not improve. Independently of these clinical trials, prospective studies using amyloid PET imaging and magnetic resonance

imaging (MRI) have suggested that Aβ deposition is a slow process.[21] It is likely that modifying the symptoms of AD will require a different strategy.

The other protein aggregate hallmark of AD, tau NFTs, are also a target of drug development; however, less is known about the formation of NFTs in comparison to Aβ plaques. NFTs are mainly composed of hyperphosphorylated tau protein. Six tau isoforms are expressed in the human brain, resulting from alternative splicing. Isoforms are typically described by the presence or absence of a 31-amino acid repeat from exon 10. Inclusion results in 4 repeats (4R) and absence in 3 repeats (3R); these repeated sections are used to bind to and promote microtubule assembly.[22] Nonpathogenic tau protein is responsible for supporting microtubules and it has been shown that phosphorylation of tau negatively regulates this interaction.[23] This is a stark difference between amyloid-precursor protein, whose nonpathogenic function is still unknown. It remains a question in the field if tau phosphorylation equates aggregation, yet this pathway has been considered as druggable (figure 1.5).[24-25]

Multiple kinases are capable of phosphorylating tau protein, though glycogen synthase kinase 3β (GSK3β) was first identified as a possible target. Inhibition of GSK3β has been considered in the effort to decrease tau phosphorylation and was shown to be efficacious in an AD animal model.[26] However, tideglusib failed to meet its cognitive endpoint in phase II trial.[27] Other kinase inhibitors are being considered, but it should be noted that selectivity and specificity for kinases is difficult in drug design. Similar to amyloid targeting strategies, tau protein itself is considered a possible drug target. Tau stabilizing and phosphorylated tau (p-tau) clearing immunotherapies have begun entering phase II clinical trial, and it will be interesting to observe if these have significant effects on cognition.[13]

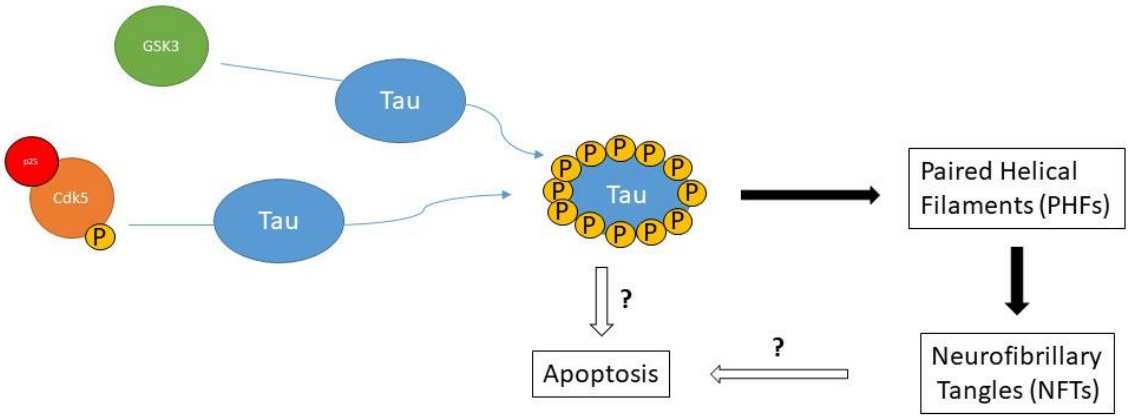

Figure 1.5. Proposed mechanism of tau hyperphosphorylation and deposition. Showing two possible kinases, GSK3 and Cdk5. Filled arrows are known phenomenon, being that they've been reproducible in animal models. Both p-tau and NFTs are theorized to cause apoptosis.

Neuroinflammation as an Alternative Pathway

The preliminary approaches in AD (the amyloid hypothesis) have not been clinically successful to date; however, they have greatly advanced the understanding of AD and opened up alternative pathways. The neuroinflammation hypothesis states that chronic inflammation precedes Aβ accumulation and tau deposition, and could play a role in the activation of these pathways. Inflammation in the CNS, like in the peripheral immune system, is a protective response that is carefully regulated. Innate immunity is the first line of defense against pathogens. In the periphery, innate immunity is mediated by phagocytes including macrophages and dendritic cells.[28] The other branch of the immune system, acquired immunity, is later stage and relies on the generation of antigen-specific receptors on lymphocytes. In the discussion of neuroinflammation, the innate immune system is considered key as it is faster in response, and unless the blood-brain barrier (BBB) is severely damaged, the CNS is considered immune privileged and free of lymphocytes.[28]

The innate immune system recognizes microorganisms through pattern-recognition receptors (PRRs). In the CNS, the main mediator is the microglia, a cell type of the myeloid lineage and having macrophage character. Microglia is a cell population that constitutively

expresses PRRs, but is usually in its resting state.[29] In response to injury, microglia become active, change phenotype, and alter their shape (figure 1.6). Reactive microgliosis is a self-limiting function. In culture it has been shown that most reactive microglia undergo apoptosis afterwards. In addition to microglia, astrocytes also play a role in innate immunity. Astrocytes are the most abundant non-neuronal cell type and are critical for the homeostatic balance of the neurovascular unit (i.e.: uptake of neurotransmitters, production of neurotrophic factors, ion homeostasis, metabolic support of neurons, and BBB maintenance).[30-31] Astrocytes also express PRRs and are capable of secreting soluble factors (such as chemokines) to activate neighboring microglial cells into their M1 state.[30]

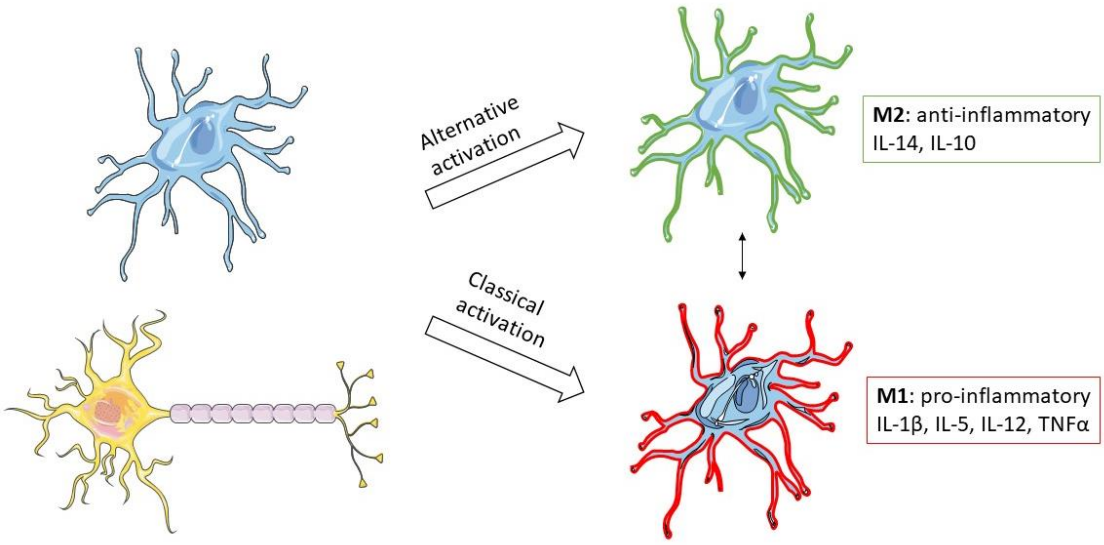

Figure 1.6. Microglial activation. Classical activation, or the M1 type, is pro-inflammatory and results in the expression of cytokines that will activate neighboring cells. Alternative activation, or the M2 type, releases IL-14, IL-10 and other anti-inflammatory cytokines that will damped a response from neighboring cells. It is theorized that activated microglia can transform in and out of these two states.

Evidence for innate immune responses in AD are rooted in the finding that Aβ peptide induces an inflammatory response in microglia.[32] Furthermore a link between mutations in genes encoding triggering receptor expressed on myeloid cells 2 (TREM2) and AD confirmed an association between neurodegeneration and the immune system.[33] TREM2 is expressed on

microglia cells and activates phagocytosis; however, the normal function is not well understood. It has been found that TREM2 signaling negatively regulates the PRR toll-like receptor (TLR) signaling pathways.[34] The most common rs75932628 variant causes an R47H substitution,[35] and is a functional variant that impairs the interaction of TREM2 with neurons and plaques during amyloid plaque accumulation; it is predicted to triple the risk of developing AD.[33]

Soluble immune factors, cytokines and chemokines, are known to distribute through the CSF and eventually be cleared through the blood system. A minimally invasive strategy to quantify immune response in the CNS is to quantify these biomarkers in the CSF or blood. However, because of the similar mechanism of innate immunity between the CNS and periphery, determining neuroinflammation independently of peripheral inflammation is challenging. It has so far been possible to quantify Aβ peptide and p-tau from the blood; however, their utility as diagnostic biomarkers has not been proven.[36] Interpreting these soluble factors has been difficult because the mechanism, and time course, of clearance is unknown in this disease state. Instead of evaluating soluble factors in the CSF or blood, we aim to employ the molecular imaging technique, Positron Emission Tomography (PET).

Positron Emission Tomography

PET is a non-invasive *in vivo* imaging technique that provides biochemical information. This form of nuclear imaging utilizes a bioactive molecule substituted with a positron emitting radioisotope; when the bioactive molecule interacts with its target *in vivo*, the positron decays are detected over time. This collection of decays per time and location allows researchers to observe biochemical processes *in vivo* (figure 1.7).[37] In order to correlate this dynamic information with structural data, PET is often combined with a structural technique such as computed tomography (CT) or magnetic resonance (MR) imaging. Common PET isotopes are carbon-11, fluorine-18,

nitrogen-13, oxygen-15, and gallium-68.[38] Due to half-life constraints and incorporation into small molecules, carbon-11 and fluorine-18 are used the most frequently (table 1.1).

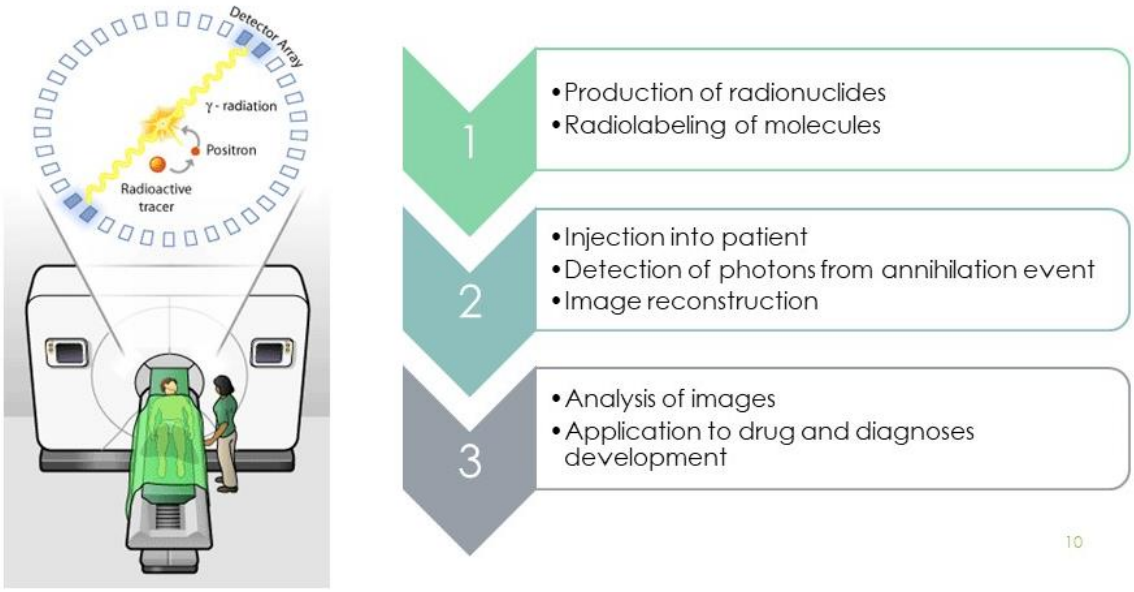

Figure 1.7. Bench to bedside process of PET imaging. Due to the short half-life of the radionuclide, production of the molecule occurs on site. After the cyclotron produced radioisotope is made, it is chemically incorporated into the molecule. After quality control testing, the radionuclide containing molecule can be injected into the patient. During the PET scan, the scanner detects the annihilation event from the decayed positron colliding with a neighboring electron. After the scan, the image can be reconstructed based on time, activity, and which detector recorded the incident.

Table 1.1 Common PET Radioisotopes Half-lives

Isotope	**Half-life (min)**
Carbon-11	20.4
Nitrogen-13	9.98
Oxygen-15	2.03
Fluorine-18	109.8
Gallium-68	67.71

Amyloid and Tau PET

Molecular imaging agents were developed in tandem to many of the aforementioned drug targets in the amyloid and tau pathways (figure 1.8). The inspiration for Aβ imaging agents was based on fluorescent dyes, which were classically used by pathologists to label protein aggregates in post-mortem human brain tissue. [^{18}F]FDDNP, based on 2-[1-[6-(dimethylamino)-

2-naphthyl]ethylidene]malononitrile (DDNP), was developed by Huang and Barrio at UCLA.[39] In humans, [^{18}F]FDDNP is extensively metabolized; polar radiometabolites were found to be BBB permeable.[40] The presence of brain-penetrating metabolites has made this radioligand impossible to use in a human study without the inclusion of metabolite-corrected plasma input function. Furthermore the low signal to noise ratio was not ideal for use. Concurrent with these efforts, [^{11}C]6-OH-BTA-1 ([^{11}C]Pittsburgh Compound B; [^{11}C]PiB) was developed, based on the fluorescent pigment, thioflavin T to be selective for Aβ plaques and be more brain penetrating.[41] [^{11}C]PiB was widely adopted in human PET imaging and was used as the target engagement determinant for multiple clinical trials (figure 1.9); however, fluorine-18 ligands are often preferred for human use because of the flexibility in synthesis and scanning time. A closely related fluorine-18 analogue of [^{11}C]PiB, [^{18}F]flutemetamol has been proven similar in detecting Aβ deposition and discriminating AD from healthy control.[42] Another ligand, [^{18}F]NAV4694, is being widely used and has demonstrated enough sensitivity to distinguish mild cognitive impairment (MCI) from AD.[43] From a different scaffold, [^{18}F]florbetaben[44] and [^{18}F]florbetapir[45] have also been developed for human use; however, it has been suggested that these ligands also bind to tau, but not α-synuclein (the protein aggregate distinct of PD).[46] Because of the similar β-sheet structure, designing selectivity between Aβ plaque, NFTs, and α-synuclein inclusions has been challenging; however, the growing interest of the role of tau in AD inspired dedicated research in this area.

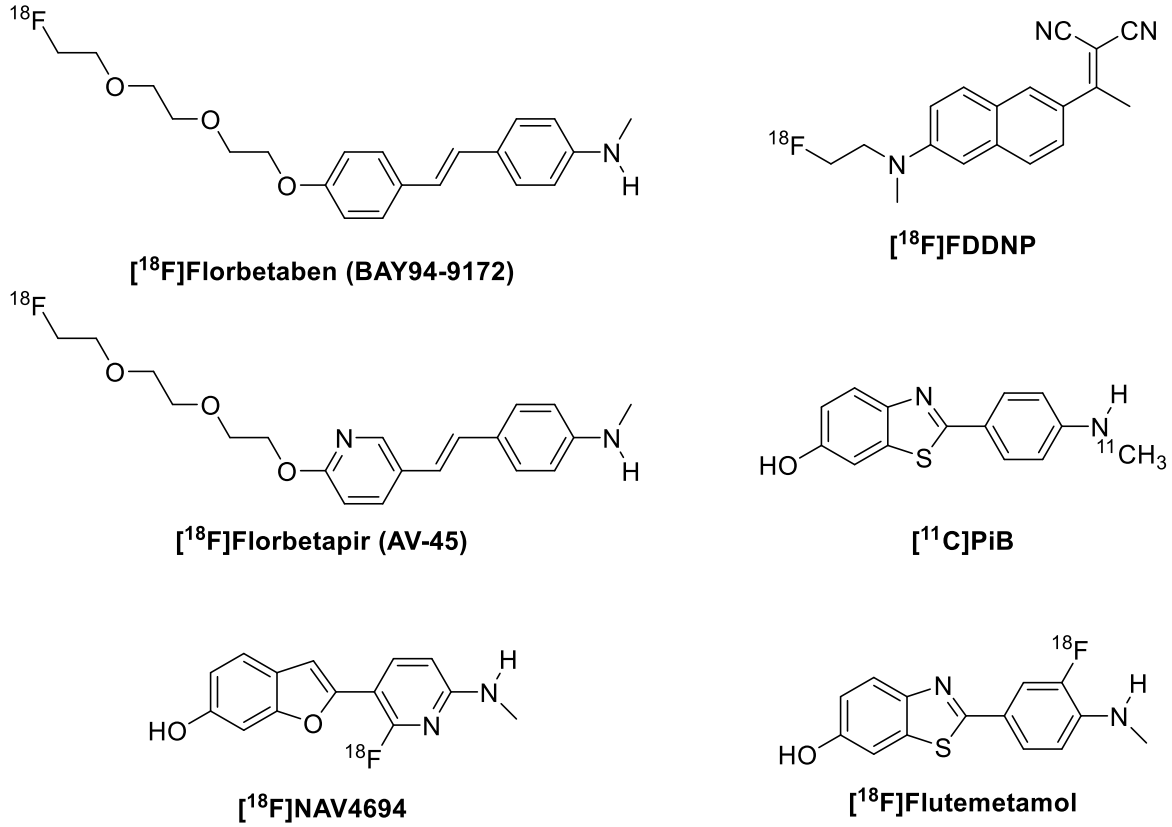

Figure 1.8. Aβ PET Radioligands. Florbetapir, florbetaben, and flutemetamol are FDA approved.

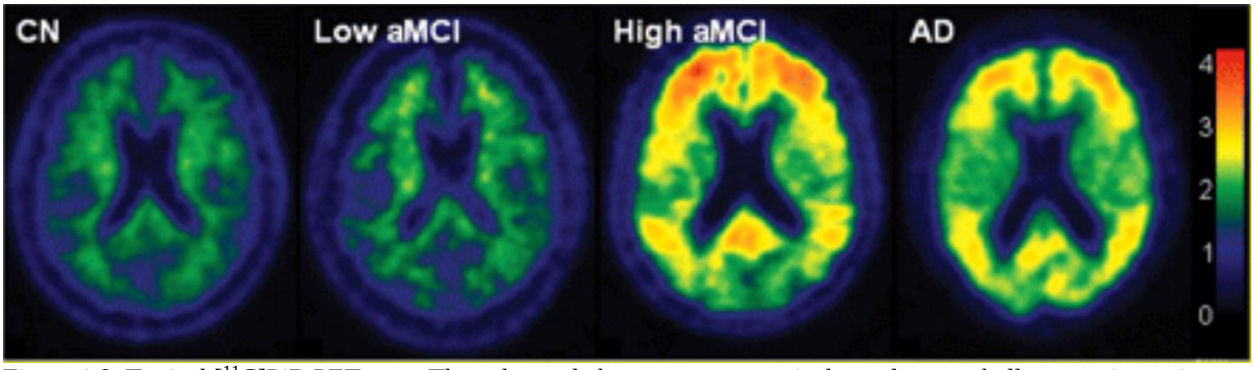

Figure 1.9. Typical [^{11}C]PiB PET scan. The color scale bar represents cortical voxel-to-cerebellar retention ratio. CN: cognitive normal. Low aMCI: low amyloid Mild Cognitive Impairment, high aMCI: high amyloid mild cognitive impairment. Reprinted with permission.[47]

Tau PET radioligands were developed more recently and seemingly were pushed through clinical translation at a faster pace than the amyloid ligands.[48] The first generation tau tracers are considered to be [^{11}C]PBB3, [^{18}F]THK5351, and [^{18}F]AV-1451 (figure 1.10). [^{11}C]PBB3 was developed to bind both 3R and 4R tau inclusions,[49] though it is not widely used because of

photoisomerization occurring during radiosynthesis[50] and brain-penetrating metabolites in humans.[51] Tohoku University developed a small library of compounds,[52-53] [^{18}F]THK5351 being the molecule with the highest brain uptake. This radioligand showed promising preliminary results in human PET imaging;[54] however, the authors described significant off-target binding to monoamine oxidase-B (MAO-B) which limits the use of the ligand.[55-56] [^{18}F]Flortaucipir, discovered by Siemens[57] and translated by Avid Radiopharmaceuticals/ Eli Lilly & Company, boasted a greater selectivity for tau over Aβ and has become the most widely used first generation tau tracer. Clinical trials have shown a significant correlation between tau burden and cognitive impairment as measured by [^{18}F]flortaucipir (figure 1.11);[58] however, there are similar concerns about off-target binding to MAO-B.[59] The second generation tau radioligand, [^{18}F]MK-6240, was developed specifically with off-target binding in mind and does not share MAO-B as a binding partner.[60] Additionally, the overall uptake of [^{18}F]MK-6240 is significantly higher than [^{18}F]flortaucipir which could make analysis of the images easier.[61] [^{18}F]MK-6240 is not without faults though- unexplained, nonspecific uptake in the meninges has been observed in some patients.[62] There are many efforts to develop second generation tau PET imaging agents including [^{11}C]RO6931643,[^{11}C]RO6924963, [^{18}F]RO695948,[63] [^{18}F]JNJ64349311,[64] and [^{11}C]N-methyl-lansporazole.[65] Continued use of these agents will investigate NFTs' relationship to cognition and serve as treatment monitoring agents in upcoming clinical trials for tau modulating drugs.

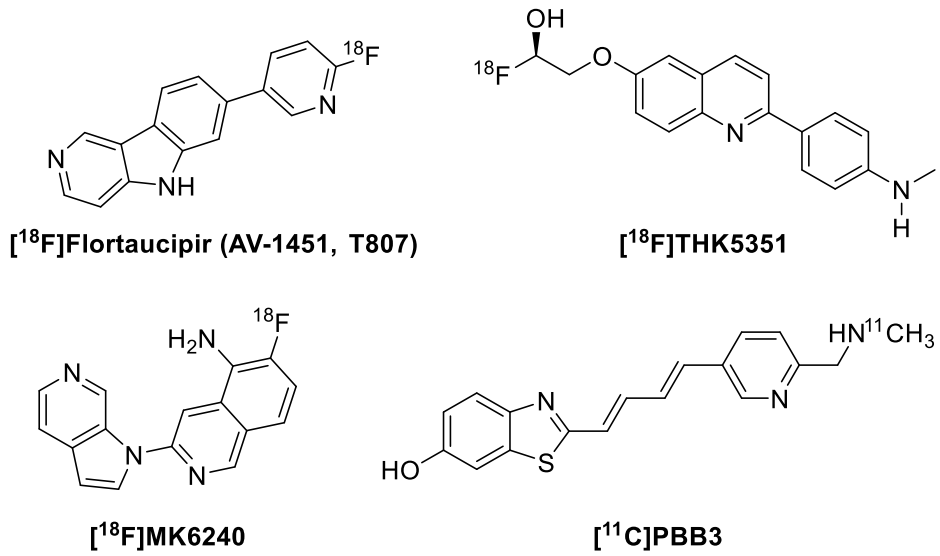

Figure 1.10. Tau PET ligands.

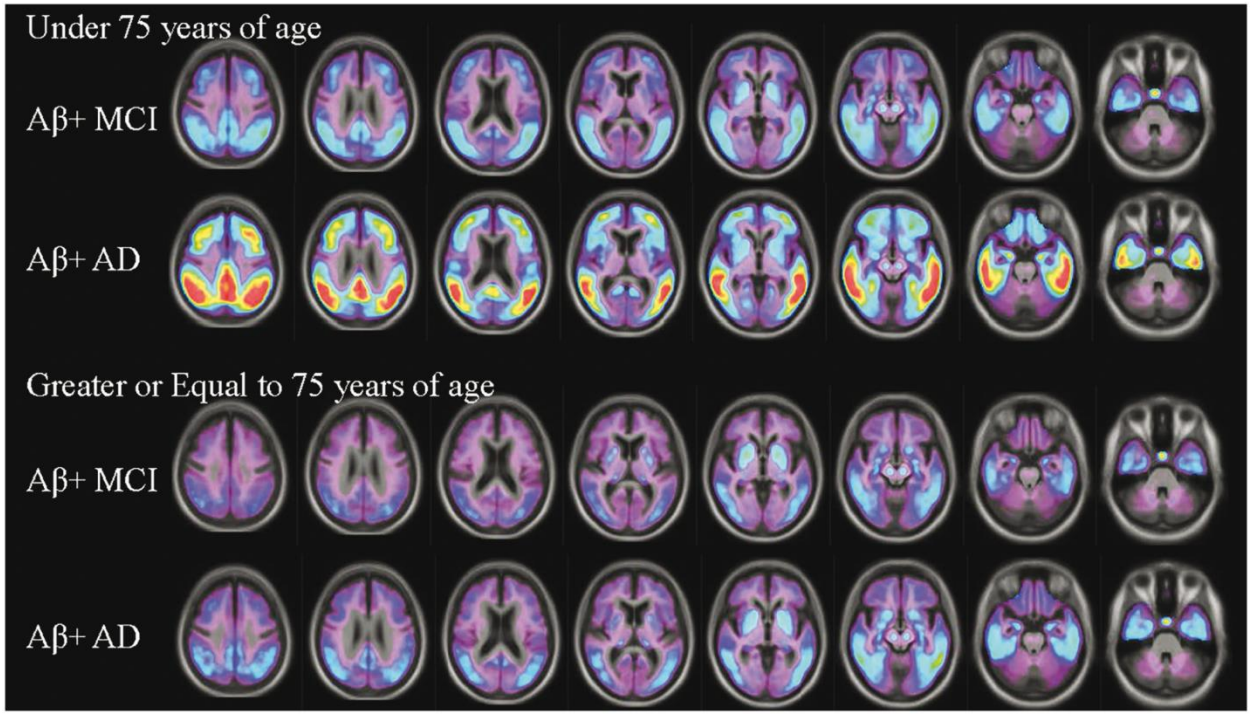

Figure 1.11 [^{18}F]AV-1451 PET Scan. Mean flortaucipir voxel-wise SUVr images for Aβ+ MCI and Alzheimer's disease subjects <75 years and ≥75 years old. Figure reprinted under the terms of the Creative Commons Attribution Non-Commercial License.[66]

Neuroinflammation imaging biomarkers

Developing PET imaging agents for new biomarkers of disease has been happening in tandem with drug discovery since the development of PET.[67] The utility of small molecule radioligands to confirm *in vivo* target engagement for drug companies was immediately realized.

Molecular imaging has also been used to extend knowledge of disease states with this new window into physiology. Throughout this section, the most popular biomarkers will be discussed including their inflammatory biology and imaging efforts.

Translocator protein (18 kDa)

Translocator protein (18 kDa), TSPO, is responsible for cholesterol transport from the outer mitochondrial-membrane to the inner mitochondrial-membrane. Other endogenous ligands of TSPO include porphyrins and endozepines, a family of neuropeptides.[68] Endozepines are synthesized in the peripheral nervous system by Schwann cells, in which production increases in response to local injury.[69] TSPO expression is highest in adrenal, gonad, and brain tissue.[70] Researchers explained the high level of expression in these tissues by their importance in steroidogenesis and cholesterol use. TSPO has been identified to have many distinct physiological roles: steroidogenesis,[71] apoptosis, and cell proliferation.[72]

The benzodiazepine, Ro 5-4864, was the first high affinity agonist for TSPO and through pharmacological studies, PK11195 was developed as an antagonist.[73] PK11195 was utilized to biochemically characterize TSPO in cell lines,[74] pharmacologically in rodent models,[75] and autoradiographically (with the tritiated version) on tissue.[76] Through these studies, TSPO was found to be expressed in fetal rat glial cultures[77] and immature rat astrocytes;[78] this was supported by rodent models of excitotoxic brain damage *in vivo*.[75] This evidence was used to justify TSPO as a biomarker for neuroinflammation and develop PK11195 as a PET radioligand for human use.

[^{11}C]*N*-methyl-PK11195 ([^{11}C]PK11195) was first synthesized in 1984 (figure 1.12).[79] One of the most important [^{11}C]PK11195 human studies was performed at the University of Michigan; eight patients with a clinical diagnosis of probable AD underwent PET scans and MRI

to compare the hemisphere structures.[80] After quantitative analysis of the [^{11}C]PK11195 PET scans, the authors determined that the radioligand does not detect the presence of microgliosis or cellular inflammation.[80] The signal to noise ratio of [^{11}C]PK11195 was poor and would not be easy to utilize in a meaningful clinical setting.

In response to the poor tracer characteristics of [^{11}C]PK11195, researchers developed the "second generation" of TSPO antagonists: [^{11}C]PBR28,[81] [^{18}F]DPA-714,[82-83] [^{18}F]FEPPA,[84] [^{11}C]DAA1106,[85] [^{18}F]PBR06,[86] [^{18}F]PBR111 (figure 1.12).[87] A new second generation TSPO ligand [^{18}F]GE-180, has shown greater sensitivity than [^{18}F]PBR06 in detecting decreased microglial activation in a mouse model of AD.[88] Despite the improved signal to noise ratio of these tracers, the aryloxanalide backbone caused a different mode of binding than PK11195 and suffered variable binding in humans.[89-90] A single nucleotide polymorphism (SNP), A147T, severely lowers the binding affinity of these tracers to TSPO and the resultant occupancy in tissue.[89] After an exhaustive kinetic study and genotyping "high affinity," "mixed affinity," and "low affinity" binding individuals, a compartmental model was developed for [^{11}C]PBR28;[90] however, the clinical use of these tracers is still complicated by the lack of a reference region. Reference regions are defined brain structures that are void of specific binding. Having a reference region allows for simpler image analysis by using the ratio of a region of interest and the reference region, called standard uptake value ratio (SUVR).

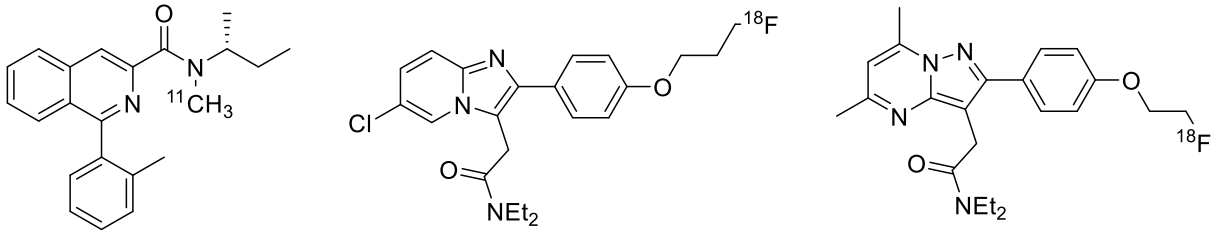

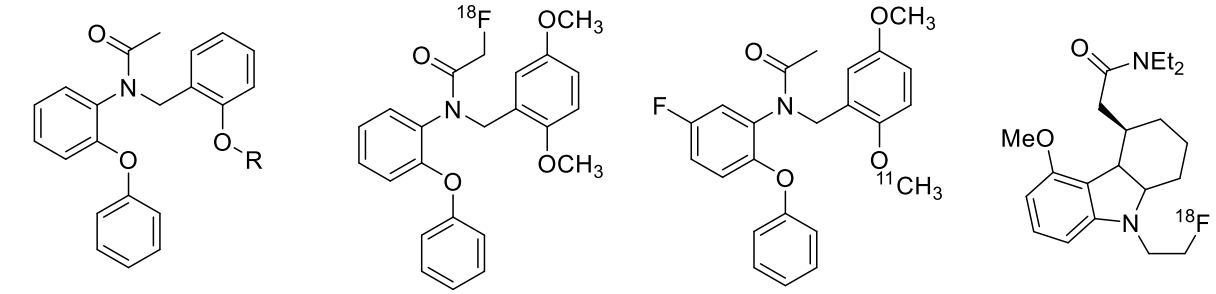

Figure 1.12. TSPO PET radioligands.

Cyclooxygenase (COX)

The enzyme cyclooxygenase (COX), also known as prostaglandin (PG) H synthase, is an integral membrane glycoprotein. There are two forms, encoded by distinct genes, -1 and -2, which preform the critical first steps in prostanoid formation.[91] Prostanoids, a subclass of eicosanoids, consist of prostaglandins, thromboxanes, and the prostacyclins. Prostaglandins are mediators of inflammatory and anaphylactic reactions; prostacyclins are active in the resolution of inflammation. Thromboxanes are mediators of vasoconstriction.[92] In the inflammatory response, eicosanoids are required for the initiation and resolution phases. As such, these molecules are critical autocrine factors to regulate vascular tone and platelet aggregation, but also the resolution of inflammation by lipoxins.[93] COX is unique in the way it catalyzes two chemical reactions: first the bis-oxygenase activity catalyzing arachidonic acid to PGG_2 and

second the peroxidase activity to reduce PGG_2 to PGH_2. The product, PGH_2, can then be converted to the various prostanoids.[93]

COX-1 and COX-2 are functionally identical and structurally similar, with important differences in the COX-2 active site and an 18 amino acid insert in the COX-2 terminus.[92] COX-1 is constitutively active and maintains basal levels of prostanoids; COX-2 is inducible under chronic and acute states of inflammation. This difference in expression is clearly demonstrated by the TATA box in the promoter of the COX-2 gene. A third form of the protein, COX-3, has been identified in canine and human cortex, but the functional role is largely unknown.[91] In rodents, the COX-3 variant was determined to have no cyclooxygenase activity.[93]

One of the most widely used drug classes, non-steroidal anti-inflammatories (NSAIDs) are the main inhibitors of COX, used for the treatment of pain and inflammation. The classical NSAIDs: aspirin and ibuprofen, are non-selective for the two isozymes. A dangerous side effect of habitual NSAID use is stomach ulcers, due to the unintended inhibition of COX-1 in the gastrointestinal tract.[93] In response to this, medicinal chemists developed the specific COX-2 inhibitors, Zomepirac (RS104897), RS57067,[92] Celecoxib, and Rofecoxib.[94] These inhibitors were then used as the basis for [^{18}F]SC58125 (figure 1.13), which demonstrated COX-2 binding in activated macrophages; however, the tracer uptake in baboons appeared nonspecific in the brain.[94] [^{11}C]Celecoxib itself was developed as a PET ligand (figure 1.13).[95] However, much of the use has been focused on evaluating "biliary excretion," which it was found unsuitable.[96] When [^{11}C]celecoxib and [^{11}C]rofecoxib were evaluated in normal mice and an ischemic brain injury model, it was determined that they were not sensitive enough to detect COX-2 *in vivo*.[97]

COX-1 has also been evaluated *in vivo* through the use of [^{11}C]ketoprofen methyl ester [^{11}C]KTP-Me.[98] In a rodent model of microglial activation, this PET ligand was able to monitor

the time dependent activation of COX-1. However, this study is one of the only ones to demonstrate COX-1 as an inducible factor in inflammation. The main concern with targeting either COX-1 or COX-2 is the ability to see the small increase in expression, over the high basal level of COX-1, this has limited its use as an imaging biomarker to date.

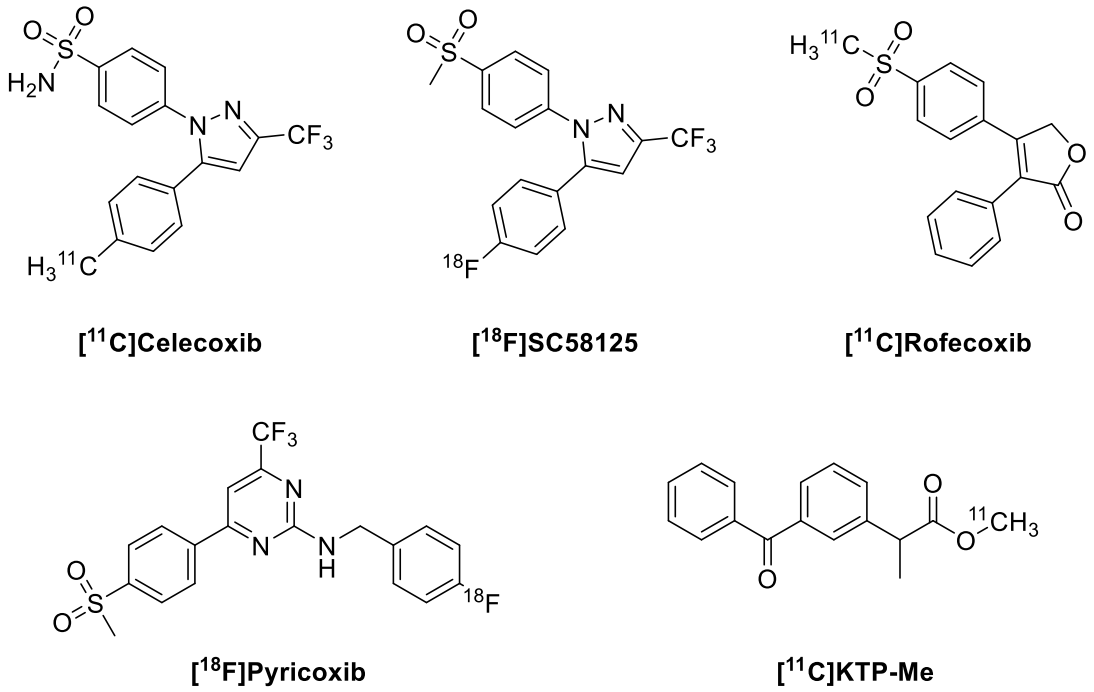

Figure 1.13. COX PET radioligands.

Reactive Oxygen Species (ROS)

One of the most straightforward strategies for detecting neuroinflammation is to detect the presence of reactive oxygen species (ROS). Nitric oxide (NO) is a gaseous free radical, which can occur in cells from the conversion of L-arginine to L-citrulline by nitric oxide synthases.[32] In macrophages, microglia, and astrocytes the production of NO is highly regulated by Ca^{2+}/ calmodulin dependent isoforms (iNOS). This enzymatic process is highly variable *in vitro* based on different conditions of cell culture. Thus it has been challenging to elucidate this pathway. In human brain tissue expression of iNOS has been detected in NFT bearing neurons[99] and hippocampal sections of AD brain tissue.[100] Another reactive oxygen species is superoxide,

the anionic form of oxygen gas. It is normally removed from cells by superoxide dismutase (SOD), but during high levels of NADPH oxidase activity, superoxide can react with NO to form peroxynitrite. Peroxynitrite is damaging to DNA and proteins within the cell; the DNA damage can activate necroptosis or apoptosis (figure 1.14).[101]

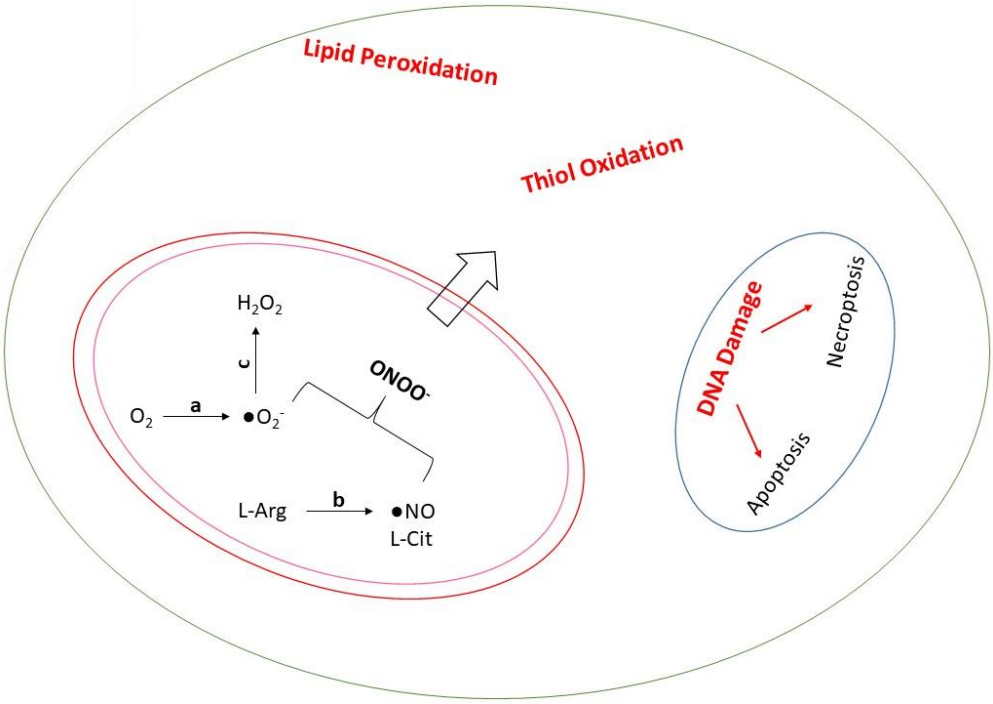

Figure 1.14. ROS formation and selected damage pathway. A) Superoxide can be formed from NADPH oxidase, xanthine oxidase, COX, and NOS. B) Nitric oxide is a byproduct of NOS catalyzed conversion of arginine to citrulline. C) Superoxide is normally transformed into hydrogen peroxide by SOD. Presence of ROS in the cytoplasm can result in lipid peroxidation, thiol oxidation of sulfur containing amino acids and cofactors, and DNA damage in the nucleus.

The first chemical biology probe for observing ROS was hydromethidine, which is a fluorescent after oxidation. Studies with [^{3}H]hydromethidine (HM) demonstrated blood brain barrier permeability as well as trapping after oxidation *in vivo*.[102] The same group radiolabeled this compound with carbon-11 (figure 1.15).[103] Evaluation with a lipopolysaccharide (LPS) induced model of neuroinflammation revealed an increase in radioligand uptake which was mirrored on tissue in autoradiography studies. The fluorescence based compounds require reaction with ROS, which in theory provides a level of sensitivity in brain areas of high

inflammation over others. This reaction based technique has been expanded to other molecular scaffolds as well.

The compound [^{11}C]1-methyl-1,4-DHQ-3-carboxamide ([^{11}C]DHQ1) relies on irreversible trapping after oxidation by ROS in the central nervous system (figure 1.15).[104] The lipophilic form, structurally based on the cofactor NADH, can passively diffuse, while the oxidized form cannot and will be trapped; this phenomenon was demonstrated in apocynin-treated mice. The tracer was rapidly cleared from the non-apocynin treated animals; however, the authors argue that one method is not sufficient to measure redox status.[105] A similar effort to this trapping includes [^{18}F]ROStrace, based on the dihydroethidium dye.[106] The authors claim that one day post LPS injection, mice had increased uptake of [^{18}F]ROStrace which correlated to "worse off" inflammation scores.[107] [^{18}F]FLT Boronate-caged are also designed to react with ROS. Fluorothymidine (FLT) mimics endogenous substrates that are transported into cells that are proliferating quickly by ENT1, phosphorylated by TK1, and trapped.[108] The chemo-selective cage structure ensured transport to the correct cellular type and that the thymidine analogue would not be incorporated into DNA. In principle, this technique was successful but at this time it has not been evaluated in the CNS.

Finally, there has been one reaction-based effort that does not rely on trapping to occur. [^{11}C]Ascorbic Acid (vitamin C) was carbon-11 labeled by our lab in collaboration with UCSF and Stanford, in addition to its oxidized partner, [^{11}C]DHA. The purpose of this study was to evaluate the model in cancer cells; however, it is an interesting technique that could be applied to the CNS. Vitamin C is actively transported by sodium dependent vitamin C transporter (SVCT1-2) which is a relatively slow process. Once oxidized by a two-electron transfer into DHA, that compound can be transported through the glucose transporter (GLUT) much faster. It was

assumed, and shown in cancer cell lines, that intracellular accumulation of [^{11}C]VitC is an oxidation-dependent process, while [^{11}C]DHA accumulation is not.[109]

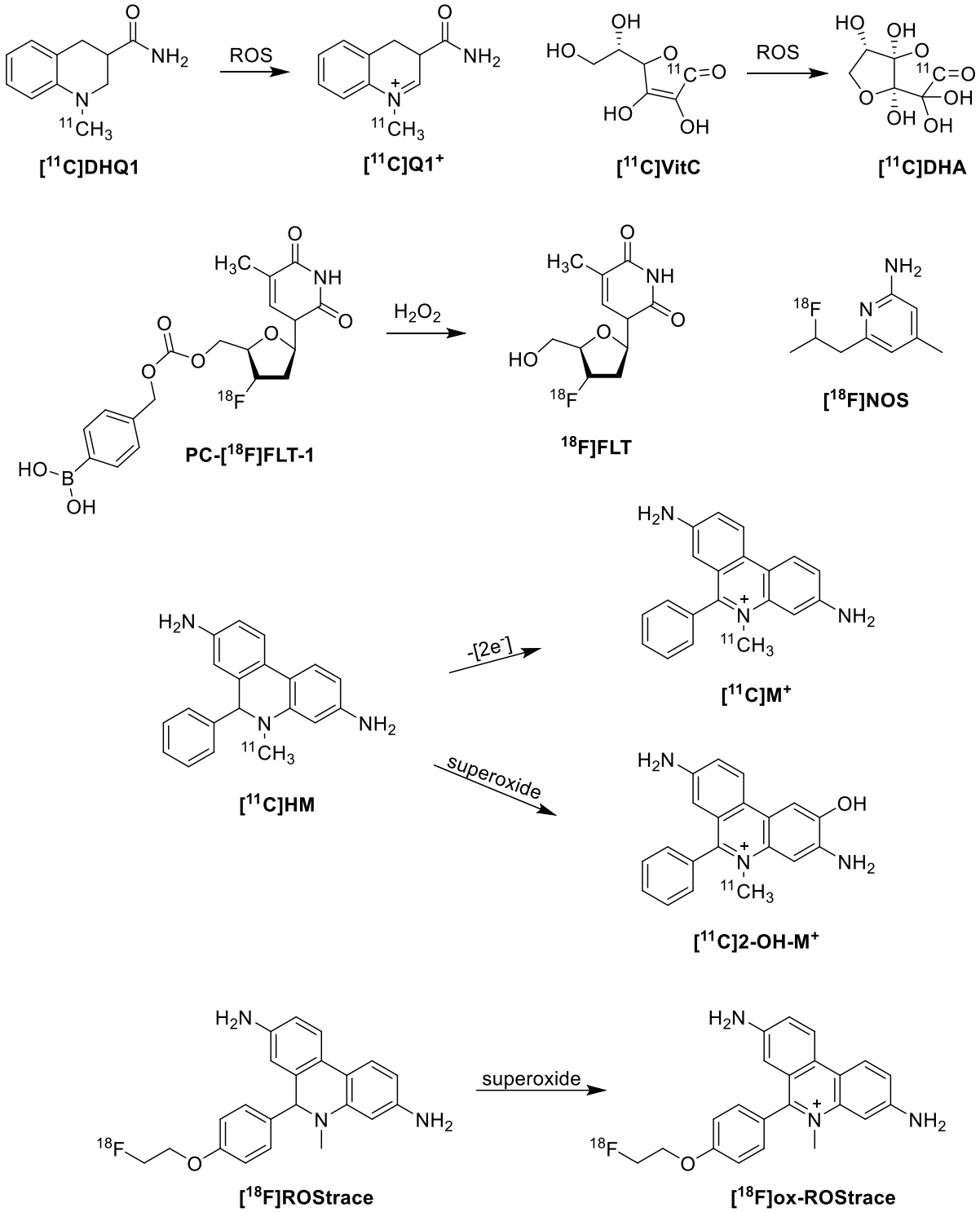

Figure 1.15. PET tracers and ligand for Reactive Oxygen Species.

Monoamine Oxidase (MAO)

Monoamine oxidases (MAOs) are flavin containing enzymes found on the outer-mitochondrial membranes. Two isozymes, MAO-A and –B, are responsible for the oxidative metabolism of the monoamine neurotransmitters (dopamine, serotonin, epinephrine, norepinephrine, histamine, among others).[110] Both isozymes are expressed in the CNS, though their active site structural differences influence their substrate preferences. Serotonin is the preferred substrate of MAO-A. As such inhibitors for MAO-A have been developed for treatment of major depressive disorder.[111] MAO-B has been found to be expressed in dopaminergic neurons and in astrocytes. Through immunoreactivity studies, MAO-B has been found near Aβ in human brain tissue sections.[112]

Irreversible inhibitors, [^{11}C]L-deprenyl and [^{11}C]clorgyline, were first used for MAO-B and –A PET imaging, respectively, and to map the distribution of MAO in the human brain (figure 1.16).[113] Due to high noise observed *in vivo*, [^{11}C]clorgyline was replaced in use with the reversible ligand [^{11}C]harmine. To improve *in vivo* pharmacokinetics of the MAO-B tracer, deuterium substitution was utilized to make [^{11}C]deprenyl-d_2 ([^{11}C]DED). [^{11}C]DED imaging has been utilized in many human trials and demonstrated astrocyte activation in MCI and AD patients, supporting the hypothesis of neuroinflammation.[114]

[^{11}C]DED is not the ideal PET ligand for MAO imaging however, because it is metabolized *in vivo* to [^{11}C]methamphetamine.[115] The presence of a brain penetrating metabolite, with specific binding partners different to that of the parent, complicates image analysis. A study with reserpine, an adrenergic blocking agent, confirmed in mice that [^{11}C]deprenyl and the resultant [^{11}C]methamphetamine metabolite binding is not specific to MAO-B. An alternative strategy to using this irreversible inhibitor, was to utilize [^{11}C]1-methyl-4-phenyl-1,2,3,6-

tetrahydropyridine ([^{11}C]MPTP).[116-117] MPTP is a selective substrate for MAO-B; however, it is known to cause dopaminergic cell death from its reactive metabolite MPP^+ irreversibly binding to the electron transport chain.[118-119] This toxicity prevents its use for human PET imaging. In a similar approach, with a nontoxic substrate, we have previously developed aryl-oxy-derivatives of MPTP for MAO PET imaging.[120] Further development of substrates for trapped metabolite imaging of MAO-B will be discussed in chapter 3.

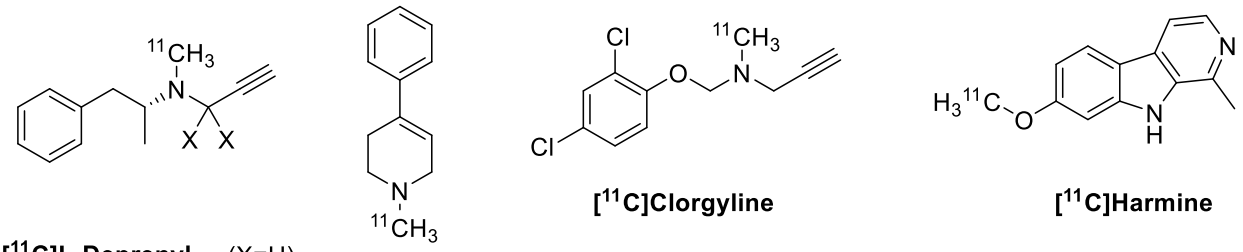

Figure 1.16. PET tracers and ligands for Monoamine Oxidases.

Receptor for Advanced Glycation End-products (RAGE)

Advanced glycation end-products (AGEs) are non-enzymatically glycated macromolecules that are regarded as signs of inflammation.[121] These molecules are recognized by the receptor for advanced glycation end-products (RAGE), a pattern recognition receptor (PRR) of the immunoglobulin G family. RAGE signals through ligand-induced homo- or hetero-dimerization, allowing for intracellular ligand binding. This results in pro-inflammatory transcription and the eventual release of soluble cytokines and chemokines.[122]

RAGE overexpression has been documented in multiple types of inflamed vascular tissue, including lung[123] and brain.[124-125] There have been few PET imaging efforts for RAGE because it is a relatively new biomarker and there are not many small molecule inhibitors known. Our efforts to develop small molecule radioligands for RAGE, and subsequent investigation into RAGE as a biomarker for neuroinflammation will be described in chapters 5 and 6.

Hypothesis, overarching dissertation goals, and chapter outline

As outlined previously, PET imaging of neuroinflammation is a growing field with roots in the classical biomarkers of peripheral inflammation (TSPO and COX). Clinical use of these radioligands has provided necessary insight into the physiology of neurodegeneration which supports the overall hypothesis. The goals of my dissertation work were broadly to develop novel approaches to imaging neuroinflammation. The specific aims of each chapter will be outlined therein; however, the work is intended to be applied to neurodegenerative disorders to investigate the inflammation component. The second chapter in this work explores off-target binding of a first generation tau tracer, [^{18}F]flortaucipir ([^{18}F]AV-1451; [^{18}F]T807). This chapter investigates a widely used tau tracer and its relationship to monoamine oxidase- B (MAO-B). MAO-B in its own right plays a role in the activation of microglia (microgliosis) and is considered an inflammatory biomarker. Chapter 2 considers the challenges in interpreting PET data from a tau tracer, while unintentionally observing changes in MAO-B activity. The subsequent chapter 3 describes my efforts in the development of a radiotracer (substrate) for trapped metabolite imaging of MAO-B activity. These experiments highlight the necessity of understanding enzymatic mechanism as well as brain pharmacokinetics for successful tracer design. Chapter 4 continues in the exploration of MAO-B as a biomarker; however, it mostly serves as a proof-of-concept for dual PET- magnetic resonance (MR) imaging. It has been long thought that the need in MR for high unlabeled tracer mass would make dual modality imaging with the same ligand impossible. We demonstrate with substrates that do not saturate the enzyme that these imaging modalities can work in tandem. These chapters combined summarize my investigations into MAO-B and my efforts in developing a PET tracer for the enzyme. The remaining two chapters both focus on a far less known biomarker of inflammation, the receptor

for advanced glycation end-products (RAGE). Chapter 5 describes the preliminary and subsequent efforts to develop a small molecule ligand for RAGE, despite the receptor's endogenous ligands being large peptides and other biomolecules. Chapter 6 takes a step back so to speak, and considers if RAGE is a biomarker for *neuro*inflammation at all, being that the majority of previous work in this field has only considered RAGE's role in peripheral inflammation. The last experiment performed in this body of work was the development of the LPS mouse model of neuroinflammation and evaluating for RAGE. The final chapter of this work provides overall conclusions and recommendations for future steps for each of these projects.

References

1. Gao, H.-M.; Hong, J.-S., Why neurodegenerative diseases are progressive: uncontrolled inflammation drives disease progression. *Trends in Immunology* **2008,** *29* (8), 357-365.
2. Gaugler, J.; James, B.; Johnson, T.; Marin, A.; Weuve, J. Alzheimer's Disease Facts and Figures. https://www.alz.org/media/HomeOffice/Facts%20and%20Figures/facts-and-figures.pdf.
3. Minter, M. R.; Taylor, J. M.; Crack, P. J., The contribution of neuroinflammation to amyloid toxicity in Alzheimer's disease. *Journal of Neurochemistry* **2016,** *136* (3), 457-474.
4. Kim, D. H.; Yeo, S. H.; Park, J.-M.; Choi, J. Y.; Lee, T.-H.; Park, S. Y.; Ock, M. S.; Eo, J.; Kim, H.-S.; Cha, H.-J., Genetic markers for diagnosis and pathogenesis of Alzheimer's disease. *Gene* **2014,** *545* (2), 185-193.
5. Cerejeira, J.; Lagarto, L.; Mukaetova-Ladinska, E., Behavioral and Psychological Symptoms of Dementia. *Frontiers in Neurology* **2012,** *3* (73).
6. Yang, L.; Yan, J.; Jin, X.; Jin, Y.; Yu, W.; Xu, S.; Wu, H., Screening for dementia in older adults: comparison of mini-mental state examination, mini-cog, clock drawing test and AD8. *PLoS One* **2016,** *11* (12), e0168949/1-e0168949/9.
7. Glenner, G. G., Reprint of "Alzheimer's disease: Initial report of the purification and characterization of a novel cerebrovascular amyloid protein". *Biochemical and Biophysical Research Communications* **2012,** *425* (3), 534-539.
8. Goldgaber, D.; Lerman, M. I.; McBride, O. W.; Saffiotti, U.; Gajdusek, D. C., Characterization and chromosomal localization of a cDNA encoding brain amyloid of Alzheimer's disease. *Science* **1987,** *235* (4791), 877-880.
9. Bekris, L. M.; Yu, C. E.; Bird, T. D.; Tsuang, D. W., Review article: Genetics of Alzheimer disease. *Journal of Geriatric Psychiatry and Neurology* **2010,** *23* (4), 213-227.
10. Levin, O. S.; Vasenina, E. E., 25 Years of the Amyloid Hypothesis of the Origin of Alzheimer's Disease: Advances, Failures, and New Perspectives. *Neurosci. Behav. Physiol.* **2017,** *47* (9), 1065-1070.
11. Kumar, D.; Ganeshpurkar, A.; Kumar, D.; Modi, G.; Gupta, S. K.; Singh, S. K., Secretase inhibitors for the treatment of Alzheimer's disease: Long road ahead. *European Journal of Medicinal Chemistry* **2018,** *148*, 436-452.
12. Doody, R. S.; Raman, R.; Farlow, M.; Iwatsubo, T.; Vellas, B.; Joffe, S.; Kieburtz, K.; He, F.; Sun, X.; Thomas, R. G.; Aisen, P. S.; Siemers, E.; Sethuraman, G.; Mohs, R., A phase 3 trial of semagacestat for treatment of Alzheimer's disease. *N. Engl. J. Med.* **2013,** *369* (4), 341-350.
13. Jackson, R.; Paul, G.; Shi, J.; Sabbagh, M., Why do trials for Alzheimer's disease drugs keep failing? A discontinued drug perspective for 2010-2015 AU - Mehta, Dev. *Expert Opinion on Investigational Drugs* **2017,** *26* (6), 735-739.
14. Mergott, D. J.; May, P. C.; Dean, R. A.; Lowe, S. L.; Monk, S. A.; Boggs, L. N.; Brier, R. A.; Calligaro, D. O.; Cocke, P. J.; Daugherty, L. L.; Day, T. A.; Ereshefsky, L.; Friedrich, S.; Gevorkyan, H.; Gonzales, C. R.; Hall, D. G.; Jhee, S. S.; Lin, S.; LaBell, E. S.; Lindstrom, T. D.; Mathes, B. M.; Nakano, M.; Sanchez-Felix, M. V.; Sheehan, S. M.; Stout, S. L.; Timm, D. E.; Vaught, G. M.; Watson, B. M.; Willis, B. A.; Winneroski, L. L.; Yang, Z.; Hudziak, K. J.; Beck, J. P.; Schiffler, M. A.; Boyer, R. D.; Yen, M.; Martenyi, F.; Citron, M.; Audia, J. E. In *Chemistry, pre-clinical characterization, and clinical translation of BACE inhibitors*, American Chemical Society: 2014; pp MEDI-35.
15. Egan, M. F.; Kost, J.; Tariot, P. N.; Aisen, P. S.; Cummings, J. L.; Vellas, B.; Sur, C.; Mukai, Y.; Voss, T.; Furtek, C.; Mahoney, E.; Mozley, L. H.; Vandenberghe, R.; Mo, Y.; Michelson, D., Randomized trial of verubecestat for mild-to-moderate Alzheimer's disease. *N. Engl. J. Med.* **2018,** *378* (18), 1691-1703.
16. Salloway, S.; Sperling, R.; Fox, N. C.; Blennow, K.; Klunk, W.; Raskind, M.; Sabbagh, M.; Honig, L. S.; Porsteinsson, A. P.; Ferris, S.; Reichert, M.; Ketter, N.; Nejadnik, B.; Guenzler, V.; Miloslavsky, M.; Wang, D.; Lu, Y.; Lull, J.; Tudor, I. C.; Liu, E.; Grundman, M.; Yuen, E.; Black, R.;

Brashear, H. R., Two phase 3 trials of bapineuzumab in mild-to-moderate Alzheimer's disease. *N. Engl. J. Med.* **2014,** *370* (4), 322-333.
17. Doody, R. S.; Thomas, R. G.; Farlow, M.; Iwatsubo, T.; Vellas, B.; Joffe, S.; Kieburtz, K.; Raman, R.; Sun, X.; Aisen, P. S.; Siemers, E.; Liu-Seifert, H.; Mohs, R., Phase 3 trials of solanezumab for mild-to-moderate Alzheimer's disease. *N. Engl. J. Med.* **2014,** *370* (4), 311-321.
18. Relkin, N., Clinical Trials of Intravenous Immunoglobulin for Alzheimer's Disease. *Journal of Clinical Immunology* **2014,** *34* (1), 74-79.
19. Boxer, A. L., Bapineuzumab AU - Kerchner, Geoffrey A. *Expert Opinion on Biological Therapy* **2010,** *10* (7), 1121-1130.
20. Arndt, J. W.; Qian, F.; Smith, B. A.; Quan, C.; Kilambi, K. P.; Bush, M. W.; Walz, T.; Pepinsky, R. B.; Bussière, T.; Hamann, S.; Cameron, T. O.; Weinreb, P. H., Structural and kinetic basis for the selectivity of aducanumab for aggregated forms of amyloid-β. *Scientific Reports* **2018,** *8* (1), 6412.
21. Villemagne, V. L.; Burnham, S.; Bourgeat, P.; Brown, B.; Ellis, K. A.; Salvado, O.; Szoeke, C.; Macaulay, S. L.; Martins, R.; Maruff, P.; Ames, D.; Rowe, C. C.; Masters, C. L., Amyloid β deposition, neurodegeneration, and cognitive decline in sporadic Alzheimer's disease: a prospective cohort study. *Lancet Neurol.* **2013,** *12* (4), 357-367.
22. Goedert, M.; Spillantini, M. G., Propagation of Tau aggregates. *Mol. Brain* **2017,** *10*, 18/1-18/9.
23. Spillantini, M. G.; Goedert, M., Tau pathology and neurodegeneration. *The Lancet Neurology* **2013,** *12* (6), 609-622.
24. Fallacara, A. L.; Trist, I. M. L.; Schenone, S.; Botta, M., Inhibitors of tau-phosphorylating kinases. *Top. Med. Chem.* **2017,** *24* (Alzheimer's Disease II), 119-158.
25. Lindsley, C. W.; Hooker, J. M., Beyond the amyloid hypothesis of Alzheimer's disease: Tau pathology takes center stage. *ACS Chem. Neurosci.* **2018,** *9* (11), 2519.
26. Eldar-Finkelman, H.; Eisenstein, M.; Licht-Murava, A. Glycogen synthase kinase-3 inhibitors and their therapeutic use. WO2014207743A2, 2014.
27. Lovestone, S.; Boada, M.; Dubois, B.; Huell, M.; Rinne, J. O.; Huppertz, H.-J.; Calero, M.; Andres, M. V.; Gomez-Carrillo, B.; Leon, T.; del Ser, T., A Phase II Trial of Tideglusib in Alzheimer's Disease. *J. Alzheimer's Dis.* **2015,** *45* (1), 75-88.
28. Akira, S.; Uematsu, S.; Takeuchi, O., Pathogen recognition and innate immunity. *Cell (Cambridge, MA, U. S.)* **2006,** *124* (4), 783-801.
29. Ladeby, R.; Wirenfeldt, M.; Garcia-Ovejero, D.; Fenger, C.; Dissing-Olesen, L.; Dalmau, I.; Finsen, B., Microglial cell population dynamics in the injured adult central nervous system. *Brain Research Reviews* **2005,** *48* (2), 196-206.
30. Farina, C.; Aloisi, F.; Meinl, E., Astrocytes are active players in cerebral innate immunity. *Trends in Immunology* **2007,** *28* (3), 138-145.
31. Waisman, A.; Liblau, R. S.; Becher, B., Innate and adaptive immune responses in the CNS. *The Lancet Neurology* **2015,** *14* (9), 945-955.
32. Heneka, M. T.; O'Banion, M. K., Inflammatory processes in Alzheimer's disease. *J. Neuroimmunol.* **2007,** *184* (1-2), 69-91.
33. Heppner, F. L.; Ransohoff, R. M.; Becher, B., Immune attack: the role of inflammation in Alzheimer disease. *Nat Rev Neurosci* **2015,** *16* (6), 358-372.
34. Takahashi, K., Role of triggering receptor expressed on myeloid cells 2 in neuroinflammation and neurodegeneration of the central nervous system. *Clin. Exp. Neuroimmunol.* **2018,** *9* (4), 219-224.
35. Guerreiro, R.; Wojtas, A.; Bras, J.; Carrasquillo, M.; Rogaeva, E.; Majounie, E.; Cruchaga, C.; Sassi, C.; Kauwe, J. S. K.; Younkin, S.; Hazrati, L.; Collinge, J.; Pocock, J.; Lashley, T.; Williams, J.; Lambert, J.-C.; Amouyel, P.; Goate, A.; Rademakers, R.; Morgan, K.; Powell, J.; St. George-Hyslop, P.; Singleton, A.; Hardy, J., TREM2 Variants in Alzheimer's Disease. *New England Journal of Medicine* **2013,** *368* (2), 117-127.
36. Clark, L. F.; Kodadek, T., The Immune System and Neuroinflammation as Potential Sources of Blood-Based Biomarkers for Alzheimer's Disease, Parkinson's Disease, and Huntington's Disease. *ACS Chemical Neuroscience* **2016**.

37. Phelps, M. E., Positron emission tomography provides molecular imaging of biological processes. *Proceedings of the National Academy of Sciences* **2000,** *97* (16), 9226-9233.
38. Qaim, S. M.; Clark, J. C.; Crouzel, C.; Guillaume, M.; Helmeke, H. J.; Nebeling, B.; Pike, V. W.; Stöcklin, G., PET radionuclide production. In *Radiopharmaceuticals for positron emission tomography*, Springer: 1993; pp 1-43.
39. Agdeppa, E. D.; Kepe, V.; Liu, J.; Flores-Torres, S.; Satyamurthy, N.; Petric, A.; Cole, G. M.; Small, G. W.; Huang, S.-C.; Barrio, J. R., Binding characteristics of radiofluorinated 6-dialkylamino-2-naphthylethylidene derivatives as positron emission tomography imaging probes for β-amyloid plaques in Alzheimer's disease. *J. Neurosci.* **2001,** *21* (24), RC189/1-RC189/5.
40. Luurtsema, G.; Schuit, R. C.; Takkenkamp, K.; Lubberink, M.; Hendrikse, N. H.; Windhorst, A. D.; Molthoff, C. F. M.; Tolboom, N.; van Berckel, B. N. M.; Lammertsma, A. A., Peripheral metabolism of [18F]FDDNP and cerebral uptake of its labelled metabolites. *Nuclear Medicine and Biology* **2008,** *35* (8), 869-874.
41. Mathis, C. A.; Wang, Y.; Holt, D. P.; Huang, G.-F.; Debnath, M. L.; Klunk, W. E., Synthesis and Evaluation of 11C-Labeled 6-Substituted 2-Arylbenzothiazoles as Amyloid Imaging Agents. *J. Med. Chem.* **2003,** *46* (13), 2740-2754.
42. Hatashita, S.; Yamasaki, H.; Suzuki, Y.; Tanaka, K.; Wakebe, D.; Hayakawa, H., [18F]Flutemetamol amyloid-beta PET imaging compared with [11C]PIB across the spectrum of Alzheimer's disease. *European Journal of Nuclear Medicine and Molecular Imaging* **2014,** *41* (2), 290-300.
43. Nair, A. K.; Brooks, H.; Feijo, F.; Kanya, M.; Nair, M.; Colborn, D.; Shuping, J.; Potter, B.; Seibyl, J.; Reninger, C., IMAGING MILD COGNITIVE IMPAIRMENT WITH A SECOND GENERATION TRACER NAV4694 HAS NEAR PERFECT INTER-RATER RELIABILITY. *Alzheimer's & Dementia: The Journal of the Alzheimer's Association* **2014,** *10* (4), P101-P102.
44. Villemagne, V. L.; Ong, K.; Mulligan, R. S.; Holl, G.; Pejoska, S.; Jones, G.; O'Keefe, G.; Ackerman, U.; Tochon-Danguy, H.; Chan, J. G., Amyloid imaging with 18F-florbetaben in Alzheimer disease and other dementias. *Journal of Nuclear Medicine* **2011**, jnumed. 111.089730.
45. Wong, D. F.; Rosenberg, P. B.; Zhou, Y.; Kumar, A.; Raymont, V.; Ravert, H. T.; Dannals, R. F.; Nandi, A.; Brasić, J. R.; Ye, W.; Hilton, J.; Lyketsos, C.; Kung, H. F.; Joshi, A. D.; Skovronsky, D. M.; Pontecorvo, M. J., In vivo imaging of amyloid deposition in Alzheimer disease using the radioligand 18F-AV-45 (florbetapir [corrected] F 18). *Journal of nuclear medicine : official publication, Society of Nuclear Medicine* **2010,** *51* (6), 913-920.
46. Fodero-Tavoletti, M. T.; Brockschnieder, D.; Villemagne, V. L.; Martin, L.; Connor, A. R.; Thiele, A.; Berndt, M.; McLean, C. A.; Krause, S.; Rowe, C. C.; Masters, C. L.; Dinkelborg, L.; Dyrks, T.; Cappai, R., In vitro characterization of [18F]-florbetaben, an Aβ imaging radiotracer. *Nuclear Medicine and Biology* **2012,** *39* (7), 1042-1048.
47. Jack, C. R., Jr.; Lowe, V. J.; Senjem, M. L.; Weigand, S. D.; Kemp, B. J.; Shiung, M. M.; Knopman, D. S.; Boeve, B. F.; Klunk, W. E.; Mathis, C. A.; Petersen, R. C., 11C PiB and structural MRI provide complementary information in imaging of Alzheimer's disease and amnestic mild cognitive impairment. *Brain* **2008,** *131* (Pt 3), 665-80.
48. Klunk, W. E., Molecular imaging: What is right and what is an illusion? *Alzheimer's & Dementia: Diagnosis, Assessment & Disease Monitoring* **2018,** *10*, 217-220.
49. Maruyama, M.; Shimada, H.; Suhara, T.; Shinotoh, H.; Ji, B.; Maeda, J.; Zhang, M.-R.; Trojanowski, John Q.; Lee, Virginia M. Y.; Ono, M.; Masamoto, K.; Takano, H.; Sahara, N.; Iwata, N.; Okamura, N.; Furumoto, S.; Kudo, Y.; Chang, Q.; Saido, Takaomi C.; Takashima, A.; Lewis, J.; Jang, M.-K.; Aoki, I.; Ito, H.; Higuchi, M., Imaging of Tau Pathology in a Tauopathy Mouse Model and in Alzheimer Patients Compared to Normal Controls. *Neuron* **2013,** *79* (6), 1094-1108.
50. Hashimoto, H.; Kawamura, K.; Igarashi, N.; Takei, M.; Fujishiro, T.; Aihara, Y.; Shiomi, S.; Muto, M.; Ito, T.; Furutsuka, K.; Yamasaki, T.; Yui, J.; Xie, L.; Ono, M.; Hatori, A.; Nemoto, K.; Suhara, T.; Higuchi, M.; Zhang, M.-R., Radiosynthesis, photoisomerization, biodistribution, and metabolite

analysis of 11C-PBB3 as a clinically useful PET probe for imaging of tau pathology. *J. Nucl. Med.* **2014,** *55* (9), 1532-1538.
51. Kimura, Y.; Ichise, M.; Ito, H.; Shimada, H.; Ikoma, Y.; Seki, C.; Takano, H.; Kitamura, S.; Shinotoh, H.; Kawamura, K.; Zhang, M.-R.; Sahara, N.; Suhara, T.; Higuchi, M., PET quantification of tau pathology in human brain with 11C-PBB3. *J. Nucl. Med.* **2015,** *56* (9), 1359-1365.
52. Okamura, N.; Suemoto, T.; Furumoto, S.; Suzuki, M.; Shimadzu, H.; Akatsu, H.; Yamamoto, T.; Fujiwara, H.; Nemoto, M.; Maruyama, M., Quinoline and benzimidazole derivatives: candidate probes for in vivo imaging of tau pathology in Alzheimer's disease. *Journal of Neuroscience* **2005,** *25* (47), 10857-10862.
53. Okamura, N.; Furumoto, S.; Harada, R.; Tago, T.; Yoshikawa, T.; Fodero-Tavoletti, M.; Mulligan, R. S.; Villemagne, V. L.; Akatsu, H.; Yamamoto, T., Novel 18F-labeled arylquinoline derivatives for noninvasive imaging of tau pathology in Alzheimer disease. *J nucl med* **2013,** *54* (8), 1420-7.
54. Lockhart, S. N.; Baker, S. L.; Okamura, N.; Furukawa, K.; Ishiki, A.; Furumoto, S.; Tashiro, M.; Yanai, K.; Arai, H.; Kudo, Y.; Harada, R.; Tomita, N.; Hiraoka, K.; Watanuki, S.; Jagust, W. J., Dynamic PET measures of tau accumulation in cognitively normal older adults and Alzheimer's disease patients measured using [18F] THK-5351. *PLoS One* **2016,** *11* (6), e0158460/1-e0158460/16.
55. Villemagne, V.; Dore, V.; Okamura, N.; Baxendale, D.; Harada, R.; Mulligan, R.; Furumoto, S.; Salvado, O.; Yanai, K.; Masters, C.; Rowe, C., To tau or to MAO-B? Most of the 18F-THK5351 signal is blocked by selegiline. *Journal of Nuclear Medicine* **2018,** *59* (supplement 1), 1644.
56. Ng, K. P.; Pascoal, T. A.; Mathotaarachchi, S.; Therriault, J.; Kang, M. S.; Shin, M.; Guiot, M.-C.; Guo, Q.; Harada, R.; Comley, R. A., Monoamine oxidase B inhibitor, selegiline, reduces 18 F-THK5351 uptake in the human brain. *Alzheimer's research & therapy* **2017,** *9* (1), 25.
57. Xia, C.-F.; Arteaga, J.; Chen, G.; Gangadharmath, U.; Gomez, L. F.; Kasi, D.; Lam, C.; Liang, Q.; Liu, C.; Mocharla, V. P.; Mu, F.; Sinha, A.; Su, H.; Szardenings, A. K.; Walsh, J. C.; Wang, E.; Yu, C.; Zhang, W.; Zhao, T.; Kolb, H. C., (18)F]T807, a novel tau positron emission tomography imaging agent for Alzheimer's disease. *Alzheimers Dement* **2013,** *9* (6), 666-76.
58. Sperling, R. A.; Mormino, E. C.; Schultz, A. P.; Betensky, R. A.; Papp, K. V.; Amariglio, R. E.; Hanseeuw, B. J.; Buckley, R.; Chhatwal, J.; Hedden, T.; Marshall, G. A.; Quiroz, Y. T.; Donovan, N. J.; Jackson, J.; Gatchel, J. R.; Rabin, J. S.; Jacobs, H.; Yang, H.-S.; Properzi, M.; Kirn, D. R.; Rentz, D. M.; Johnson, K. A., The impact of amyloid-beta and tau on prospective cognitive decline in older individuals. *Ann. Neurol.* **2019,** *85* (2), 181-193.
59. Vermeiren, C.; Motte, P.; Viot, D.; Mairet-Coello, G.; Courade, J.-P.; Citron, M.; Mercier, J.; Hannestad, J.; Gillard, M., The tau positron-emission tomography tracer AV-1451 binds with similar affinities to tau fibrils and monoamine oxidases. *Mov. Disord.* **2018,** *33* (2), 273-281.
60. Hostetler, E. D.; Walji, A. M.; Zeng, Z.; Miller, P.; Bennacef, I.; Salinas, C.; Connolly, B.; Gantert, L.; Haley, H.; Holahan, M.; Purcell, M.; Riffel, K.; Lohith, T. G.; Coleman, P.; Soriano, A.; Ogawa, A.; Xu, S.; Zhang, X.; Joshi, E.; Della Rocca, J.; Hesk, D.; Schenk, D. J.; Evelhoch, J. L., Preclinical characterization of 1♂F-MK-6240, a promising PET tracer for in vivo quantification of human neurofibrillary tangles. *J. Nucl. Med.* **2016,** *57* (10), 1599-1606.
61. Lohith, T. G.; Bennacef, I.; Salinas, C. A.; Riffel, K.; Hostetler, E. D.; Evelhoch, J. L.; Sur, C.; Vandenberghe, R.; Vandenbulcke, M.; Declercq, R.; Reynders, T.; Telan-Choing, N. F.; Celen, S.; Bormans, G.; Serdons, K.; Van, L. K.; Tsai, K.; Walji, A.; Forman, M.; Stoch, A.; Struyk, A., Brain Imaging of Alzheimer Dementia Patients and Elderly Controls with (18)F-MK-6240, a PET Tracer Targeting Neurofibrillary Tangles. *J Nucl Med* **2019,** *60* (1), 107-114.
62. Betthauser, T. J.; Zammit, M. D.; Murali, D.; Converse, A. K.; Barnhart, T. E.; Christian, B. T.; Betthauser, T. J.; Cody, K. A.; Zammit, M. D.; Converse, A. K.; Christian, B. T.; Stone, C. K.; Rowley, H. A.; Johnson, S. C.; Johnson, S. C., In Vivo Characterization and Quantification of Neurofibrillary Tau PET Radioligand (18)F-MK-6240 in Humans from Alzheimer Disease Dementia to Young Controls. *J Nucl Med* **2019,** *60* (1), 93-99.

63. Honer, M.; Gobbi, L.; Knust, H.; Muri, D.; Koerner, M.; Borroni, E.; Kuwabara, H.; Valentine, H.; Dannals, R. F.; Wong, D. F.; Kuwabara, H.; Valentine, H.; Wong, D. F.; Wong, D. F.; Wong, D. F.; Wong, D. F., Preclinical Evaluation of (18)F-RO6958948, (11)C-RO6931643, and (11)C-RO6924963 as Novel PET Radiotracers for Imaging Tau Aggregates in Alzheimer Disease. *J Nucl Med* **2018,** *59* (4), 675-681.
64. Declercq, L.; Verbruggen, A.; Bormans, G.; Rombouts, F.; Marien, J.; Langlois, X.; Macdonald, G.; Moechars, D.; Koole, M.; Van, L. K.; Fierens, K.; Andres, J. I.; Schmidt, M.; Vanduffel, W.; Tousseyn, T.; Vandenberghe, R., Preclinical Evaluation of (18)F-JNJ64349311, a Novel PET Tracer for Tau Imaging. *J Nucl Med* **2017,** *58* (6), 975-981.
65. Fawaz, M. V.; Brooks, A. F.; Rodnick, M. E.; Carpenter, G. M.; Shao, X.; Desmond, T. J.; Sherman, P. S.; Quesada, C. A.; Hockley, B. G.; Kilbourn, M. R.; Albin, R. L.; Frey, K. A.; Scott, P. J. H., High affinity radiopharmaceuticals based upon lansoprazole for PET imaging of aggregated tau in Alzheimer's Disease and Progressive Supranuclear Palsy: synthesis, preclinical evaluation, and lead selection. *ACS Chemical Neuroscience* **2014,** *5*, 718-730.
66. Pontecorvo, M. J.; Devous, M. D., Sr.; Navitsky, M.; Lu, M.; Arora, A. K.; McGeehan, A.; Lim, N. C.; Xiong, H.; Joshi, A. D.; Siderowf, A.; Mintun, M. A.; Salloway, S.; Schaerf, F. W.; Jennings, D., Relationships between flortaucipir PET tau binding and amyloid burden, clinical diagnosis, age and cognition. *Brain* **2017,** *140* (3), 748-763.
67. Matthews, P. M.; Rabiner, E. A.; Passchier, J.; Gunn, R. N., Positron emission tomography molecular imaging for drug development. *British Journal of Clinical Pharmacology* **2012,** *73* (2), 175-186.
68. Rupprecht, R.; Papadopoulos, V.; Rammes, G.; Baghai, T. C.; Fan, J.; Akula, N.; Groyer, G.; Adams, D.; Schumacher, M., Translocator protein (18 kDa) (TSPO) as a therapeutic target for neurological and psychiatric disorders. *Nat. Rev. Drug Discovery* **2010,** *9* (12), 971-988.
69. Lacor, P.; Gandolfo, P.; Tonon, M.-C.; Brault, E.; Dalibert, I.; Schumacher, M.; Benavides, J.; Ferzaz, B., Regulation of the expression of peripheral benzodiazepine receptors and their endogenous ligands during rat sciatic nerve degeneration and regeneration: a role for PBR in neurosteroidogenesis. *Brain Research* **1999,** *815* (1), 70-80.
70. Papadopoulos, V.; Baraldi, M.; Guilarte, T. R.; Knudsen, T. B.; Lacapère, J.-J.; Lindemann, P.; Norenberg, M. D.; Nutt, D.; Weizman, A.; Zhang, M.-R.; Gavish, M., Translocator protein (18kDa): new nomenclature for the peripheral-type benzodiazepine receptor based on its structure and molecular function. *Trends in Pharmacological Sciences* **2006,** *27* (8), 402-409.
71. Lacapère, J.-J.; Papadopoulos, V., Peripheral-type benzodiazepine receptor: structure and function of a cholesterol-binding protein in steroid and bile acid biosynthesis. *Steroids* **2003,** *68* (7), 569-585.
72. Veenman, L.; Papadopoulos, V.; Gavish, M., Channel-like functions of the 18-kDa translocator protein (TSPO): regulation of apoptosis and steroidogenesis as part of the host-defense response. *Curr. Pharm. Des.* **2007,** *13* (23), 2385-2405.
73. File, S. E.; Pellow, S., RO5-4864, a ligand for benzodiazepine micromolar and peripheral binding sites: Antagonism and Enhancement of behavioural effects. *Psychopharmacology* **1983,** *80* (2), 166-170.
74. Decaudin, D.; Castedo, M.; Nemati, F.; Beurdeley-Thomas, A.; De Pinieux, G.; Caron, A.; Pouillart, P.; Wijdenes, J.; Rouillard, D.; Kroemer, G.; Poupon, M.-F., Peripheral Benzodiazepine Receptor Ligands Reverse Apoptosis Resistance of Cancer Cells in Vitro and In vivo. *Cancer Resarch* **2002,** *62*, 1388-1393.
75. Karchewski, L. A.; Bloechlinger, S.; Woolf, C. J., Axonal injury-dependent induction of the peripheral benzodiazepine receptor in small-diameter adult rat primary sensory neurons. *European Journal of Neuroscience* **2004,** *20* (3), 671-683.
76. Vowinckel, E.; Reutens, D.; Becher, B.; Verge, G.; Evans, A.; Owens, T.; Antel, J. P., PK11195 binding to the peripheral benzodiazepine receptor as a marker of microglia activation in multiple sclerosis and experimental autoimmune encephalomyelitis. *J. Neurosci. Res.* **1997,** *50* (2), 345-353.

77. McCarthy, K. D.; Harden, T. K., Identification of two benzodiazepine binding sites on cells cultured from rat cerebral cortex. *J. Pharmacol. Exp. Ther.* **1981,** *216* (1), 183-91.
78. Itzhak, Y.; Baker, L.; Norenberg, M. D., Characterization of the peripheral-type benzodiazepine receptors in cultured astrocytes: Evidence for multiplicity. *Glia* **1993,** *9* (3), 211-218.
79. Camsonne, R.; Crouzel, C.; Comar, D.; Maziere, M.; Prenant, C.; Sastre, J.; Moulin, M. A.; Syrota, A., Synthesis of N-(11C)methyl, N-(1-methylpropyl), 1-(2-chlorophenyl)isoquinoleine carboxamide-3 (PK 11195): a new ligand for peripheral benzodiazepine receptors. *J. Labelled Compd. Radiopharm.* **1984,** *21* (10), 985-91.
80. Groom, G. N.; Junck, L.; Foster, N. L.; Frey, K. A.; Kuhl, D. E., PET of peripheral benzodiazepine binding sites in the microgliosis of Alzheimer's disease. *J Nucl Med* **1995,** *36* (12), 2207-10.
81. Brown, A. K.; Fujita, M.; Fujimura, Y.; Liow, J.-S.; Stabin, M.; Ryu, Y. H.; Imaizumi, M.; Hong, J.; Pike, V. W.; Innis, R. B., Radiation dosimetry and biodistribution in monkey and man of 11C-PBR28: a PET radioligand to image inflammation. *J. Nucl. Med.* **2007,** *48* (12), 2072-2079.
82. James, M. L.; Fulton, R. R.; Vercoullie, J.; Henderson, D. J.; Garreau, L.; Chalon, S.; Dolle, F.; Selleri, S.; Guilloteau, D.; Kassiou, M., DPA-714, a new translocator protein-specific ligand: synthesis, radiofluorination, and pharmacologic characterization. *J. Nucl. Med.* **2008,** *49* (5), 814-822.
83. Damont, A.; Hinnen, F.; Kuhnast, B.; Schollhorn-Peyronneau, M.-A.; James, M.; Luus, C.; Tavitian, B.; Kassiou, M.; Dolle, F., Radiosynthesis of [18F]DPA-714, a selective radioligand for imaging the translocator protein (18 kDa) with PET. *J. Labelled Compd. Radiopharm.* **2008,** *51* (7), 286-292.
84. Wilson, A. A.; Garcia, A.; Parkes, J.; McCormick, P.; Stephenson, K. A.; Houle, S.; Vasdev, N., Radiosynthesis and initial evaluation of [18F]-FEPPA for PET imaging of peripheral benzodiazepine receptors. *Nucl. Med. Biol.* **2008,** *35* (3), 305-314.
85. Zhang, M.-R.; Kida, T.; Noguchi, J.; Furutsuka, K.; Maeda, J.; Suhara, T.; Suzuki, K., [11C]DAA1106: radiosynthesis and in vivo binding to peripheral benzodiazepine receptors in mouse brain. *Nucl. Med. Biol.* **2003,** *30* (5), 513-519.
86. Imaizumi, M.; Briard, E.; Zoghbi, S. S.; Gourley, J. P.; Hong, J.; Musachio, J. L.; Gladding, R.; Pike, V. W.; Innis, R. B.; Fujita, M., Kinetic evaluation in nonhuman primates of two new PET ligands for peripheral benzodiazepine receptors in brain. *Synapse (Hoboken, NJ, U. S.)* **2007,** *61* (8), 595-605.
87. Dolle, F.; Hinnen, F.; Damont, A.; Kuhnast, B.; Fookes, C.; Pham, T.; Tavitian, B.; Katsifis, A., Radiosynthesis of [^{18}F]PBR111, a selective radioligand for imaging the translocator protein (18 kDa) with PET. *J. Labelled Compd. Radiopharm.* **2008,** *51* (14), 435-439.
88. James, M. L.; Belichenko, N. P.; Shuhendler, A. J.; Hoehne, A.; Andrews, L. E.; Condon, C.; Nguyen, T.-V. V.; Reiser, V.; Jones, P.; Trigg, W., [18F] GE-180 PET Detects Reduced Microglia Activation After LM11A-31 Therapy in a Mouse Model of Alzheimer's Disease. *Theranostics* **2017,** *7* (6), 1422.
89. Owen, D. R.; Howell, O. W.; Tang, S.-P.; Wells, L. A.; Bennacef, I.; Bergstrom, M.; Gunn, R. N.; Rabiner, E. A.; Wilkins, M. R.; Reynolds, R.; Matthews, P. M.; Parker, C. A., Two Binding Sites for [3H]PBR28 in Human Brain: Implications for TSPO PET Imaging of Neuroinflammation. *Journal of Cerebral Blood Flow & Metabolism* **2010,** *30* (9), 1608-1618.
90. Owen, D. R.; Yeo, A. J.; Gunn, R. N.; Song, K.; Wadsworth, G.; Lewis, A.; Rhodes, C.; Pulford, D. J.; Bennacef, I.; Parker, C. A.; StJean, P. L.; Cardon, L. R.; Mooser, V. E.; Matthews, P. M.; Rabiner, E. A.; Rubio, J. P., An 18-kDa Translocator Protein (TSPO) Polymorphism Explains Differences in Binding Affinity of the PET Radioligand PBR28. *Journal of Cerebral Blood Flow & Metabolism* **2012,** *32* (1), 1-5.
91. Minghetti, L., Cyclooxygenase-2 (COX-2) in Inflammatory and Degenerative Brain Diseases. *Journal of Neuropathology & Experimental Neurology* **2004,** *63* (9), 901-910.
92. Luong, C.; Miller, A.; Barnett, J.; Chow, J.; Ramesha, C.; Browner, M. F., Flexibility of the NSAID binding site in the structure of human cyclooxygenase-2. *Nat. Struct. Biol.* **1996,** *3* (11), 927-933.

93. Phillis, J. W.; Horrocks, L. A.; Farooqui, A. A., Cyclooxygenases, lipoxygenases, and epoxygenases in CNS: Their role and involvement in neurological disorders. *Brain Research Reviews* **2006,** *52* (2), 201-243.
94. McCarthy, T. J.; Sheriff, A. U.; Graneto, M. J.; Talley, J. J.; Welch, M. J., Radiosynthesis, in vitro validation, and in vivo evaluation of 18F-labeled COX-1 and COX-2 inhibitors. *J. Nucl. Med.* **2002,** *43* (1), 117-124.
95. Prabhakaran, J.; Majo, V. J.; Simpson, N. R.; Van Heertum, R. L.; Mann, J. J.; Kumar, J. S. D., Synthesis of [11C]celecoxib: A potential PET probe for imaging COX-2 expression. *J. Labelled Compd. Radiopharm.* **2005,** *48* (12), 887-895.
96. Takashima-Hirano, M.; Takashima, T.; Katayama, Y.; Wada, Y.; Sugiyama, Y.; Watanabe, Y.; Doi, H.; Suzuki, M., Efficient sequential synthesis of PET Probes of the COX-2 inhibitor [11C]celecoxib and its major metabolite [11C]SC-62807 and in vivo PET evaluation. *Bioorganic & Medicinal Chemistry* **2011,** *19* (9), 2997-3004.
97. Ji, B.; Kumata, K.; Onoe, H.; Kaneko, H.; Zhang, M.-R.; Seki, C.; Ono, M.; Shukuri, M.; Tokunaga, M.; Minamihisamatsu, T.; Suhara, T.; Higuchi, M., Assessment of radioligands for PET imaging of cyclooxygenase-2 in an ischemic neuronal injury model. *Brain Res.* **2013,** *1533*, 152-162.
98. Shukuri, M.; Takashima-Hirano, M.; Tokuda, K.; Takashima, T.; Matsumura, K.; Inoue, O.; Doi, H.; Suzuki, M.; Watanabe, Y.; Onoe, H., In vivo expression of cyclooxygenase-1 in activated microglia and macrophages during neuroinflammation visualized by PET with 11C-ketoprofen methyl ester. *Journal of Nuclear Medicine* **2011,** *52* (7), 1094-1101.
99. Vodovotz, Y.; Lucia, M. S.; Flanders, K. C.; Chesler, L.; Xie, Q.-W.; Smith, T. W.; Weidner, J.; Mumford, R.; Webber, R.; Nathan, C., Inducible nitric oxide synthase in tangle-bearing neurons of patients with Alzheimer's disease. *Journal of Experimental Medicine* **1996,** *184* (4), 1425-1433.
100. Lee, S. C.; Zhao, M.-L.; Hirano, A.; Dickson, D. W., Inducible nitric oxide synthase immunoreactivity in the Alzheimer disease hippocampus: association with Hirano bodies, neurofibrillary tangles, and senile plaques. *Journal of neuropathology and experimental neurology* **1999,** *58* (11), 1163-1169.
101. Janssen, B.; Mach, R. H.; Vugts, D. J.; Windhorst, A. D., PET Imaging of Microglial Activation-Beyond Targeting TSPO. *Molecules* **2018,** *23* (3).
102. Abe, K.; Takai, N.; Fukumoto, K.; Imamoto, N.; Tonomura, M.; Ito, M.; Kanegawa, N.; Sakai, K.; Morimoto, K.; Todoroki, K.; Inoue, O., In Vivo Imaging of Reactive Oxygen Species in Mouse Brain by using [3H]Hydromethidine as a Potential Radical Trapping Radiotracer. *Journal of Cerebral Blood Flow & Metabolism* **2014,** *34* (12), 1907-1913.
103. Wilson, A. A.; Sadovski, O.; Nobrega, J. N.; Raymond, R. J.; Bambico, F. R.; Nashed, M. G.; Garcia, A.; Bloomfield, P. M.; Houle, S.; Mizrahi, R.; Tong, J., Evaluation of a novel radiotracer for positron emission tomography imaging of reactive oxygen species in the central nervous system. *Nuclear Medicine and Biology* **2017,** *53*, 14-20.
104. Okamura, T.; Okada, M.; Kikuchi, T.; Wakizaka, H.; Zhang, M.-R., A (11)C-labeled 1,4-dihydroquinoline derivative as a potential PET tracer for imaging of redox status in mouse brain. *Journal of Cerebral Blood Flow & Metabolism* **2015,** *35* (12), 1930-1936.
105. Brendel, M.; Jaworska, A.; Probst, F.; Overhoff, F.; Korzhova, V.; Lindner, S.; Carlsen, J.; Bartenstein, P.; Harada, R.; Kudo, Y.; Haass, C.; Van Leuven, F.; Okamura, N.; Herms, J.; Rominger, A., Small-animal PET imaging of tau pathology with 18F-THK5117 in 2 transgenic mouse models. *J. Nucl. Med.* **2016,** *57* (5), 792-798.
106. Hou, C.; Hsieh, C.-J.; Li, S.; Lee, H.; Graham, T. J.; Xu, K.; Weng, C.-C.; Doot, R. K.; Chu, W.; Chakraborty, S. K.; Dugan, L. L.; Mintun, M. A.; Mach, R. H., Development of a Positron Emission Tomography Radiotracer for Imaging Elevated Levels of Superoxide in Neuroinflammation. *ACS Chem. Neurosci.* **2018,** *9* (3), 578-586.
107. Kamel, D.; Gray, C.; Walia, J. S.; Kumar, V., PARP Inhibitor Drugs in the Treatment of Breast, Ovarian, Prostate and Pancreatic Cancers: An Update of Clinical Trials. *Curr. Drug Targets* **2018,** *19* (1), 21-37.

108. Carroll, V.; Michel, B. W.; Blecha, J.; VanBrocklin, H.; Keshari, K.; Wilson, D.; Chang, C. J., A Boronate-Caged [18F]FLT Probe for Hydrogen Peroxide Detection Using Positron Emission Tomography. *Journal of the American Chemical Society* **2014,** *136* (42), 14742-14745.
109. Carroll, V.; Truillet, C.; Shen, B.; Flavell, R.; Shao, X.; Evans, M.; VanBrocklin, H.; Scott, P.; Chin, F.; Wilson, D., [11 C] Ascorbic and [11 C] dehydroascorbic acid, an endogenous redox pair for sensing reactive oxygen species using positron emission tomography. *Chemical Communications* **2016,** *52* (27), 4888-4890.
110. Singer, T. P.; Castagnoli, N., Jr.; Trevor, A., Structural and mechanistic studies on monoamine oxidases A and B. *Neurol. Neurobiol.* **1988,** *42A* (Progr. Catecholamine Res., Pt. A), 75-82.
111. Meyer, J. H.; Ginovart, N.; Boovariwala, A.; Sagrati, S.; Hussey, D.; Garcia, A.; Young, T.; Praschak-Rieder, N.; Wilson, A. A.; Houle, S., Elevated monoamine oxidase A levels in the brain: an explanation for the monoamine imbalance of major depression. *Arch. Gen. Psychiatry* **2006,** *63* (11), 1209-1216.
112. Levitt, P.; Pintar, J. E.; Breakefield, X. O., Immunocytochemical demonstration of monoamine oxidase B in brain astrocytes and serotonergic neurons. *Proceedings of the National Academy of Sciences of the United States of America* **1982,** *79* (20), 6385-6389.
113. Fowler, J. S.; MacGregor, R. R.; Wolf, A. P. Synthesis and use of 11C-labeled suicide substrates for mapping the distribution of monoamine oxidase in living bodies by positron emission tomography. US853119A0, 1987.
114. Carter, S. F.; Schoell, M.; Almkvist, O.; Wall, A.; Engler, H.; Laangstroem, B.; Nordberg, A., Evidence for astrocytosis in prodromal Alzheimer disease provided by 11C-deuterium-L-deprenyl: a multitracer PET paradigm combining 11C-Pittsburgh compound B and 18F-FDG. *J. Nucl. Med.* **2012,** *53* (1), 37-46.
115. Cumming, P.; Yokoi, F.; Chen, A.; Deep, P.; Dagher, A.; Reutens, D.; Kapczinski, F.; Wong, D. F.; Gjedde, A., Pharmacokinetics of radiotracers in human plasma during positron emission tomography. *Synapse (N. Y.)* **1999,** *34* (2), 124-134.
116. Livni, E.; Spellman, J. P.; Correia, J. A.; Alpert, N. M.; Brownwell, G. L.; Strauss, H. W.; Elmaleh, D. R., [11C]MPTP: A potential tracer for Parkinson's Disease Research in Laboratory Animals. *J Nucl Med* **1986,** *27*, 1600-1603.
117. Hartvig, P.; Linquist, N. G.; Aquilonius, S. M.; Bergstrom, K.; Eckernas, S. A.; Gullberg, P.; Larsson, B.; Lindberg, B. S.; Lundqvist, H.; et, a. In *Regional kinetics in the brain of rhesus monkey of 11C-MPTP evaluated with positron emission tomography (PET)*, Academic: 1986; pp 615-19.
118. Chiba, K.; Trevor, A.; Castagnoli, N., Jr., Metabolism of the neurotoxic tertiary amine, MPTP, by brain monoamine oxidase. *Biochem. Biophys. Res. Commun.* **1984,** *120* (2), 574-8.
119. Heikkila, R. E.; Hess, A.; Duvoisin, R. C., Dopaminergic neurotoxicity of 1-methyl-4-phenyl-1,2,5,6-tetrahydropyridine (MPTP) in the mouse: relationships between monoamine oxidase, MPTP metabolism and neurotoxicity. *Life Sci* **1985,** *36* (3), 231-6.
120. Brooks, A. F.; Shao, X.; Quesada, C. A.; Sherman, P.; Scott, P. J. H.; Kilbourn, M. R., In Vivo Metabolic Trapping Radiotracers for Imaging Monoamine Oxidase-A and -B Enzymatic Activity. *ACS Chemical Neuroscience* **2015,** *6* (12), 1965-1971.
121. Neeper, M.; Schmidt, A. M.; Brett, J.; Yan, S. D.; Wang, F.; Pan, Y. C.; Elliston, K.; Stern, D.; Shaw, A., Cloning and expression of a cell surface receptor for advanced glycosylation end products of proteins. *Journal of Biological Chemistry* **1992,** *267* (21), 14998-5004.
122. Giri, R.; Shen, Y.; Stins, M.; Du Yan, S.; Schmidt, A. M.; Stern, D.; Kim, K.-S.; Zlokovic, B.; Kalra, V. K., β-Amyloid-induced migration of monocytes across human brain endothelial cells involves RAGE and PECAM-1. *American Journal of Physiology - Cell Physiology* **2000,** *279* (6), C1772-C1781.
123. Buckley, S. T.; Ehrhardt, C., The receptor for advanced glycation end products (RAGE) and the lung. *J Biomed Biotechnol* **2010,** *2010*, 917108.
124. Choi, B.-R.; Cho, W.-H.; Kim, J.; Lee, H. J.; Chung, C.; Jeon, W. K.; Han, J.-S., Increased expression of the receptor for advanced glycation end products in neurons and astrocytes in a triple transgenic mouse model of Alzheimer's disease. *Experimental & Molecular Medicine* **2014,** *46* (2), e75.

125. Sun, M.; Hong, Y.; Hou, X.; Ma, Y.; Shen, C.; Yin, Q.; Chen, J.; Luo, D.; Liu, X., Effect of FPS-ZM1 on the metabolism of Aβ induced by advanced glycation end products in hippocampus. *Shandong Daxue Xuebao, Yixueban* **2014,** *52* (7), 1-6, 10.

CHAPTER 2
Monoamine Oxidase B as an off-target of [^{18}F]AV-1451

1. Introduction

Control of abberant tau pathology has emerged as a leading strategy in Alzheimer's Disease (AD) treatment following the late stage failure of anti-amyloid targeting therapies. While amyloid-beta (Aβ) plaque is found extracellularly and is one of the hallmarks of AD pathology, strategies to clear Aβ and prevent further aggregation have not been successful to ameliorate cognitive impairment in patients.[1] Hyperphosphorylated tau composes the intracellular aggregate, neurofibrillary tangles (NFTs), and consistently correlates with cognition based on Braak staging.[1-2] This is an important difference and improvement upon Aβ pathology because dementia free patients have been found to be amyloid positive based on positron emission tomography (PET) imaging studies.[3] Amyloid targeting therapeutic strategies to date (outlined in chapter 1), have failed to improve cognition based outcome measures; it is the hope with NFT pathology having a higher correlation with cognition that targeting tau in both therapeutic interventions and for imaging technologies will be more successful. PET is a noninvasive, *in vivo* imaging modality that has been successfully used in multiple stages of the drug discovery and development process. AD research has benefited greatly from [^{11}C]Pittsburgh Compound B ([^{11}C]PiB: an Aβ selective agent) PET imaging for patient enrollment into clinical trials and treatment monitoring.[4] As the community shifts focus toward tau pathology, selective tau PET agents have been developed for the same uses.[5-8]

Of the first generation tau PET agents, [^{18}F]AV-1451 (flortaucipir, [^{18}F]T807), has been most widely used in clinical studies.[9-22] In AD patients, [^{18}F]AV-1451 standard uptake value ratio (SUVR) was significantly higher with more advanced clinical stage (AD > mild cognitive impairment > older cognitively normal).[19] Furthermore, when these patients were classified based on Aβ load (+ or -), the pattern of [^{18}F]AV-1451 distribution in Aβ+ was similar to cross-sectional distribution of tau reported in post-mortem pathologies.[19] In addition to imaging AD patients, [^{18}F]AV-1451 has been used to evaluate sporadic Creutzfield-Jakob disease (CJD). CJD is a rare human prion disease with rapidly progressive dementia, in which tau pathology has been found cerebral spinal fluid. However, *in vivo* [^{18}F]AV-1451 PET imaging suggested no unique pattern of retention in the brain.[11] In order to differentiate AD from the related dementia with Lewy bodies (DLB), [^{18}F]AV-1451 has been investigated as a possible tool. Kantarci and coworkers found the AD dementia group had a significantly higher uptake in the medial temporal lobe than the DLB group.[15] However, diagnosis requires a complete understanding of the PET ligand and its binding pattern- and there is documented non-tau, or "off-target" binding of [^{18}F]AV-1451.

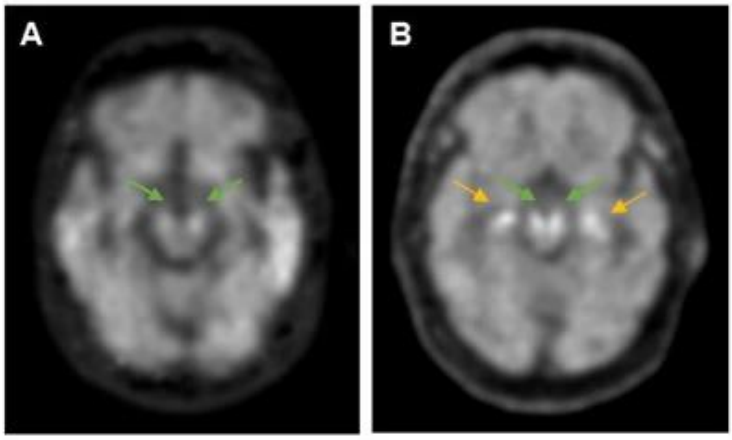

Figure 2.1. Human [^{18}F]AV-1451 PET Scans. A. MCI. B. Cognitive Normal. Green arrows point to the substantia nigra. Yellow arrows point to the choroid plexus.

Through our own analysis, we have observed tracer accumulation in the substantia nigra and choroid plexus regions in both MCI and cognitively normal patients (figure 2.1). Time activity curves of these regions of interest reveal slower clearance, which might indicate specific binding. Independent validation efforts from several groups have confirmed localization of this tracer with NFTs, visualized by immunological methods, while simultaneously revealing off-target tracer accumulation, particularly to pigmented cells of both the CNS and the periphery.[10, 16] While [^{18}F]AV-1451 binds to these cells, it should be noted that no biochemical assays have been conducted to confirm off-target binding to neuromelanin itself (as opposed to a cellular component which may be found with melanin and in neuromelanin-containing cells). The choroid plexus is near the hippocampus and the concern for nonspecific binding is that this signal will spill over into the region of interest. A human clinical trial was performed to evaluate any binding differences in the choroid plexus (CP) between African American participants compared to white participants; the rationale being that melanin and melanocytes are higher in African American participants.[9] Although no race differences were found, high CP signal affected the measurement in the hippocampus.[9]

Neuromelanin containing cells, chiefly in the substantia nigra are known to be involved in the dopaminergic system and to contain high amounts of monoamine oxidase (MAO).[23] *In vitro* studies have revealed high-affinity interactions between [^{18}F]AV-1451 and MAO;[24-25] however, it is not yet confirmed if these results translate to human imaging. Hansen and coworkers retrospectively analyzed a small cohort of patients taking MAO-B inhibitors and its effect on [^{18}F]AV-1451 binding and retention.[26] While their results indicate no effect on uptake, binding, nor retention, it is critical to note that these patients were determined to be tau negative. Another limitation of this study is the lack of paired block and unblocked data, as well as the

unknown length of time the patients had been taking MAO inhibitors. It is known from [^{11}C]deprenyl-d_2 ([^{11}C]DED: an irreversible MAO-B inhibitor) imaging that therapeutic doses successfully block MAO to an extreme extent and that it can take up greater than 3 weeks to recycle those enzymes.[27] Performing this study in patients who chronically take MAO inhibitors would essentially ensure no effect could be observed, because the enzyme would still be inhibited therapeutically.

A different first generation tau PET ligand, [^{18}F]THK5351 also suffers from off-target binding to MAO. *In vivo* [^{18}F]THK5351 retention was observed in areas not associated with tau, and it was noted that [^{18}F]THK5351 SUVR was significantly correlated to MAO-B level.[28] In a prospective study, using MAO inhibitor naïve patients, Ng and coworkers demonstrated a significant difference in [^{18}F]THK5351 binding and retention after pretreatment with deprenyl.[29] The confirmation of off-target binding to MAO-B *in vivo* has significantly limited the use of this radioligand. The finding from this prospective study, and the limitations of the retrospective [^{18}F]AV-1451 trial,[26] encouraged us to continue the investigation into [^{18}F]AV-1451's off-target binding.

Off-target binding of ligands used for PET imaging is problematic when distinct regions of brain structures need to be compared. In tau imaging, brain structures in the medial temporal lobe are important because tau pathology is considered to begin forming in the entorhinal cortex.[30] The neighboring hippocampus is a region often used to determine "positivity" in tau PET imaging as well; it is more associated with Braak stages IV and V.[2] In the case of [^{18}F]AV1451, the choroid plexus (CP) and substantia nigra (SN) are very close to these structures and the off target binding could "spill" into these regions of interest; this would cause an artificial increase in the signal. Furthermore, the proposed off-target binding partner MAO-B

has significant expression in the reference region, the cerebellar gray cortex.[31] In human PET imaging, the measure SUVR is often used. This is the standard uptake value ratio of the region of interest normalized to the reference region. Ideally, the reference region is void of specific binding. If [^{18}F]AV-1451 is binding to MAO-B *in vivo*, it is very possible that this effect is not only responsible for the SN retention, but also could be affecting the SUVR measure through specific binding in the cerebellum.

Herein, we report the *in vitro* and *in vivo* evaluation of [^{18}F]AV-1451 in respect to its binding to MAO. Inhibition assays with MAO-A and MAO-B confirmed that it is an inhibitor for both isozymes. In respect to the brain, MAO-B is more highly abundant[32] and was the focus for studies using post-mortem human brain tissue sections. *In vivo* blocking studies were performed in healthy non-human primates to monitor the influence of reversible MAO inhibitors on [^{18}F]AV-1451 binding and retention.

2. Results

In Vitro Binding Assessment

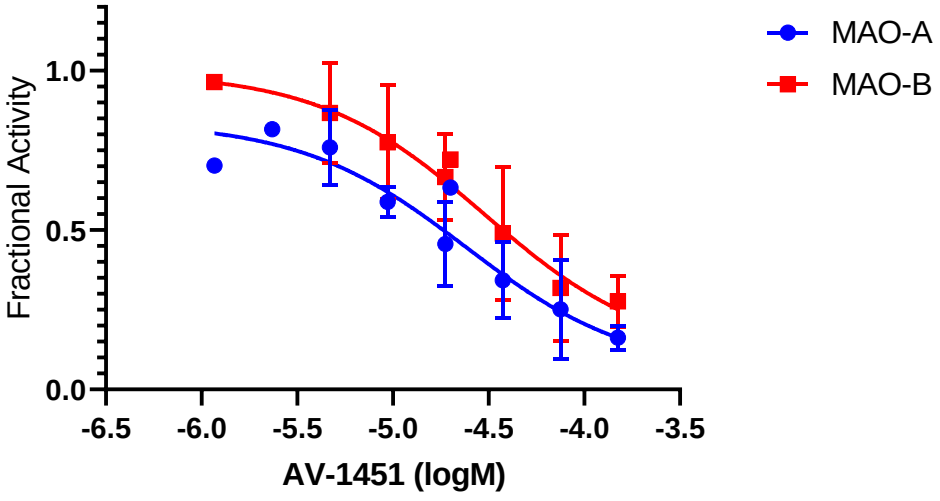

Figure 2.2. AV-1451 inhibition of MAO-A and MAO-B turnover. MAO-A: K_i = 10.48 μM, R^2 = 0.8132, n = 4; MAO-B: K_i = 15.14 μM, R^2 = 0.8285, n = 4.

MAO-A and MAO-B inhibition assays revealed AV-1451 is a weak, nonselective inhibitor of both enzymes (figure 2.2). Activity assay used the previously described Cou substrate and monitored the appearance of fluorescent product.[33] Substrate was used at K_M for MAO-A and –B respectively, IC_{50}'s and K_i's were calculated using GraphPad Prism 7.02.

[^{18}F]AV-1451 MAO-B binding was further evaluated on postmortem human brain tissue sections in the presence of the irreversible inhibitor deprenyl. Substantia nigra (SN) and cerebellum (CBL) sections were used in this study because of the nonspecific binding observed in the substantia nigra during human [^{18}F]AV-1451 PET scans and the cerebellum's use as a reference region. Specific binding of [^{18}F]AV-1451 to tissue was determined from subtraction of the total binding signal from nonspecific binding (in excess of [^{19}F]AV-1451). Specific binding was approximately 400 times higher in diseased SN sections in comparison to age matched control SN sections; this increase is consistent to a much lesser extent in CBL sections. Total binding of [^{18}F]AV-1451 was significantly diminished in competition with deprenyl in both SN and CBL sections (figure 2.3). Cognitive normal tissue sections for both SN and CBL did not have statistically significant differences in [^{18}F]AV-1451 total compared to nonspecific, nor the MAO-B inhibition challenges.

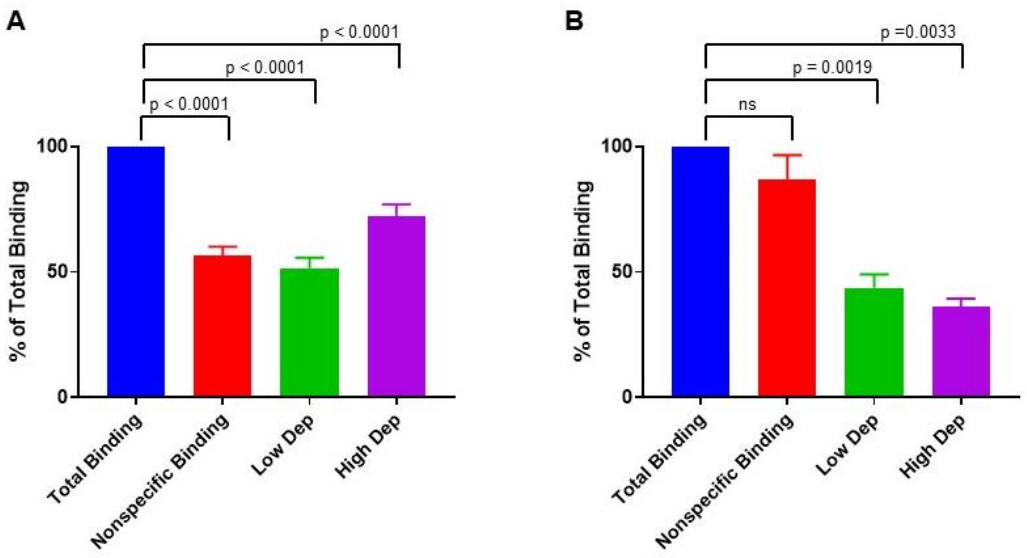

Figure 2.3 [^{18}F]AV-1451 binding to human brain tissue sections. A, substantia nigra (SN), B, cerebellum (CBL). Binding is normalized to section area and individual experimental dose (range +/- sem, n=4). Average +/- standard error of the mean is shown for four diseased individuals. Specific binding was calculated as the difference of nonspecific binding from total. Averages are shown as percent of total binding. Low deprenyl challenge was 500 nM, high deprenyl is excess. Significance calculated using Tukey's multiple comparisons test.

Immunohistochemistry was performed on these postmortem tissue sections to determine the relationship between [^{18}F]AV-1451 binding, MAO-B expression, and tau load. Compared to sections from age-matched controls, MAO-B immunoreactivity was 3-fold higher in diseased SN sections and 2-fold higher in diseased CBL sections (figure 2.4). In the AD and DLB conditions, where substantia nigra and cerebellum tissue from the same patient was available, MAO-B immunoreactivity was ~4 times higher in the substantia nigra compared to the cerebellum, while anti-tau reactivity was only found in the diseased SN sections. Pearson correlation tests were performed to compare MAO-B or tau immunoreactivity and the various [^{18}F]AV-1451 binding conditions. The only significant correlation found was MAO-B immunoreactivity and [^{18}F]AV-1451 total binding in diseased SN tissue sections (figure 2.5; r= 0.9592, p= 0.0408).

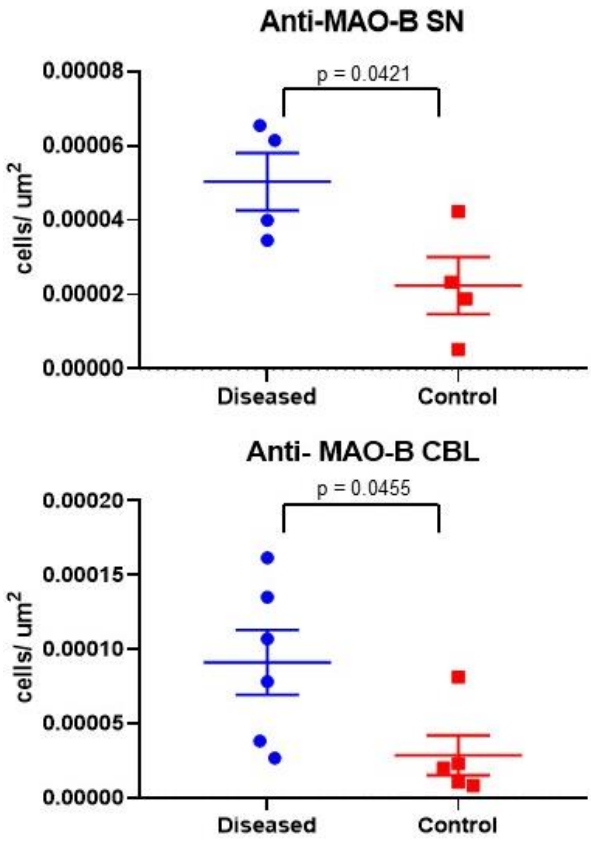

Figure 2.4. Immunoreactivity on postmortem human brain tissue sections. Top: substantia nigra (SN) sections comparing diseased brain tissue to cognitive normal control for MAO-B immunoreactivity. Bottom: cerebellum (CBL) sections comparing diseased brain tissue to cognitive normal control for MAO-B immunoreactivity.

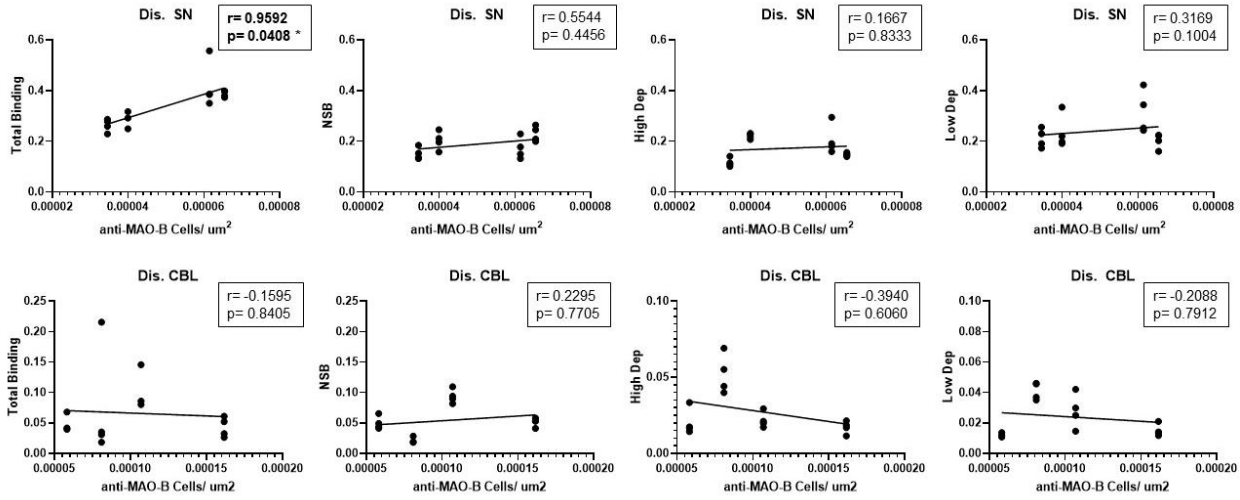

Figure 2.5. Correlations between MAO-B immunoreactivity and [^{18}F]AV-1451 binding. Pearson correlations calculated in GraphPad Prism 8.01, individual boxes display the calculated r and p values. * indicates significance.

Small Animal Blocking Studies

In nonhuman primate brain, blocking with the reversible MAO-A inhibitor moclobemide resulted in a modest increase in SUV_{peak} in the cerebellum and basal ganglia, while pretreatment with the reversible MAO-B inhibitor lazabemide produced minor increases in the SUV_{peak} of the two regions (figure 2.6). SUV values in the final four frames of imaging (approximately 55, 65, 75, and 85 minutes post-injection) for a region of interest were averaged and divided by the averaged cerebellar SUV to afford SUVRs (figure 2.7). Following pretreatment with lazabemide, the normalized value in the basal ganglia increased slightly, while blocking with moclobemide decreased.

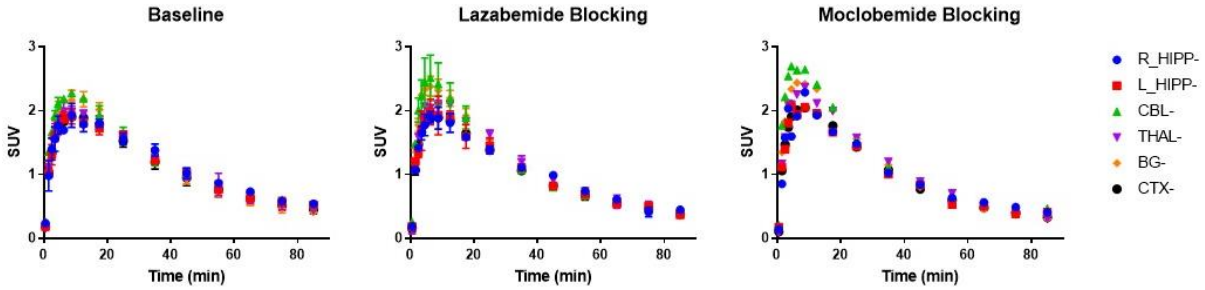

Figure 2.6 [^{18}F]AV-1451 time activity curves of nonhuman primate brain PET imaging studies. Summed frames presented as SUV. R_HIPP- right hippocampus, L_HIPP- left hippocampus, CBL- cerebellum, THAL- thalamus, BG- basal ganglia, CTX- cortex.

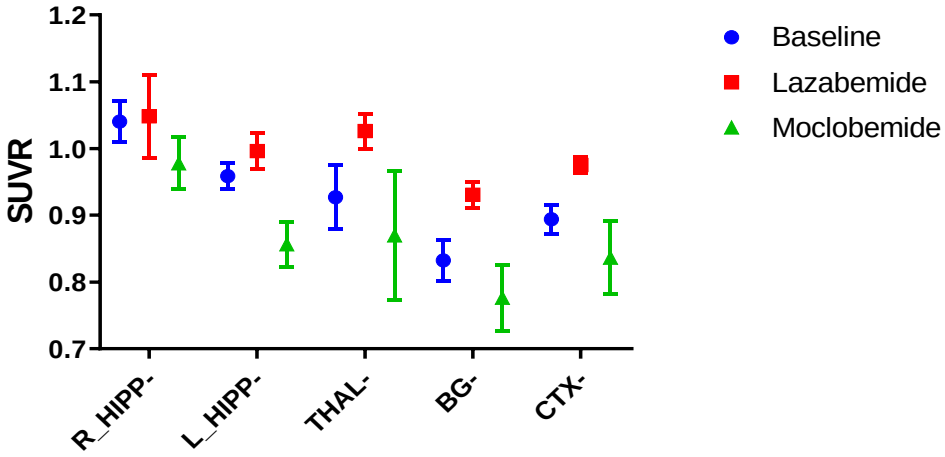

Figure 2.7. Averaged last four frames of dynamic PET scan in nonhuman primate brain. (n=2/ study) normalized to cerebellum.

3. Discussion

Tau PET imaging is a popular shift in neurodegenerative research from amyloid imaging, and however popular, it has noted limitations.[7] It is widely acknowledged AV-1451 shows nonspecific binding in the substantia nigra region.[34] Several groups have independently investigated this phenomenon with conflicting results regarding the cause of this off-target binding.[35-36] While an *in vitro* screen reported during AV-1451's initial development did not identify any binding partners that warranted a toxicity concern,[37] several groups, including our own, have identified MAO-B as a significant off-target binding partner.[38-39]

[^{18}F]AV-1451 shares this burden with other first generation tau tracers like [^{18}F]THK5351, which also was shown to have significant binding to MAO-B, both on tissue and in human PET imaging studies with a MAO-B inhibitor.[29, 40] Despite longstanding concerns regarding binding to MAO, [^{18}F]AV-1451 has not been evaluated in a similar prospective study. Hansen and coworkers evaluated a retrospective cohort and determined no influence of MAO inhibitors on AV-1451 binding, though the scope of this study was limited.[26]

Human [^{18}F]AV-1451 scans performed in our PET center have revealed binding in the substantia nigra, which appears to be specific based on a slower clearance compared to the reference region (figure 2.1). This finding and the aforementioned debate in the community about nonspecific binding led our *in vitro* investigation into [^{18}F]AV-1451. In our previously developed activity assay, AV-1451 was determined to be a non-selective inhibitor of MAO-A and –B (MAO-A: K_i = 10.48 μM; MAO-B: K_i = 15.14 μM). Though not a strong inhibitor, it is similar to the behavior of a structurally related compound, norharmane (MAO-A: K_i = 19.63 μM; MAO-B: K_i = 8.52 μM). Norharmane, despite this relatively weak inhibitory constant, is a

classically used MAO inhibitor (figure 2.8). AV-1451 has a γ- carboline ring system, while norharmane has a β- carboline ring system.

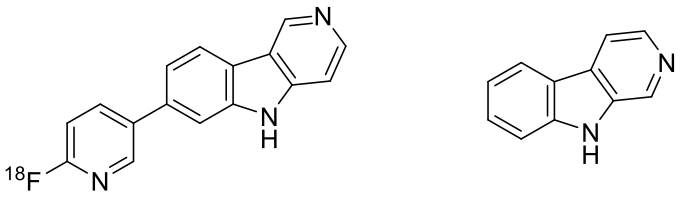

[^{18}F]AV-1451 **Norharmane**

Figure 2.8. Structures of AV-1451 and Norharmane.

Using postmortem tissue, we challenged the binding of [^{18}F]AV-1451 with co-incubation of the radioligand and the irreversible MAO-B inhibitor deprenyl (K_i= 90 nM). Deprenyl significantly lowered radioligand binding in both diseased and age-matched control SN and CBL tissue sections. The specific binding of [^{18}F]AV-1451 is low (~50%) and deprenyl blocking closely mirrors the magnitude of nonspecific binding in these experiments. We believe this to be the first published study of competition between [^{18}F]AV-1451 and an MAO-B inhibitor using autoradiographic methods on frozen brain tissue.

Independent autoradiography with [^{18}F]AV-1451 has been performed by multiple groups, with conflicting results likely stemming from variation in methods. While the original report characterizing [^{18}F]AV-1451 did not contain autoradiography studies, it described above 50% inhibition at the norepinephrine transporter (NET), vesicular monoamine transporter (VMAT), N-methyl-D-aspartate (NMDA) receptor, and mu opioid receptor at 10 μM. The authors also declared no inhibition of MAO-A/B at 1 μM, and thus no concern for toxicity.[41] At tracer quantities, toxicity is almost never a concern, nonspecific binding however is often considered. In 2015, it was reported that the "neuromelanin containing cells" in the substantia nigra was a robust area of off-target binding for [^{18}F]AV-145.[34] The methods used for this tissue experiment were highly unorthodox however, fixing frozen sections in 100% methanol before binding with

the radioligand, and washing with ethanol.[34] Fixing frozen tissue is almost never used in autoradiography because of the significant changes that occur in the membrane; to observe small molecule binding in a more "*in vivo*"-like system, hydrated frozen tissue is the standard. Fixed tissue is more commonly used in immunohistochemical experiments. Especially with a molecular target such as NFTs, with multiple possible binding sites, every aspect of the experimental design needs to be considered for its influence. When Pike and coworkers at the NIH evaluated [^{3}H]AV-1451 and another first generation tau tracer, [^{3}H]THK523, freeze-thaw and buffer effects were evaluated rigorously on the human brain homogenates.[42] The authors found that the best conditions for reproducibility when using AD brain tissue homogenate was to re-homogenize the tissue after thawing, to treat the suspension to a high-power ultrasonic probe, and to use 0.1% Tween-20 in PBS as the assay medium.

Also in 2015, the other first generation tau tracers developed at Tohuku University were being evaluated for MAO binding.[29,43] The group responded to this report with their own investigation and confirmed the finding of [^{18}F]THK5351 and [^{18}F]THK532 as MAO binding partners.[44] Through further binding experiments, [^{18}F]AV-1451 was found to have nanomolar affinity to MAO-A (K_d= 1.6 nM) and could be competed with clorgyline (irreversible MAO-A inhibitor).[38] While Merck was developing their own tau tracer, [^{18}F]MK-6240, MAO binding became a concern. Hostetler and coworkers confirmed clorglyine competition decreases [^{3}H]AV-1451 binding in human brain homogenates.[45] Again, these studies utilized fresh frozen and rehydrated brain tissue, not fixed. There also could be a difference in the experimental specific binding when alcoholic buffers are used in the wash steps. Arstad[43] and Marquie[34] describe very low nonspecific binding in comparison to what we've observed experimentally, and this could be directly related to differences in wash steps.

Immunoreactivity studies determined a significant increase in MAO-B abundance in diseased substantia nigra, and a significant correlation was found between total [^{18}F]AV-1451 binding and MAO-B immunoreactivity in this tissue. Despite the significant difference in MAO-B immunoreactivity in the diseased CBL compared to cognitive normal, a similar correlation was not found with total [^{18}F]AV-1451 total binding (figure 2.5). It is possible the trend could not be observed because of the high variability observed across individuals in this region and also due to the lack of tau in this region.[46] Through our autoradiography methodology, no observable specific binding was found in the cerebellum (figure 2.3); however, there was a significant effect when challenged with deprenyl. This result in combination with the high abundance of MAO-B as measured in immunoreactivity, suggests the presence of binding to MAO-B in the cerebellum. However, binding that can be displaced by deprenyl, but not AV-1451, would not be classified as nonspecific. This result requires more interpretation and possible follow up studies.

To further investigate the role of MAO in the substantia nigra and cerebellum, [^{18}F]AV-1451 PET scans were done in healthy nonhuman primates. In the brain of the rhesus macaque, [^{18}F]AV-1451 distributes nonspecifically (as would be expected in a non-diseased model), though it is interesting that SUV is highest in the cerebellum. Standardizing "equilibrium" [^{18}F]AV-1451 retention to cerebellar uptake disproportionately masks the decrease in SUV resulting from MAOI pretreatment in the nonhuman primate brain (figure 2.7). In fact, it has been suggested that the clinical interpretation of [^{18}F]AV-1451 scans should not rely on the use of the cerebellum as a reference region because of concerns regarding off-target binding, and our work supports that suggestion by the significant abundance of MAO-B and displaceability on tissue. While both of these preclinical models are non-diseased, these studies suggest that the *in*

vitro blocking effects of MAO inhibitors could reasonably translate to signal displacement in a prospective human investigation.

While these experiments have several limitations, we hope to encourage the tau PET community to continue vetting [^{18}F]AV-1451 and other tau PET agents in human use. Enzymatic activity assays and tissue binding assays are limiting because they can be heavily influenced by experimental procedure. We aimed to provide a logical experimental design, in particular with our handling of post-mortem human tissue. The nonhuman primate PET scans shown do not include arterial input correction, and we have tried to remedy this by considering the later frames of the scan. Despite these limitations, our data indicate AV-1451 inhibits monoamine oxidase activity *in vitro* and binds to MAO-B on tissue sections. *In vivo,* MAO inhibitors change the uptake of AV-1451 in the cerebellum, the reference region for tau PET.

Furthermore, our interest in monoamine oxidase extends beyond its role as an off-target binding partner for this tracer. MAO-B is a marker of astrocytosis, with evidence for its co-expression with amyloid plaques dating back to the early 1980's.[47-50] The changes of MAO-B activity itself has been investigated with irreversible inhibitors, reversible inhibitors, and substrates in PET imaging. It is quite unfortunate that not only does AV-1451 have an off-target binding partner, but that this binding partner also has a role in neurodegeneration. Our immunoreactivity studies show that MAO-B expression is increased in diseased substantia nigra and cerebellum sections, meaning observed changes in AV-1451 uptake in those regions may not be from tau deposition alone. From these *in vitro* and *in vivo* findings, we assert that a prospective study into the influence of MAO-B on [^{18}F]AV-1451 PET scans is necessary. To truly interpret SUVR, we need to understand the binding events in the cerebellum.

4. Methods

Radiochemistry

[^{18}F]AV-1451 was prepared as previously described, by Dr. Andy Mossine.[51] The synthesis of [^{18}F]AV-1451 was fully-automated using a General Electric (GE) TRACERLab FX_{FN} synthesis module. [^{18}F]Fluoride (~1400 mCi) was produced via the $^{18}O(p,n)^{18}F$ nuclear reaction with a GE PETtrace cyclotron equipped with a high-yield fluorine-18 target. [^{18}F]Fluoride was delivered in a 1.5-mL bolus of [^{18}O]H_2O to the synthesis module and trapped on a QMA-Light sep-pak cartridge to remove [^{18}O]H_2O. [^{18}F]Fluoride was then eluted into the reaction vessel with potassium carbonate (3.5 mg in 500 μL of water). The solution of $K_{2.2.2}$ (15 mg in 1 mL of ethanol) was added to the reaction vessel, and the [^{18}F]fluoride was azeotropically dried by heating the reaction vessel to 100 °C and drawing full vacuum for 6 min. After this time, the reaction vessel was subjected to both an argon stream and a simultaneous vacuum draw for 9 min at 100 °C. The solution of AV-1451 N-Boc nitro-precursor in DMSO (0.5 mg in 500 μL) was added to the dried [^{18}F]fluoride, and was heated to 130 °C with stirring for 10 min. Subsequently, the reaction mixture was cooled to 50 °C, diluted with HPLC mobile phase (3 mL), and purified by semi-preparative HPLC (column: Phenomenex Gemini NX C18, 5 micron, 10x250 mm; mobile phase: 40% Ethanol 10 mM Na_2HPO_4 pH: 9.3 ± 0.2; flow rate: 3 mL/min; UV: 254 nm). The product peak (t_R = 21–22 min) was collected into the dilution flask where it was concomitantly diluted with 50 mL of sterile water. The resulting solution was passed through an Oasis HLB cartridge, which was then washed with 10 mL of sterile water. [^{18}F]AV-1451 was eluted with 0.5 mL of EtOH (USP for injection) and collected in the Tracerlab FX_{FN} product vial, containing 3 mL of saline (USP). The Sep-Pak was washed with 6.5 mL of saline to bring the final formulation volume to 10 mL. The final drug product was

dispensed into a septum sealed, sterile, pyrogen-free glass vial through a 0.22 μm sterile filter and submitted for QC testing.

Human Brain Imaging

Potential research subjects were identified by the investigators from the Neurology Cognitive Disorders and Movement Disorders clinics (IRB study#: HUM00124161). Eligibility screening involved review of existing medical records to establish diagnosis and absence of exclusionary criteria. Subjects were positioned on the PET scanner table, lying comfortably on their back. They were asked to lie quietly, to stay awake and to keep their eyes open. A low-dose X-ray CT scan of the head was performed for attenuation correction of emission PET images. [^{18}F]AV-1451 was injected as an IV bolus and dynamic PET imaging began immediately for 60 minutes: 4 x 30 sec frames; 3 x 1 min frames, 2 x 2.5 min frames; 6 x 5 min; 2 x 10 min. After a several minute break, additional brain images were made from 75 – 105 minutes: 3 x 10 min.

MAO Inhibition Assay

Off-target binding of [^{19}F]AV-1451 was assessed *in vitro* by quantifying the inhibition of 4-methyl-7-((1-methyl-1,2,3,6-tetrahydropyridin-4-yl)oxy)-2H-chromen-2-one (Cou) turnover by recombinant human MAO as previously reported.[33] Briefly, inhibition was determined using human MAO-A and –B Supersomes (Corning Gentest) at a concentration of 80 μg/ml. Fresh stocks of Cou was dissolved in DMSO to give a 10 mM stock and subsequently diluted in borate buffer (pH 8.4) to 40 μM (MAO-A) and 1 μM (MAO-B). Fresh AV-1451 stock was dissolved in DMSO and further diluted for the assay range 1 to 300 μM. Reaction progress was measured by appearance of fluorescent product, 7-hydroxy-4-methyl-coumarin. Reactions were monitored in real time using a Biotek Hybrid plate reader (excitation 360nm, emission 460 nm) at 37°C;

reactions progressed for 60 minutes and fluorescent reads were measured every 5 minutes. The resultant fluorescence units were converted to concentration of product using a reference standard curve. Inhibition curves were plotted and parameters computed in GraphPad Prism (version 7.03). Assays were done in duplicate, in two independent experiments using fresh stock of enzyme, test compound, and reference standard. Outliers which met the Grubb's test were removed.

Human Tissue Studies.

Tissue Preparation.

Postmortem brain tissue from Alzheimer's disease, Dementia with Lewy Bodies, and age-matched cognitively normal patients was obtained from the University of Michigan Alzheimer's Disease Center Brain Bank. Brain sections were cut using a microtome to 20 µm sections and thaw-mounted onto poly-lysine coated glass slides. Slides utilized for immunohistochemistry were fixed in Davidson's fixative (8.1% formaldehyde, 33.3% ethanol, 11.1% acetic acid, Eosin Y stain) for 24 hours and then rinsed with 70% ethanol to remove residual formaldehyde before use. Slides utilized for autoradiography were stored at -80 °C until the day of experiment.

Immunohistochemistry

Fixed tissue sections were incubated in PBS with 1% SDS for 5 min. Sections were then washed 3 x 5 min in PBS before quenching in 70% methanol with 0.3% hydrogen peroxide for 15 min. All slides were washed 3 x 5 min in PBS-T (PBS, 0.4% Triton-X-100, pH 7.4) and blocked for 30 min with PBS-TBA (PBS, 0.4% Triton-X-100, 1% BSA, 0.025% sodium azide, pH 7.4) before incubating in a 1:200 dilution of primary antibody (anti-tau (R&D Systems, AF3494, 1:200) and MAO-B (Invitrogen, PIPA528338,1:200) in PBS-TBA overnight. Finally,

brain sections were washed 3 x 5 minutes in PBS-T to remove unbound antibody. Tissue sections were incubated in a 1:200 dilution of secondary antibody (anti-goat-IgG, Vector Laboratories BA-5000, anti-rabbit-IgG, Vector Laboratories BA-1000) in PBS-TBA for 2 hr and washed 3 x 5 min with PBS-T. All incubations were carried out at room temperature. Slides were developed as instructed using the VECTASTAIN Elite ABC Kit (Standard) (Vector Laboratories PK-6100). Tissue sections were then washed 3 x 5 min in PBS-T before incubating for 4 min in a 0.5% w/v solution of diaminobenzidine in PBS-T (filtered) with 0.001% hydrogen peroxide. Giemsa counterstaining was utilized to visualize nucleus and cytoplasm in cells. Tissue sections were washed for 5 min in dH_2O prior to overnight incubation in a 1:50 solution of Giemsa in dH_2O. Slides were then rinsed for 30 sec in dH_2O, 2 x 4 min in n-butanol, and 1 min in xylene. Permount was applied to the fixed tissue to attach coverslips to the polylysine-coated glass slides and allowed to set for 45 min prior to quantification. All incubations were carried out at room temperature.

Two tissue sections from each individual were used for each primary antibody and counted. Immunoreactivity was quantified using StereoInvestigator. A region was drawn around the entire tissue section and using the serial section manager, 5% of the section was counted and picked using a randomized rotation. Immunoreactivity is presented as cells/ μm^2. Statistical analyses were performed in GraphPad Prism (8.01).

Autoradiography

Off-target binding of [^{18}F]AV-1451 on tissue was assessed by autoradiography in sections from the substantia nigra and cerebellum. Brain sections on slides were removed from -80°C freezer and thawed at room temperature for 5 min before rehydration in phosphate buffer saline (PBS, pH 7.4) for another 5 min. Tissue sections were incubated with [^{18}F]AV-1451 in the

presence or absence of the irreversible MAO-B inhibitor L-Deprenyl at two concentrations (500 nM and in excess). All sections were washed 3 x 2 min with PBS at 4 °C and then rinsed in dH_2O for 30 sec at 4 °C to remove unbound radioactivity. Finally, slides were dried under the continuous airflow for 30 min before exposure to a high-resolution phosphoimaging plate for 10 minutes. The exposed plate was scanned using a GE Typhoon FLA 7000 phosphoimager. Image analysis was performed using ImageQuant (Molecular Dynamics) software. Regions of interest were drawn and converted to nmole specific molar activity.

Primate Imaging.

General Considerations.

All animal studies were performed in accordance with standards set by the University of Michigan Institutional Animal Care and Use Committee (IACUC).

Primate imaging studies.

Imaging was done using mature female rhesus macaques (n=2, 4.673 ± 0.425 mCi, weight = 8.25 ± 0.15 kg). The monkey was anesthetized (isoflurane), intubated, and positioned in a Concorde MicroPET P4 scanner. Pharmacological intervention with the reversible inhibitors moclobemide (MAO-A selective, 1 mg/kg) or lazabemide (MAO-B selective, 0.5 mg/kg) was administered by infusion 10 minutes prior to tracer injection. Following a transmission scan, the animal was injected i.v with [^{18}F]AV-1451 (4.673 ± 0.425 mCi, n=5) as a bolus over 1 min, and the brain imaged for 90 min (5 x 1 min frames – 2 x 2.5 min frames – 2 x 5 min frames – 7 x 10 min frames).

Image Analysis.

Emission data were corrected for attenuation and scatter, and reconstructed using the 3D maximum a priori method (3D MAP algorithm). Using a summed image of the entire data set,

3D volumes of interest (VOI) were determined by placing a seed voxel in the middle of various brain regions, and then using region- specific thresholds to automatically determine the extent of each VOI. VOIs were determine for the whole brain, striatum, thalamus, cortex, hippocampus, and cerebellum. Previous data sets in the same primate were used as reference determining specific VOIs ([^{11}C]Flumazenil for cortex and cerebellum, [^{11}C]DTBZ for striatum, [^{11}C]Carfentenil for thalamus and hippocampus). The VOIs were then applied to the full dynamic data sets to obtain the regional tissue time-radioactivity curves. Time activity curves were normalized between studies by the animal weight and amount of activity injected to result in percent injected dose per gram.

5. References

1. Giacobini, E.; Gold, G., Alzheimer disease therapy—moving from amyloid-β to tau. *Nature Reviews Neurology* **2013,** *9*, 677.
2. Braak, H.; Braak, E., Neuropathological stageing of Alzheimer-related changes. *Acta neuropathologica* **1991,** *82* (4), 239-259.
3. Engler, H.; Klunk, W.; Nordberg, A.; Blomqvist, G.; Holt, D.; Wang, Y.; Bergström, M.; Huang, G.-f.; Estrada, S.; Debnath, M.; Barletta, J.; Sandell, J.; Wall, A.; Antoni, G.; Mathis, C.; Långström, B. In *First PET Study with a Benzothiazol Amyloidimaging Agent (PIB) in Alzheimer's Disease Patients and Healthy Volunteers*, The Living Brain and Alzheimer's Disease, Berlin, Heidelberg, 2004//; Hyman, B. T.; Demonet, J.-F.; Christen, Y., Eds. Springer Berlin Heidelberg: Berlin, Heidelberg, 2004; pp 123-137.
4. van Dyck, C. H., Anti-Amyloid-β Monoclonal Antibodies for Alzheimer's Disease: Pitfalls and Promise. *Biological Psychiatry* **2018,** *83* (4), 311-319.
5. Lois, C.; Johnson, K. A.; Gonzalez, I.; Price, J. C., PET imaging of tau protein targets: a methodology perspective. *Brain Imaging Behav* **2018**.
6. Barrio, J. R., The Irony of PET Tau Probe Specificity. *Journal of Nuclear Medicine* **2018,** *59* (1), 115-116.
7. Klunk, W. E., Molecular imaging: What is right and what is an illusion? *Alzheimer's & Dementia: Diagnosis, Assessment & Disease Monitoring* **2018,** *10*, 217-220.
8. Schoell, M.; Maass, A.; Mattsson, N.; Ashton, N. J.; Blennow, K.; Zetterberg, H.; Jagust, W., Biomarkers for tau pathology. *Mol. Cell. Neurosci.* **2018**, Ahead of Print.
9. Lee, C. M.; Jacobs, H. I. L.; Marquie, M.; Becker, J. A.; Andrea, N. V.; Jin, D. S.; Schultz, A. P.; Frosch, M. P.; Gomez-Isla, T.; Sperling, R. A.; Johnson, K. A., 18F-Flortaucipir Binding in Choroid Plexus: Related to Race and Hippocampus Signal. *J. Alzheimer's Dis.* **2018,** *62* (4), 1691-1702.
10. Coakeley, S.; Cho, S. S.; Koshimori, Y.; Rusjan, P.; Ghadery, C.; Kim, J.; Lang, A. E.; Houle, S.; Strafella, A. P., [18F]AV-1451 binding to neuromelanin in the substantia nigra in PD and PSP. *Brain Struct. Funct.* **2018,** *223* (2), 589-595.
11. Day, G. S.; Gordon, B. A.; Perrin, R. J.; Cairns, N. J.; Beaumont, H.; Schwetye, K.; Ferguson, C.; Sinha, N.; Bucelli, R.; Musiek, E. S.; Ghoshal, N.; Ponisio, M. R.; Vincent, B.; Mishra, S.; Jackson, K.; Morris, J. C.; Benzinger, T. L. S.; Ances, B. M., In vivo [(18)F]-AV-1451 tau-PET imaging in sporadic Creutzfeldt-Jakob disease. *Neurology* **2018,** *90* (10), e896-e906.
12. Utianski, R. L.; Whitwell, J. L.; Schwarz, C. G.; Jack, C. R., Jr.; Senjem, M. L.; Tosakulwong, N.; Duffy, J. R.; Clark, H. M.; Machulda, M. M.; Petersen, R. C.; Lowe, V. J.; Josephs, K. A., Tau-PET imaging with [18F]AV-1451 in primary progressive apraxia of speech. *Cortex* **2018,** *99*, 358-374.
13. Hammes, J.; Leuwer, I.; Bischof, G. N.; Drzezga, A.; van Eimeren, T., Multimodal correlation of dynamic [18F]-AV-1451 perfusion PET and neuronal hypometabolism in [18F]-FDG PET. *Eur. J. Nucl. Med. Mol. Imaging* **2017,** *44* (13), 2249-2256.
14. Marquie, M.; Siao Tick Chong, M.; Anton-Fernandez, A.; Verwer, E. E.; Saez-Calveras, N.; Meltzer, A. C.; Ramanan, P.; Amaral, A. C.; Gonzalez, J.; Normandin, M. D.; Frosch, M. P.; Gomez-Isla, T., [F-18]-AV-1451 binding correlates with postmortem neurofibrillary tangle Braak staging. *Acta Neuropathol.* **2017,** *134* (4), 619-628.
15. Kantarci, K.; Lowe, V. J.; Boeve, B. F.; Senjem, M. L.; Tosakulwong, N.; Lesnick, T. G.; Spychalla, A. J.; Gunter, J. L.; Fields, J. A.; Graff-Radford, J.; Ferman, T. J.; Jones, D. T.; Murray, M. E.; Knopman, D. S.; Jack, C. R., Jr.; Petersen, R. C., AV-1451 tau and β-amyloid positron emission tomography imaging in dementia with Lewy bodies. *Ann. Neurol.* **2017,** *81* (1), 58-67.
16. Marquie, M.; Normandin, M. D.; Meltzer, A. C.; Chong, M. S. T.; Andrea, N. V.; Anton-Fernandez, A.; Klunk, W. E.; Mathis, C. A.; Ikonomovic, M. D.; Debnath, M.; Bien, E. A.; Vanderburg, C. R.; Costantino, I.; Makaretz, S.; DeVos, S. L.; Oakley, D. H.; Gomperts, S. N.; Growdon, J. H.; Domoto-Reilly, K.; Lucente, D.; Dickerson, B. C.; Frosch, M. P.; Hyman, B. T.; Johnson, K. A.; Gomez-Isla, T., Pathological correlations of [F-18]-AV-1451 imaging in non-alzheimer tauopathies. *Ann. Neurol.* **2017,** *81* (1), 117-128.

17. Makaretz, S. J.; Quimby, M.; Collins, J.; McGinnis, S.; Dickerson, B. C.; Makris, N.; McGinnis, S.; Johnson, K. A.; Schultz, A.; Dickerson, B. C.; Schultz, A.; Johnson, K. A.; Dickerson, B. C.; Vasdev, N.; Johnson, K. A., Flortaucipir tau PET imaging in semantic variant primary progressive aphasia. *J Neurol Neurosurg Psychiatry* **2017**.
18. Wooten, D. W.; Guehl, N. J.; Verwer, E. E.; Shoup, T. M.; Yokell, D. L.; Zubcevik, N.; Vasdev, N.; Zafonte, R. D.; Johnson, K. A.; El Fakhri, G.; Normandin, M. D., Pharmacokinetic Evaluation of the Tau PET Radiotracer 18F-T807 (18F-AV-1451) in Human Subjects. *Journal of Nuclear Medicine* **2017,** *58* (3), 484-491.
19. Pontecorvo, M. J.; Devous, M. D., Sr.; Navitsky, M.; Lu, M.; Arora, A. K.; McGeehan, A.; Lim, N. C.; Xiong, H.; Joshi, A. D.; Siderowf, A.; Mintun, M. A.; Salloway, S.; Schaerf, F. W.; Jennings, D., Relationships between flortaucipir PET tau binding and amyloid burden, clinical diagnosis, age and cognition. *Brain* **2017,** *140* (3), 748-763.
20. Wooten, D. W.; Guehl, N. J.; Verwer, E. E.; Shoup, T. M.; Yokell, D. L.; Zubcevik, N.; Vasdev, N.; Zafonte, R. D.; Johnson, K. A.; El Fakhri, G.; Normandin, M. D., Pharmacokinetic evaluation of the Tau PET radiotracer 18F-T807 (18F-AV-1451) in human subjects. *J. Nucl. Med.* **2017,** *58* (3), 484-492.
21. Hahn, A.; James, G. M.; Lanzenberger, R.; Schain, M.; Strandberg, O. T.; Hansson, O.; Erlandsson, M.; Sjolin, P.; Olsson, T. G.; Hagerstrom, D.; Jogi, J.; Smith, R.; Hansson, O., Modeling Strategies for Quantification of In Vivo (18)F-AV-1451 Binding in Patients with Tau Pathology. *J Nucl Med* **2017,** *58* (4), 623-631.
22. Shcherbinin, S.; Schwarz, A. J.; Joshi, A.; Navitsky, M.; Flitter, M.; Shankle, W. R.; Devous, M. D., Sr.; Mintun, M. A., Kinetics of the tau PET tracer 18F-AV-1451 (T807) in subjects with normal cognitive function, mild cognitive impairment, and Alzheimer disease. *J. Nucl. Med.* **2016,** *57* (10), 1535-1542.
23. Nagatsu, T.; Sawada, M., Molecular mechanism of the relation of monoamine oxidase B and its inhibitors to Parkinson's disease: possible implications of glial cells. *J. Neural Transm., Suppl.* **2006,** *71* (Oxidative Stress and Neuroprotection), 53-65.
24. Rombouts, F.; Moechars, D.; Andres, J. I.; MacDonald, G.; Chupakhin, V.; Langlois, X.; Bormans, G.; Declercq, L. In *[18F]JNJ-311, a novel tau PET ligand*, American Chemical Society: 2016; pp MEDI-178.
25. Lemoine, L.; Gillberg, P.-G.; Nordberg, A.; Svedberg, M.; Stepanov, V.; Jia, Z.; Nag, S.; Halldin, C.; Huang, J.; Tian, H.; Ghetti, B.; Okamura, N.; Higuchi, M.; Nordberg, A., Comparative binding properties of the tau PET tracers THK5117, THK5351, PBB3, and T807 in postmortem Alzheimer brains. *Alzheimers Res Ther* **2017,** *9* (1), 96.
26. Hansen, A. K.; Brooks, D. J.; Borghammer, P., MAO-B Inhibitors Do Not Block In Vivo Flortaucipir([18F]-AV-1451) Binding. *Molecular Imaging and Biology* **2018,** *20* (3), 356-360.
27. Fowler, J. S.; Wang, G.-J.; Logan, J.; Xie, S.; Volkow, N. D.; MacGregor, R. R.; Schlyer, D. J.; Pappas, N.; Alexoff, D. L.; et, a., Selective reduction of radiotracer trapping by deuterium substitution: Comparison of carbon-11-L-deprenyl and carbon-11-deprenyl-D2 for MAO B mapping. *J. Nucl. Med.* **1995,** *36* (7), 1255-62.
28. Ishiki, A.; Tomita, N.; Arai, H.; Furukawa, K.; Harada, R.; Kudo, Y.; Okamura, N.; Yanai, K.; Okamura, N.; Rowe, C. C.; Villemagne, V. L.; Villemagne, V. L.; Furumoto, S.; Tashiro, M.; Furukawa, K., Tau imaging with [(18) F]THK-5351 in progressive supranuclear palsy. *Eur J Neurol* **2017,** *24* (1), 130-136.
29. Ng, K. P.; Pascoal, T. A.; Mathotaarachchi, S.; Therriault, J.; Kang, M. S.; Shin, M.; Guiot, M.-C.; Guo, Q.; Harada, R.; Comley, R. A.; Massarweh, G.; Soucy, J.-P.; Okamura, N.; Gauthier, S.; Rosa-Neto, P., Monoamine oxidase B inhibitor, selegiline, reduces 18F-THK5351 uptake in the human brain. *Alzheimer's Research & Therapy* **2017,** *9* (1), 25.
30. Lewis, J.; Dickson, D. W., Propagation of tau pathology: hypotheses, discoveries, and yet unresolved questions from experimental and human brain studies. *Acta Neuropathol.* **2016,** *131* (1), 27-48.

31. Arnett, C. D.; Fowler, J. S.; MacGregor, R. R.; Schlyer, D. J.; Wolf, A. P.; Långström, B.; Halldin, C., Turnover of Brain Monoamine Oxidase Measured In Vivo by Positron Emission Tomography Using l-[11C]Deprenyl. *Journal of Neurochemistry* **1987,** *49* (2), 522-527.
32. Saura, J.; Kettler, R.; Da Prada, M.; Richards, J., Quantitative enzyme radioautography with 3H-Ro 41-1049 and 3H-Ro 19- 6327 in vitro: localization and abundance of MAO-A and MAO-B in rat CNS, peripheral organs, and human brain. *The Journal of Neuroscience* **1992,** *12* (5), 1977-1999.
33. Drake, L. R.; Brooks, A. F.; Mufarreh, A. J.; Pham, J. M.; Koeppe, R. A.; Shao, X.; Scott, P. J. H.; Kilbourn, M. R., Deuterium Kinetic Isotope Effect Studies of a Potential in Vivo Metabolic Trapping Agent for Monoamine Oxidase B. *ACS Chemical Neuroscience* **2018**.
34. Marquie, M.; Normandin, M. D.; Vanderburg, C. R.; Costantino, I. M.; Bien, E. A.; Rycyna, L. G.; Klunk, W. E.; Mathis, C. A.; Ikonomovic, M. D.; Debnath, M. L.; Vasdev, N.; Dickerson, B. C.; Gomperts, S. N.; Growdon, J. H.; Johnson, K. A.; Frosch, M. P.; Hyman, B. T.; Gomez-Isla, T., Validating novel tau positron emission tomography tracer [F-18]-AV-1451 (T807) on postmortem brain tissue. *Ann. Neurol.* **2015,** *78* (5), 787-800.
35. Choi, J. Y.; Cho, H.; Ahn, S. J.; Lee, J. H.; Ryu, Y. H.; Lee, M. S.; Lyoo, C. H., Off-Target 18F-AV-1451 Binding in the Basal Ganglia Correlates with Age-Related Iron Accumulation. *Journal of Nuclear Medicine* **2018,** *59* (1), 117-120.
36. Hansen, A. K.; Knudsen, K.; Lillethorup, T. P.; Parbo, P.; Fedorova, T.; Audrain, H.; Bender, D.; Borghammer, P.; Landau, A. M.; Ostergaard, K.; Brooks, D. J., In vivo imaging of neuromelanin in Parkinson's disease using 18F-AV-1451 PET. *Brain* **2016,** *139* (Pt 7), 2039-49.
37. Xia, C.-F.; Arteaga, J.; Chen, G.; Gangadharmath, U.; Gomez, L. F.; Kasi, D.; Lam, C.; Liang, Q.; Liu, C.; Mocharla, V. P.; Mu, F.; Sinha, A.; Su, H.; Szardenings, A. K.; Walsh, J. C.; Wang, E.; Yu, C.; Zhang, W.; Zhao, T.; Kolb, H. C., (18)F]T807, a novel tau positron emission tomography imaging agent for Alzheimer's disease. *Alzheimers Dement* **2013,** *9* (6), 666-76.
38. Vermeiren, C.; Motte, P.; Viot, D.; Mairet-Coello, G.; Courade, J.-P.; Citron, M.; Mercier, J.; Hannestad, J.; Gillard, M., The tau positron-emission tomography tracer AV-1451 binds with similar affinities to tau fibrils and monoamine oxidases. *Mov. Disord.* **2018,** *33* (2), 273-281.
39. Lemoine, L.; Gillberg, P.-G.; Svedberg, M.; Stepanov, V.; Jia, Z.; Huang, J.; Nag, S.; Tian, H.; Ghetti, B.; Okamura, N.; Higuchi, M.; Halldin, C.; Nordberg, A., Comparative binding properties of the tau PET tracers THK5117, THK5351, PBB3, and T807 in postmortem Alzheimer brains. *Alzheimer's Research & Therapy* **2017,** *9* (1), 96.
40. Villemagne, V.; Dore, V.; Okamura, N.; Baxendale, D.; Harada, R.; Mulligan, R.; Furumoto, S.; Salvado, O.; Yanai, K.; Masters, C.; Rowe, C., To tau or to MAO-B? Most of the 18F-THK5351 signal is blocked by selegiline. *Journal of Nuclear Medicine* **2018,** *59* (supplement 1), 1644.
41. Zhang, W.; Arteaga, J.; Cashion, D. K.; Chen, G.; Gangadharmath, U.; Gomez, L. F.; Kasi, D.; Lam, C.; Liang, Q.; Liu, C.; Mocharla, V. P.; Mu, F.; Sinha, A.; Szardenings, A. K.; Wang, E.; Walsh, J. C.; Xia, C.; Yu, C.; Zhao, T.; Kolb, H. C., A Highly Selective and Specific PET Tracer for Imaging of Tau Pathologies. *J. Alzheimer's Dis.* **2012,** *31* (3), 601-612.
42. Cai, L.; Qu, B.; Hurtle, B. T.; Dadiboyena, S.; Diaz-Arrastia, R.; Pike, V. W., Candidate PET Radioligand Development for Neurofibrillary Tangles: Two Distinct Radioligand Binding Sites Identified in Postmortem Alzheimer's Disease Brain. *ACS Chem. Neurosci.* **2016,** *7* (7), 897-911.
43. Sander, K.; Lashley, T.; Gami, P.; Gendron, T.; Lythgoe, M. F.; Rohrer, J. D.; Schott, J. M.; Revesz, T.; Fox, N. C.; Årstad, E., Characterization of tau positron emission tomography tracer [18F] AV-1451 binding to postmortem tissue in Alzheimer's disease, primary tauopathies, and other dementias. *Alzheimer's & dementia: the journal of the Alzheimer's Association* **2016,** *12* (11), 1116-1124.
44. Harada, R.; Yoshikawa, T.; Yanai, K.; Harada, R.; Ishiki, A.; Furukawa, K.; Tomita, N.; Arai, H.; Kudo, Y.; Kai, H.; Kitamoto, T.; Sato, N.; Sasano, H.; Furukawa, K.; Furumoto, S.; Watanuki, S.; Hiraoka, K.; Ishikawa, Y.; Funaki, Y.; Iwata, R.; Tashiro, M.; Yanai, K.; Okamura, N.; Tago, T.; Nakamura, T.; Okamura, N., Correlations of (18)F-THK5351 PET with Postmortem Burden of Tau and Astrogliosis in Alzheimer Disease. *J Nucl Med* **2018,** *59* (4), 671-674.

45. Hostetler, E. D.; Walji, A. M.; Zeng, Z.; Miller, P.; Bennacef, I.; Salinas, C.; Connolly, B.; Gantert, L.; Haley, H.; Holahan, M.; Purcell, M.; Riffel, K.; Lohith, T. G.; Coleman, P.; Soriano, A.; Ogawa, A.; Xu, S.; Zhang, X.; Joshi, E.; Della Rocca, J.; Hesk, D.; Schenk, D. J.; Evelhoch, J. L., Preclinical characterization of 1♂F-MK-6240, a promising PET tracer for in vivo quantification of human neurofibrillary tangles. *J. Nucl. Med.* **2016,** *57* (10), 1599-1606.
46. Hu, W.; Wu, F.; Zhang, Y.; Gong, C.-X.; Iqbal, K.; Liu, F., Expression of tau pathology-related proteins in different brain regions: a molecular basis of tau pathogenesis. *Front. Aging Neurosci.* **2017,** *9*, 311/1-311/14.
47. Levitt, P.; Pintar, J. E.; Breakefield, X. O., Immunocytochemical demonstration of monoamine oxidase B in brain astrocytes and serotonergic neurons. *Proceedings of the National Academy of Sciences of the United States of America* **1982,** *79* (20), 6385-6389.
48. Nakamura, S.; Kawamata, T.; Akiguchi, I.; Kameyama, M.; Nakamura, N.; Kimura, H., Expression of monoamine oxidase B activity in astrocytes of senile plaques. *Acta Neuropathologica* **1990,** *80* (4), 419-425.
49. Jossan, S. S.; Gillberg, P. G.; d'Argy, R.; Aquilonius, S. M.; Låangstro¨m, B.; Halldin, C.; Oreland, L., Quantitative localization of human brain monoamine oxidase B by large section autoradiography using l-[3H]deprenyl. *Brain Research* **1991,** *547* (1), 76-80.
50. Ekblom, J.; Jossan, S. S.; Bergström, M.; Oreland, L.; Walum, E.; Aquilonius, S.-M., Monoamine oxidase-B in astrocytes. *Glia* **1993,** *8* (2), 122-132.
51. Mossine, A. V.; Brooks, A. F.; Henderson, B. D.; Hockley, B. G.; Frey, K. A.; Scott, P. J. H., An updated radiosynthesis of [(18)F]AV1451 for tau PET imaging. *EJNMMI Radiopharm Chem* **2017,** *2* (1), 7.

CHAPTER 3
Trapped Metabolite PET Imaging of Monoamine Oxidase B

Monoamine oxidase (MAO) is a very well characterized enzyme *in vitro* and *in vivo*. We aimed to join the field of MAO PET imaging with a new approach, using substrates as opposed to using inhibitors. For much of this project, we focused on the prediction of *in vivo* kinetics based on *in vitro* enzyme kinetics.[1]

1. Introduction

Monoamine neurotransmitters of the classical type catecholamines (dopamine, epinephrine, and norepinephrine), indolamines (serotonin), and imidazoleamines (histamine), as well as trace amines (e.g phenethylamine and tyramine) have been a heavily studied family of small molecules due to their critical roles in the central nervous system (CNS). The metabolism of monoamines is key to their influence in various disease states. Monoamine oxidase is an outer-mitochondrial membrane bound, flavin-containing enzyme which oxidizes these substrates. There are two isozymes, A and B, which are encoded by independent genes and have structural differences (figure 3.1). These two enzymes have long been the target of drug development for an array of neurological and psychiatric diseases and disorders with numerous marketed compounds developed.[2] This body of work has provided a varying type of starting points for the development of positron emission tomography (PET) imaging, ranging from irreversible and reversible inhibitors to substrates. Each approach has presented its own challenges and limitations as the radiochemistry community has endeavored to develop MAO PET imaging

agents to better understand MAO pathophysiology to improve patient management and support drug development.

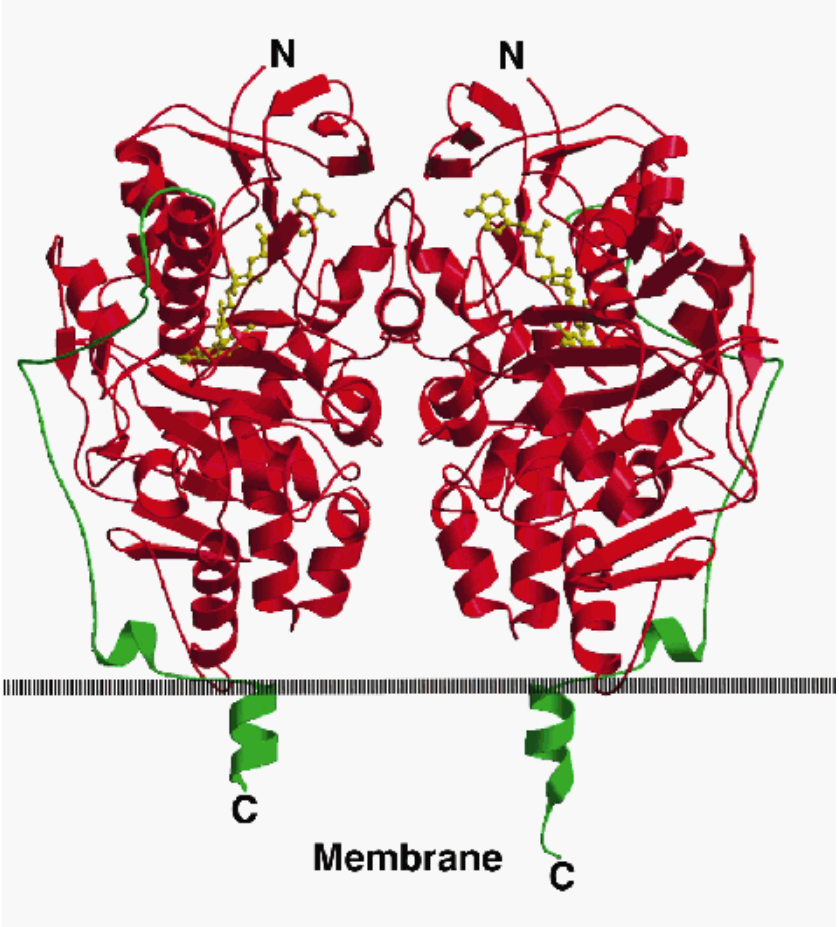

Figure 3.1. MAO-B Structure. MAO-B acts in a homodimer, and has a short membrane-spanning domain. Structure shown with inhibitor deprenyl bound (yellow sticks). Reprinted with permission.[3]

The first MAO ligands to be used as PET imaging agents in humans were propargylamines: [^{11}C]clorgyline (**3.1**) and [^{11}C]deprenyl (**3.2**), selective for MAO-A and –B respectively (figure 3.2). Fowler and coworkers demonstrated the rapid brain uptake in humans and confirmed the irreversibility by the plateau in the time activity curve (TAC).[4] The distribution of radioactivity was highest in the corpus striatum, thalamus, and brainstem which paralleled respective MAO immunoreactivity on human brain tissue sections. These agents were confirmed as being MAO inhibitors through a blocking study with phenelzine, a non-selective MAO inhibitor. The analysis in human studies showed the agents were flow limited due, to a fast

rate of irreversible inhibition. Deuterated analogues were prepared to improve pharmacokinetic parameters and data analysis by slowing the rate trapping via the kinetic isotope effect (KIE). This approach worked well for the imaging of MAO-B by [^{11}C]deprenyl-d_2 ([^{11}C]DED);[5] however, [^{11}C]clorgyline-d_2 was limited by the high non-specific binding observed. Less of the imaging agent being trapped lead to a lower ratio in a region of interest relative to background non-specific binding.

The deuterium KIE for deprenyl and deprenyl-d_2 was measurable *in vivo* in the brain and peripheral organs. Fowler and coworkers illustrated this in a series of human studies involving smokers- because nicotine is a known MAO inhibitor, and they hypothesized that the effect of nicotine on the monoaminergic system could be evaluated with MAO-B PET imaging. In the brain, nicotine use in smokers resulted in lower overall MAO-B activity compared to a non-smoker, yet higher activity than an individual with pharmacological intervention (figure 3.3).[6] A similar effect was observed in the peripheral organs.[7] When utilizing both [^{11}C]deprenyl and [^{11}C]DED, the deuterium kinetic isotope was able to be calculated *in vivo*, a confirmation to the assumed enzymatic mechanism.

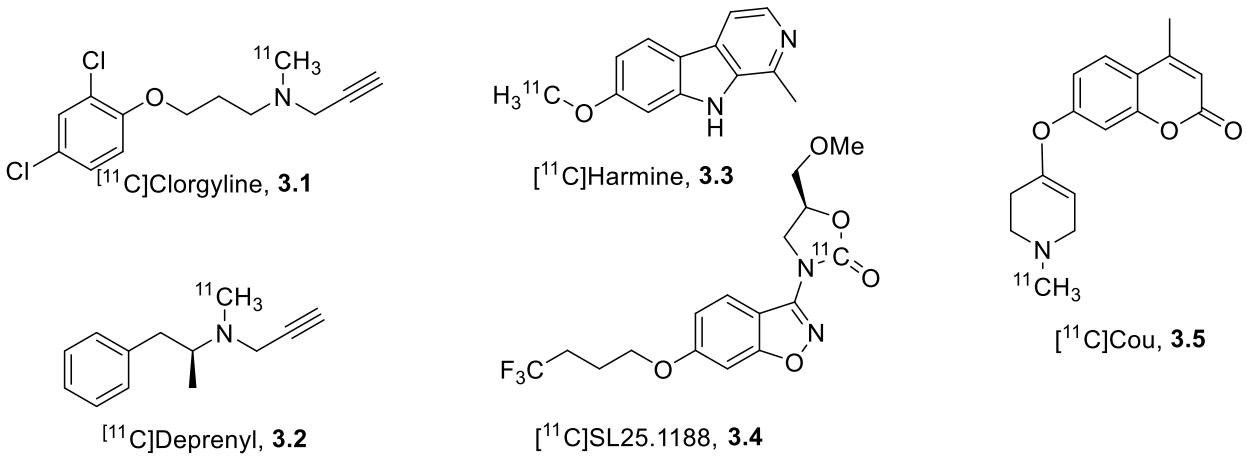

Figure 3.2. MAO Inhibitors and substrates for PET imaging.

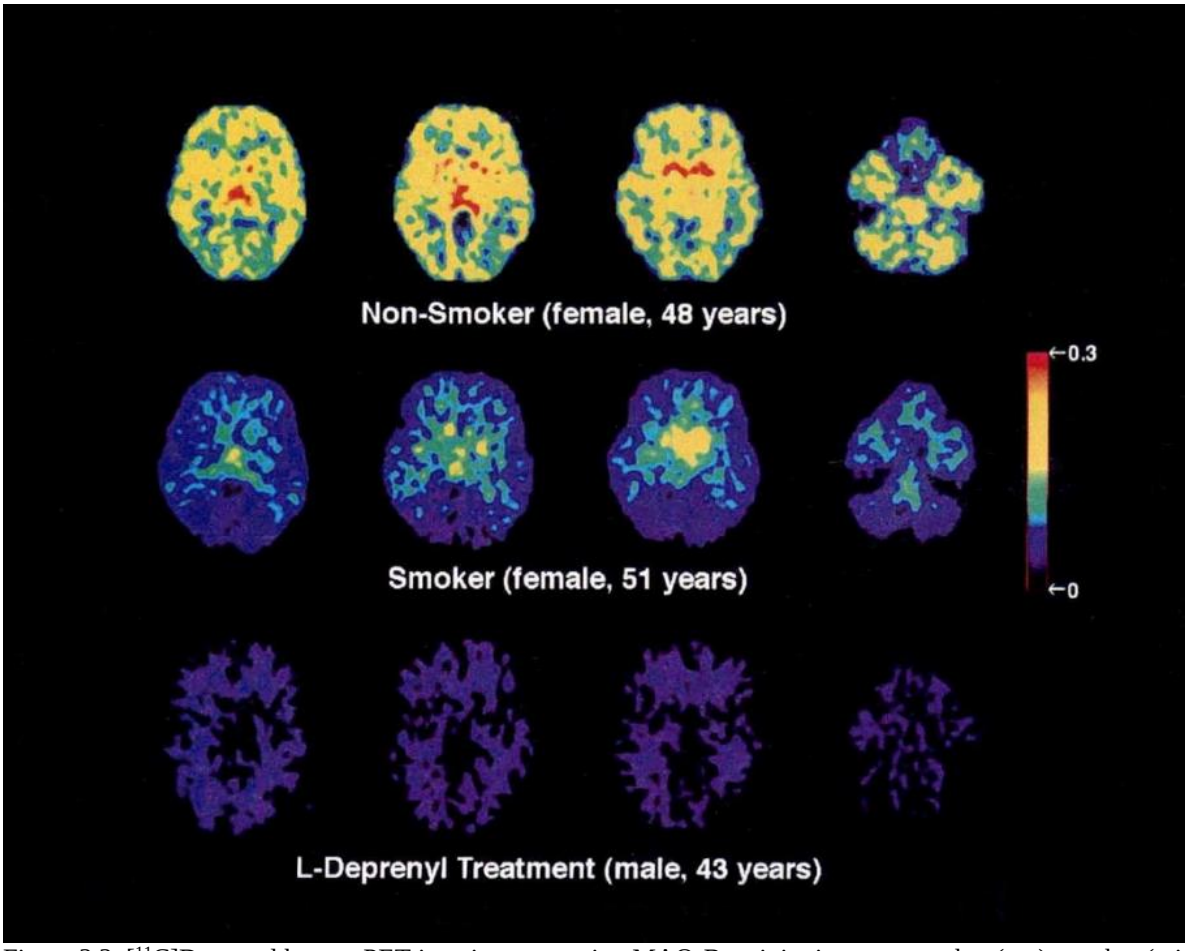

Figure 3.3. [^{11}C]Deprenyl human PET imaging comparing MAO-B activity in a non-smoker (top), smoker (middle), and pharmacologically blocked patient (bottom). Reprinted with permission.[6]

The irreversible inhibitors provided a strong foundation for PET imaging of monoamine oxidases with the mapping of expression and investigations into MAO-B's role in disease. As previously mentioned, MAO-A imaging was not improved upon the development of [^{11}C]clorgyline-d_2.[8] [^{11}C]Harmine (**3.3**), a reversible ligand, was utilized for further evaluation of MAO-A in the CNS.[9-13] Although MAO-B expression is higher in the human brain, MAO-A has been recognized for its utility in treatment of psychiatric disorders.[14] It was theorized that native levels of monoamine neurotransmitters were lower in subjects with major depressive disorder, explaining why inhibitors of monoamine transporters, receptors (SSRI's, NSRI's), and MAO-A itself (MAOI's) are successful treatments.

In 2006, a cohort of 17 subjects with depression received PET scans with [^{11}C]harmine after a 5 month hiatus from treatment to eliminate possible pharmacological effects.[15] The [^{11}C]harmine scan included blood sampling and was fit using an unconstrained 2-compartment model with the goal being to determine individuals' distribution volume (MAO DV), or the ratio k_3 and k_4 (the radioligand transfer between free and nonspecific to the to specific binding compartment) normalized by flow (K_1/ k_2). The depressed subject cohort was compared to a control cohort of similar size and demographic with the overarching result being increased DV's (34%) in all regions of interest examined. The most significant increase was observed in the prefrontal cortex, temporal cortex, posterior cingulate, and thalamus which strongly supports the original hypothesis of decreased monoamine neurotransmitters in depressed individuals. Although these results are significant, this trial is limited by distribution volume (DV) as a measure of MAO-A density because there is no differentiation between the free and nonspecific binding. The assumption, however, is that these parameters are not likely to be different between individuals. The ability to image psychiatric disorders and quantify physiological changes offers the potential to improve the understanding and treatment of the disorders, making the continued development and use of MAO PET imaging agent of interest. In similar study designs, [^{11}C]harmine PET has been used to further investigate MAO-A's influence on psychiatric and mood disorders and in the study of addiction.

After the mapping of MAO-B in normal human brains of healthy control subjects, [^{11}C]deprenyl-d_2 ([^{11}C]DED) was used to investigate the monoaminergic system in various disorders, particularly neurodegeneration. It has long been recognized that monoamine oxidases play a role in the activation of astrocytes. In 1980, MAO-B was found to be overexpressed in brain sections of senile dementia patients compared to age-matched controls by

immunohistochemistry.[16] Follow up studies determined the cells overexpressing MAO-B were astrocytes in only two neuronal areas: brainstem raphe and hypothalamus.[17] Counterstaining with Congo red and Thioflavin S confirmed that these activated astrocytes were associated with senile plaques, later identified as amyloid plaques.[18-20] Although MAO-B expression also increases in normal aging, it was identified as a possible marker for activated astrocytes that could be useful in PET imaging.

Carter and coworkers performed a multitracer trial using [^{18}F]fludeoxyglucose ([^{18}F]FDG, which images glucose metabolism), [^{11}C]PiB, and [^{11}C]DED PET imaging to investigate the differences between AD and MCI patients.[21] Co-localization of MAO-B expressing astrocytes and amyloid plaques has been shown in human brain sections, indicating the possibility of MAO-B involvement in AD. Additionally, [^{11}C]DED binding on human tissue was determined to be highest in the earlier Braak stages. This study design aimed to demonstrate that MAO-B PET imaging could be predictive of MCI before advanced AD in patients. Each subject, 7 AD, 8 MCI, and 14 age-matched controls, received three PET scans, without arterial blood sampling, using cerebellar gray as the reference region. The MCI cohort was divided into subgroups of [^{11}C]PiB^{+} and [^{11}C]PiB^{-}. Increased [^{11}C]DED binding in the frontal and parietal cortices were found in both PiB^{+} and PiB^{-} MCI groups, as well as the AD cohort. Interestingly, [^{11}C]DED binding appeared higher and widespread in the PiB^{+} MCI group. Despite the small cohort sizes, the authors argued that these results are evidence of astrocytosis in AD progression. Follow up studies in the same study design have been reported more recently in autosomal dominant AD patients from the same authors.[22]

Clinical use of [^{11}C]DED is limited because of its brain penetrant metabolite, [^{11}C]methamphetamine, which can complicate analysis given its binding to alternate targets in

the same tissue (scheme 3.1). In general, the irreversible inhibitor approach in PET imaging has the major advantage in pharmacokinetic modeling over reversible ligands. Fitting to two compartment models is easier when the affinity of the ligand is very high, or irreversible. Having no washout after irreversible binding can simplify this interpretation. However, irreversibility can be detrimental if one desires to perform multiple PET scans in the same individual. Fowler and coworkers demonstrated that it takes approximately one month in healthy individuals to turn over and re-express MAO-B, as visualized by [^{11}C]DED.[5] If multiple scans are necessary in the same individual, irreversible inhibitors may be inappropriate for a study design.

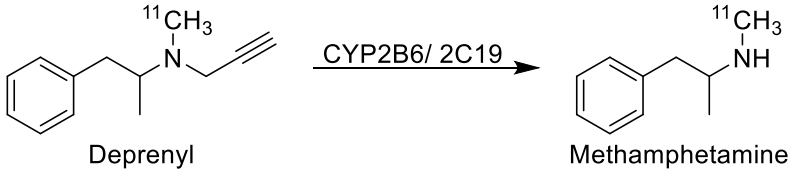

Scheme 3.1. Metabolism of [^{11}C]deprenyl into [^{11}C]methamphetamine.

Reversible inhibitors for MAO-B PET imaging have also been developed, in an effort to avoid interpreting the brain penetrating metabolite of [^{11}C]DED. [^{11}C]SL25.1188 (**3.4**), a selective inhibitor for MAO-B was originally reported by Saba and coworkers.[23] However, its synthesis required the use of [^{11}C]phosgene ([^{11}C]$COCl_2$) which is not a radiochemical technique commonly available in a radiochemistry lab or desirable given the toxic properties of phosgene. The Vasdev laboratory in Toronto optimized this synthesis using [^{11}C]fixation using CO_2 produced in the cyclotron target directly and further advanced this tracer for human use.[24] This preliminary human evaluation demonstrated high maximum standard uptake value (SUV_{NB}) and relatively high regional uptake values (~6) in comparison to [^{11}C]DED, though this is likely also owed to the increased blood-brain barrier permeability of the radioligand. Regional uptake corresponds to regional concentrations of MAO-B as measured by immunoblot as expected. These experiments fit well in a two compartment model and were reproducible; future studies

will explore different patient populations. Selectivity studies in human populations also need to be performed. Reversible inhibitors, such as [^{11}C]SL25.1188 and [^{11}C]harmine are objectively more challenging to clinically translate compared to irreversible inhibitors. In order to not be flow-limited, reversible inhibitors must have very high affinities to their target. And despite this, both irreversible and reversible inhibitors have a limited signal capability by having a limited 1:1 relationship with the target enzyme. Conversely, substrates do not inhibit the enzyme and theoretically have an increased signal potential.

As an alternate to inhibition, we have investigated the use of selective MAO substrates to form trapped metabolites for imaging MAO enzymatic activity. Imaging of enzyme substrates is analogous to imaging with transporter substrates as the analysis of transporter kinetics is the same as utilized for enzyme turnover with the V_{max}, $K_{M,}$ and K_{cat} of interest; this differs from radioligands where the K_d (or in the case of competitive binding K_I) values are of interest. In this approach an MAO substrate with good brain uptake and efflux will form a product (radiometabolite) when it is oxidized by MAO. The development of a radiotracer substrate is an approach that has been used successfully and most famously in the development of fludeoxyglucose, which is a glucose transport substrate that is subsequently trapped in the tissue through phosphorylation by hexokinase.

The substrates for MAO were based on 1-methyl-4-phenyl-1,2,3,6-tetrahydropyridine (MPTP). In the 1980s, MPTP (1-methyl-4-phenyl-1,2,3,6-tetrahydropyridine) was determined as a contaminant in the illicit synthesis of the synthetic opiate desmethylprodine (MPPP), resulting in symptoms of Parkinson's disease in drug users.[25-29] It was subsequently shown that MPTP is a substrate and inhibitor of MAO-B, producing dopaminergic cell death via the toxic metabolite 1-methyl-4-phenylpyridinium (MPP^+).[30] The MAO oxidation of MPTP and other

tetrahydropyridines has been extensively studied, as has the mechanism of cellular toxicity of MPP^+, and MPTP remains a valuable tool in Parkinson's disease research. In the 1990's the Castagnoli lab developed an analogue of MPTP that contained an ether linkage between the tetrahydropyridine and a second arene. These substrates, instead of forming MPP+ (or a related toxic metabolite), are hydrolyzed to two benign metabolites. A series of these radiotracers have been prepared and investigated for selectivity and suitability for human translation, including [^{11}C]4-methyl-7-(pyridin-4-yloxy)-2H-chromen-2-one ([^{11}C]Cou; **3.5**).

Although PET imaging with irreversible inhibitors of monoamine oxidases A and B has provided an abundance of information regarding the biology of the human brain, there remains a limitation. Irreversible inhibitors by nature are restricted to a 1:1 stoichiometry with their target enzyme. Substrates, however, do not deactivate the enzyme and potentially allow that reaction stoichiometry to increase. It is with this approach in mind, we have aimed to develop substrates for monoamine oxidases to monitor their activities *in vivo*. Trapped metabolite imaging has a long history of success in PET, particularly with FDG. *In vivo* PET studies in rhesus macaque brain using [^{11}C]Cou demonstrated that the metabolite formed by MAO-B oxidation and subsequent hydrolysis (figure 3.4A) was rapidly and efficiently trapped in the brain, which could be blocked by pretreatment with the reversible MAO-B inhibitor lazabemide.[31]

Although successful as an *in vivo* metabolic trapping substrate, the pharmacokinetics of [^{11}C]Cou were suboptimal, as the rapid trapping rate made it difficult to discriminate between regions of high and low MAO enzymatic activity (figure 3.4B).

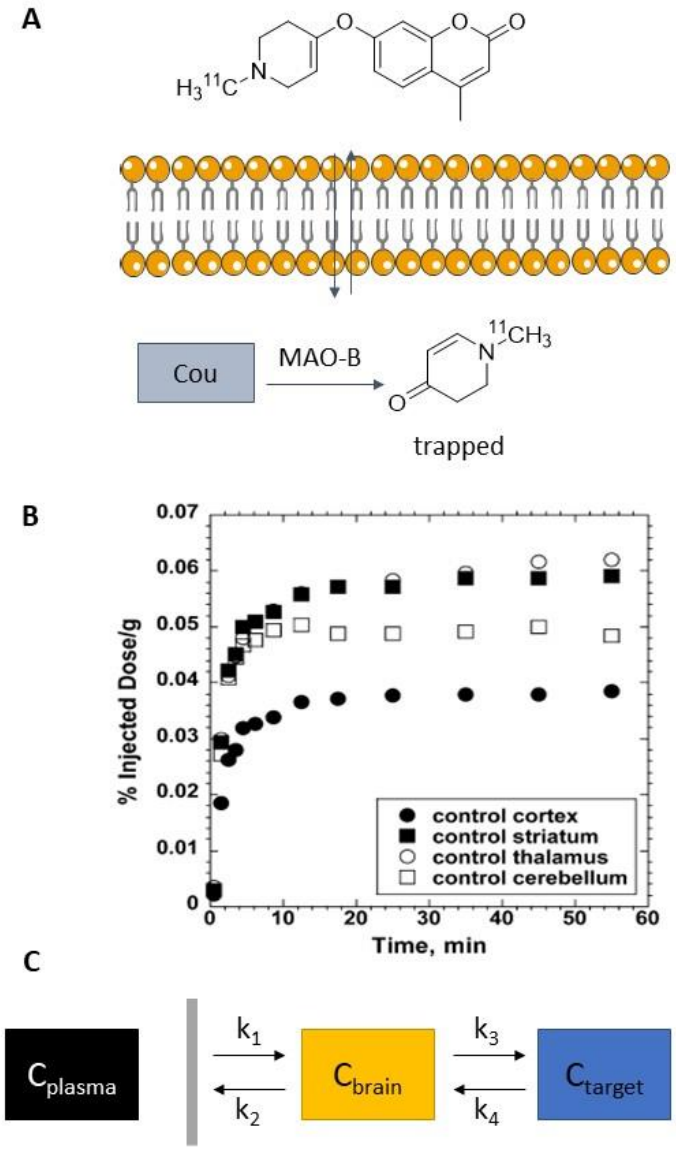

Figure 3.4 *In vivo* trapping of [^{11}C]Cou. A). Cartoon model of the substrate passively diffusing across the cellular membrane and subsequently being oxidized by MAO. B) Time activity curve of [^{11}C]Cou in nonhuman primate brain. C) Simplified kinetic model of radiotracer's behavior *in vivo*. Diffusing in and out of the brain corresponds to k_1 and k_2 respectively, the ratio equal to K_1. Trapping in the target cell is k_3, and there should be no k_4 if 100% trapping occurs

That limitation is similar to what was observed for the irreversibly-binding MAO-B radiotracer [^{11}C]deprenyl, where the *in vivo* pharmacokinetics were slowed and sensitivity improved using the kinetic isotope effect induced by deuterium atoms at the location critical for the rate-determining oxidation step.[5] As kinetic isotope effect experiments using deuterium substitutions on the tetrahydropyridine ring have demonstrated that the hydrogen abstraction step is also rate

limiting in the MAO-B mediated oxidation of MPTP,[32] we have attempted to apply this concept to improve the *in vivo* pharmacokinetics of [^{11}C]Cou (figure 3.5). In this chapter, we report here the synthesis of two deuterated derivatives of [^{11}C]Cou and a comparison of their *in vitro* kinetics and *in vivo* brain pharmacokinetics.

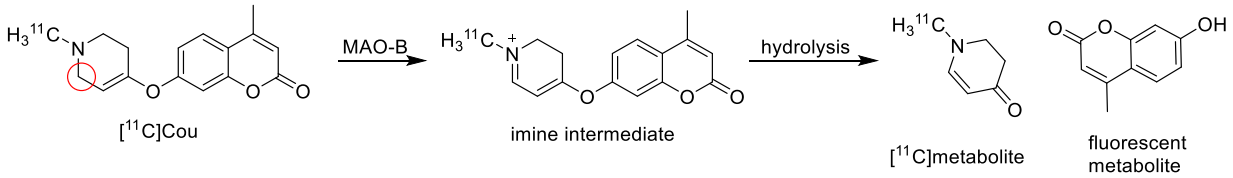

Figure 3.5. MAO catalyzed oxidation and subsequent hydrolysis of Cou substrate. The 4-aryloxytetrahydropyridine substrate [^{11}C]Cou is oxidized by monoamine oxidase to form an iminium intermediate, which is rapidly hydrolyzed to yield a polar carbon-11 species and a fluorescent coumarin as metabolites. Red circle around the alpha carbon to the amine.

2. Results

Chemistry

The synthesis of Cou-d_3 is shown in Scheme 3.2A: 1-Methyl-4-((4-methyl-2-oxo-2H-chromen-7-yl)oxy)pyridin-1-ium (**3.6**) was prepared by reacting 4-chloro-N-methyl-pyridinium with 4-methylumbeliferone in a solution of sodium methoxide in DMF. Reduction of the pyridinium with sodium borodeuteride in deuterated methanol yielded Cou-d_3 (**3.7**). The carbon-11 radiolabeling was done using N-[^{11}C]methylation of the pyridine (**3.8**) in ethanol-d_6, followed by addition of sodium borodeuteride to form carbon-11 labeled product **3.7b** as previously described (Scheme 3.2B).[31]

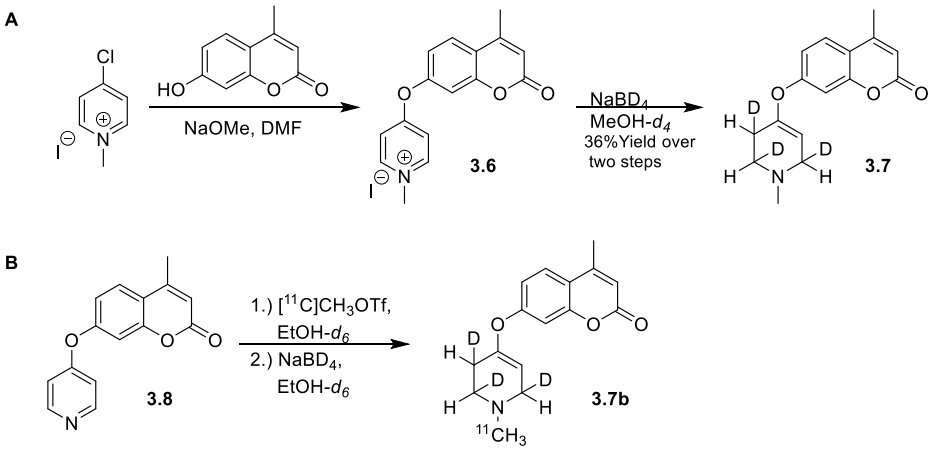

Scheme 3.2. Synthesis and Radiochemical synthesis of Cou-d_3 and [^{11}C]Cou-d_3. All carbon-11 syntheses were performed with Dr. Xia Shao and Dr. Allen Brooks.

The synthesis of Cou-d_7 is described in Scheme 3.3A: Iodocoumarin (**3.9**) was prepared via Pechmann condensation by treating 3-iodophenol with ethyl acetoacetate in an acidic solution. Reaction of **3.9** with p-toluenesulfonic acid and mCPBA in dichloromethane gave the iodonium salt (**3.10**), which was converted to the 4-methoxyphenyl substituted iodonium salt (**3.11**). A subsequent substitution reaction with 4-phenol-d_5 yielded the pyridine Cou-d_7 precursor (**3.12**). N-Methylation and reduction of the resulting pyridinium with sodium borodeuteride in deuterated methanol yielded Cou-d_7 (**3.14**). The carbon-11 radiolabeling was conducted as previously described using **3.12** as a precursor (Scheme 3.3B) by alkylation with [^{11}C]methyl triflate followed by addition of sodium borodeuteride to form carbon-11 labeled product **3.14b** as previously described.[31]

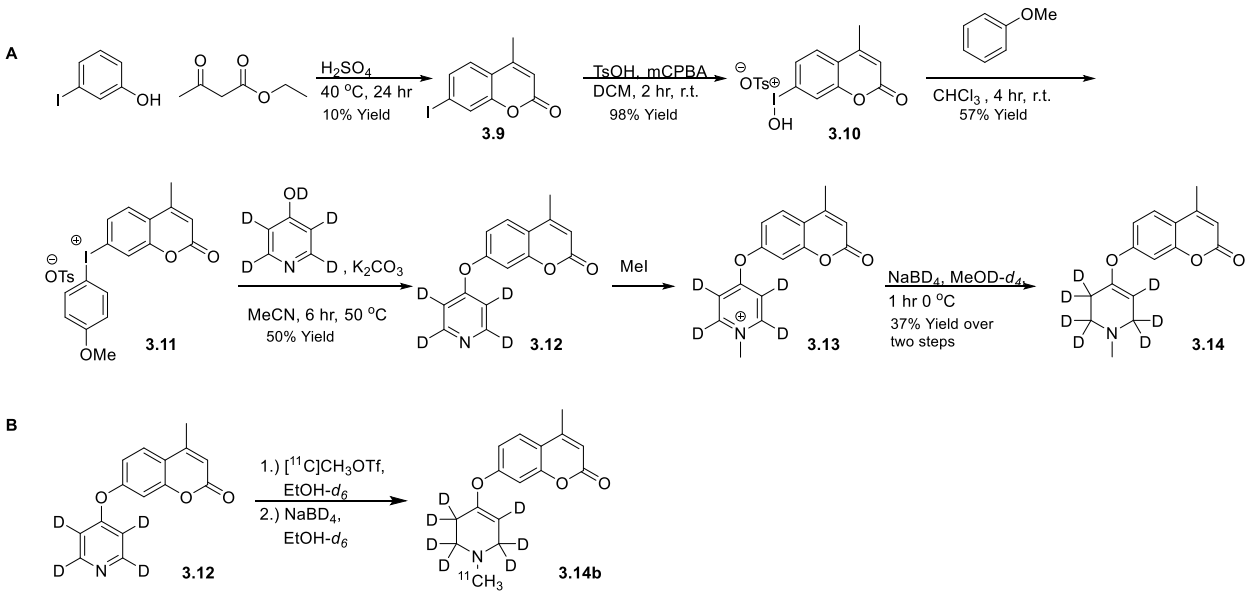

Scheme 3.3. Synthesis and Radiochemical synthesis of Cou-d_7 and [^{11}C]Cou-d_7. Cou-d_7 standard was synthesized by Tony Mufarreh and Allen Brooks. All carbon-11 syntheses were performed with Dr. Xia Shao and Dr. Allen Brooks.

Biology

In vitro kinetic parameters were determined by incubation of substrates (Cou, Cou-d_3, and Cou-d_7) with human MAO-B Supersomes and monitoring the appearance of the fluorescent coumarin product (ex: 360/ em: 460 nm) released after oxidation and hydrolysis. Supersomes were chosen instead of purified hMAO-B protein because of the increased activity. Supersomes are commercially available mitochondrial membrane preparations from insect cells overexpressing human MAO-B. During assay development, purified hMAO-B was used and the activity was very poor. Supersome assay conditions were optimized based on literature precedent. PBS, Tris-HCl, HEPES, and borate buffers were screened for maximal activity. Kynuramine, an established MAO substrate, was used for optimization. Using the Cou substrate, buffers were additionally screened for solubility and maximum fluorescence signal. Borate buffer was chosen for these properties. All three substrates displayed well-behaved Michaelis-Menten kinetics (figure 3.6). There were no significant observed kinetic isotope effects based on the turnover (V_{max}) or enzymatic efficiency (V_{max}/K_M) (Table 3.1).

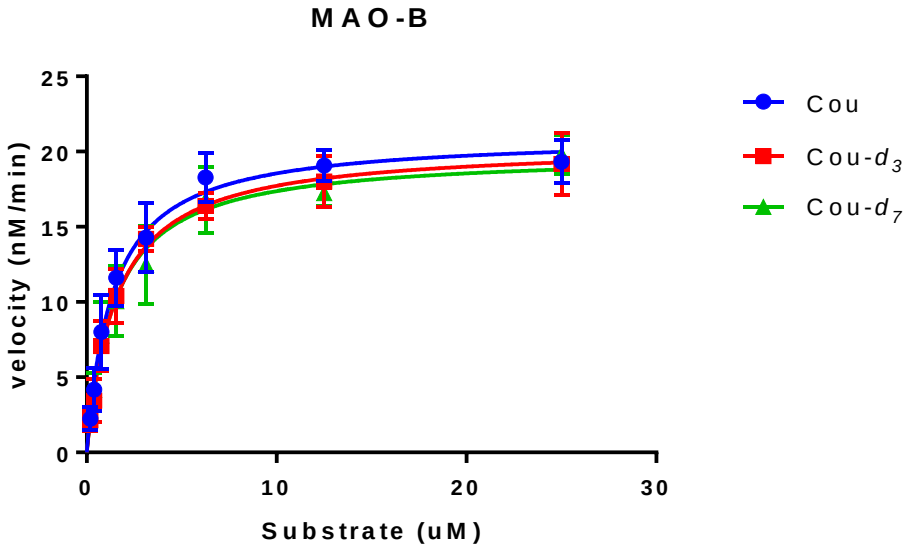

Figure 3.6. *In vitro* kinetics for Cou and deuterium-substituted substrates. The velocity of fluorescent product appearance was plotted against concentration of substrates. Michaelis-Menten Kinetic parameters were calculated in GraphPad Prism (n= 6) and are displayed in table 3.1.

Table 3.1. Michaelis-Menten Kinetic parameters for Cou and deuterium-substituted substrates.

	Cou	**Cou-d_3**	**Cou-d_7**
K_M (uM)	1.35 ± 0.12	1.55 ± 0.12	1.56 ± 0.15
V_{max} (nM/min)	21.1 ± 0.56	20.5 ± 0.48	19.9 ± 0.65
V_{max}/K_M	15.63 ± 1.44	13.23 ± 1.08	12.75 ±1.51
$^{D}(V_{max})$	---	1.03 ± 0.036	1.06 ± 0.045
$^{D}(V_{max}/K_M)$	---	1.18 ± 0.15	1.23 ± 0.16

The *in vivo* pharmacokinetics of the three MAO-B substrates were evaluated in rhesus monkey brain using PET imaging. The brain uptake and distribution of these MAO-B substrates were imaged in an adult female rhesus macaque (n=2 per substrate). Radiolabeled compounds were injected intravenously and the regional brain distributions of radioactivity were determined using dynamic microPET imaging (figure 3.7). Tissue time-radioactivity curves were generated for cerebellum, basal ganglia, and cortex (figure 3.8) and showed no significant changes in the shapes of the curves in any brain region for either of the deuterated substrates (figure 3.8)

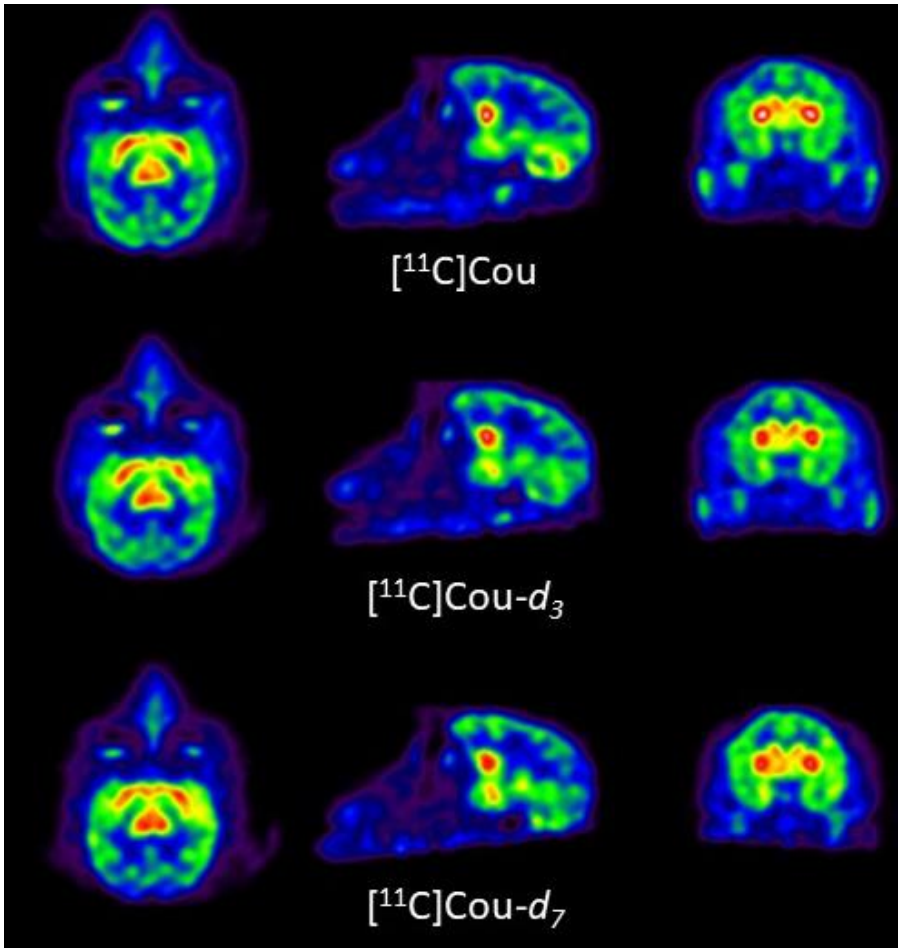

Figure 3.7. PET imaging of [^{11}C] Cou, [^{11}C]Cou-d_3, and [^{11}C]Cou-d_7 in the rhesus monkey brain.

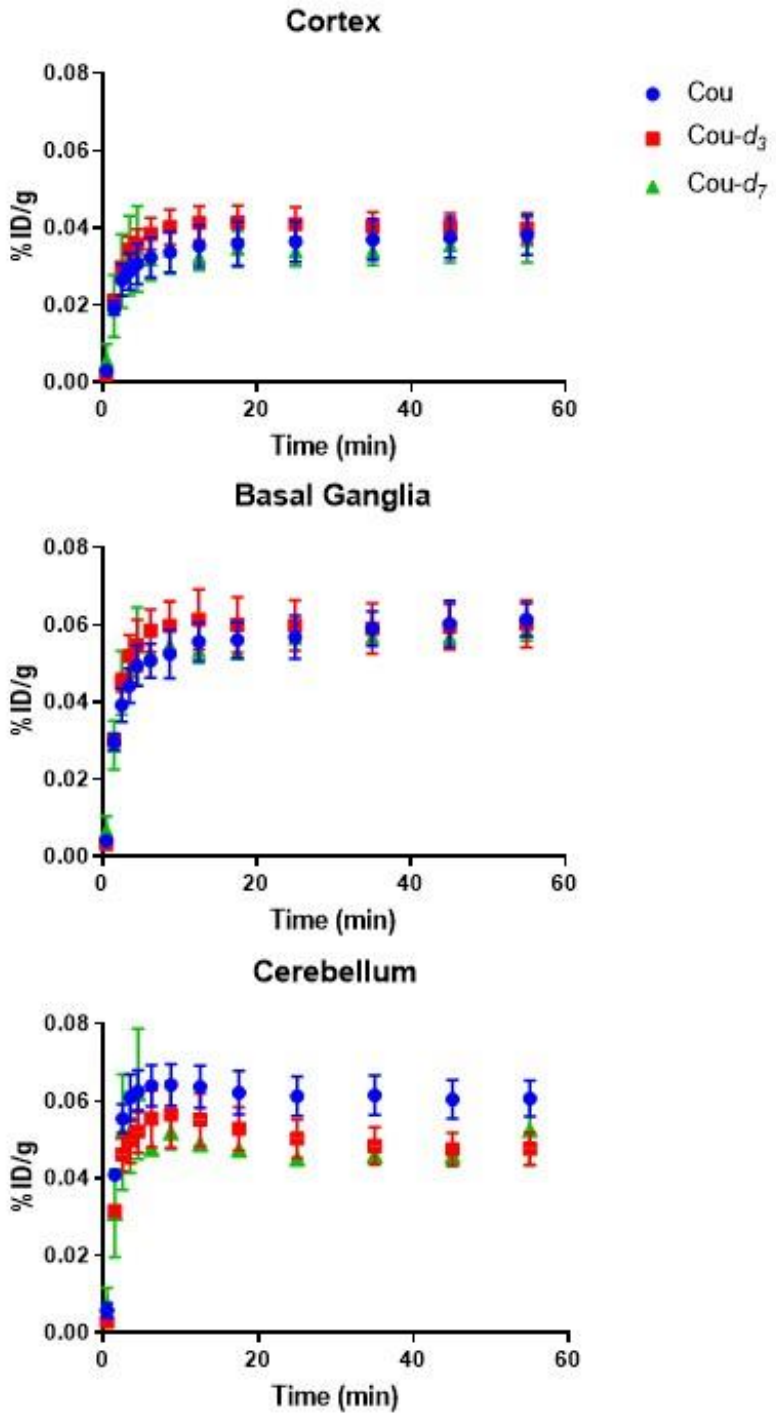

Figure 3.8. Regional tissue time-radioactivity curves for PET imaging of [^{11}C] Cou, [^{11}C]Cou-d_3, and [^{11}C]Cou-d_7 in the rhesus monkey brain.

3. Discussion

Kinetic isotope effects have been clearly demonstrated for a number of amine substrates of the monoamine oxidases, leading to the conclusion that the abstraction of an allylic hydrogen at the position alpha to the nitrogen is the rate limiting step.[32-35] This has been exploited in the design of PET imaging agents for monoamine oxidases, where incorporation of deuterium has been used to slow down the rate of irreversible trapping of [^{11}C]deprenyl, resulting in improved *in vivo* pharmacokinetics in animals and humans.[5] *In vitro* kinetic isotope effects have also been demonstrated for MAO oxidation of MPTP and related analogues, [32-33] prompting our expectation that deuterium substitution could be employed to modify the *in vivo* pharmacokinetics of our newly developed MAO substrate, [^{11}C]Cou. It was therefore surprising that our *in vitro* assays of MAO-B activity showed no isotope effect for deuterium substitution of Cou (Table 3.1); in comparison, kinetic isotope effect values for MAO oxidation of MPTP-6,6-d_2 to the corresponding 1-methyl-4-phenyl-2,3-dihydropyridinium species were 3.55 (V_{max}) and 8.01 (V_{max}/ K_m).[32]

The *in vivo* studies in primate brain for [^{11}C]Cou-d_3 and [^{11}C]Cou-d_7 were also consistent with the lack of a deuterium substitution effect because the pharmacokinetic curves for radiotracer trapping were similar for all three substrates, showing a rapid uptake to a plateau with very little washout of radioactivity, consistent with irreversible trapping. This is markedly different than the effect seen for [^{11}C]deprenyl-d_2, where incorporation of deuterium resulted in a significant egress of radioactivity after peak uptake and a lower plateau level of trapped radioactivity, and thus very different shapes for the brain time-radioactivity curves.[5]

Based on the mechanism of MAO-mediated oxidation of amines, and the known effect of deuterium substitution on MPTP oxidation kinetics, it is reasonable to assume the oxidation of [^{11}C]Cou should also proceed via abstraction of the allylic C-6 proton alpha to the ring nitrogen

(figure 3.8). The lack of a kinetic isotope effect both *in vitro* and *in vivo* suggest that the proton abstraction step was not rate limiting. A possible explanation lies in the observation that our studies actually detect the final metabolites, the radioactive N-[^{11}C]-methylpyridinone (*in vivo* PET) or the fluorescent coumarin (*in vitro* assays; figure 3.5) that form after a second step of hydrolysis of the intermediate 1-methyl-4-phenoxy-2,3-dihydropyridinium species (in contrast, the *in vitro* kinetic studies of deuterated MPTP measured the dihydropyridinium species). Thus, it is possible that the hydrolysis step was partially rate limiting and obscuring any effect from the deuterium substitution, an example of a masked kinetic isotope effect.[34]

The enzymatic mechanism of MAO has been investigated thoroughly; however, the mode of C-H bond breakage is not entirely agreed upon. The two main mechanistic theories involve either hydrogen abstraction or hydride transfer, which differ in their respective intermediates, but both claim that this step is rate limiting. Silverman and coworkers spent the better part of two decades gathering evidence against a possible radical mechanism and for the hydrogen abstraction mechanism.[36-39] Investigating inhibitors of the enzyme supported the presence of a covalently bound intermediate to the FAD cofactor, indicating a hydrogen atom transfer. This mechanism was further strengthened by crystallographic evidence of the covalently bound inhibitor, deprenyl, in 2002.[3] The Edmondson,[40-41] Castagnoli,[32-33, 42-45] and Heikkila[27-28, 46-48] groups also greatly contributed to the investigation into the MAO mechanism. Similar to Silverman's kinetic experiments, all of these groups were able to demonstrate primary kinetic isotope effects upon deuterium substitution at the carbon alpha to the monoamine (figure 3.4, red circle). Regardless of the identity of the C-H bond breakage, hydride or hydrogen atom, there is evidence for this to be 1) rate limiting and 2) highly sensitive to isotopic exchange.[25-26, 32, 40-41, 43] Our results at face value would indicate that with our substrate, it is not rate limiting. However,

masking effects of complex enzymatic mechanisms have been observed in similar oxidoreductase enzymes, though not documented in MAO-B itself.[34] Masking is the phenomenon in which non-rate limiting steps are insensitive to isotope changes. In a complex enzymatic mechanism such as MAO-B (figure 3.8), there are reversible steps before and after the rate limiting step. The first reversible step, association of the substrate to the enzyme and FAD in its oxidized state (k_1 and k_2), is isotopically insensitive. This can be assumed from the lack of binding isotope effect, or the change in Michaelis-Menten constant (K_m; table 3.1). The rate limiting step (k_3) is irreversible and followed by either re-oxidation of the FAD cofactor (irreversible, k_4) or release of the imine product (reversible, k_4' and k_5') and then followed by hydrolysis. In both instances, it is likely that these steps are isotopically insensitive based on the experimentally obtained turnover rates (V_{max}; table 3.1). In previously mentioned kinetic studies, the assays detected the immediate imine product formation, not the fully hydrolyzed final product. It is feasible then, that these additional steps are masking the primary kinetic isotope effect expected through deuterium substitution. It also possible that the oxidation step undergoes a different mechanism than the polar nuclear mechanism (figure 3.8). Although it is more likely that the deuterium kinetic isotope effect is masked in this substrate. Deprenyl, being an irreversibly inhibitor, does not proceed through the entire enzymatic mechanism. The deuterium KIE observed in deprenyl-d_2 could be visible because it does not include k_4, k_5, and k_6.

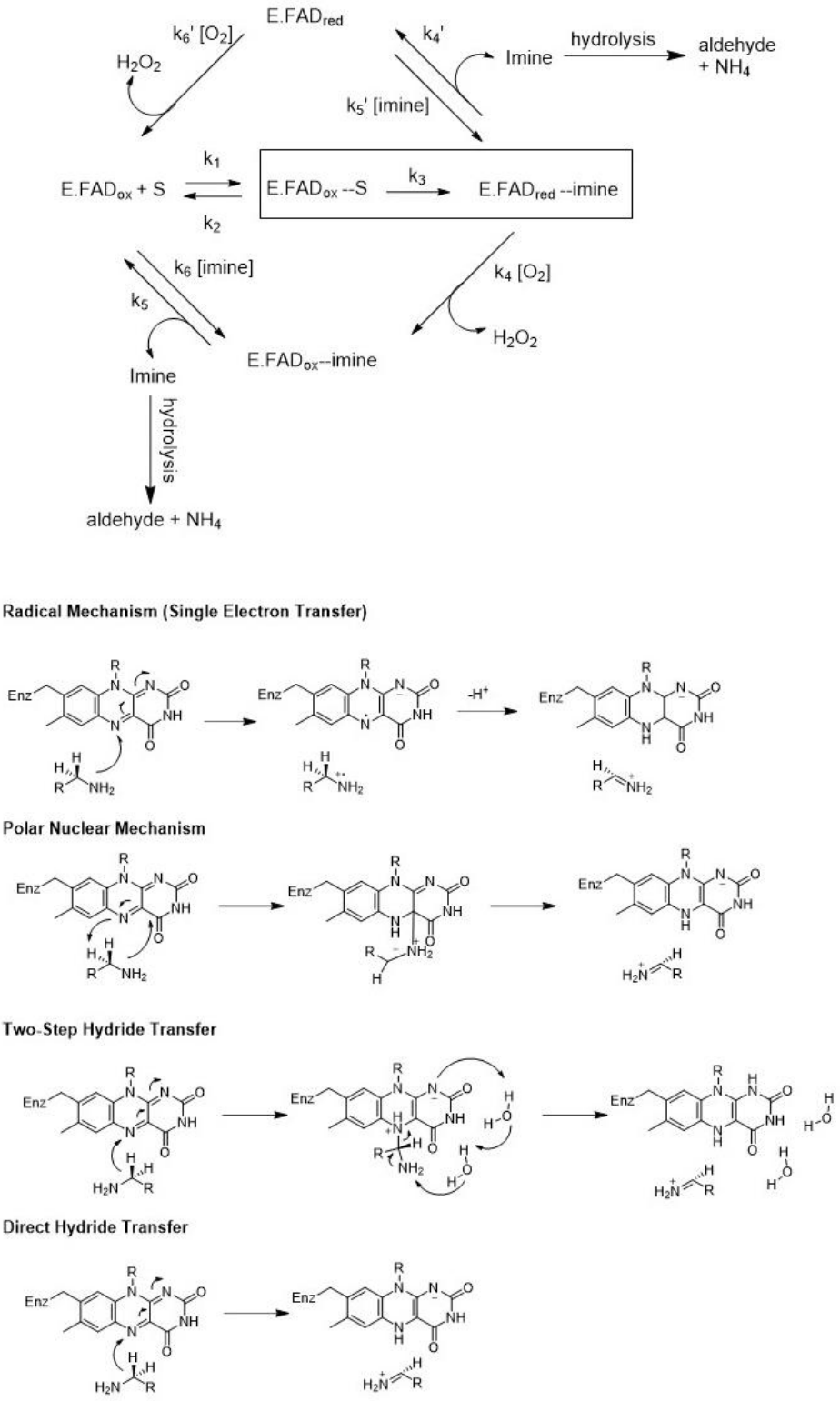

Figure 3.9. Proposed monoamine oxidase mechanisms.

4. Conclusion

The objective of this study was to utilize deuterium substitution to alter the *in vivo* pharmacokinetics of [^{11}C]Cou, a metabolically-trapped PET imaging agent for MAO-B that shows rapid and essentially irreversible retention in the primate brain. From a compartmental modeling perspective, the goal was to reduce the rate of trapping (k_3) such that a portion of the radiotracer taken up into the brain would flow back out (k_2): this was exactly what had been achieved with deuteration of the irreversible radioligand [^{11}C]deprenyl.[5] Unfortunately, deuterium substitution of [^{11}C]Cou failed to produce any significant change of *in vitro* kinetics or *in vivo* pharmacokinetics. Future efforts to improve the *in vivo* behavior of metabolically-trapped MAO substrates for PET imaging will likely require further exploration of alternative 4-aryloxy substituents.[49]

5. Methods

Biology.

Michaelis-Menten kinetic parameters were determined using human MAO-A and –B Supersomes (Corning Gentest) at a concentration of 80 µg/ml. Fresh stocks of substrate (Cou, Cou-d_3, or Cou-d_7) were dissolved in DMSO to give a 10 mM stock and subsequently diluted in 100 mM borate buffer (pH 8.4) to various concentrations ranging from 200 µM to 1 nM. Reaction progress was measured by appearance of fluorescent product, 7-hydroxy-4-methyl-coumarin. Reactions were monitored in real time using a Biotek Hybrid plate reader (excitation 360 nm, emission 460 nm) at 37 °C; reactions progressed for 60 minutes and fluorescent reads were measured every 5 minutes. The resultant fluorescence units were converted to concentration of product using a reference standard curve. Michaelis-Menten curves were plotted and parameters computed in GraphPad Prism (version 7.03). Assays were done in duplicate, in

six independent experiments using fresh stock of enzyme, test compound, and reference standard. Outliers which met the Grubb's test were removed.

Radiochemistry.

General Considerations

Reagents and solvents were commercially available and used without further purification, unless otherwise noted. Sodium chloride (0.9% USP) and sterile water for injection (USP) were purchased from Hospira; dehydrated alcohol for injection (USP) was obtained from Akorn Inc. Shimalite-Nickle was purchased from Shimadzu, iodine was obtained from EMD, phosphorous pentoxide was acquired from Fluka, molecular sieves were purchased from Alltech, and HPLC columns were acquired from Phenomenox. Other synthesis components were obtained as follows: sterile filters were purchased from Millipore, C18-light Sep-Paks and Porapak Q were purchased from Waters Corporation, and 10 cc sterile vials were obtained from HollisterStier. Sep-paks were flushed with 10 mL of ethanol followed by 10 mL of sterile water prior to use.

General Procedure for Radiochemical Synthesis.

Production of carbon-11-labeled radiotracers was carried out using a Tracerlab FXC-Pro automated radiochemistry synthesis module (General Electric, GE). [^{11}C]Carbon dioxide was produced using a GE PETTrace cyclotron (40 μA beam for 20 min) and converted by standard procedures into carbon-11-labeled methyl triflate ([^{11}C]CH_3OTf). The [^{11}C]CH_3OTf in helium carrier gas was bubbled into a vial containing a solution of precursor (1 mg) dissolved in ethanol or ethanol-d6 (0.2 mL). At the completion of transfer of radioactivity into the reaction vial, the ethanol solution was then transferred to a second conical vial containing sodium borohydride or sodium borodeuteride (2 mg) in ethanol or ethanol-d_6 (0.2 mL). The resulting mixture was stirred

for 5 min at room temperature, and then the reaction was quenched by addition of HPLC buffer. The crude product was loaded onto semipreparative HPLC loop. The product was purified by reverse-phase chromatography (Prodigy ODS prep, 250 x 10 mm, 10 μ, 4 mL/min, eluted with 30% CH_3CN, 70% H_2O 10 mM NH_4OAc) collected, diluted into H_2O (40 mL), and reformulated using a C-18 extraction disk into a final 5 mL total volume of 10% ethanol in saline. The doses were assessed via standard quality control techniques and were appropriate for nonhuman primate studies. Overall synthesis times were 30 min from end-of-bombardment. Radiochemical yields were not optimized and are reported uncorrected for radioactive decay. Molar specific activity greater than 7000 Ci/mmol.

Primate Imaging.

General Considerations.

All animal studies were performed in accordance with standards set by the University of Michigan Institutional Animal Care and Use Committee (IACUC).

Primate imaging studies.

Imaging was done using a mature female rhesus macaque (n=6, weight= 8 ± 1 kg) over 36 months. The monkey was anesthetized (isoflurane), intubated, and positioned in a Concorde MicroPET P4 scanner. Following a transmission scan, the animal was injected i.v with [^{11}C]COU (4.7 ± 0.2 mCi, n=2), [^{11}C]COU-d_3 (4.8 ± 0.4 mCi, n=2), or [^{11}C]Cou-d_7 (0.86 ± 0.7 mCi, n=2), as a bolus over 1 min, and the brain imaged for 90 min (5 x 1 min frames – 2 x 2.5 min frames – 2 x 5 min frames – 7 x 10 min frames).

Image Analysis.

Emission data were corrected for attenuation and scatter, and reconstructed using the 3D maximum a priori method (3D MAP algorithm). Using a summed image of the entire data set,

3D volumes of interest (VOI) were determined by placing a seed voxel in the middle of various brain regions, and then using region- specific thresholds to automatically determine the extent of each VOI. VOIs were determine for the whole brain, striatum, thalamus, cortex, hippocampus, and cerebellum. Previous data sets in the same primate were used as reference determining specific VOIs ([^{11}C]Flumazenil for cortex and cerebellum, [^{11}C]DTBZ for striatum, [^{11}C]Carfentenil for thalamus and hippocampus). The VOIs were then applied to the full dynamic data sets to obtain the regional tissue time-radioactivity curves. Time activity curves were normalized between studies by the animal weight and amount of activity injected to result in percent injected dose per gram.

Chemistry.

General Considerations.

All solvents and reagents were commercially available and used without further purification unless otherwise stated. 7-Methylumbeliferone was obtained from Sigma-Aldrich. NMR spectra were recorded with a Varian 400 MHz instrument at room temperature with tetramethylsilane (TMS) as an internal standard. Mass spectra were performed on a Micromass LCT time-of-flight mass spectrometer or an Agilent Q-TOF HPLC-MS employing the electrospray ioinization (ESI) method. High-performance liquid chromatography (HPLC) was performed using a Shimadzu LC-2010A HT system equipped with a Bioscan B-FC-1000 radiation detector.

4-methyl-7-((1-methyl-1,2,3,6-tetrahydropyridin-4-yl-2,3,6-d_3)oxy)-2H-chromen-2-one (**3.7**): 4-Methylumbeliferone (0.72 mmol) was added to sodium methoxide (0.87 mmol) dissolved in DMF (3 mL) and the mixture stirred for 10 min. 4-Chloro-1-methylpyridin-1-ium triflate (0.73 mmol) was added, and the reaction was stirred for 18 h. The solvent was removed in vacuo, and

the resulting intermediate was suspending in methanol-d_4 (3 mL). The reaction mixture was cooled to 0°C in a water ice bath, and sodium borodeuteride (2.9 mmol) was added slowly. After 1 h, the solvent was removed *in vacuo*. Water and ethyl acetate were added to the residue, and the mixture was transferred to a separatory funnel. The product was extracted with ethyl acetate (3x), dried over sodium sulfate, filtered, and concentrated *in vacuo*. The product was purified by flash silica gel chromatography (dichloromethane, methanol gradient) and collected as a white solid in 36% yield. Rf: 0.34 (SiO2, 1:9 methanol: dichloromethane); ^{1}H NMR (500 MHz; CD_3OD_3)/δ (ppm): 7.75 (1H, d, J = 10), 7.05 (1H, dd, J = 10, 5), 7.00 (1H, s), 6.22 (1H, s), 5.22 (1H, s), 3.07 (1H, d, J=10), 2.73 (1H, d, J= 5), 2.37 (3H,s), 2.36 (3H, s), 2.30 (1H,d, J=5); . ^{2}H NMR (61.402 MHz; CD_3OD / δ (ppm): 3.06 (1D, s), 2.73 (1D, s), 2.36 (1D, s), 2.33 (1D, s); HRMS: calculated for [M]+ (M =$C_{16}H_{14}D_3NO_3$), 275.1470, found 275.1469.

7-iodo-4-methyl-2H-chromen-2-one **(3.9)***:* A mixture of 3-iodophenol (4.3 g, 38.4 mmol) and ethyl acetoacetate (5.0 g, 38.4 mmol) were cooled to 0 ˚C. Sulfuric acid (12 ml, 38 mmol) was added dropwise, and the mixture stirred for 20 h at 40 °C. The resulting solution was slowly poured into a water-ice water mixture (200 ml); the resulting precipitate was collected by filtration, dissolved in DCM, and dried over sodium sulfate. The product was collected as a (green) solid in 10% yield. Rf: 0.425 (SiO_2, 2:1=hexane:ethyl acetate); ^{1}H NMR (400 MHz; $CDCl_3$)/δ (ppm): 7.75 (1H, d, J = 1.65), 7.72 (1H, dd, J = 8.33, 1.65), 7.52 (1H, d, J = 8.33), 6.36 (1H, q, J= 1.22), 2.45 (3H, d, J = 1.22); HRMS: calculated for [M]+(M = $C_{10}H_7IO_2$), 286.9490, found 286.9560.

Hydroxy(4-methyl-2-oxo-2H-chromen-7-yl)iodonium 4-methylbenzenesulfonate **(3.10)***:* In a flame dried flask, a mixture of 7-iodo-4-methyl-2H-chromen-2-one [3.9] (0.2 g, 0.7 mmol), meta-chloroperbenzoic acid (mCPBa) (0.12 g, 0.7 mmol) and p-toluenesulfonic acid

monohydrate ($TsOH•H_2O$) (0.13 g, 0.7 mmol) were dissolved in dichloromethane (2 mL) and stirred for 2 hours under Argon. The solution was quenched with diethyl ether (2 ml), and the resulting precipitate was collected by filtration and dried *in vacuo*. The product was collected as a (yellow) solid in 73% yield. ^{1}H NMR (400 MHz; C_2D_6OS/ δ (ppm): 8.28 (1H, d, J = 1.69), 8.11 (1H, dd, 8.48, 1.69), 7.95 (1H, d, J = 8.48), 7.82 (1H, d, J = 1.63), 7.71 (1H, dd, J = 8.30, 1.63), 7.51 (1H, d, J = 8.30), 7.1 (1H, d, J = 8.48), 6.58 (1H, d, J = 1.22), 6.43 (1H, q, J = 1.20), 2.40 (3H, d, J = 1.20), 2.45 (3H, d, J = 1.22).

(4-methoxyphenyl)(4-methyl-2-oxo-2H-chromen-7-yl)iodonium 4-methylbenzenesulfonate **(3.11)*:*** Hydroxy(4-methyl-2-oxo-2H-chromen-7-yl)iodoium 4-methylbenzenesulfonate [3.10] (0.26 g, 0.86 mmol) and anisole (0.23 g, 2.15 mmol) were dissolved in chloroform (7 ml) and stirred overnight at room temperature (25 °C). The solvent was removed *in vacuo*; the resulting precipitate was washed with diethyl ether. The solution was dried *in vacuo*, and the product was collected as a (yellow) solid in 76% yield. ^{1}H NMR (400 MHz; DMSO-d_6/ δ (ppm): 8.33 (1H, d, J = 1.68), 8.19 (2H, d, J = 8.58), 8.08 (1H, dd, J = 8.19, 1.68), 7.83 (1H, d, J = 8.19), 7.43 (2H, d, J = 8.58), 6.51 (1H, q, J = 1.23), 3.76 (3H, s), 2.38 (3H, d, J = 1.23); HRMS: calculated for [M]+(M = $C_{17}H_{14}IO_3$+), 392.998, found 392.9982.

4-methyl-7-(pyridine-4-yl-d_4)oxy)-2H-chromen-2-one **(3.12)*:*** In a flame dried flask, a mixture of 4-hydroxypyridine-d_5 (0.054 g, 0.51 mmol) and potassium carbonate (0.14 g, 1.02 mmol) were dissolved in acetonitrile (3 ml) and stirred for 5 min at room temperature (25 °C). (4-methoxyphenyl)(4-methyl-2-oxo-2H-chromen-7-yl)iodonium 4-methylbenzenesulfonate [3.11] (0.20 g, 0.51 mmol) was added and the mixture stirred overnight at 50 °C. The solution was quenched with H_2O, extracted with DCM, and dried over Na_2SO_4. Product was purified by silica gel flash chromatography eluted with Hexane: Ethyl Acetate gradient mobile phase. The product

was collected as a (red) solid in 38% yield. Rf: 0.268 (SiO_2, Ethyl Acetate); ^1H NMR (400 M Hz; $CDCl_3$)/δ (ppm): 7.64 (1H, d, J = 6.19), 7.04 (1H, dd, J = 6.19, 2.28), 7.02 (1H, d, J = 2.28), 6.27 (1H, q, J = 1.06), 2.42 (3H, d, J = 1.06); HRMS: calculated for [M]+(M = $C_{15}H_7D_4NO_3$), 258.0990, found 258.1065.

4-methyl-7-((1-methyl-1,2,3,6-tetrahydrophyridin-4-yl-2,2,3,3,5,6,6-d_7)oxy)-2H-chromen-2one **(3.14)*:*** In a flame dried flask, a mixture of 4-methyl-7-(pyridine-4-yl-d_4)oxy)-2H-chromen-2-one [3.12] (0.077 g, 0.3 mmol) was dissolved in 1,2–dichloroethene (3ml). Methyl Trifluoromethansulfonate (2 ml) was added to reaction mixture slowly, solution stirred for 1 hour at 60 °C. Mixture washed with diethyl ether, precipitate (white) was collected by filtration, resulting in intermediate 1-methy-4-((4-methyl-2-oxo-2H-chromen-7-yl)pyridine-1-ium-2,3,5,6-d_4 [3.13]. Intermediate re-suspended in methanol-d_4 (3 ml), cooled to 0 °C, then sodium borodeuteride (0.031 g, 0.74 mmol) added slowly. Mixture stirred for 1 hour at room temperature (25 °C). Solution quenched with H_2O and extracted in ethyl acetate and purified by column chromatography (dichloromethane: methanol mobile phase). The product was collected as a (yellow) solid in 37% yield. Rf: 0.233 (SiO_2, 9:1=dichloromethane: ethyl acetate); ^1H NMR (400 MHz; $CDCl_3$)/δ (ppm): 7.50 (1H, d, J = 8.35), 6.97 (1H, m), 6.95 (1H, d, J = 2.25), 6.16 (1H, s), 2.39 (3H, s). ^2H NMR (61.402 MHz; $CHCl_3$/ δ (ppm): 5.20 (1D, s), 3.01 (2D, s), 2.66 (2D, s), 2.33 (2D, s); HRMS: calculated for [M]+(M = $C_{16}H_{10}D_7NO_3$), 279.1721, found 279.1722.

6. References

1. Drake, L. R.; Brooks, A. F.; Mufarreh, A. J.; Pham, J. M.; Koeppe, R. A.; Shao, X.; Scott, P. J. H.; Kilbourn, M. R., Deuterium Kinetic Isotope Effect Studies of a Potential in Vivo Metabolic Trapping Agent for Monoamine Oxidase B. *ACS Chemical Neuroscience* **2018**.
2. Youdim, M. B. H.; Edmondson, D.; Tipton, K. F., The therapeutic potential of monoamine oxidase inhibitors. *Nature Reviews Neuroscience* **2006,** *7*, 295.
3. Binda, C.; Newton-Vinson, P.; Hubálek, F.; Edmondson, D. E.; Mattevi, A., Structure of human monoamine oxidase B, a drug target for the treatment of neurological disorders. *Nature Structural and Molecular Biology* **2002,** *9* (1), 22.
4. Fowler, J. S.; MacGregor, R. R.; Wolf, A. P.; Arnett, C. D.; Dewey, S. L.; Schlyer, D.; Christman, D.; Logan, J.; Smith, M.; Sachs, H.; Aquilonius, S. M.; Bjurling, P.; Halldin, C.; Hartvig, P.; Leenders, K. L.; Lundquist, H.; Oreland, L.; Stalnacke, C. G.; Langstrom, B., Mapping human brain monoamine oxidase A and B with carbon eleven-labeled suicide inactivators and PET. *Science* **1987,** *235*, 481+.
5. Fowler, J. S.; Wang, G.-J.; Logan, J.; Xie, S.; Volkow, N. D.; MacGregor, R. R.; Schlyer, D. J.; Pappas, N.; Alexoff, D. L.; Patlak, C.; Wolf, A. P., Selective Reduction of Radiotracer Trapping by Deuterium Substitution: Comparison of Carbon-11-L-Deprenyl and Carbon-11-Deprenyl-D2 for MAO B Mapping. *Journal of Nuclear Medicine* **1995,** *36* (7), 1255-1262.
6. Fowler, J. S.; Volkow, N.; Wang, G.-J.; Pappas, N.; Logan, J.; MacGregor, R.; Alexoff, D.; Shea, C.; Schlyer, D.; Wolf, A., Inhibition of monoamine oxidase B in the brains of smokers. *Nature* **1996,** *379* (6567), 733.
7. Fowler, J. S.; Logan, J.; Gene-Jack, W.; Volkow, N. D.; et al., PET imaging of monoamine oxidase B in peripheral organs in humans. *The Journal of Nuclear Medicine* **2002,** *43* (10), 1331-8.
8. Fowler, J. S.; Logan, J.; Ding, Y. S.; Franceschi, D.; Wang, G. J.; Volkow, N. D.; Pappas, N.; Schlyer, D.; Gatley, S. J.; Alexoff, D.; Felder, C.; Biegon, A.; Zhu, W., Non-MAO A binding of clorgyline in white matter in human brain. *J. Neurochem.* **2001,** *79* (5), 1039-1046.
9. Matthews, B. A.; Kish, S. J.; Xu, X.; Boileau, I.; Rusjan, P. M.; Wilson, A. A.; DiGiacomo, D.; Houle, S.; Meyer, J. H., Greater Monoamine Oxidase A Binding in Alcohol Dependence. *Biol. Psychiatry* **2014,** *75* (10), 756-764.
10. Kolla, N. J.; Matthews, B.; Wilson, A. A.; Houle, S.; Bagby, R. M.; Links, P.; Simpson, A. I.; Hussain, A.; Meyer, J. H., Lower Monoamine Oxidase-A Total Distribution Volume in Impulsive and Violent Male Offenders with Antisocial Personality Disorder and High Psychopathic Traits: An [11C] Harmine Positron Emission Tomography Study. *Neuropsychopharmacology* **2015,** *40* (11), 2596-2603.
11. Sacher, J.; Rekkas, P. V.; Wilson, A. A.; Houle, S.; Romano, L.; Hamidi, J.; Rusjan, P.; Fan, I.; Stewart, D. E.; Meyer, J. H., Relationship of Monoamine Oxidase-A Distribution Volume to Postpartum Depression and Postpartum Crying. *Neuropsychopharmacology* **2015,** *40* (2), 429-435.
12. Kolla, N. J.; Dunlop, K.; Downar, J.; Links, P.; Michael Bagby, R.; Wilson, A. A.; Houle, S.; Rasquinha, F.; Simpson, A. I.; Meyer, J. H., Association of ventral striatum monoamine oxidase-A binding and functional connectivity in antisocial personality disorder with high impulsivity: A positron emission tomography and functional magnetic resonance imaging study. *Eur. Neuropsychopharmacol.* **2016,** *26* (4), 777-786.
13. Kolla, N. J.; Chiuccariello, L.; Wilson, A. A.; Houle, S.; Links, P.; Bagby, R. M.; McMain, S.; Kellow, C.; Patel, J.; Rekkas, P. V.; Pasricha, S.; Meyer, J. H., Elevated Monoamine Oxidase-A Distribution Volume in Borderline Personality Disorder Is Associated with Severity Across Mood Symptoms, Suicidality, and Cognition. *Biol. Psychiatry* **2016,** *79* (2), 117-126.
14. Finberg, J. P. M., Update on the pharmacology of selective inhibitors of MAO-A and MAO-B: Focus on modulation of CNS monoamine neurotransmitter release. *Pharmacology & Therapeutics* **2014,** *143* (2), 133-152.
15. Meyer, J. H.; Ginovart, N.; Boovariwala, A.; Sagrati, S.; Hussey, D.; Garcia, A.; Young, T.; Praschak-Rieder, N.; Wilson, A. A.; Houle, S., Elevated monoamine oxidase A levels in the brain: an

explanation for the monoamine imbalance of major depression. *Arch. Gen. Psychiatry* **2006,** *63* (11), 1209-1216.
16. Oreland, L.; Fowler, C. J.; Carlsson, A.; Magnusson, T., Monoamine oxidase -A and -B activity in the rat brain after hemitransection. *Life Sciences* **1980,** *26* (2), 139-146.
17. Levitt, P.; Pintar, J. E.; Breakefield, X. O., Immunocytochemical demonstration of monoamine oxidase B in brain astrocytes and serotonergic neurons. *Proceedings of the National Academy of Sciences of the United States of America* **1982,** *79* (20), 6385-6389.
18. Nakamura, S.; Kawamata, T.; Akiguchi, I.; Kameyama, M.; Nakamura, N.; Kimura, H., Expression of monoamine oxidase B activity in astrocytes of senile plaques. *Acta Neuropathologica* **1990,** *80* (4), 419-425.
19. Jossan, S. S.; Gillberg, P. G.; d'Argy, R.; Aquilonius, S. M.; Låangstro¨m, B.; Halldin, C.; Oreland, L., Quantitative localization of human brain monoamine oxidase B by large section autoradiography using l-[3H]deprenyl. *Brain Research* **1991,** *547* (1), 76-80.
20. Ekblom, J.; Jossan, S. S.; Bergström, M.; Oreland, L.; Walum, E.; Aquilonius, S.-M., Monoamine oxidase-B in astrocytes. *Glia* **1993,** *8* (2), 122-132.
21. Carter, S. F.; Schoell, M.; Almkvist, O.; Wall, A.; Engler, H.; Laangstroem, B.; Nordberg, A., Evidence for astrocytosis in prodromal Alzheimer disease provided by 11C-deuterium-L-deprenyl: a multitracer PET paradigm combining 11C-Pittsburgh compound B and 18F-FDG. *J. Nucl. Med.* **2012,** *53* (1), 37-46.
22. Choo, I. L. h.; Carter, S. F.; Schoell, M. L.; Nordberg, A., Astrocytosis measured by 11C-deprenyl PET correlates with decrease in gray matter density in the parahippocampus of prodromal Alzheimer's patients. *Eur. J. Nucl. Med. Mol. Imaging* **2014,** *41* (11), 2120-2126.
23. Saba, W.; Valette, H.; Peyronneau, M. A.; Bramoullé, Y.; Coulon, C.; Curet, O.; George, P.; Dollé, F.; Bottlaender, M., [11C] SL25. 1188, a new reversible radioligand to study the monoamine oxidase type B with PET: Preclinical characterisation in nonhuman primate. *Synapse* **2010,** *64* (1), 61-69.
24. Rusjan, P. M.; Wilson, A. A.; Miler, L.; Fan, I.; Mizrahi, R.; Houle, S.; Vasdev, N.; Meyer, J. H., Kinetic modeling of the monoamine oxidase B radioligand [11C]SL25.1188 in human brain with high-resolution positron emission tomography. *J. Cereb. Blood Flow Metab.* **2014,** *34* (5), 883-889.
25. Salach, J. I.; Singer, T. P.; Castagnoli, N., Jr.; Trevor, A., Oxidation of the neurotoxic amine 1-methyl-4-phenyl-1,2,3,6-tetrahydropyridine (MPTP) by monoamine oxidases A and B and suicide inactivation of the enzymes by MPTP. *Biochem. Biophys. Res. Commun.* **1984,** *125* (2), 831-5.
26. Chiba, K.; Trevor, A.; Castagnoli, N., Jr., Metabolism of the neurotoxic tertiary amine, MPTP, by brain monoamine oxidase. *Biochem. Biophys. Res. Commun.* **1984,** *120* (2), 574-8.
27. Heikkila, R. E.; Cabbat, F. S.; Manzino, L.; Duvoisin, R. C., Effects of 1-methyl-4-phenyl-1,2,5,6-tetrahydropyridine on neostriatal dopamine in mice. *Neuropharmacology* **1984,** *23* (6), 711-13.
28. Heikkila, R. E.; Hess, A.; Duvoisin, R. C., Dopaminergic neurotoxicity of 1-methyl-4-phenyl-1,2,5,6-tetrahydropyridine in mice. *Science* **1984,** *224* (4656), 1451-3.
29. Castagnoli, N.; Chiba, K.; Trevor, A. J., Potential Bioactivation Pathways for the Neurotoxin 1-methyl-4-phenyl-1,2,3,6-tetrahydropyridine (MPTP). *Life Sciences* **1985,** *36*, 223-230.
30. Maret, G.; Testa, B.; Jenner, P.; Tayar, N. E.; Carrupt, P.-A., The MPTP Story: Mao Activates Tetrahydropyridine Derivatives to Toxins Causing Parkinsonism. *Drug Metabolism Reviews* **1990,** *22* (4), 291-332.
31. Brooks, A. F.; Shao, X.; Quesada, C. A.; Sherman, P.; Scott, P. J. H.; Kilbourn, M. R., In Vivo Metabolic Trapping Radiotracers for Imaging Monoamine Oxidase-A and -B Enzymatic Activity. *ACS Chemical Neuroscience* **2015,** *6* (12), 1965-1971.
32. Ottoboni, S.; Caldera, P.; Trevor, A.; Castagnoli, N., Jr., Deuterium isotope effect measurements on the interactions of the neurotoxin 1-methyl-4-phenyl-1,2,3,6-tetrahydropyridine with monoamine oxidase B. *J. Biol. Chem.* **1989,** *264* (23), 13684-8.
33. Pretorius, A.; Ogunrombi, M. O.; Terre'Blanche, G.; Castagnoli, N.; Bergh, J. J., Deuterium isotope effects for the oxidation of 1-methyl-3-phenyl-3-pyrrolinyl analogues by monoamine oxidase B. *Bioorganic & Medicinal Chemistry* **2008,** *16*, 8813-8817.

34. Wang, Z.; Roston, D.; Kohen, A., Chapter 6 - Experimental and Theoretical Studies of Enzyme-Catalyzed Hydrogen-Transfer Reactions. In *Advances in Protein Chemistry and Structural Biology*, Christov, C.; Karabencheva-Christova, T., Eds. Academic Press: 2012; Vol. 87, pp 155-180.
35. Mavri, J.; Matute, R. A.; Chu, Z. T.; Vianello, R., Path Integral Simulation of the H/D Kinetic Isotope Effect in Monoamine Oxidase B Catalyzed Decomposition of Dopamine. *The Journal of Physical Chemistry B* **2016,** *120* (14), 3488-3492.
36. Silverman, R. B.; Hoffman, S. J.; Catus, W. B., A mechanism for mitochondrial monoamine oxidase catalyzed amine oxidation. *Journal of the American Chemical Society* **1980,** *102* (23), 7126-7128.
37. Silverman, R. B.; Zelechonok, Y., Evidence for a hydrogen atom transfer mechanism or a fast proton/electron transfer mechanism for monoamine oxidase. *The Journal of Organic Chemistry* **1992,** *57* (23), 6373-6374.
38. Silverman, R. B.; Zhou, J. P.; Eaton, P. E., Inactivation of monoamine oxidase by (aminomethyl)cubane. First evidence for an α-amino radical during enzyme catalysis. *J. Am. Chem. Soc.* **1993,** *115* (19), 8841-2.
39. Silverman, R. B.; Lu, X.; Zhou, J. J. P.; Swihart, A., Monoamine Oxidase B-Catalyzed Oxidation of Cinnamylamine 2,3-Oxide. Further Evidence against a Nucleophilic Mechanism. *J. Am. Chem. Soc.* **1994,** *116* (25), 11590-1.
40. Edmondson, D. E.; Bhattacharyya, A. K.; Walker, M. C., Spectral and kinetic studies of imine product formation in the oxidation of p-(N,N-dimethylamino)benzylamine analogs by monoamine oxidase B. *Biochemistry* **1993,** *32* (19), 5196-5202.
41. Miller, J. R.; Edmondson, D. E.; Grissom, C. B., Mechanistic probes of monoamine oxidase B catalysis: Rapid-scan stopped flow and magnetic field independence of the reductive half-reaction. *J. Am. Chem. Soc.* **1995,** *117* (29), 7830-1.
42. Shinka, T.; Castagnoli, N.; Wu, E. Y.; Hoag, M. K. P.; Trevor, A. J., Cation-exchange high-performance liquid chromatography assay for the nigrostriatal toxicant 1-methyl-4-phenyl-1,2,3,6-tetrahydropyridine and its monoamine oxidase B generated metabolites in brain tissue. *Journal of Chromatography* **1987,** *398*, 279-287.
43. Castagnoli, N., Jr.; Sparatore, A.; Ottoboni, S.; Leung, L.; Trevor, A., Mechanistic studies on the MPTP inactivation of MAO B. *Int. Congr. Ser. - Excerpta Med.* **1987,** *750* (Pharmacology), 875-8.
44. Naiman, N.; Rollema, H.; Johnson, E.; Castagnoli, N., Jr., Studies on 4-benzyl-1-methyl-1,2,3,6-tetrahydropyridine, a nonneurotoxic analog of the parkinsonian inducing agent 1-methyl-4-phenyl-1,2,3,6-tetrahydropyridine. *Chem. Res. Toxicol.* **1990,** *3* (2), 133-8.
45. Anderson, A. H.; Kuttab, S.; Castagnoli, N., Deuterium Isotope Effect Studies on the MAO-B Catalyzed Oxidation of 4-Benzyl-1-cyclopropyl-1,2,3,6-tetrahydropyridine. *Biochemistry* **1996,** *35* (10), 3335-3340.
46. Heikkila, R. E.; Manzino, L.; Cabbat, F. S.; Duvoisin, R. C., Protection against the dopaminergic neurotoxicity of 1-methyl-4-phenyl-1,2,5,6-tetrahydropyridine by monoamine oxidase inhibitors. *Nature* **1984,** *311* (5985), 467-9.
47. Heikkila, R. E.; Hess, A.; Duvoisin, R. C., Dopaminergic neurotoxicity of 1-methyl-4-phenyl-1,2,5,6-tetrahydropyridine (MPTP) in the mouse: relationships between monoamine oxidase, MPTP metabolism and neurotoxicity. *Life Sci* **1985,** *36* (3), 231-6.
48. Heikkila, R. E.; Youngster, S. K.; Manzino, L.; Cabbat, F. S.; Duvoisin, R. C., Effects of 1-methyl-4-phenyl-1,2,5,6-tetrahydropyridine and related compounds on the uptake of [3H]3,4-dihydroxyphenylethylamine and [3H]5-hydroxytryptamine in neostriatal synaptosomal preparations. *J Neurochem* **1985,** *44* (1), 310-3.
49. Kalgutkar, A. S.; Castagnoli, K.; Hall, A.; Castagnoli, N., Novel 4-(Aryloxy)tetrahydropyridine Analogs of MPTP as Monoamine Oxidase A and B substrates. *Journal of Medicinal Chemistry* **1994,** *37*, 944-949.

CHAPTER 4
Monoamine Oxidase: Dual PET-MR Imaging

The development of a PET/ magnetic resonance spectroscopy (MRS) hybrid imaging agent would allow for functional imaging by both methods with a single agent. Enzyme substrates that form metabolites for detection present an interesting opportunity as two unique metabolites can be generated, one for each modality. In addition, we hypothesize that at the concentrations obtained *in vivo* substrates should not inhibit uptake or enzymatic reaction; thus, they can overcome the challenge of the high concentration required for MRS while providing sufficient radioactivity for PET imaging at the resulting low molar activity. Here we investigate the possibility of imaging a MAO substrate that upon enzymatic reaction produces two metabolites: one for detection by PET and the other MRS.[1]

1. Introduction

Positron emission tomography (PET) imaging is a non-invasive molecular imaging method that has been utilized for decades to provide functional information based on the PET radioisotope (β+ decay) labelled molecule used.[2-3] Functional imaging is often paired with a form of structural imaging (computed tomography (CT), magnetic resonance (MR), etc). The combination of structural and functional imaging allows for an improved analysis of PET imaging data. Most PET scanners for clinical use include a CT scanner for this purpose. Recently, PET-MR scanners have been developed and allow for improved resolution over PET-CT.

MR imaging utilizes the nuclear magnetic resonance phenomenon in which nuclei in a strong magnetic field are perturbed by a weak oscillating magnetic field, producing an electromagnetic signal. Radio frequency (RF) pulses are used to excite the nuclear spin energy transition; the relaxation process, or returning to equilibrium after the excited state, is measured and offers different contrast.[4] Variation in RF pulses applied and collected allows for different types of images. Two variables that can be altered are repetition time (TR), the amount of time between pulse sequences applied to the same slice, and time to echo (TE), the time between the RF pulse delivered and the receipt of the echo signal.[4] Two common MRI sequences are T1-weighted and T2-weighted. T1-weighted images are produced by short TE and TR times; conversely T2 weighted images use longer TE and TR properties.[5] T1-weighted imaging can also be performed with the contrast agent galadinium.[6]

Typically, it is thought that high molar activity, the amount of radioactive isotope relative to non-radioactive isotopes defined by the amount of radioactivity for the moles of the molecule, is required for PET imaging (>1,000 Ci/mmol). Therefore, it is commonly thought to be incompatible with the higher concentrations of imaging agents required for alternate functional imaging methods like magnetic resonance spectroscopy (MRS).[7] For imaging with ligands, agents that bind to a target protein such as the antagonist [^{11}C]raclopride for the D_2 dopamine receptor, this has been demonstrated by studies of PET imaging/autoradiography with the radioligand at decreasing molar activities, demonstrating loss in signal as expected from the Scatchard equation.[8] Given the recent development of PET/MR imaging instruments it could be possible to not only combine the functional data from PET imaging with the morphological/structural data from magnetic resonance (MR) imaging but also functional MRS imaging data, provided a molecular imaging agent could be developed to provide PET and MRS

data. This would require a PET imaging agent that can provide data at the high concentration required for MRS imaging and the resulting low molar activity known to be problematic for radioligands.

We hypothesized that trapped metabolite imaging agents such as the monoamine oxidase (MAO) substrates developed by our laboratory[9] can provide PET imaging data at high concentration/low molar activity required for MRS. Since these enzyme substrates should not exhibit substrate inhibition *in vivo* they could provide PET data at low molar activity. To provide more evidence for this hypothesis, we evaluated the acetylcholine esterase (AchE) substrate 1-methylpiperidin-4-yl propionate (PMP) as well. AchE is an enzyme that catalyzes the hydrolysis of the neurotransmitter acetylcholine, and is thought to be one of the fastest enzymes.[10] It was chosen to show that if the enzyme is not saturated by the necessary MR concentration, the PET time activity curve shape will not change.

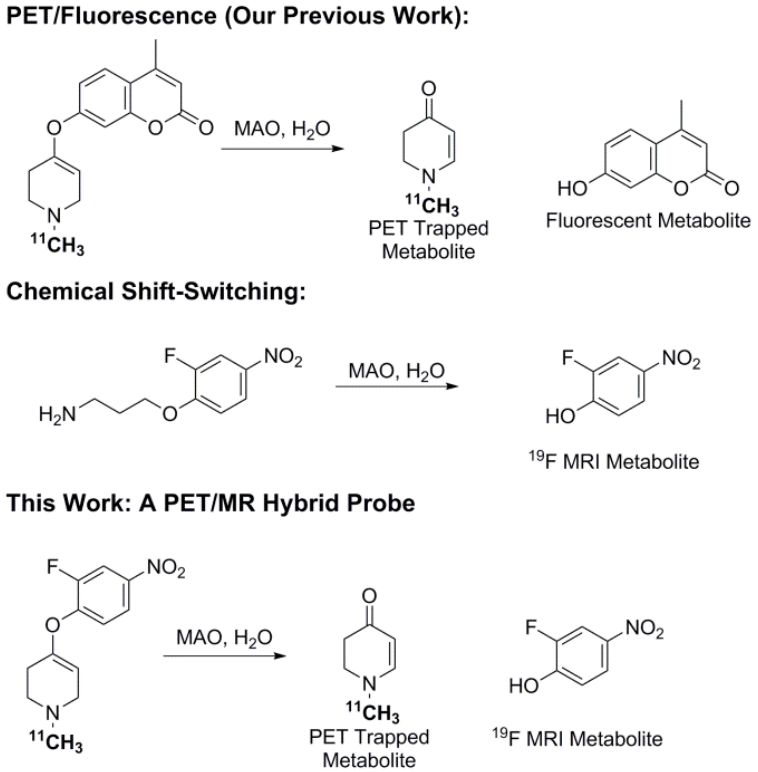

Figure 4.1 Design of PET/MR hybrid probe. Structure based on previous work developing a PET/Fluorescence probe and a related report on a chemical shift-switching MR probe, resulting in PET/MR probe investigated.

Imaging MAO has been of active interest as it is a marker of astrogliosis in neurodegenerative diseases.[9, 11-13] Our laboratory has explored the development of carbon-11 radiolabelled substrates of MAO-B for use as PET imaging agents (see chapter 3).[9] In our work, we have developed several PET imaging agents based on work from the Castagnoli lab[14] and initial reports of a MAO-B selective fluorogenic probe.[15] This led us to produce and evaluate a PET/fluorescence hybrid imaging agent (figure 4.1). Previously, Yamiguchi et. al. reported a MAO substrate MRS agent they described as a chemical shift-switching agent, as the ^{19}F NMR signal of the substrate could be distinguished from that of the metabolite formed. The metabolite formed is a phenol just as that formed using our tetrahydropyridine pharmacophore. Therefore, we hypothesized that combining our previous approach for a PET imaging MAO agent with the phenol of interest from Yamiguchi's work would produce a PET/MRS hybrid imaging agent that yielded both PET active and MRS active metabolites upon enzymatic reaction with MAO.

Trapped metabolite imaging agents are enzyme substrates that in their parent form can freely cross into cells but upon reaction form a labelled metabolite that is trapped where the enzymatic reaction occurred, providing a measure of enzyme present based on the extent of trapping in the region of interest during image pharmacokinetic analysis. We propose that enzymes substrates have the added benefit that they can be designed to produce multiple metabolites with capability of being imaged (figure 4.1). While an appropriately designed single trapped product would allow for PET/MRS hybrid imaging, the formation of two metabolites also allows for the possibility of PET/MRS hybrid bifunctional imaging. First, to test our hypothesis we needed to investigate a known trapped metabolite imaging agent at low and high molar activities to test if our hypothesis that enzyme substrates can provide PET imaging data at low molar activity.

2. Results and Discussion

1-[^{11}C]Methylpiperidin-4-yl Propionate (PMP) is a substrate for acetylcholinesterase (AChE) used in the study of Alzheimer's and Parkinson's disease to measure the activity of AChE in cholinergic neurons.[16-17] The radiotracer, an ester substrate, is hydrolyzed *in vivo* by AChE forming a hydrophilic metabolite, 1-[^{11}C]methylpiperidin-4-ol, that is trapped in the compartment where the reaction occurs. PMP precursor and standard were prepared as previously described (scheme 4.1).[18] Experiments at high and low molar activity resulted in time activity curves for the region of interest drawn around the brain that were nearly identical. For the low molar activity dose, 3 mg of the unlabelled standard was included in the dose injected (10 mg/mL dose, 300 µL injected, 0.52 mCi injected). This resulted in a 0.03 Ci/mmol dose compared to a standard dose prepared at 7,000 Ci/mmol. Time activity curve data demonstrated that the low molar activity dose produced usable PET data even though it was diluted 200,000 fold (figure 4.2). In fact, the time activity curve showed higher standardized uptakes values (SUV) at later times. With imaging at low molar activity demonstrate with a trapped metabolite, we advanced next evaluated our hypothesis that a MAO substrate could produce both PET and MRS imaging metabolites.

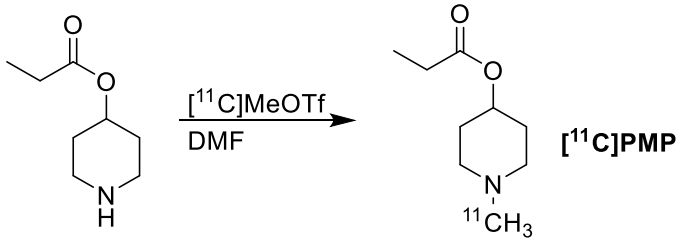

Scheme 4.1. Radiosynthesis of [^{11}C]PMP. Performed as previously described.[18-19]

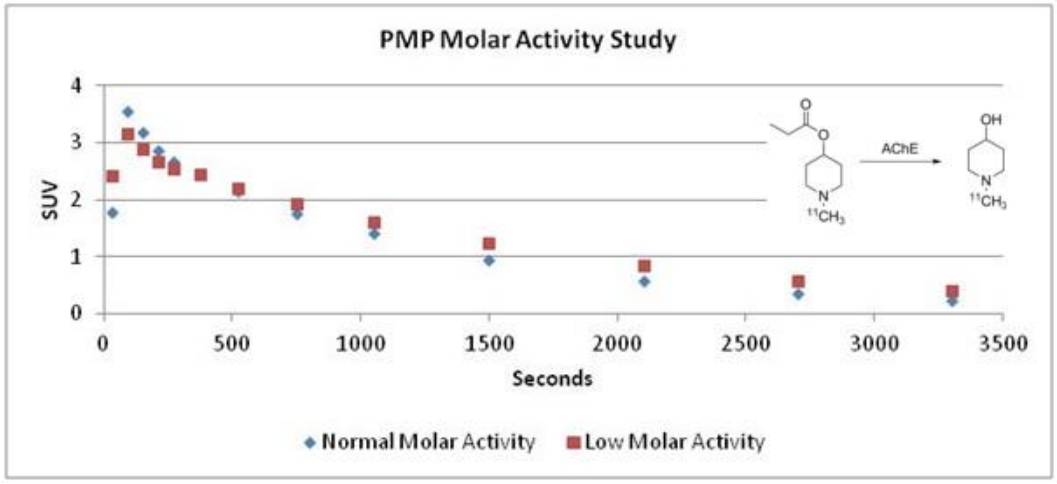

Figure 4.2. [^{11}C]PMP Rodent Brain PET Imaging. Comparison of normal (7,000 Ci/mmol) vs. low (0.03 Ci/mmol) molar activity demonstrates quality data can be obtained at low molar activity.

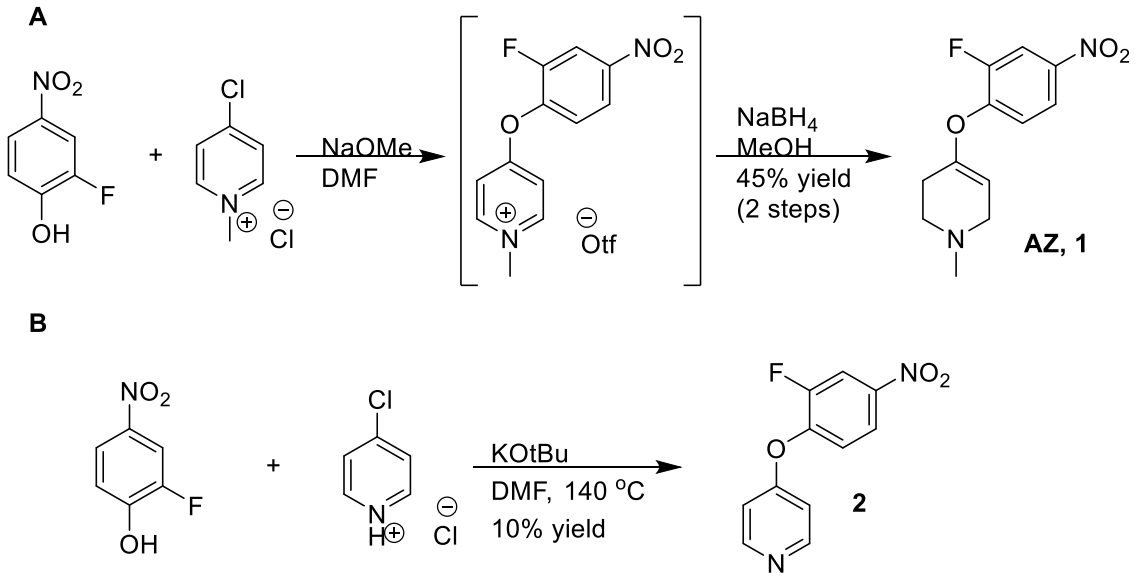

Scheme 4.2. Synthesis of AZ reference standard and precursor. A) Synthesis of reference standard (1). B. Synthesis of precursor for radiolabeling (2).

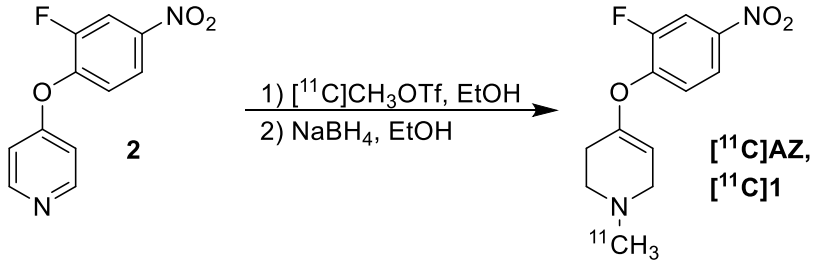

Scheme 4.3. Radiosynthesis of [^{11}C]AZ. Carbon-11 synthesis performed with the assistance of Dr. Xia Shao and Dr. Allen Brooks.

We prepared the required reference standard (AZ) and precursor for radiolabelling consistent with procedures from our previous work (scheme 4.2). We then utilized the change in absorbance between the substrate, AZ, and the metabolite, 2-Fluoro-4-nitrophenol, to perform Michaelis-Menten kinetic analysis. The results of those experiments are presented in figure 4.3 and show that AZ is a substrate for MAO-A and –B. The chemical shift-switching probe described by Yamiguichi is MAO-A selective with a K_M of 37.2 μM. AZ has a lower K_M for MAO-A at 19 μM, but even though its K_M for MAO-B is higher the observed k_{cat} is also higher, resulting in similar kinetic efficiency (k_{cat}/ K_M; specificity constant) for AZ with MAO-A or –B (table 4.1). The analysis confirmed AZ was a suitable substrate for further analysis as it had a lower K_M than the previous shift-switching probe (37.2 μM) and natural MAO substrates (serotonin, 137 μM).[20] ^{19}F NMR experiments of AZ and 2-fluoro-4-nitrophenol demonstrated that AZ could be utilized as a MRS (chemical shift-switching) agent. To confirm this in our experimental conditions, enzymatic reactions with MAO-A and AZ were run to 2 time points (15 and 90 min) and quenched by addition of excess clorgyline (10 μM). In figure 4.4 the signal for the substrate at -130.9 ppm is replaced by signal for phenol metabolite at -136.4 ppm over time. With AZ confirmed *in vitro* as a MAO chemical shift-switching agent, carbon-11 labelling was undertaken to observe if [^{11}C]AZ could be utilized as a PET imaging agent at low molar activity.

The procedure to radiolabel [^{11}C]AZ was similar to the method previously described in our work (scheme 4.3).[9] Briefly, [^{11}C]carbon dioxide was converted by standard procedure into [^{11}C]CH_3OTf and sparged thru a solution of the pyridine precursor in ethanol (1 mg, 0.2 mL). The [^{11}C]methyl pyridinium intermediate was transferred to a conical vial containing $NaBH_4$ in ethanol (2 mg, 0.3 mL) and stirred for 5 min. [^{11}C]AZ was then purified by HPLC and reformulated into a 10% ethanol in saline dose (10.6 ± 5.6 mCi; non-decay corrected 1.2%

radiochemical yield based on 900 mCi of starting [^{11}C]CH_3OTf; 30 min from end of bombardment) for use in animal imaging studies. For doses of low molar activity [^{11}C]AZ, reference standard was added to the saline used for reformulation and in both cases molar activity was calculated by standard curve analysis using HPLC (UV-254 nm) of the dose solution.

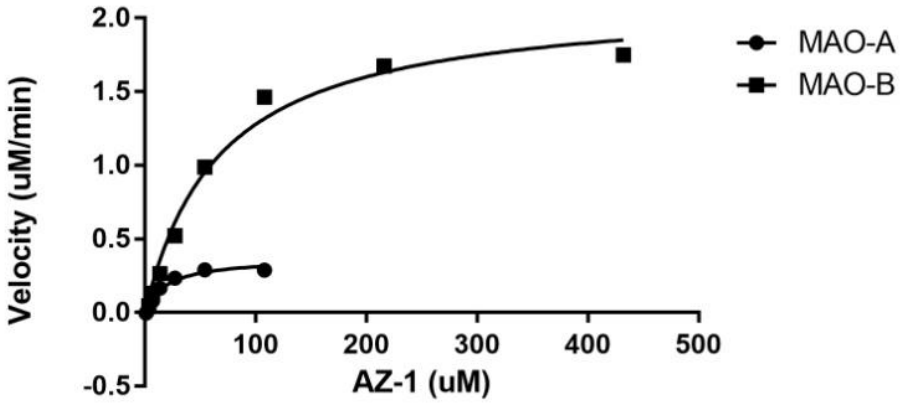

Figure. 4.3 Michaelis-Menten kinetic analysis data for MAO-A and –B by absorbance assay.

Table 4.1. Michaelis-Menten kinetic parameters for AZ in MAO-A and MAO-B.

	k_{cat} (min^{-1})	**K_M (μM)**	**k_{cat}/K_M ($min^{-1}μM^{-1}$)**
MAO-A	0.0416 ± 0.0016	19 ± 2.3	0.0022
MAO-B	0.24 ± 0.048	67 ± 4.5	0.0036

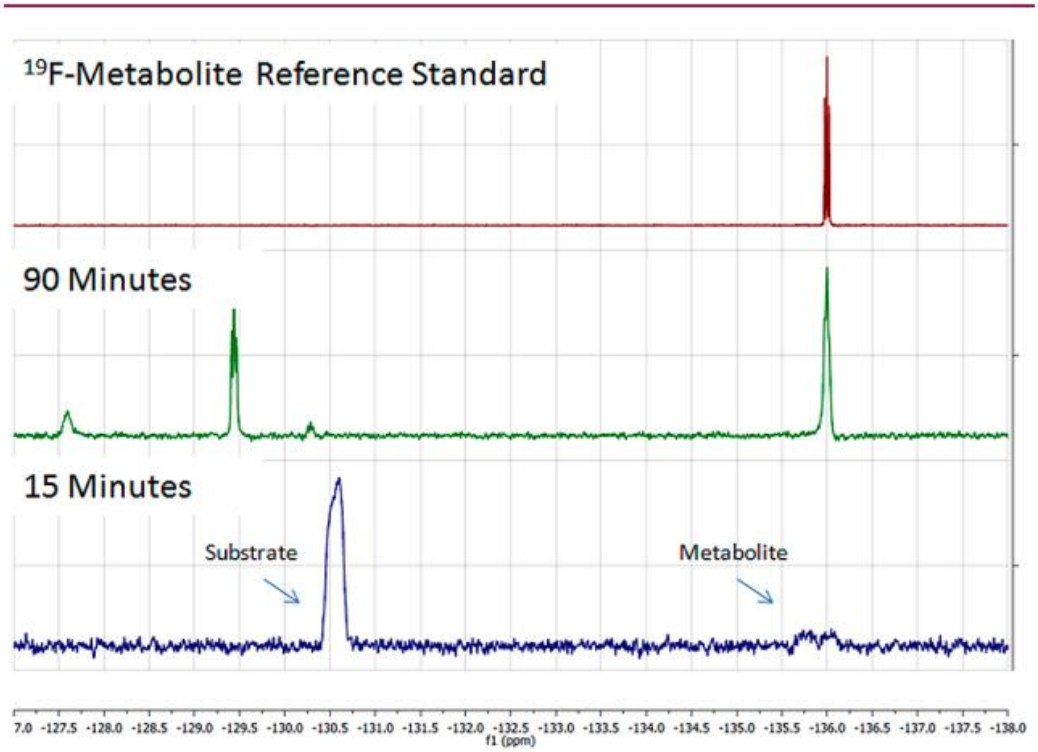

Figure 4.4. ^{19}F NMR experiments (376 MHz). Time-dependent formation of 2-fluoro-4-nitrophenol metabolite (-136 ppm) and secondary metabolite (-129 ppm) via oxidation of substrate AZ (-130 ppm) by MAO-A.

Imaging in Sprague Dawley rats was carried out with [^{11}C]AZ at high (normal molar activity for clinical use of PET radiotracers) and low molar activity. Experiments conducted at high (7,000 Ci/mmol) and low (0.68 Ci/mmol) molar activity [^{11}C]AZ gave the same time activity curve shape, and again higher SUV in the later frames was observed with the lower molar activity [^{11}C]AZ doses, as seen in figure 4.5. In addition, the reconstructed Sprague Dawley images with all frames summed demonstrate the greater uptake of low molar activity [^{11}C]AZ as more activity is observable in the PET images (higher nCi/cc signal; high molar activity 0.44 mCi, low molar activity 0.47 mCi injected).

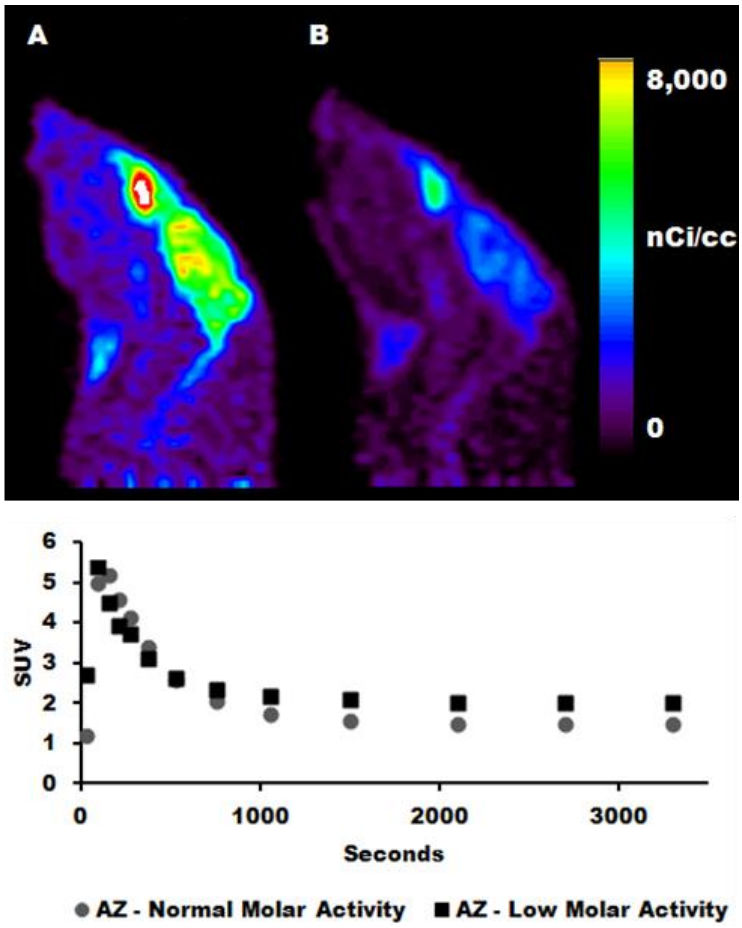

Figure 4.5 Summed frame images of [^{11}C]AZ. A) sagittal plane from low molar activity experiment vs. B) from high (normal) molar activity. Time activity comparison corrected to SUV (n=2) for each experiment.

3. Conclusion

PET imaging of trapped metabolites formed from enzyme substrates can be achieved at high concentration and resulting low molar activity, which is required for any potential hybrid PET/MRS imaging agent. In fact, lower molar activity resulted in a higher SUV late, which improves detection of enzymatic activity. Enzymatic substrates that form trapped metabolites are a promising way forward to design PET/MRS hybrid imaging agents. The ability to form two metabolites where one is PET active and the other MRS active also raises the possibility of designing bifunctional PET/MRS hybrid imaging agents in addition to using the approach to design a probe that measure the same data by both PET and MRS. The development of

PET/MRS imaging agents will allow for collecting functional data from both PET and MR instruments, taking advantage of the development of PET/MR systems. Substrate imaging as evidence by such radiotracers as [^{11}C]PMP and others demonstrates the utility of substrate based imaging in the study pathology, staging of disease and monitoring treatment. With the concept validated, work is currently underway investigating the design of PET/MRS probes that are more sensitive to facilitate use in animal studies.

4. Methods

Chemistry

General Considerations.

All solvents and reagents were commercially available and used without further purification unless otherwise stated. 2-Fluoro-4-nitrophenol, 4-hydroxypyridine, and 4-chloropyridine hydrochloride were obtained from Sigma-Aldrich. NMR spectra were recorded with a Varian 400 MHz instrument at room temperature with tetramethylsilane (TMS) as an internal standard. Mass spectra were performed on a Micromass LCT time-of-flight mass spectrometer or an Agilent Q-TOF HPLC-MS employing the electrospray ionization (ESI) method. High-performance liquid chromatography (HPLC) was performed using a Shimadzu LC-2010A HT system equipped with a Bioscan B-FC-1000 radiation detector.

Preparation of 4-(2-fluoro-4-nitrophenoxy)-1-methyl-1,2,3,6-tetrahydropyridine (**1**): 2-Fluoro-4-nitrophenol (0.11 g; 0.72 mmol) was added to sodium methoxide (0.047 g; 0.87 mmol) dissolved in DMF (3 mL), and the mixture was stirred for 10 min. 4-Chloro-1-methylpyridin-1-ium triflate (0.20 g; 0.72 mmol) was added, and the reaction was stirred for 18 h. The solvent was removed *in vacuo*, and the resulting intermediate was suspended in methanol (3 mL). The reaction mixture was cooled to 0 °C in a water ice bath, and NaBH4 (0.069 g; 1.81 mmol) was added slowly.

After 1 h, the solvent was removed *in vacuo*. Water and ethyl acetate were added to the residue, and the mixture was transfer to a separatory funnel. The product was extracted with ethyl acetate (3×), dried over sodium sulfate, filtered, and concentrated *in vacuo*. The product was purified by flash silica gel chromatography (dichloromethane, methanol gradient; 0%MeOH/100% DCM 10%MeOH/90%DCM). The product was collected as a yellow semi-solid in 45% yield (0.082 g). ^{1}H NMR (400 MHz; MeOH-d4)/δ (ppm): 7.99-7.95 (2H, m), 7.26 (1H, t, J = 8.7), 5.03 (1H, br), 2.96 (2H, dd, J = 6.0, 2.6), 2.66 (2H, t, J = 6.0), 2.33-2.31 (5H, m); ^{19}F NMR (376 MHz; MeOH-d4)/δ (ppm): -130.0; HRMS calcd for [M + H]+ (M = $C_{12}H_{13}FN_2O_3$), 253.0983; found, 253.0983.

Preparation of 4-(2-fluoro-4-nitrophenoxy)pyridine (**2**): Phenol starting material (0.25 g; 1.6 mmol) was added to potassium tert-butoxide (0.33 g; 2.9 mmol) dissolved in DMF (7 mL). The reaction mixture was heated at 140 °C, 4-chloropyridine hydrochloride (0.20 g; 1.33 mmol) was added, and the reaction was stirred for 18 h. The reaction was cooled to room temperature and quenched with aqueous saturated sodium bicarbonate. The product was extracted with ethyl acetate (3×), dried over sodium sulfate, filtered, and concentrated *in vacuo*. The product was purified by flash silica gel chromatography (hexanes, ethyl acetate gradient; 0%EtOAc/100% hexanes 50% EtOAc/50% hexanes). The product was collected as a red solid in 10% yield (0.031 g). ^{1}H NMR (400 MHz; MeOH-d4)/δ (ppm): 8.41 (2H, d, J = 6.0), 8.17 (1H, dd, J = 10.3, 2.5), 8.10 (1H, d, J = 9.0), 7.43 (1H, t, J = 8.5), 7.0 (2H, d, J = 6.0); ^{19}F NMR (376 MHz; MeOH-d4)/δ (ppm): -126.9; HRMS calcd for [M + H]+ (M = $C_{11}H_7FN_2O_3$), 235.0513; found, 235.0514.

Biology

Absorbance Assay

Experimental Michaelis-Menten kinetic parameters were calculated for the compounds using hMAO-A and –B Supersome (Creative Biomart). In brief, assays were performed using Supersomes (mitochondrial membrane preps of insect cells overexpressing human MAO-A or –B) at a concentration of 80 ug/ml. Fresh stocks of substrate were dissolved in DMSO and diluted to various concentrations ranging from 200 uM to 1 nM. Reaction progress was measured by appearance of absorbant product, 2-fluoro-4- nitrophenol. Reactions were monitored in real time using a Biotek Hybrid plate reader (absorbance 410 nm) at 37 °C for 60 min. The resultant absorbance units were converted to concentration of product using a reference standard curve. Michaelis-Menten curves were plotted and parameters computed in GraphPad Prism. Assays were done in duplicate, in three independent experiments using fresh stock of enzyme, test compound, and reference standard.

^{19}F NMR Assay

Turnover was observed for compounds using MAO-A Supersome (Creative Biomart). In brief, assays were performed using Supersomes (mitochondrial membrane preps of insect cells overexpressing human MAO-A) at a concentration of 12 unit/ml (unit of activity defined by manufacturer and varied stock to stock). Fresh stocks of substrate were dissolved in DMSO and diluted to 100 uM in HEPES (100mM, pH 7.4). Reaction progressed in glass vials at 37 °C until desired stop time. Reaction was stopped at 0, 15, and 90 minutes by addition of clorgyline in excess (1.6 mM). Entire reaction solutions were transferred to a 5 mm NMR tube for ^{19}F-NMR spectroscopy. NMR spec details: ^{19}F NMR experiments were performed on a Varian 400 MHz instrument (376 MHz for ^{19}F-NMR) at room temperature, 4096 scans were performed for each sample with a 1 second relaxation delay between scans, and data was analyzed with Mnova software from Mestrelab Research.

Radiochemistry

General Considerations

Reagents and solvents were commercially available and used without further purification, unless otherwise noted. Sodium chloride (0.9% USP) and sterile water for injection (USP) were purchased from Hospira; dehydrated alcohol for injection (USP) was obtained from Akorn Inc. Shimalite-Nickle was purchased from Shimadzu, iodine was obtained from EMD, phosphorus pentoxide was acquired from Fluka, molecular sieves were purchased from Alltech, and HPLC columns were acquired from Phenomenex. Other synthesis components were obtained as follows: sterile filters were acquired from Millipore, C18-light Sep-Paks and Porapak Q were purchased from Waters Corporation, and 10 cc sterile vials were obtained from HollisterStier. Sep-Paks were flushed with 10 mL of ethanol followed by 10 mL of sterile water prior to use.

Radiochemical Synthesis of 4-(2-fluoro-4-nitrophenoxy)-1-[11C]methyl-1,2,3,6-tetrahydropyridine (**[^{11}C]AZ)**: Production was carried out as previously described using a TracerLab FXC-Pro automated radiochemistry synthesis module (General Electric, GE).[9] [^{11}C]Carbon dioxide was produced using a GE PETTrace cyclotron (40 μA beam for 30 min) and converted by standard procedures into carbon-11- labeled methyl triflate ([^{11}C]CH_3OTf). The [^{11}C]CH_3OTf in helium carrier gas was bubbled into a vial containing a solution of 4-(2-fluoro-4-nitrophenoxy)pyridine (1 mg) dissolved in ethanol (0.2 mL). At the completion of transfer of radioactivity into the reaction vial, the ethanol solution was then transferred to a second conical vial containing sodium borohydride (2 mg) in ethanol (0.3 mL). The resulting mixture was stirred for 5 min at room temperature, and then the reaction was quenched by addition of HPLC buffer (30% MeCN, 10 mM NH_4OAc, pH 4.5). The crude product was loaded onto a semi-preparative HPLC loop. The product was purified by reverse-phase chromatography (Prodigy

ODS prep, 250 × 10 mm, 10 μ, 4 mL/min), collected (retention time of 5.7 min), diluted into dilution flask containing H_2O (40 S10 mL) and 1% NH_4OH (2 mL), and reformulated using a C-18 extraction disk into a final 5 mL total volume of 10% ethanol in saline. The doses produced (10.6 ± 5.6 mCi; non-decay corrected Radiochemical Yield = 1.2% based on 900 mCi of starting [^{11}C]CH_3OTf; Radiochemical Purity greater than 99%) were assessed via standard quality control techniques and were appropriate for rodent and nonhuman primate studies. Overall synthesis times were 30 min from end-of-bombardment.

Radiochemical Synthesis of [^{11}C]Methylpiperidin-4-yl proprionate **([^{11}C]PMP***)*: Production was carried out as previously described using a TracerLab FXC-Pro automated radiochemistry synthesis module (General Electric, GE).[19] [^{11}C]Carbon dioxide was produced using a GE PETTrace cyclotron (40 μA beam for 30 min) and converted by standard procedures into carbon-11- labeled methyl triflate ([^{11}C]CH_3OTf). The [^{11}C]CH_3OTf in helium carrier gas was bubbled into a vial containing a solution of precursor (0.5 mg) dissolved in DMF (0.1 mL). 4-piperidinyl propionate hydrochloride (0.5 ± 0.1 mg) was dissolved in aqueous saturated sodium bicarbonate (~20 μL) and ethyl ether (2 mL) was added, and the solution was mixed vigorously on a vortex mixture for 1 min. Anhydrous sodium sulfate (0.5 g) was then added to absorb the water, and the dried ether was filtered into DMF (100 μL). The ether was evaporated under nitrogen, leaving the precursor in DMF as freebase. [^{11}C]methyl triflate was bubbled through the precursor solution at 15 mL/min for 3 min. The reaction mixture was then diluted with 1 mL of HPLC mobile phase and purified using semipreparative HPLC (column: Phenomonex Luna C18, 250 × 10 mm, mobile phase: 20 mm NH_4OAc in 5% EtOH, flow rate: 4 mL/min). The product peak was collected (RT ~12–14 min) for 2 min (8 mL), diluted with USP saline (2 mL) to

provide a final ethanol concentration <5%, and passed through a 0.22 μm sterilizing filter into a sterile dose vial.

Rodent PET Imaging

General Considerations

All animal studies were performed in accordance with the standards set by the University Committee on Use and Care of Animals (IACUC) at the University of Michigan. Rodent imaging studies were done with female Sprague Dawley rats. The animals were anesthetized (isoflurane), intubated, and positioned in a Concorde MicroPET R4 scanner.

Normal molar activity [^{11}C]PMP Scan (animal weight = 264 g): Following a transmission scan, the animal was injected i.v. (via tail vein catheter as a bolus over 1 min) with [^{11}C]PMP (0.33 mCi; 7,000 Ci/mmol) and the head imaged for 60 min (5 x 1 min frames – 2 x 2.5 min frames – 2 x 5 min frames – 4 x 10 min frames). *Low molar activity [^{11}C]PMP Scan* (animal weight = 299 g): Following a transmission scan, the animal was injected i.v. (via tail vein catheter as a bolus over 1 min) with [^{11}C]PMP (0.52 mCi; 0.03 Ci/mmol) and the head imaged for 60 min (5 x 1 min frames – 2 x 2.5 min frames – 2 x 5 min frames – 4 x 10 min frames). *Normal molar activity [^{11}C]AZ Scan* (n = 2, animal weight = 182, 358 g): Following a transmission scan, the animal was injected i.v. (via tail vein catheter as a bolus over 1 min) with [^{11}C]AZ (0.45, 0.44 mCi; 3000, 7000 Ci/mmol) and the head imaged for 60 min (5 x 1 min frames – 2 x 2.5 min frames – 2 x 5 min frames – 4 x 10 min frames). *Low molar activity [^{11}C]AZ Scan* (n = 2, animal weight = 324, 270 g): Following a transmission scan, the animal was injected i.v. (via tail vein catheter as a bolus over 1 min) with [^{11}C]AZ (0.47, 0.56 mCi; 0.68, 0.30 Ci/mmol) and the head imaged for 60 min (5 x 1 min frames – 2 x 2.5 min frames – 2 x 5 min frames – 4 x 10 min frames). In each case, emission data were corrected for attenuation and scatter, and reconstructed using the 3D

maximum a priori (3D MAP) method. By using a summed image, regions of interest (ROI) were drawn over the whole brain on multiple planes, and the volumetric ROIs were then applied to the full dynamic data set to generate time-radioactivity curves.

5. References

1. Brooks, A. F.; Drake, L. R.; Shao, X.; Zhao, A.; Scott, P. J. H.; Kilbourn, M. R., Evaluation of Enzyme Substrate Radiotracers as PET/MRS Hybrid Imaging Agents. *ACS Med. Chem. Lett.* **2018,** *9* (11), 1140-1143.
2. Miller, P. W.; Long, N. J.; Vilar, R.; Gee, A. D., Synthesis of 11C, 18F, 15O, and 13N radiolabels for positron emission tomography. *Angewandte Chemie International Edition* **2008,** *47* (47), 8998-9033.
3. Brooks, A. F.; Topczewski, J. J.; Ichiishi, N.; Sanford, M. S.; Scott, P. J., Late-stage [18 F] fluorination: new solutions to old problems. *Chemical science* **2014,** *5* (12), 4545-4553.
4. Dale, B. M.; Brown, M. A.; Semelka, R. C., *MRI: basic principles and applications*. John Wiley & Sons: 2015.
5. Shiroishi, M. S.; Castellazzi, G.; Boxerman, J. L.; D'Amore, F.; Essig, M.; Nguyen, T. B.; Provenzale, J. M.; Enterline, D. S.; Anzalone, N.; Dörfler, A.; Rovira, À.; Wintermark, M.; Law, M., Principles of T2*-weighted dynamic susceptibility contrast MRI technique in brain tumor imaging. *Journal of Magnetic Resonance Imaging* **2015,** *41* (2), 296-313.
6. Villringer, A.; Rosen, B. R.; Belliveau, J. W.; Ackerman, J. L.; Lauffer, R. B.; Buxton, R. B.; Chao, Y.-S.; Wedeenand, V. J.; Brady, T. J., Dynamic imaging with lanthanide chelates in normal brain: Contrast due to magnetic susceptibility effects. *Magnetic Resonance in Medicine* **1988,** *6* (2), 164-174.
7. Dietz, C.; Ehret, F.; Palmas, F.; Vandergrift, L. A.; Jiang, Y.; Schmitt, V.; Dufner, V.; Habbel, P.; Nowak, J.; Cheng, L. L., Applications of high-resolution magic angle spinning MRS in biomedical studies II—Human diseases. *NMR in Biomedicine* **2017**.
8. Noguchi, J.; Zhang, M.-R.; Yanamoto, K.; Nakao, R.; Suzuki, K., In vitro binding of [11C] raclopride with ultrahigh specific activity in rat brain determined by homogenate assay and autoradiography. *Nuclear medicine and biology* **2008,** *35* (1), 19-27.
9. Brooks, A. F.; Shao, X.; Quesada, C. A.; Sherman, P.; Scott, P. J. H.; Kilbourn, M. R., In Vivo Metabolic Trapping Radiotracers for Imaging Monoamine Oxidase-A and -B Enzymatic Activity. *ACS Chemical Neuroscience* **2015,** *6* (12), 1965-1971.
10. Rosenberry, T. L., Strategies to Resolve the Catalytic Mechanism of Acetylcholinesterase. *Journal of Molecular Neuroscience* **2010,** *40* (1), 32-39.
11. Vasdev, N.; Sadovski, O.; Garcia, A.; Dollé, F.; Meyer, J. H.; Houle, S.; Wilson, A. A., Radiosynthesis of [11C] SL25. 1188 via [11C] CO2 fixation for imaging monoamine oxidase B. *Journal of Labelled Compounds and Radiopharmaceuticals* **2011,** *54* (10), 678-680.
12. Saba, W.; Valette, H.; Peyronneau, M. A.; Bramoullé, Y.; Coulon, C.; Curet, O.; George, P.; Dollé, F.; Bottlaender, M., [11C] SL25. 1188, a new reversible radioligand to study the monoamine oxidase type B with PET: Preclinical characterisation in nonhuman primate. *Synapse* **2010,** *64* (1), 61-69.
13. Bernard, S.; Fuseau, C.; Schmid, L.; Milcent, R.; Crouzel, C., Synthesis and in vivo studies of a specific monoamine oxidase B inhibitor: 5-[4-(benzyloxy) phenyl]-3-(2-cyanoethyl)-1, 3, 4-oxadiazol-[11 C]-2 (3H)-one. *European journal of nuclear medicine* **1996,** *23* (2), 150-156.
14. Kalgutkar, A. S.; Castagnoli, K.; Hall, A.; Castagnoli, N., Novel 4-(Aryloxy)tetrahydropyridine Analogs of MPTP as Monoamine Oxidase A and B substrates. *Journal of Medicinal Chemistry* **1994,** *37*, 944-949.
15. Long, S.; Chen, L.; Xiang, Y.; Song, M.; Zheng, Y.; Zhu, Q., An activity-based fluorogenic probe for sensitive and selective monoamine oxidase-B detection. *ChemComm* **2012,** *48*, 7164-7166.
16. Koeppe, R. A.; Frey, K. A.; Snyder, S. E.; Meyer, P.; Kilbourn, M. R.; Kuhl, D. E., Kinetic modeling of N-[11C]methylpiperidin-4-yl propionate: alternatives for analysis of an irreversible positron emission tomography tracer for measurement of acetylcholinesterase activity in human brain. *J. Cereb. Blood Flow Metab.* **1999,** *19* (10), 1150-1163.
17. Bohnen, N.; Müller, M.; Koeppe, R.; Studenski, S.; Kilbourn, M.; Frey, K.; Albin, R., History of falls in Parkinson disease is associated with reduced cholinergic activity. *Neurology* **2009,** *73* (20), 1670-1676.

18. Snyder, S. E.; Tluczek, L.; Jewett, D. M.; Nguyen, T. B.; Kuhl, D. E.; Kilbourn, M. R., Synthesis of 1-[11C]methylpiperidin-4-yl propionate ([11C]PMP) for in vivo measurements of acetylcholinesterase activity. *Nucl. Med. Biol.* **1998,** *25* (8), 751-754.
19. Shao, X.; Hoareau, R.; Runkle, A. C.; Tluczek, L. J. M.; Hockley, B. G.; Henderson, B. D.; Scott, P. J. H., Highlighting the versatility of the Tracerlab synthesis modules. Part 2: fully automated production of [11C]-labeled radiopharmaceuticals using a Tracerlab FXC-Pro. *Journal of Labelled Compounds and Radiopharmaceuticals* **2011,** *54* (14), 819-838.
20. Youdim, M. B.; Edmondson, D.; Tipton, K. F., The therapeutic potential of monoamine oxidase inhibitors. *Nature Reviews Neuroscience* **2006,** *7* (4), 295.

CHAPTER 5
Imaging the Receptor for Advanced Glycation End-products

As an alternative to monoamine oxidase (MAO), the novel biomarker the receptor for advanced glycation end products (RAGE) was evaluated for its utility in neuroinflammation. The literature surrounding this receptor was incredibly light in comparison to MAO- and we were excited to explore this new biology in two approaches. The preliminary extracellular approach has been published,[1] and we hope to submit the second manuscript soon.

1. Introduction

Chronic inflammation of the central nervous system (CNS) features a series of concerted actions to identify a harmful agent, limit its impact, and repair any damage.[2] The neuroinflammatory state can be described pathophysiologically by the presence of cytokines and chemokines in the cerebral spinal fluid (CSF) and interstitial spaces, blood-brain barrier (BBB) dysfunction, activated microglia, and infiltration of peripheral immune cells within the CNS.[2] In a neuroinflammatory state, overactivated microglia cause aberrant damage because of a self-propagating destructive cycle in which activated microglia secrete proinflammatory signals and in turn activate neighboring microglia and astrocytes.[3]

Advanced glycation end products (AGEs) are a common biomarker of inflammation *in vitro* and are the result of non-enzymatic and nonspecific glycation of macromolecules in an oxidative environment.[4] In addition to inactivating enzymes, glycation can cause aggregation and protein cross-linking.[4] AGEs cause an inflammation cascade by signaling through the Receptor for Advanced Glycation End products (RAGE), an integral membrane receptor in the

immunoglobulin-G family.[5-7] RAGE is a pattern recognition receptor and recognizes a variety of ligands: the non-enzymatically glycated amino acid residue carboxymethyllysine (CML), insulin, HMGB1, S100B, Aβ peptide, and others.[5] Ligand binding to RAGE homodimers or RAGE-Toll-like receptor heterodimers results in activation of a variety of downstream signaling pathways, though one of the only known intracellular RAGE ligand is diaphanous 1 (Dia-1).[8-9] Through this intracellular signaling, NF-κB is activated which initiates transcription of cytokines and other proinflammatory mediators and a positive feedback loop in which RAGE expression is increased.[6] Microglia have been documented overexpressing RAGE in hippocampal neurons, an area of the brain strongly associated with neurodegeneration.[10-12] There are multiple splice-isoforms of RAGE which have been speculated to act differently than the full length, membrane bound form of RAGE (figure 5.1). The soluble esRAGE (formed from alternative mRNA splicing) circulates and possibly acts as a scavenger receptor, sequestering ligands from the full length receptor.[13] The full length receptor is upregulated in the presence of its ligands, but little is understood about ectodomain shedding and the relationship with esRAGE in this state.

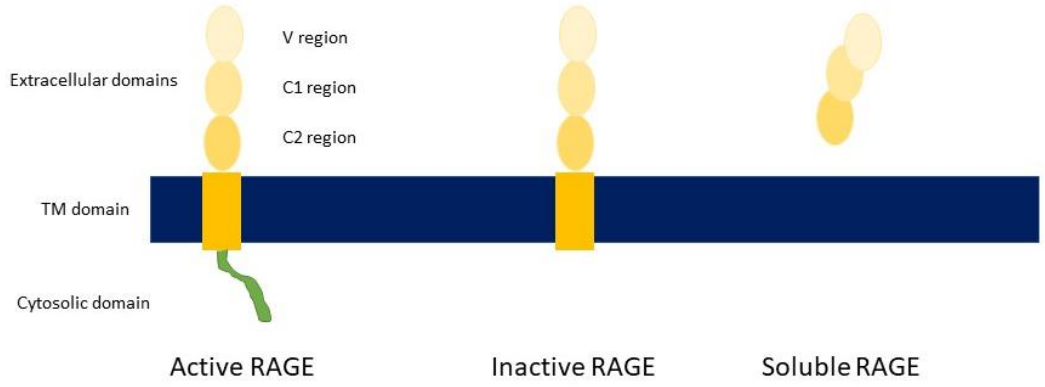

Figure 5.1 RAGE domains and common isoforms. The active form of the receptor contains all three extracellular domains, a transmembrane region, and a short, disordered intracellular domain. The intracellular domain is required for signaling. An inactive form of this receptor contains all of the extracellular domains; however, the cytosolic domain has been cleaved. Ligand binding to this form does not result in intracellular signaling. The soluble form of RAGE lacks the transmembrane and cytosolic domains. It considered to be a "decoy" or scavenger receptor.

A recombinant form of the soluble RAGE (sRAGE) was engineered to be used as a RAGE inhibitor.[14] Inhibition of RAGE through this method was shown to block the development and progression of many pathological states in animal models: cardiovascular disease,[15] diabetes,[14] and cancer.[16] Therapeutic efforts to inhibit RAGE have had limited success to date. The small molecule inhibitor of the extracellular domain, azeliragon (TTP-488), failed efficacy in phase II and phase III clinical trials in mild-cognitive impaired Alzheimer's disease (AD) patients.[17] Antibody, peptide, and DNA aptamer-based inhibitors have shown preclinical success, none have been translated clinically yet.

Imaging the receptor for advanced glycation end-products would provide the necessary visualization of the receptor's involvement in disease. Previous imaging efforts include ^{99m}Tc-labeled anti-RAGE antibodies for SPECT imaging, which showed promise in the mouse model of hind limb ischemia.[18] However, major limitations of antibody imaging agents are the long biological half-life and high background signal. Another biologic approach was [^{18}F]S100A4, a small protein ligand for RAGE. Although it was never used after this preliminary synthesis because the labeled product was unstable and only had micromolar affinity for RAGE.[19] Recently, Konopka *et al.,* reported a RAGE-targeted nanoparticle approach for imaging using the fourth generation PAMAM dendrimer and a NOTA chelator for rhodamine (fluorescence) or copper-64 (PET imaging).[20] The authors developed a multimodal nanoparticle to target RAGE with the attached ligand, CML modified human serum albumin. The nanoparticle was evaluated in a mouse model of peripheral arterial damage (PAD): hind limb ischemia in non-diabetic mice. In the model, PET imaging showed 3.4x higher uptake in hind limbs of the ischemic mice compared to normal mice at one week, which is supported by previous immunohistochemistry analysis of this model.[18] A limitation of this study is non-specific binding. An investigation into

other binding partners is surely required; in the HUVEC binding experiment the anti-RAGE competition only blocked 80% of nanoparticle binding. Despite the success of these efforts, each of them are macromolecules and would have limited use in the CNS. Our approach for CNS PET imaging of RAGE requires small molecule ligands and we have explored radioligands for the extracellular and intracellular domains.

2. Extracellular Approach

A number of small-molecule mediators of RAGE interactions have been reported.[21-22] N-Benzyl-4-chloro-N-cyclohexylbenzamide (FPS-ZM1, figure 5.2) is a multimodal RAGE-specific inhibitor that reduced amyloid-β (Aβ) mediated brain dysfunction in a mouse model of AD. Despite having high lipophilicity (CLogP = 5.25; ChemBioDraw), FPS-ZM1 appeared to be a promising scaffold around which to develop a PET radiotracer because of its high affinity (25 nM K_i against RAGE−Aβ1−40), BBB permeability,[21] lack of toxicity in mice or cells, and amenability to nucleophilic aromatic radiofluorination. Moreover, in a mouse model of AD with confirmed Aβ pathology (aged $APP^{sw/0}$ mice overexpressing human Aβ), FPS-ZM1 was found to inhibit RAGE-mediated influx of circulating Aβ into the CNS and reduce microglia activation.[21] The failed therapeutic agent azeliragon (TTP-488) was briefly considered for PET imaging; however, due its large size and lipophilicity it was not chosen for development. In this work, we report the synthesis and preliminary preclinical evaluation of [^{18}F]RAGER (figure 5.2).

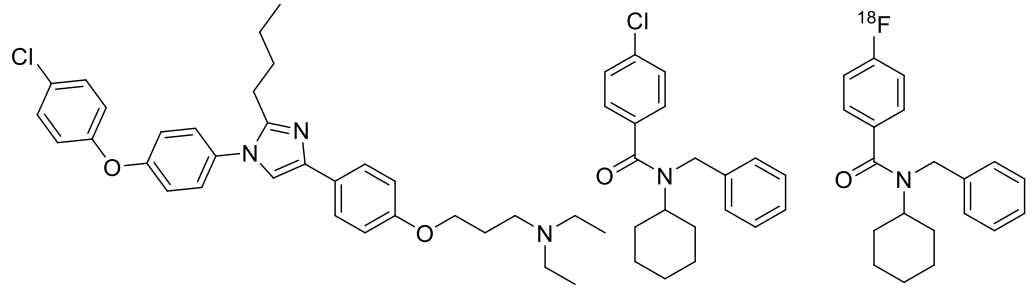

Azeliragon FPS-ZM1 [^{18}F]RAGER

Figure 5.2. Small molecule inhibitors and PET radioligands for RAGE.

2.1 Chemistry

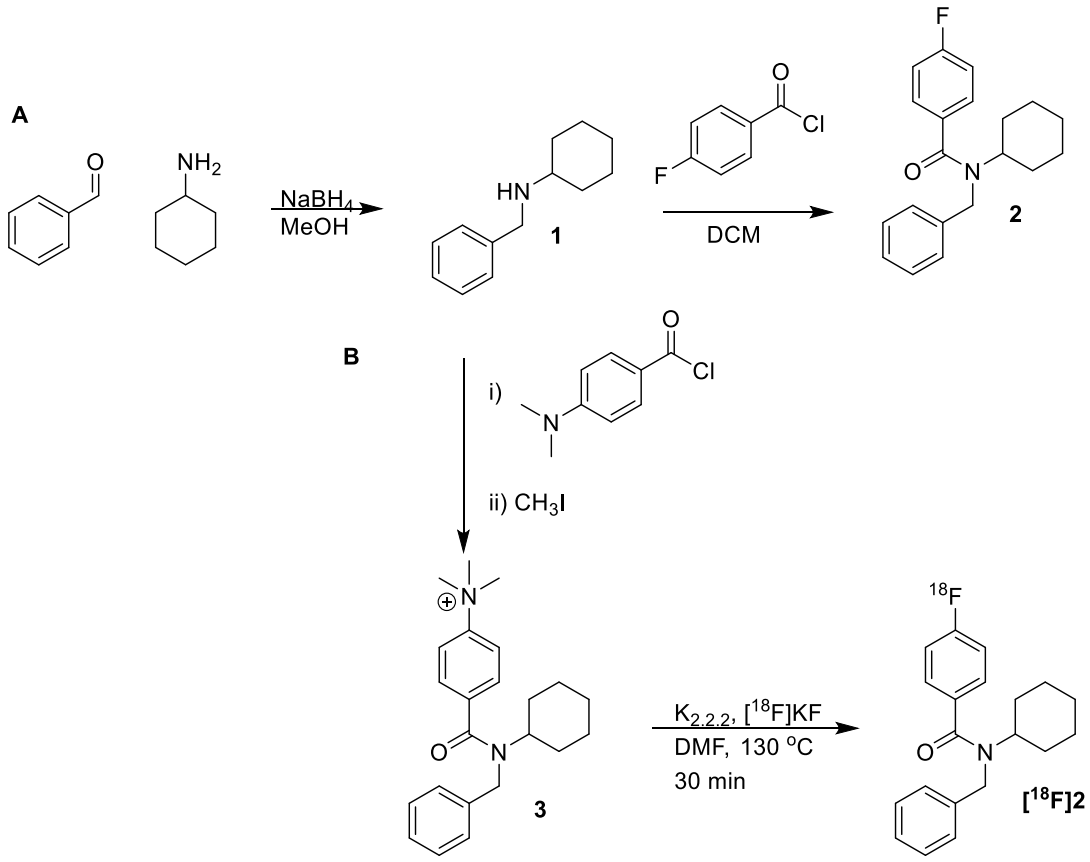

Scheme 5.1. A. Synthesis of RAGER HPLC reference standard (2). B. Synthesis of precursor radiosynthesis (3) and radioligand ([^{18}F]2).

The first step when developing novel PET radiotracers is to synthesize both the precursor to be radiolabeled and the corresponding unlabeled reference standard to confirm identity of the radiolabeled product by HPLC. Unlabeled reference standard **2** was produced in good yield (80% over two steps) via a reductive amination of benzaldehyde and cyclohexylamine to give **1**, followed by acylation with 4-fluorobenzoyl chloride (Scheme 5.1). Trimethylammonium precursor **3** was prepared for radiolabeling as the charged precursor and uncharged product were expected to have markedly different retention times by reverse-phase HPLC. Precursor **3** was synthesized in the same manner as the reference standard, by acylation of intermediate **1** with p-

(N, N dimethylamino)benzoyl chloride; subsequent alkylation with methyl iodide provided **3** in 10% yield (over three steps).

Radiosynthesis of [^{18}F]RAGER was automated using a commercial synthesis module (General Electric Tracerlab FX_{FN}) by reacting trimethylammonium precursor **3** with [^{18}F]fluoride in the presence of Kryptofix-2.2.2 ($K_{2.2.2}$) in DMF at 130 °C for 30 min. Subsequent purification by semipreparative HPLC and reformulation yielded [^{18}F]RAGER (**4**) in satisfactory radiochemical yield (44 ± 10 mCi; 2.9% nondecay corrected based upon 1.5 Ci of [^{18}F]fluoride), excellent radiochemical purity (RCP) (>99%), and high specific activity (3740 ± 495 Ci/mmol); n = 6. Formulated [^{18}F]RAGER was stable for at least 60 min after the end of synthesis.

2.2 Tissue Studies

Tissue samples from an Alzheimer's patient were obtained, along with samples from a healthy control, to evaluate [^{18}F]RAGER. RAGE expression is known to be significantly elevated in the cortex.[23-24] In AD cortex sections, a 2.9-fold increase in RAGE expression was observed compared with normal control tissue. This is consistent with the known increased expression of RAGE in AD from the literature.[24] Adjacent sections were then incubated with [^{18}F]RAGER, **4** (figure 5.3). The images confirm colocalization of [^{18}F]RAGER in gray matter areas with known RAGE expression, previously identified by immunohistochemistry. There was higher uptake in the AD samples than the normal control samples. Nonspecific binding was investigated by repeating incubations in the presence of 1000-fold excess of unlabeled RAGER, which confirmed that binding in the gray matter regions was displaceable to background levels. However, despite the reported specificity of the parent compound,[21] we did observe significant nonspecific binding in the white matter (the white matter signal in the nonspecific binding experiments shown in figure 5.4 actually appears higher than that for the total binding

experiments. The cause of this is unclear, but it is possible that all of the displaced radiotracer in the nonspecific samples gets retained in the white matter leading to the higher signal.

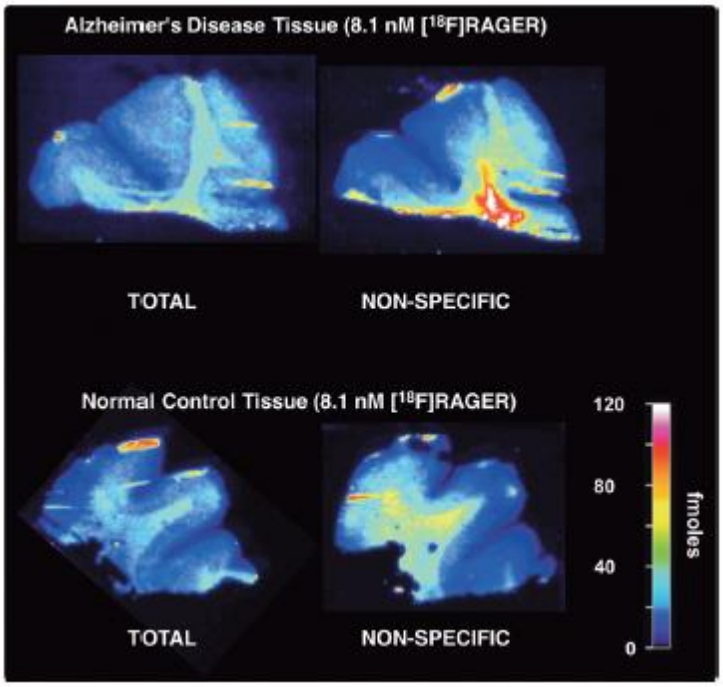

Figure 5.3. *In vitro* binding of [^{18}F]RAGER to human brain tissue sections. Both AD and normal cognitive control tissues are from frontal cortex.

Although RAGER has lower lipophilicity (experimental log P = 3.5; CLogP = 4.85, ChemBioDraw) than FPS-ZM1 (CLogP = 5.25, ChemBioDraw), it is still lipophilic, and we believe this is the origin of the high white matter binding. Correcting for nonspecific binding allowed estimation of K_d and B_{max} in both the AD tissue and normal control tissue (Table 5.1). Using both AD and control tissue samples, the K_d was found to be approximately 15 nM, similar to the reported K_i of 25 nM for FPS-ZM1. The B_{max} in AD tissue was found to be 2.8-fold higher than the B_{max} in normal control tissue, which is also consistent with the 2.9-fold increase in RAGE expression confirmed by immunohistochemistry (vide supra). The binding potential (BP), estimated by the B_{max}/K_d value, is useful forpredicting the suitability of a radiotracer for imaging a target binding site in human subjects. [^{18}F]RAGER has a BP of 1.86 in AD tissue, suggesting

potential suitability of this scaffold for future applications in clinical PET imaging and the feasibility of imaging RAGE with PET.

Table 5.1. *In Vitro* Binding assessment of [^{18}F]RAGER using human cortical brain sections.

	K_d (nM)	**B_{max} (nM)**	**BP (B_{max}/ K_d)**
AD	15.5	28	1.86
Cognitive Normal	15.5	10	0.65

2.3. Preclinical Imaging

In vivo behavior of the radiotracers was investigated initially in rodents (n = 3). PET scans were conducted in Sprague−Dawley rats, and imaging was conducted for 90 min postinjection of the radiotracer. Following the scan, images were summed (figure 5.4A) and a region-of-interest (ROI) was drawn over the whole brain on multiple planes. The volumetric ROIs were then applied to the full dynamic data set to generate a time−radioactivity curve (figure 5.4B). The curve showed rapid uptake of [^{18}F]RAGER (peak SUV ≈ 2.5). Peak uptake occurred within 3 min post injection and was followed by virtually complete washout over the duration of the PET scan.

Encouraged by these results, we also evaluated the imaging properties of [^{18}F]RAGER in non-human primates. Similar imaging results were obtained in rhesus macaque (Figure 5.4C). A ROI was drawn initially for the whole brain and used to generate a time−radioactivity curve (Figure 5.4D), which revealed rapid uptake of [^{18}F]RAGER in the primate brain (peak SUV ≈ 2.3). Peak uptake again occurred within 3 min postinjection, and was followed by washout over the duration of the PET scan. Washout was faster in rodents than primates, and we attribute this to increased tissue volumes and lower blood flow in the primates.

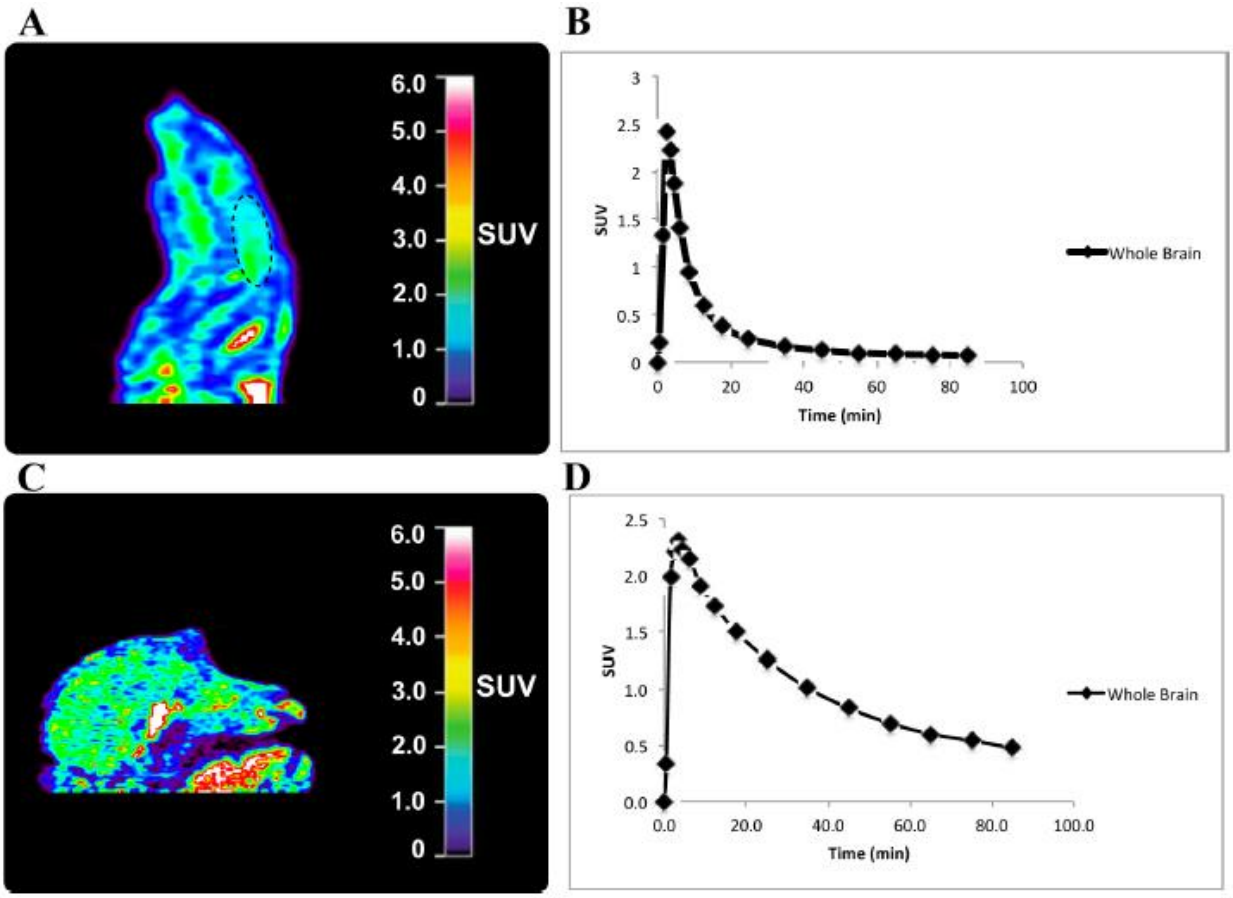

Figure 5.4. Representative microPET imaging data for rodent and nonhuman primate. A, summed images 0−90 min post-iv-injection of the radiotracer (dotted oval = brain); B, rodent whole brain time−radioactivity curves) and non-human primate C, summed images 0−90 min post-iv injection of the radiotracer; D, nonhuman primate whole brain time−radioactivity curves) imaged with [^{18}F]RAGER.

The radiotracer provided reasonable levels of uptake in all gray matter regions (peak SUVs range from 2−4; see Figure 5.5 for regional time− radioactivity curves of [^{18}F]RAGER in non-human primate brain). For example, there was high uptake apparent in the cortex and cerebellum, which agrees with the reported distribution of RAGE.[24] Notably, there was also extensive bilateral uptake and markedly slower washout associated with the hippocampal regions, which suggests specific binding. This is also consistent with the known expression of RAGE, where it has been shown that some RAGE expression is normal in the healthy hippocampus but that elevated levels are present in the hippocampus of the Alzheimer's disease brain.[24]

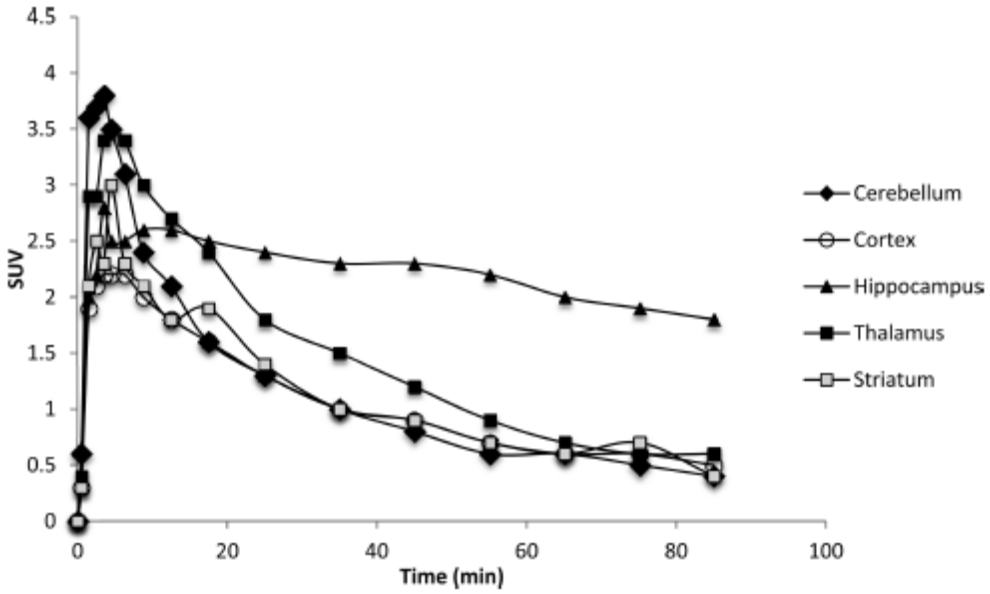

Figure 5.5 [^{18}F]RAGER regional time−radioactivity curves in the non-human primate brain. Presented as standardized uptake value (SUV).

Very little white matter binding was apparent, in contrast to the high degrees of nonspecific binding that complicated the *in vitro* studies described above, although there was extensive uptake in the brain stem and an unknown region outside of the brain (possibly tissue associated with the nasal cavity). The cause of differing nonspecific binding between the *in vitro* and *in vivo* studies could simply be that there is less [^{18}F]RAGER available to bind in the brain during the *in vivo* studies because of uptake in the periphery (there is high RAGE expression in the lung[25]), binding to circulating soluble RAGE or could be due to metabolism effects. To investigate the latter possibility, we next investigated metabolism of RAGER.

2.4. Metabolism and Biodistribution

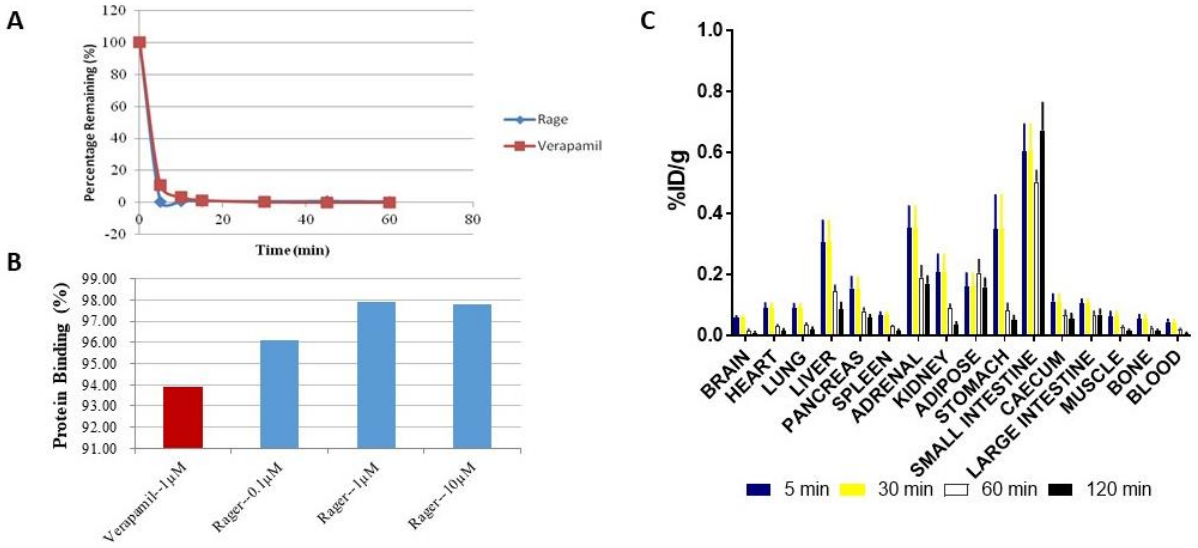

Figure 5.6 RAGER metabolism, plasma protein binding, and biodistribution. A) Metabolism in rat liver microsomes (verapamil shown as assay control). B) Plasma protein binding (verapamil shown as assay control). C) Biodistribution in normal Sprague dawley rat.

Metabolism of RAGER was examined by incubation with rat liver microsomes (figure 5.6A). The LC-MS/MS data analysis indicates extremely fast metabolism of the radiotracer, with a half-life of 0.66 min and only ~0.5% of authentic RAGER remaining at 5 min. Although we have not confirmed this metabolism profile *in vivo*, the rodent time−radioactivity curves are consistent with rapid metabolism and do not suggest that any labeled metabolites enter the brain. Rapid metabolism would explain the difference between the high nonspecific binding observed *in vitro* and the low levels apparent in the PET images. We have also not examined metabolism in primates but would expect it to be slower than that in rats. This could lead to higher nonspecific binding in primates, which would be consistent with the slower washout apparent in the primate time−radioactivity curves (figure 5.4). The rapid metabolism also suggests that brain uptake in known areas of RAGE expression is likely occurring before first pass metabolism, which is again consistent with the rapid peak uptake of the radiotracer in both rats and primates.

Plasma protein binding analysis revealed 96% of the small molecule radioligand is plasma protein bound, indicating a very low free fraction available to pass through the BBB and

engage in specific binding to RAGE (figure 5.6B). Plasma protein binding is not often a primary concern in radioligand development. In multiple parameter operator prediction tools, it is ranked after lipophilicity, hydrogen bond donors and acceptors, and apparent permeability.[26] There is not a consensus on what qualifies as an acceptable free fraction in plasma for a radioligand, considering that [^{11}C]flumazenil has 40% and [^{11}C]raclopride has 98% plasma protein binding.[27-28] It is also unclear whether plasma protein binding is a direct predictor of nonspecific binding once the radioligand has entered the CNS, though plasma protein binding and nonspecific binding both correlate with lipophilicity.

To further evaluate this radioligand, biodistribution studies were performed in normal Sprague Dawley rats (n=4/ sex/ time point) at four different time points (5, 30, 60 and 120 minutes post radioligand injection (figure 5.6C). As expected from the rodent PET imaging, the radioligand was completely washed out of the brain after 30 minutes. There is no bone uptake, indicating there is not radiolysis or metabolic defluorination. Independently, Kong *et al.*[29] and Bongarzone *et al.*[30] have also investigated [^{18}F]fluoro-FPS-ZM1 and [^{11}C]FPS-ZM1 as a radioligand for RAGE. Results across the three groups have been similar: blood-brain barrier permeability was confirmed in rodent and biodistribution trends were similar to those determined in mice. Interestingly, although RAGE is documented to be highly expressed in the lungs, there is no observable accumulation of [^{18}F]RAGER in this organ. This lack of lung uptake was also observed in the biodistribution of the RAGE targeting nanoparticle and further investigation is required.[20]

2.5. Off-Target Binding

To evaluate any potential off-target binding partners, the LeadProfile Screen was performed (Cerep Panlabs). At a concentration of 10 μM, the extracellular ligand RAGER only

achieved >50% inhibition in 4 assays: androgen receptor, $GABA_A$ receptor, dopamine transporter, and melatonin MT_1 receptor (table 5.2). A dose response curve was generated for these four targets and the IC_{50}'s and K_i's were determined. [^{19}F]RAGER exhibited a K_i of 93 nM for MT_1; the other three off-targets all showed K_i's of greater than 1 μM. At radioligand concentrations, only MT_1 was considered a possible off-target binding partner warranting further experiments. Compared to the 15 nM K_D for [^{18}F]RAGER in tissue, the radiotracer exhibited a 6 fold higher affinity for RAGE compared to MT_1. [^{3}H]Melatonin was utilized as the competitive ligand for binding in the assay and it is assumed that [^{18}F]RAGER binds in the same site.

Table 5.2. Off-target binding of RAGER. All assays were performed at 10 μM [^{19}F]RAGER to determine the percent inhibition; secondary dose response IC_{50}'s and K_i's are reported. Full table available in Appendix A.

Assay Name	**Species**	**% Inhibition**	**IC_{50} (μM)**	**K_i (μM)**
Androgen	Human	59	4.37	2.57
$GABA_A$	Rat	55	10.4	8.46
Dopamine Transporter	Human	52	8.61	6.84
Melatonin MT_1	Human	96	0.18	0.093

MT_1 is a G-coupled transmembrane receptor expressed only in the CNS.[31] Its endogenous ligand, melatonin, is well known for its role in circadian rhythm control. Melatonin has not displayed any documented affinity for RAGE and has high affinity (< 1 nM) to melatonin receptors (MT_1 and MT_2).[31] MT_1 is mostly expressed in the hypothalamus, though it is also expressed at lower levels in the hippocampus and other areas of the human brain.[31] Unlike MT_1, RAGE expression is inducible by the level of inflammation in the microenvironment; in the presence of cytokines and other proinflammatory mediators, its ligands, RAGE activity and expression increases.[7] RAGE is expressed ubiquitously at low levels in the CNS and is documented to be overexpressed in hippocampal neurons in AD.[12] Studies with [^{18}F]RAGER show the highest uptake in the thalamus and basal ganglia in a healthy nonhuman primate, which

may overlap with the areas of MT_1 expression.[1] However, there is limited information available regarding the expression levels of RAGE in healthy control tissue.

To identify any areas of MT_1 expression and determine if those areas overlapped with [^{18}F]RAGER binding, immunohistochemistry was performed on fixed human brain tissue sections using mouse anti-human MT_1 antibody. To serve as the neuroinflammatory brain sections, frontal cortex tissue sections were harvested from AD and DLB patient samples. A region and age matched healthy control was used for comparison. Increased MT_1 immunoreactivity was observed in AD and DLB/AD tissue sections (figure 5.7). This phenomenon is previously documented.[32] Anti-RAGE antibodies also display increased immunoreactivity in AD and DLB tissue sections. Although the increased binding trend in disease tissue is shared by MT_1 and RAGE, there is a large difference in abundance. In diseased tissues, MT_1 is more abundant than RAGE, which indicates a real possibility for off-target binding. To validate the specific binding, [^{18}F]RAGER autoradiography on human brain sections was performed and the native MT_1 ligand, melatonin, was used as the nonspecific blocking agent.

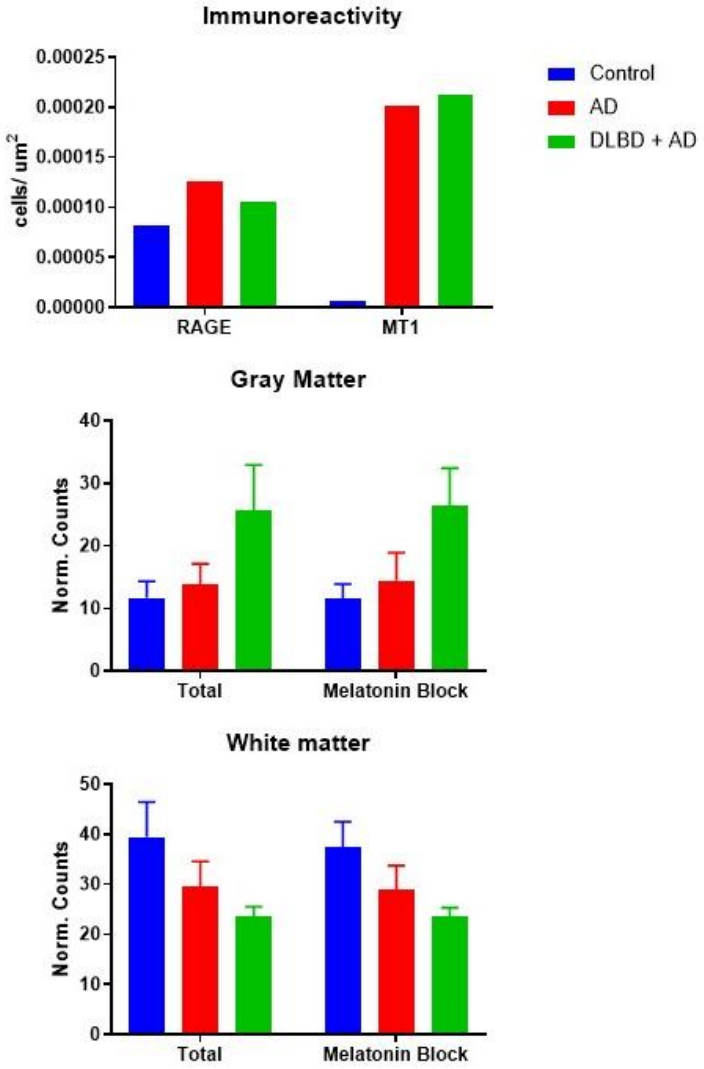

Figure 5.7. Postmortem human tissue immunoreactivity and [^{18}F]RAGER autoradiography.

Competitive binding experiments were performed with 10 µM melatonin and [^{18}F]RAGER in human brain tissue sections. Region and age matched healthy control tissue was compared with AD and DLB brain sections. Melatonin (10 µM) was not able to displace [^{18}F]RAGER in any section of human brain tissue in both control and disease brain tissue sections (figure 5.7). This indicated strongly that nonspecific binding of [^{18}F]RAGER is not due to off-target binding to MT_1.

This competitive binding experiment indicates that specific binding on tissue is not to the MT_1 receptor. This result seems to conflict with the *in vitro* assay, which used [^{3}H]melatonin for K_i determination. If RAGER has demonstrable affinity for the MT_1 receptor in the K_i assay, it is expected that at least a portion of [^{18}F]RAGER binding would be displaced by excess melatonin in both white and grey matter. As we observed, the nonspecific binding of this radioligand is high in the white matter. Additionally, based on the low MT_1 immunoreactivity of the human brain tissue in this region, it is not unreasonable that the specific binding was not affected by melatonin blocking.

Data from *in vitro* binding experiments is often difficult to correlate to *in vivo* binding behavior, so additional competitive binding studies were performed in healthy animals. Small animal PET imaging studies were first performed in healthy rodents with a non-therapeutic dose of melatonin. Melatonin is well known to cross the blood-brain barrier passively.[33] An adult Sprague Dawley rat was administered intravenously 5 µg/kg melatonin in saline 10 minutes prior to [^{18}F]RAGER bolus injection and imaging for 90 minutes. The time activity curve (TAC) was corrected for animal weights and injected dose to display the curve as standard uptake value (SUV) versus time. Melatonin blocking had no effect on [^{18}F]RAGER uptake compared to baseline (figure 5.8 A, B). Consistent with the preliminary study, washout of the radioligand occurs very quickly in the rodent brain.[1] Biodistribution studies in rodent confirm a complete washout of [^{18}F]RAGER after 60 minutes. The melatonin blocking did not change the shape of the time activity curve (figure 5.8C).

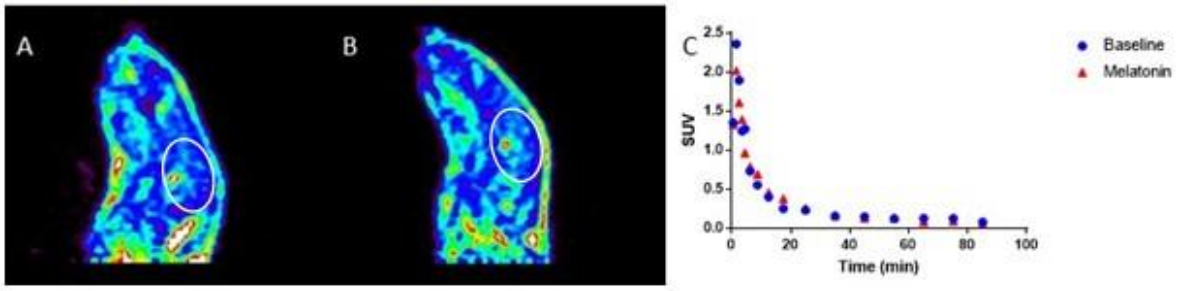

Figure 5.8. [^{18}F]RAGER rat brain imaging with melatonin blocking. A. [^{18}F]RAGER uptake in rodent whole brain (white circle). B. Melatonin Blocking of [^{18}F]RAGER in rodent brain. C. Time activity curve presented as SUV. Sagittal summed (0-90 min) PET image of rodent administered with 310 +/- 50 µCi of [^{18}F]RAGER.

Due to the quick washout of [^{18}F]RAGER in rodent brain, we did not expect to see a large decrease in specific binding. A small decrease is observed, but this could be due to the blocking agent influencing the input function (figure 5.8). The rat brain has an increased number of metabolizing enzymes in the CNS in addition to very active xenobiotic export transporters which could be responsible for the observed fast washout. In the nonhuman primate studies, washout of [^{18}F]RAGER is slower and lead us to expect that melatonin blocking might be more evident than in rodent. Specific binding was assessed with both blocking and displacement studies. We chose these two study designs to prove that if pre-administration altered the uptake that it would be due to competitive binding and not affecting an input function. Because these imaging studies are performed without arterial blood sampling, we cannot correct for input function. An infusion of blocking agent prior to the radioligand infusion could alter the input function. In the displacement study, the radioligand is infused first- and the competitor ligand is not given until 40 minutes into the scan. This design allows the competitive ligand, melatonin, to displace any specifically bound radioligand.

In the blocking study, 5 µg/kg melatonin in saline was dosed intravenously 10 minutes prior to [^{18}F]RAGER dosing and imaging for 90 minutes (figure 5.9). This PET scan with

melatonin pre-administration did not reveal any decrease in radioligand uptake, maximal SUV, or significant change in the shape of the time activity curve compared to baseline (figure 5.10).

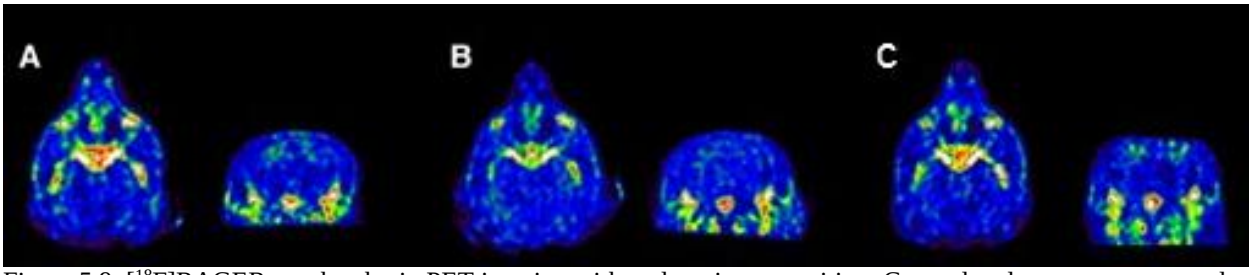

Figure 5.9. [^{18}F]RAGER monkey brain PET imaging with melatonin competition. Coronal and transverse summed (0-90 min) PET images of nonhuman primate administered with 3.6 +/- 0.7 mCi (n=4). A [^{18}F]RAGER baseline. B [^{18}F]RAGER pre-blocking 5ug/kg melatonin, C [^{18}F]RAGER displacement study with 10 μg/kg melatonin.

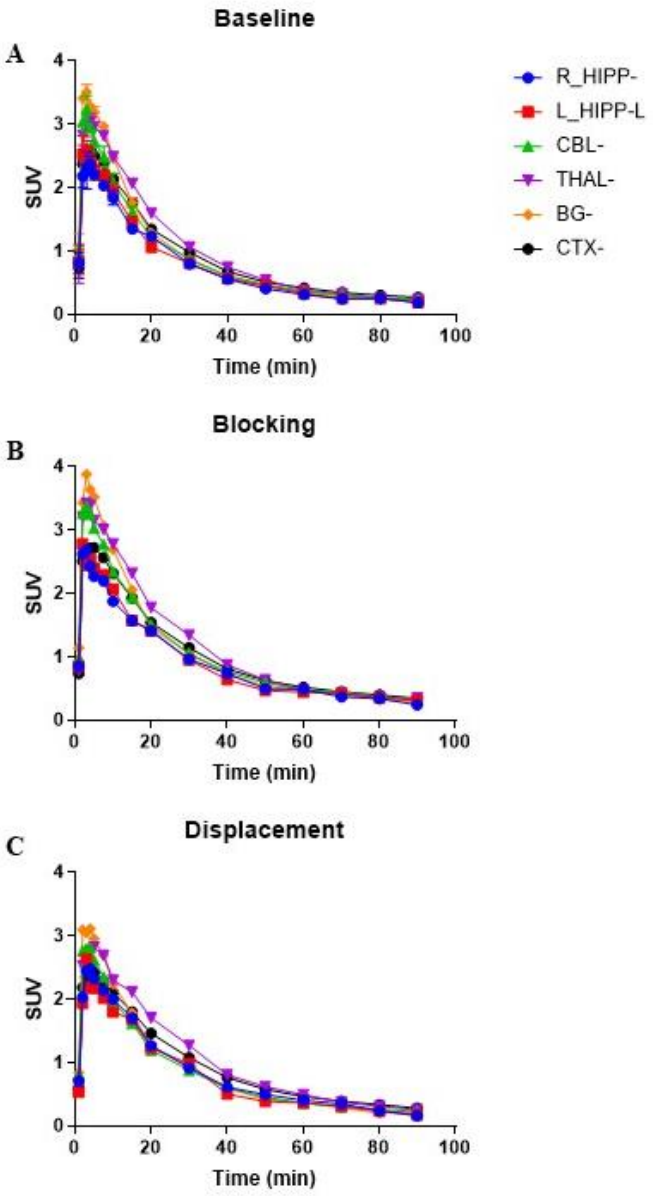

Figure 5.10. Time activity curves of nonhuman primate PET imaging studies. Presented as SUV. A. [^{18}F]RAGER baseline scans (n=2). B. [^{18}F]RAGER 5 ug/kg melatonin blocking study. C. [^{18}F]RAGER 10 ug/kg melatonin displacement study. Regions of interest displayed: R_HIPP (Right hippocampus) L_HIPP (Left hippocampus) CBL (cerebellum) THAL (thalamus) BG (basal ganglia) CTX (cortex).

A displacement study was also performed with melatonin. In this experiment, 10 µg/kg melatonin in saline was dosed 40 minutes into the 90 minute scan of [^{18}F]RAGER (figure 5.9). A higher dose of melatonin was chosen for this experiment to increase the likelihood of observing displacement. Time activity curves for baseline, blocking, and displacing studies are presented as

SUV (Figure 5.10). Similarly, this scan did not differ significantly in maximal SUV or shape from the baseline PET scan. This strongly indicates that [^{18}F]RAGER binding in the nonhuman primate is specific to RAGE and there is no specific binding to MT_1.

2.6. [^{18}F]RAGER Summary

In summary, we have demonstrated the synthesis and preliminary preclinical evaluation of [^{18}F]RAGER: the first small molecule BBB-permeable PET radioligand for the RAGE. We have confirmed upregulation of RAGE in AD post-mortem cortical tissue with immunohistochemistry and demonstrated that [^{18}F]RAGER co-localizes with areas of RAGE distribution. MicroPET imaging in rodent and non-human primate confirmed brain uptake and extensive washout, and the latter indicated that the radiotracer accumulates in areas of known RAGE expression. [^{18}F]RAGER has a BP of 1.86 in AD tissue, suggesting potential suitability of this scaffold for future applications in clinical PET imaging of RAGE, but leaving scope for improvement. Independently, Zong *et al*. developed [^{18}F]fluoro-FPS-ZM1, the same compound as [^{18}F]RAGER, and reported similar blood-brain barrier permeability in mice.[29] Bongarzone *et al*. have developed [^{11}C]FPS-ZM1 that demonstrated similar *in vivo* tissue binding characteristics to [^{18}F]RAGER.[4]

The *in vitro* screening for alternative binding partners (surprisingly) indicated that RAGER is not very promiscuous, with some interactions with DAT, Androgen, $GABA_A$, and MT_1 receptor (table 5.2). MT1 is known to be overexpressed in AD patient brains,[32] and this was confirmed in our own immunohistochemistry analysis of AD and DLB-AD brain tissue (figure 5.7). However, competitive binding studies with melatonin on brain tissue sections did not affect [^{18}F]RAGER binding (figure 5.7). This disconnect from the *in vitro* screening to *in vitro* tissue binding was a concern. The brain sections used were determined to be high in MT_1 abundance

and at 10 μM of melatonin (excess) a decrease in binding was expected if [^{18}F]RAGER bound to MT_1. We chose to move into small animal imaging, acknowledging the *in vitro* complications of working with [^{18}F]RAGER.

The solubility of RAGER is very poor. Anecdotally, we've heard from the group at King's College working with [^{11}C]FPS-ZM1 that they've also observed *increased* total binding in the presence of unlabeled compound (our experimental measure of "nonspecific binding"). This results in a calculated *negative* specific binding measurement. Together we posit the excess unlabeled compound is crashing out of solution on the tissue, and prevents the labeled [^{18}F]/[^{11}C] compound from being washed off the tissue section. Early on in this project, we attempted autoradiography with [^{18}F]RAGER and had used plastic chambers (our usual preference in order to keep the assay volume low) and we measured no activity on the tissue sections. Confused, we counted the assay buffer and the plastic chambers themselves, and found most of the activity was in the plastic! In the optimization process, we had screened different buffer additives like bovine serum albumin (BSA), Triton-X (a detergent), and Tween-20 (a detergent). In the presence of BSA, there was also no activity on the tissue- which gave us an indication about plasma protein binding, which was later confirmed (figure 5.6B). Another assay attempt we had dissolved the cold compound in methanol- when 100 μL was added to a glass chamber containing 200 mL of assay buffer, the unlabeled compound crashed out of solution and white solids could be seen at the bottom of the chamber. DMSO had to be used instead, and this was a limitation on concentrations because we prefer to keep DMSO 1% v/v or less.

Solubility issues followed us into the *in vivo* experiments as well. Not shown, we attempted a rodent blocking study with unlabeled RAGER. Although we had performed no toxicity studies in house, the original report of FPS-ZM1 had claimed tolerability up to 100

mg/kg in mouse.[21] We had chosen 1 mg/kg for a blocking study- and formulation was a problem. We contacted the first and corresponding authors of this original report to inquire of their dose formulation and received no reply. Attempts to make the salt form of RAGER were unsuccessful, though the salt form would have been easier to formulate. 10% ethanol, 5% methanol, and 1% DMSO (v/v) in water, saline, and PBS combinations were all attempted with no avail. We explored less conventional formulations and found PEG was suitable to keep RAGER in solution. The first rodent blocking study with this formulation was successful- it showed increased total uptake. Since RAGER has high plasma protein binding, and likely specific binding in the periphery, a blocking study was likely to result in an initial increase. The second rodent blocking study (of the same design) resulted in the death of the rodent during the scan. The scan was halted when blood was observed in the urine; the animal was removed from the anesthesia chamber, but unfortunately did not recover from anesthesia. This event was reported and observed as random: the first rodent had survived the scan, and the formulated blocking dose had been made fresh that morning and had passed quality control (QC) inspection. Similarly, the radioligand dose had passed QC inspection. A third blocking scan was attempted- and the rodent died during the scan with the same unexplained bleeding. We hypothesized that the unlabeled compound could be falling out of solution in the blood stream and causing damage in the liver (probably the source of bleeding). Obviously, this was a turning point in the project because we had concerns about the toxicity and safety of the compound. For the safety of our animals, we decided to no longer perform blocking studies with this compound. For the monkey blocking studies, melatonin (a well characterized and safe compound) was used, and no “self” blocking was completed.

The melatonin blocking and displacement studies indicated no *in vivo* binding of [^{18}F]RAGER to MT_1 (figure 5.10). This result combined with the *in vitro* tissue studies would indicate that MT_1 is not a binding partner and may be a complete disconnect from the Cerep panel results. We rationalize this disconnect by acknowledging that there will always be a difference between cell-based, tissue, and *in vivo* behavior of compounds based on those environments. RAGER binding is heavily influenced by the assay environment, as described through our autoradiography method development. The Cerep panel methods were out of our control in a way, so it is difficult to speculate if the specific instruments or items used in the assays (like plastic) could have influenced these results. The overall conclusion might be that RAGER has very high nonspecific binding, but this isn't observed in PET imaging.

3. Intracellular Ligand Approach

[^{18}F]RAGER was designed to inhibit ligand binding in the extracellular domains. This approach does not offer selectivity over the other isoforms of RAGE (figure 5.1). An additional concern with targeting the extracellular domain is that it is highly homologous throughout the isoforms of RAGE. There are 22 identified human isoforms of RAGE, some are active and still membrane bound, and some are soluble and free floating in the blood and CSF.[34] The most predominant isoform is sRAGE, which lacks the intracellular C-tail domain.[7] The relationship between the membrane-bound and soluble isoforms are not well understood. It could increase the noise and/or nonspecific binding *in vivo* if the radioligand had affinity to all of the isoforms of RAGE. A more appropriate domain to target with a small molecule radioligand is the intracellular C-terminus, for which there were recently identified small molecule inhibitors.[35] The intracellular C-tail is only found in active, full length RAGE which is an important distinction in the inflammation pathway.[35] With the goal of selectivity for the full length,

membrane bound isoforms of RAGE, we developed [^{18}F]InRAGER (**[^{18}F]4**) and [^{11}C]InRAGER2 (**[^{11}C]6**) and herein report the preliminary syntheses and off-target screening.

3.2 Synthesis of Reference Standards

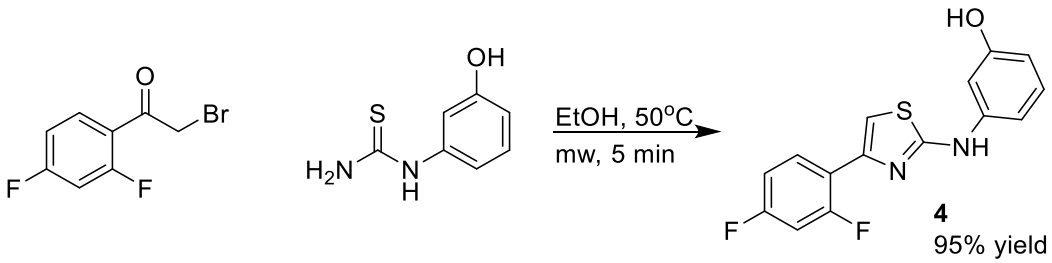

Scheme 5.2. Synthesis of InRAGER.

Synthesis of the InRAGER standard was accomplished in a one-step microwave assisted reaction. 2-bromo-2',4'-difluoro-acetophenone was added to N-(3-hydroxyphenyl)thiourea dissolved in ethanol, reaction progressed at 50 °C, 100 W, for 5 minutes stirring, procedure adapted from Kabalka and Mereddy (scheme 5.2).[36] Water was added to the reaction vessel and the resultant precipitate was collected, purification was not required.

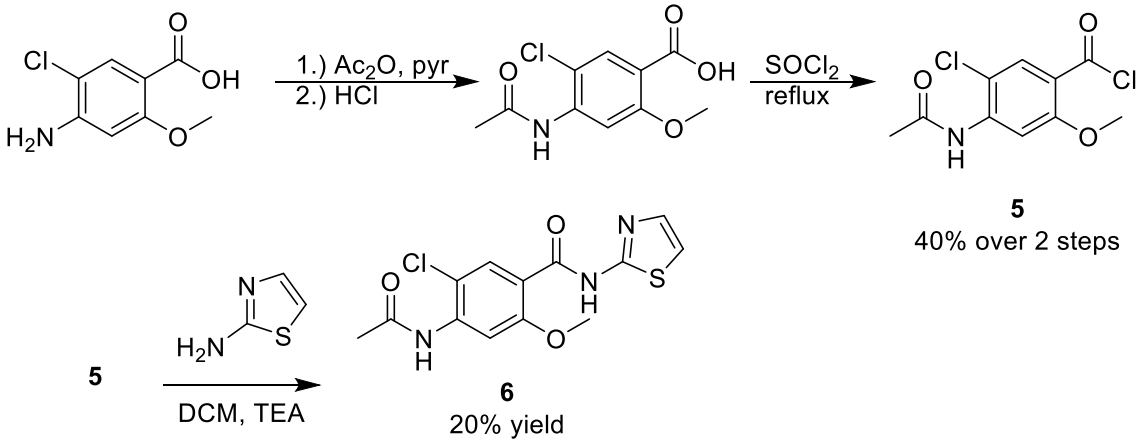

Scheme 5.3. Synthesis of [^{11}C]InRAGER2 reference standard.

Synthesis of the InRAGER2 standard was accomplished over three steps in 8% overall yield (scheme 5.3). 4-amino-5-chloro-2-methoxybenzoic acid was acetylated and then converted to 4-amino-5-chloro-2-methoxybenzoyl chloride (**5**) in neat thionyl chloride. Intermediate (**5**)

was suspended in DCM at 0 °C and TEA was added; thiazol-2-amine was added and solution progressed overnight at room temperature.

3.3 Preclinical Evaluation

InRAGER and InRAGER2 were discovered through high throughput screening, and little is known from the literature about their activities. We submitted these compounds for a biological screening assay at 10 μM (Cerep Panel). The results indicated some promiscuity of InRAGER (table 5.3). Of the 68 assays performed, InRAGER inhibited 13 of them at 60% or greater. The list contains receptors and transporters that are widely expressed throughout the CNS and would challenge the interpretation of binding *in vitro* and *in vivo* of this compound.

Table 5.3 Off-target binding of InRAGER. Full table available in Appendix A.

Assay Name	Species	% Inhibition
Adenosine A_{2A}	Human	75.7
Adenosine A_3	Human	98.8
BZD (peripheral)	Rat	63.2
CCK_1 (CCK_A)	Human	76.4
κ (KOP)	Human	83.1
EP_2	Human	73.6
5-HT_{2A}	Human	67.3
5-HT_{2B}	Human	97.1
UT	Human	77.7
norepinephrine transporter	Human	94.6
COX-1	Human	100.7%
COX-2	Human	100%
MAO-B	Human	72.7%

InRAGER2 appears to be less promiscuous than InRAGER (table 5.4). The results obtained from the off-target screening indicated the 5-HT_{2B}, adenosine A_3, benzodiazepine, and UT receptors and COX-1 enzyme are shared off-targets of both InRAGER and InRAGER2 (tables 5.3 and 5.4). Additionally, InRAGER2 has a modest IC_{50} for the constitutively expressed COX-1 enzyme. These CNS off-targets will be considered during translation to imaging.

Table 5.4 Off-target binding of InRAGER2. Full table available in Appendix A.

Assay Name	Species	% Inhibition	IC_{50} (μM)	K_i (μM)
5-HT_{2B}	Human	95.1	0.26	0.13
Adenosine A_3	Human	74.6	1.4	0.83
BZD (peripheral)	Rat	84.9	0.48	0.44
COX-1	Human	71.8	12	NA
UT	Human	81.2	1.4	1

3.4 Radiochemistry

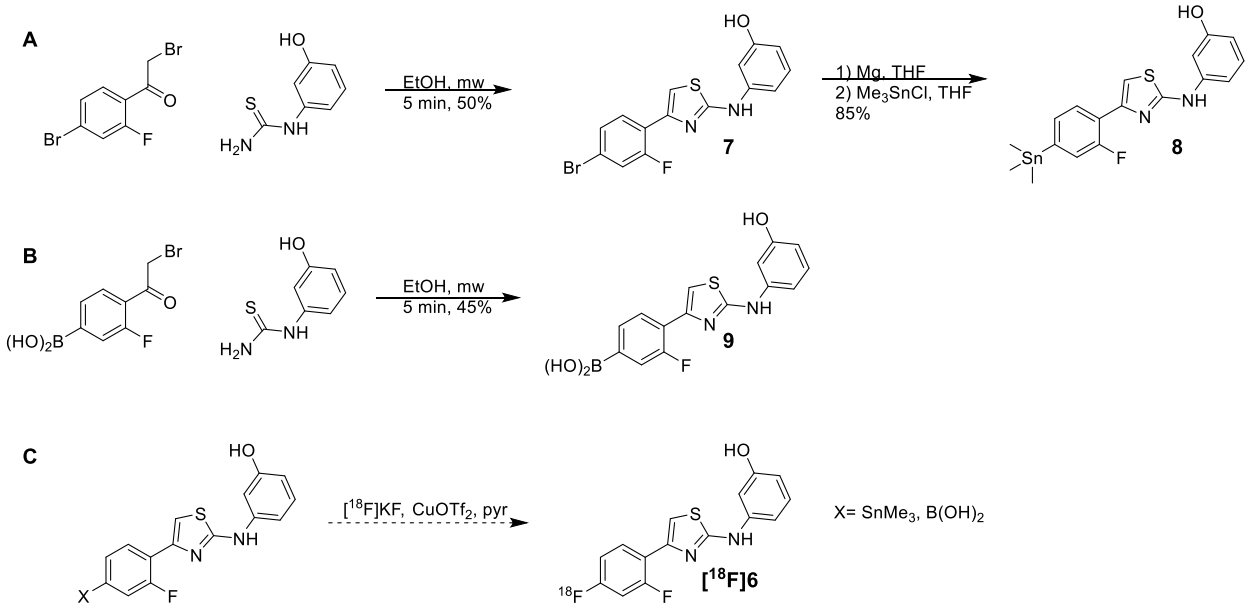

Scheme 5.4. Synthesis of precursors and radiochemical synthesis of [^{18}F]InRAGER ([^{18}F]**6**).

Strategies to radiolabel InRAGER involved our previously developed copper catalyzed fluorination methods using boronic acid[37] and arylstannane precursors.[38] Synthesis of stannane (**8**) and boronic acid (**9**) InRAGER precursors are shown in scheme 5.4A. Intermediate 3-((4-(4-bromo-2-fluorophenyl)thiazol-2-yl)amino)phenol (**7**) was synthesized by the same microwave reaction detailed in scheme 5.2. The arylbromine of **7** was formed into the Grignard and then reacted with trimethyltin chloride to form the arylstannane precursor **8** in 42% yield total. The boronic acid precursor **9** was synthesized from the same microwave reaction detailed in scheme 5.2, in 45% yield with column purification required (scheme 5.4B).

Proposed radiofluorination for both precursors **8** and **9** is shown in scheme 5.4C. First, the radiofluorination was attempted manually and followed the described optimum conditions.[37-38] No reaction was observed in the case of either precursor, despite changes in pyridine and catalyst concentration. We suspected copper binding to the thiourea moiety. In the interest of time, radiosynthesis for preliminary evaluation of [^{18}F]InRAGER in rodent was performed by radioisotopic exchange. The reference standard **4** was reacted with [^{18}F]KF in DMF at 130 °C for 30 minutes and purification on a Gemini C18 250 mm x 10 mm prep column (55% 10 mM NH_4CO_3: 45% MeCN, pH 7.4).

3.5 [^{18}F] InRAGER Imaging

PET imaging in healthy Sprague Dawley rat revealed blood-brain barrier permeability of [^{18}F]InRAGER (figure 5.11). The maximum SUV was less than the observed for [^{18}F]RAGER; however, the washout phase appears to be slower (figure 5.4B). This could signify more specific binding *in vivo* than [^{18}F]RAGER. However, when the other binding partners of [^{18}F]InRAGER are considered (table 5.3), the source of this specific binding cannot assumed to be RAGE.

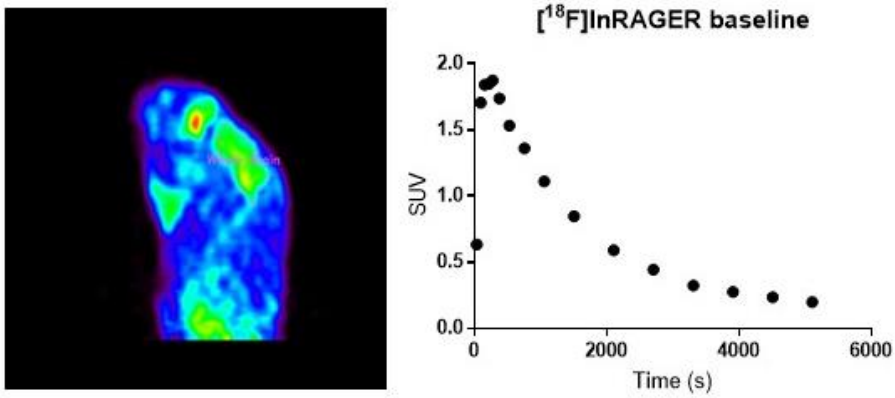

Figure 5.11. [^{18}F]InRAGER PET imaging in rodent. 0.142 mCi injected, 305 g rodent. Whole brain region is shown in the time activity curve, presented as SUV.

3.6 InRAGER Summary

The ability to decipher full-length active RAGE abundance independent from the soluble and inactive isoforms would be an exciting tool for investigating RAGE biology. Toward that end, we initiated the development of radioligands specific for the intracellular binding site of RAGE's C-terminus for Dia1, InRAGER (**4**) and InRAGER2 (**6**). Preliminary evaluation of [^{18}F]InRAGER showed good brain uptake (figure 5.11), but identified possible promiscuity in the CNS (table 5.3). Binding to multiple, highly abundant proteins in the neurovascular unit is a significant hurdle to overcome in radioligand development. In particular, the possible binding of InRAGER to adenosine and serotonin receptors, and norepinephrine transporter (NET) are concerning. The involvement of neurotransmitter systems in neurodegenerative disorders is studied in its own right (like monoamine oxidase, detailed in chapters 3 and 4), and these proteins could have their own effects in disease.

Another challenge in this radioligand strategy was the radiolabeling step itself. For a preliminary rodent imaging study, isotope exchange was utilized. In development, multiple strategies were attempted to utilize contemporary radiochemistry methods like boronic ester[37] and trimethyltin precursors.[38] In tandem with the radiochemistry optimization, the off-target binding results were obtained and the decision was made to halt this effort. We began to develop InRAGER2 as a possible carbon-11 radioligand.

The reference standard for InRAGER2 was synthesized (scheme 5.3) and fewer off-target effects were predicted from the Cerep panel (table 5.4). It is more probable that InRAGER2 could serve as a selective RAGE ligand, and this compound will be further developed. The *in vitro* characterization for RAGE is still lacking; the compound was found to inhibit the intracellular RAGE domain's binding to Dia1.[35] To our knowledge, this compound has not been evaluated for binding on tissue. Autoradiography is recommended for future evaluation of this

compound, dependent upon carbon-11 labeling is successful. Future work for this project is further detailed in chapter 7.

4. Methods

Chemistry

General Considerations

All the chemicals employed in the syntheses were sourced commercially and used without further purification. ^{1}H NMR spectra were obtained at 400 MHz on Varian NMR spectrometer in CD_3OD or d_6-DMSO solutions at room temperature with tetramethylsilane (TMS, $\delta = 0$) as an internal standard. ^{13}C NMR spectra were obtained at 100 MHz, and ^{19}F-NMR spectra were obtained at 376 MHz. Chemical shifts (δ) are reported in ppm, and coupling constants are reported in hertz. Multiplicity is defined by s (singlet), d (doublet), t (triplet), q (quartet), and m (multiplet). High performance liquid chromatography (HPLC) was performed using a Shimadzu LC-2010A HT system equipped with a Bioscan B-FC-1000 radiation detector. Mass spectra were performed on a Micromass VG 70-250-S magnetic sector mass spectrometer, Micromass AutoSpec Ultima magnetic sector mass spectrometer, or Agilent Q-TOF HPLC-MS using the electrospray ionization (ESI) method or electron ionization (EI) method.

Preparation of N-Benzyl-N-cyclohexyl-4-fluorobenzamide (**2**: RAGER). Cyclohexylamine (250 mg, 2.52 mmol) and benzaldehyde (267 mg, 2.52 mmol) were dissolved in methanol (5 mL). Sodium sulfate was added, and the mixture was stirred for 18 h at 50 °C. The mixture was filtered, and the filtrate was concentrated in vacuo. The white semisolid was redissolved in methanol and cooled to 0 °C. Sodium borohydride (133 mg, 3.53 mmol) was slowly added, and the reaction was stirred at rt for 4 h. The reaction was quenched with saturated ammonium chloride solution. The intermediate product was extracted with dichloromethane (3×) and dried

over sodium sulfate, and solvent was removed in vacuo. The intermediate product was dissolved in dichloromethane (6 mL), and the solution was cooled to 0 °C. Triethylamine (306 mg, 3.02 mmol) and 4-fluorobenzoyl chloride (439 mg, 2.77 mmol) were added, and the solution was stirred for 18 h under argon. The reaction was quenched with H_2O, and the product was extracted with dichloromethane (3×) and purified by flash chromatography (SiO_2, 3:1 = hexanes/ethyl acetate). This process yielded the product as white, crystalline solid (628 mg, 80%); R_f = 0.52 (SiO_2, 3:1 = hexanes/ethyl acetate); ^{1}H NMR (400 MHz; DMSO-*d*$_6$)/ δ (ppm) 0.97−1.63 (10H, m), 3.48 (1H, br), 4.63 (2H, s), 7.21− 7.51 (9H, m); ^{13}C NMR (100 MHz; DMSO-*d*$_6$)/δ (ppm) 25.03, 25.80, 31.45, 51.17, 59.20, 115.98, 126.85, 127.08, 128.76, 129.06, 134.14, 139.96, 163.84, 170.61; ^{19}F NMR (376.3 MHz, DMSO-*d*$_6$)/δ (ppm) −111.71(1F, s); HPLC: 98%, retention time =22 min, column Phenomenex Gemini C18, 250 mm × 4.6 mm, mobile phase 10 mM NH_4HCO_3 in 58% MeCN, plus 2 mL/L sat. NH_4OH solution, flow rate = 1.0 mL/min, wavelength = 254 nm; HRMS calculated for $[M + H]^+$ (M = $C_{20}H_{22}FNO$) 312.1758, found 312.1756.

Preparation of 4-(Benzyl(cyclohexyl)carbamoyl)-N,N,N-trimethylbenzenaminium Iodide (**3**). To a vial was added N-benzyl-Ncyclohexyl- 4-(dimethylamino)benzamide (35.0 mg, 0.104 mmol) and methyl iodide (60.7 mg, 0.428 mmol). The vial was sealed, heated to 45 °C, and stirred. Additional methyl iodide (60.7 mg, 0.428 mmol, 20 times) was added over a few hours. After 5 h, an off-white, insoluble semisolid was observed. After 12 h, the solvent was evaporated under vacuum. The solid residue was washed with hexanes (3 × 2 mL) and diethyl ether (1 × 2 mL) and dried under vacuum to yield the product as an off white solid (35.6 mg, 0.0744 mmol, 72%); R_f = 0.53 (SiO_2, 3:1 = dichloromethane/methanol); 1H NMR (400 MHz; CD3OD, 55 °C)/δ

(ppm) 1.09(3H, m), 1.59−1.73(7H, m), 3.70 (9H, s), 4.67(2H, s), 7.22−7.30(5, m), 7.66(2H, s), 7.98(2H, s); HRMS calculated for $[M+H]^+$ (M = $C_{23}H_{31}N_2O$) 351.2431, found 351.2429.

*Preparation of 3-((4-(2,4-difluorophenyl)thiazol-2-yl)amino)phenol) (**4**: InRAGER).* 2-bromo-2',4'-difluoro-acetophenone (235 mg, 1 mmol) was added to N-(3-hydroxyphenyl)thiourea (168 mg, 1 mmol) dissolved in ethanol (10 mL), reaction progressed at 50 °C, 100 W, for 5 minutes stirring.[36] Water (5 mL) was added to the reaction vessel and the resultant precipitate was collected, purification was not required. ^{1}H NMR (400 MHz; MeOD/ δ (ppm) 8.11 (1H, dd), 7.22 (1H, m) 7.08 (2H,m), 6.92 (1H, m), 6.89 (1H, m), 6.55 (2H, dd). ^{19}F NMR (347 MHz; MeOD/δ (ppm) -111 (1F,s), -109 (1F, s). HPLC: 98%, retention time= 38 min, column: Phenonomenex Gemini C18, 250 mm x 4.6 mm, mobile phase 10 mM NH_4HCO_3 in 45% MeCN at pH 7.4, flow rate= 2.0 mL/min, wavelength= 254 nm; HRMS calculated for [M+H]+ (M= $C_{15}H_{10}F_2N_2OS$) 305.0555, found 305.0563.

Preparation of 4-amino-5-chloro-2-methoxybenzoyl chloride (**5**). Acetic anhydride (6.033 mmol, 0.57 ml) was added to 4-amino-5-chloro-2-methoxybenzoic acid (5.0 mmol, 1.008 g) dissolved in pyridine (2.5 ml). The reaction stirred at room temperature for 5 hours and then the solvent was removed by rotary evaporation. Water was added (10 ml) to the solution and acidified to pH 2 with concentrated HCl. The precipitate was further washed with water, dried, and used without purification in the subsequent step. Thionyl chloride (10 mmol, 10 ml) was added to the dried intermediate and the reaction proceeded at reflux for 3 hours. Reaction was neutralized by additional of cold methanol. ^{1}H NMR (400 MHz; MeOD/ δ (ppm) 7.26 (m, 2H), 5.30 (m, 3H) 1.25 (m, 3H).

Preparation of 4-acetamido-5-chloro-2-methoxy-N-(thiazol-2-yl)benzamide (**6**: InRAGER2). Triethylamine (1.48 mmol, 205 uL) was added to intermediate 5 (0.496 mmol, 130 mg)

dissolved in DCM at 0 °C. To this stirring solution, thiazole-2-amine (0.595 mmol, 60 mg) was added. The solution stirred overnight and was warmed to room temperature. The reaction mixture was washed with water and brine, then purified (2%-10% MeOH/DCM gradient; 10g SiO_2). ^{1}H NMR (400 MHz; CD_3OD/ δ (ppm) 8.568 (m, 1H), 7.985 (m, 1H), 7.70 (m, 1H) 6.935 (m, 1H), 4.060 (s, 3H) 1.25 (s, 3H). HRMS calculated for [M+H]+ (M= $C_{13}H_{12}ClN_3O_3S$) 326.0361, found 326.0360.

Preparation of 3-((4-(4-bromo-2-fluorophenyl)thiazol-2-yl)amino)phenol (**7**) 2-bromo-2'-fluoro-acetophenone (295 mg, 1 mmol) was added to N-(3-hydroxyphenyl)thiourea (168 mg, 1 mmol) dissolved in ethanol (5 mL), reaction progressed at 50 °C, 100 W, for 5 minutes stirring. Water (5 mL) was added to the reaction vessel and the resultant precipitate was collected and washed through a frit with DCM. HRMS calculated for [M+H]+ (M= $C_{15}H_{10}BrFN_2OS$) 364.9754, found 364.9755.

Preparation of 3-((4-(2-fluoro-4-(trimethylstannyl)phenyl)thiazol-2-yl)amino)phenol (**8**) Magnesium turnings in THF were activated with heat (30 °C); at reflux, a solution of intermediate 7 in THF (1M) was added dropwise over 25 minutes. Reaction progressed at reflux overnight. The reaction mixture was cooled to room temperature and a solution of trimethyltinchloride in THF (3.4 mmol, 677 mg) was added. The reaction progressed at room temperature for three hours. To quench the reaction, it was poured into an equal volume of cold saturated NH_4Cl solution. Product was extracted with 2 x 10 mL volumes of ether, washed with water, and the solvent removed by rotary evaporation. Product was purified by column chromatography (20% EA/Hex gradient). ^{1}H NMR (400 MHz; CD_3OD/ δ (ppm) 8.067 (m, 1H), 7.41 (m, 1H), 7.23 (m, 2H), 7.14 (m, 2H) 6.56 (m, 2H), 0.67 (s, 9H).

Preparation of (3-fluoro-4-(2-((3-hydroxyphenyl)amino)thiazol-4-yl)phenyl)boronic acid (**9**) 4-bromoacetyl-3-fluorophenylboronic aicd (261 mg, 1 mmol) was added to N-(3-hydroxyphenyl)thiourea (168 mg, 1 mmol) dissolved in ethanol (5 mL), reaction progressed at 50 °C, 100 W, for 5 minutes stirring. Water (5 mL) was added to the reaction vessel and the resultant precipitate was collected, purification was not required. ^{1}H NMR (400 MHz; MeOD/ δ (ppm) 8.09 (1H, dd), 7.91 (1H, m) 7.47 (2H,m), 7.03 (1H, m), 6.89 (1H, m), 6.55 (2H, dd)). ^{19}F NMR (347 MHz; MeOD/δ (ppm) -111 (1F,s), -109 (1F, s); HRMS calculated for [M+H]+ (M= $C_{15}H_{10}BF_2N_2O_3S$) 331.0718, found 331.0728.

Radiochemistry

General Considerations

Unless otherwise stated, reagents and solvents were commercially available and used without further purification: sodium chloride, 0.9% USP, and sterile water for injection, USP, were purchased from Hospira; ethanol was purchased from American Regent; HPLC grade acetonitrile was purchased from Fisher Scientific. Other synthesis components were obtained as follows: sterile filters were obtained from Millipore; sterile product vials were purchased from Hollister-Stier; QMA-light and C18-light Sep-Paks were purchased from Waters Corporation. Sep- Paks were flushed with 10 mL of ethanol followed by 10 mL of sterile water prior to use.

*[^{18}F]RAGER (***4**). [^{18}F]KF was prepared using a TRACERLab FXFN automated radiochemistry synthesis module (General Electric, GE). [^{18}F]Fluoride was produced via the ^{18}O(p,n)^{18}F nuclear reaction using a 16 MeV GE PETTrace cyclotron (40 μA beam for 30 min generated 1500 mCi of [^{18}F]fluoride). The [^{18}F]fluoride was delivered to the synthesis module (in a 1.5 mL bolus of [^{18}O]water) and trapped on a QMA-light Sep-Pak to remove [^{18}O]water. [^{18}F]Fluoride was eluted into the reaction vessel using K_2CO_3 (3.5 mg in 0.5 mL of water). A solution of $K_{2.2.2}$ (15 mg in 1

mL of acetonitrile) was added to the reaction vessel, and the resulting solution was azeotropically dried by heating the reaction vessel to 100 °C and drawing vacuum for 4 min. After this time, the reaction vessel was subjected to an argon stream and simultaneous vacuum draw for an additional 4 min. RAGER precursor **3** (1.5 mg dissolved in 0.5 mL of DMF) was delivered to the reaction vessel, and the reaction was heated to 130 °C and stirred for 30 min. After this time, the reactor was cooled to 55 °C and 2 mL of semipreparative HPLC solvent was added to the crude reaction mixture. This mixture was injected onto a semipreparative HPLC column (column Phenomenex Gemini C18, 250 mm × 10 mm; mobile phase 10 mM NH_4HCO_3 in 58% MeCN, pH 9.0 adjusted with 2 mL/L sat. NH_4OH, flow rate = 2.5 mL/min. The product peak (~36−37 min retention time) was collected and diluted into a round-bottom flask containing 50 mL of water. The solution was then passed through a C-18 extraction disk to remove organic solvent. The disk was washed with 5 mL of sterile water. The product was eluted with 0.5 mL of ethanol followed by 4.5 mL of normal saline. The final formulation was passed through a 0.2 μM needle filter into a sterile dose vial. We obtained 44.6 ± 10 mCi (1650 ± 385 MBq), 3.0% uncorrected yield, > 99% RCP, 3740 ± 495 Ci/mmol (138 ± 18 GBq/mmol), pH = 5.5, n = 6. *Quality Control*. Quality control of radiopharmaceutical doses was conducted using the following tests. *Visual Inspection*. Doses were examined visually to confirm that they were clear, colorless, and free of particulate matter. *Dose pH*. The pH of the doses was analyzed by applying a small amount of the dose to pH-indicator strips and determined by visual comparison with the provided scale. *HPLC Analysis*. Radiochemical purity of [18F]RAGER was assessed using Shimadzu LC-2010A HT system equipped with the UV and Rad detectors (column Phenomenex Gemini C18, 250 mm × 4.6 mm; mobile phase 10 mM NH_4HCO_3 in 58% MeCN,

pH 9 adjusted with 2 mL/L sat. NH_4OH solution; flow rate = 1.0 mL/min; wavelength = 254 nm; room temperature; product peak ≈ 22.5 min.

[^{18}F]InRAGER (**6**). [^{18}F]KF was prepared using a TRACERLab FXFN automated radiochemistry synthesis module (General Electric, GE). [^{18}F]Fluoride was produced via the $^{18}O(p,n)^{18}F$ nuclear reaction using a 16 MeV GE PETTrace cyclotron (40 μA beam for 30 min generated 1500 mCi of [^{18}F]fluoride). The [^{18}F]fluoride was delivered to the synthesis module (in a 1.5 mL bolus of [^{18}O]water) and trapped on a QMA-light Sep-Pak to remove [^{18}O]water. [^{18}F]Fluoride was eluted into the reaction vessel using K_2CO_3 (3.5 mg in 0.5 mL of water). A solution of K2.2.2 (15 mg in 1 mL of acetonitrile) was added to the reaction vessel, and the resulting solution was azeotropically dried by heating the reaction vessel to 100 °C and drawing vacuum for 4 min. After this time, the reaction vessel was subjected to an argon stream and simultaneous vacuum draw for an additional 4 min. InRAGER (4) (3 mg dissolved in 0.5 mL of DMF) was delivered to the reaction vessel, and the reaction was heated to 130 °C and stirred for 30 min. After this time, the reactor was cooled to 55 °C and 2 mL of semipreparative HPLC solvent was added to the crude reaction mixture. This mixture was injected onto a semipreparative HPLC column (column Phenomenex Gemini C18, 250 mm × 10 mm; mobile phase 10 mM NH_4HCO_3 in 55% MeCN, pH 7.5, flow rate = 4 mL/min. The product peak (~35 min retention time) was collected and diluted into a round-bottom flask containing 50 mL of water. The solution was then passed through a C-18 extraction disk to remove organic solvent. The disk was washed with 5 mL of sterile water. The product was eluted with 0.5 mL of ethanol followed by 4.5 mL of normal saline. The final formulation was passed through a 0.2 μM needle filter into a sterile dose vial. We obtained 0.500 mCi in 99% RCP, pH = 5.5, n = 1. *Quality Control*. Quality control of radiopharmaceutical doses was conducted using the following tests.

Visual Inspection. Doses were examined visually to confirm that they were clear, colorless, and free of particulate matter. *Dose pH*. The pH of the doses was analyzed by applying a small amount of the dose to pH-indicator strips and determined by visual comparison with the provided scale. *HPLC Analysis*. Radiochemical purity of [^{18}F]InRAGER was assessed using Shimadzu LC-2010A HT system equipped with the UV and Rad detectors (column Phenomenex Gemini C18, 250 mm × 4.6 mm; mobile phase 10 mM NH_4HCO_3 in 55% MeCN, pH 7.5; flow rate = 2.0 mL/min; wavelength = 254 nm; room temperature; product peak ≈ 13 min.

Preclinical Evaluation

Immunohistochemistry

Fixed tissue sections were incubated in PBS with 1% SDS for 5 min. Sections were then washed 3 x 5 min in PBS before quenching in 70% methanol with 0.3% hydrogen peroxide for 15 min. All slides were washed 3 x 5 min in PBS-T (PBS, 0.4% Triton-X-100, pH 7.4) and blocked for 30 min with PBS-TBA (PBS, 0.4% Triton-X-100, 1% BSA, 0.025% sodium azide, pH 7.4) before incubating in a 1:200 dilution of primary antibody (anti-RAGE, Novus Biologics (NBP242913) or anti-MTNR1A, Life Technologies Inc (PA519109)) in PBS-TBA overnight. Finally, brain sections were washed 3 x 5 minutes in PBS-T to remove unbound antibody. Tissue sections were incubated in a 1:200 dilution of secondary antibody, anti-rabbit-IgG, Vector Laboratories BA-1000) in PBS-TBA for 2 hr and washed 3 x 5 min with PBS-T. All incubations were carried out at room temperature. Slides were developed as instructed using the VECTASTAIN Elite ABC Kit (Standard) (Vector Laboratories PK-6100). Tissue sections were then washed 3 x 5 min in PBS-T before incubating for 4 min in a 0.5% w/v solution of diaminobenzidine in PBS-T (filtered) with 0.001% hydrogen peroxide. Giemsa counterstaining was utilized to visualize nucleus and cytoplasm in cells. Tissue sections were washed for 5 min

in dH_2O prior to overnight incubation in a 1:50 solution of Giemsa in dH_2O. Slides were then rinsed for 30 sec in dH_2O, 2 x 4 min in n-butanol, and 1 min in xylene. Permount was applied to the fixed tissue to attach coverslips to the polylysine-coated glass slides and allowed to set for 45 min prior to quantification. All incubations were carried out at room temperature. Immunoreactivity was quantified using ImageQuant. A region was drawn around the entire tissue section and using the serial section manager, 5% of the section was counted and picked using a randomized rotation. Immunoreactivity is presented as cells/ μm^2. Statistical analyses were performed in GraphPad Prism (8.01).

Autoradiography

Brain sections on slides were removed from -80°C freezer and thawed at room temperature for 5 min before rehydration in phosphate buffer saline (PBS, pH 7.4) for another 5 min. Then, brain sections were incubated with a range of concentrations of [^{18}F]RAGER for K_d and B_{max} determination. Incubation times were determined by equilibrium experiments; 30 minute incubations were used for [^{18}F]RAGER. Assay buffer included 0.5% Tween-20, and all incubations were performed in glass beakers. All sections were washed 3 x 2 min with PBS at 4 °C and then rinsed in dH_2O for 30 sec at 4 °C to remove unbound radioactivity. Finally, slides were dried under the continuous airflow for 30 min before exposure to a high-resolution phosphoimaging plate for 10 minutes. The exposed plate was scanned using a GE Typhoon FLA 7000 phosphoimager. Image analysis was performed using ImageQuant (Molecular Dynamics) software.

Plasma Protein Binding and Metabolism

The University of Michigan Pharmacokinetics (PK) Core determined plasma protein binding affinities to RAGER. Three doses of RAGER were prepared in DMSO (1 mM, 100 µM,

and 10 µM) and verapamil in DMSO (100 µM) was used as a positive control. RAGER was added to mouse plasma (final RAGER concentrations of 10 µM, 1 µM, and 0.1 µM) in duplicate. 200 µL of sample was added into the sample chamber, and 350 µL of PBS buffer was added to the neighboring buffer chamber. Solutions were incubated at 37 °C for 5 hours in the sample chamber (Thermo Singlue-use RED plate). Post incubation, corresponding plasma and buffer samples were mixed in equal volume and the internal standard was added in cold acetonitrile to precipitate proteins. The solution was vortexed and incubated on ice for 30 minutes. The entire solution was centrifuged for 10 minutes at 3500 rpm; the supernatant was analyzed by LC/MS/MS (Column: Waters XBridge C18). Metabolism performed as previously described.[1]

Biodistribution in Sprague Dawley Rat

Two males (weight: 260 +/- 30 g) and two females (weight: 200 +/- 15 g) were utilized per time point were intravenously injected with [^{18}F]RAGER (n= 16, 80 +/- 40 uCi) via tail-vein at 5, 30, 60, and 120 minutes. Post-administration animals were euthanized, dissected, and then each tissue was weighed and analyzed for radioactivity using PerkinElmer 2480 automatic gamma counter. Biodistribution studies confirmed brain permeability and quick washout, with radioligand absent from brain at the 60 and 120 minute time points. Limited exposure was observed in other organs, and some accumulation was observed in the later time points in the small intestine. No bone uptake was observed indicating that there was no radiolytic defluorination of [^{18}F]RAGER.

Off-target Screening

RAGER, InRAGER, and InRAGER2 reference standards were evaluated in the LeadProfile Screen (Cerep Panlabs) set of assays. Test concentration was 10 µM. Follow up K_i and IC_{50} measurements were performed on RAGER and InRAGER2 for assays that reported >50% inhibition in the preliminary screen. Full tables of results are listed in Appendix A.

Imaging

General Considerations

All animal studies were performed in accordance with standards set by the University Committee on Use and Care of Animals (UCUCA) at the University of Michigan.

Rodent Imaging Studies

Studies were done using male Sprague Dawley rats (n=3, weights= 330 +/- 40g). The animals were anesthetized (isoflurane), intubated, and positioned in a Concorde MicroPET P4 scanner. Following a transmission scan, the animals were inject i.v (via tail vein) with [^{18}F]RAGER (310 +/- 50 uCi) as a bolus over 1 min, and the brain imaged for 90 min (5 x 1 min frames – 2 x 2.5 min frames – 2 x5 min frames – 7 x 10 min frames). For the melatonin blocking study, melatonin was injected 10 min prior to imaging (5 ug/kg iv). [^{18}F]InRAGER rodent imaging study was performed in the same manner.

Primate imaging studies

Imaging was done using a mature female rhesus macaque (n=4, weight= 7.2 +/- 0.3 kg). The monkey was anesthetized (isoflurane), intubated, and positioned in a Concorde MicroPET P4 scanner. Following a transmission scan, the animal was injected i.v with [^{18}F]RAGER (3.6 +/- 0.7 mCi) as a bolus over 1 min, and the brain imaged for 90 min(5 x 1 min frames – 2 x 2.5 min frames – 2 x5 min frames – 7 x 10 min frames). For the first melatonin blocking study, 10 minutes prior to [^{18}F]RAGER injection, the animal was given a bolus injection i.v of melatonin (5 ug/kg). For the second melatonin blocking study, the animal was given a bolus injection i.v of melatonin (10 ug/kg) 40 minutes into the [^{18}F]RAGER scan.

Image Analysis

Emission data were corrected for attenuation and scatter, and reconstructed using the 3D maximum a priori method (3D MAP algorithm). Using a summed image of the entire data set, 3D volumes of interest (VOI) were determined by placing a seed voxel in the middle of various brain regions, and then using region- specific thresholds to automatically determine the extent of each VOI. VOIs were determine for the whole brain (rodent) or whole brain, striatum, thalamus, cortex, hippocampus, and cerebellum (primate). Previous data sets in the same primate were used as reference determining specific VOIs ([^{11}C]flumazenil for cortex and cerebellum, [^{11}C]DTBZ for striatum, [^{11}C]carfentenil for thalamus and hippocampus). The VOIs were then applied to the full dynamic data sets to obtain the regional tissue time-radioactivity curves. Time activity curves were normalized between studies by the animal weight and amount of activity injected to result in standardized uptake value (SUV) curves.

5. References

1. Cary, B. P.; Brooks, A. F.; Fawaz, M. V.; Drake, L. R.; Desmond, T. J.; Sherman, P.; Quesada, C. A.; Scott, P. J. H., Synthesis and Evaluation of [^{18}F]RAGER: A First Generation Small-Molecule PET Radioligand Targeting the Receptor for Advanced Glycation Endproducts. *ACS Chemical Neuroscience* **2016,** *7* (3), 391-398.
2. Albrecht, D. S.; Granziera, C.; Hooker, J. M.; Loggia, M. L., In Vivo Imaging of Human Neuroinflammation. *ACS Chemical Neuroscience* **2016**.
3. Airas, L.; Rissanen, E.; Rinne, J. O., Imaging neuroinflammation in multiple sclerosis using TSPO-PET. *Clinical and Translational Imaging* **2015,** *3* (6), 461-473.
4. Bongarzone, S.; Savickas, V.; Luzi, F.; Gee, A. D., Targeting the Receptor for Advanced Glycation Endproducts (RAGE): A Medicinal Chemistry Perspective. *Journal of Medicinal Chemistry* **2017**.
5. Xie, J.; Méndez, J. D.; Méndez-Valenzuela, V.; Aguilar-Hernández, M. M., Cellular signalling of the receptor for advanced glycation end products (RAGE). *Cellular Signalling* **2013,** *25* (11), 2185-2197.
6. Bierhaus, A.; Humpert, P.; Morcos, M.; Wendt, T.; Chavakis, T.; Arnold, B.; Stern, D.; Nawroth, P., Understanding RAGE, the receptor for advanced glycation end products. *Journal of Molecular Medicine* **2005,** *83* (11), 876-886.
7. Schmidt, A. M.; Yan, S. D.; Yan, S. F.; Stern, D. M., The multiligand receptor RAGE as a progression factor amplifying immune and inflammatory responses. *J Clin Invest* **2001,** *108* (7), 949-955.
8. Gasiorowski, K.; Brokos, B.; Echeverria, V.; Barreto, G. E.; Leszek, J., RAGE-TLR Crosstalk Sustains Chronic Inflammation in Neurodegeneration. *Mol. Neurobiol.* **2017**, Ahead of Print.
9. Byun, K.; Yoo, Y.; Son, M.; Jeong, G.-B.; Lee, J.; Park, Y. M.; Salekdeh, G. H.; Lee, B., Advanced glycation end-products produced systemically and by macrophages: A common contributor to inflammation and degenerative diseases. *Pharmacol Ther* **2017**.
10. Choi, B.-R.; Cho, W.-H.; Kim, J.; Lee, H. J.; Chung, C.; Jeon, W. K.; Han, J.-S., Increased expression of the receptor for advanced glycation end products in neurons and astrocytes in a triple transgenic mouse model of Alzheimer's disease. *Experimental & Molecular Medicine* **2014,** *46* (2), e75.
11. Jo, W. K.; Law, A. C. K.; Chung, S. K., The neglected co-star in the dementia drama: the putative roles of astrocytes in the pathogeneses of major neurocognitive disorders. *Mol Psychiatry* **2014,** *19* (2), 159-167.
12. Sasaki, N.; Toki, S.; Chowei, H.; Saito, T.; Nakano, N.; Hayashi, Y.; Takeuchi, M.; Makita, Z., Immunohistochemical distribution of the receptor for advanced glycation end products in neurons and astrocytes in Alzheimer's disease. *Brain Research* **2001,** *888* (2), 256-262.
13. Kalea, A. Z.; Schmidt, A. M.; Hudson, B. I., Alternative splicing of RAGE: roles in biology and disease. *Front. Biosci., Landmark Ed.* **2011,** *16* (7), 2756-2770.
14. Wautier, J. L.; Zoukourian, C.; Chappey, O.; Wautier, M. P.; Guillausseau, P. J.; Cao, R.; Hori, O.; Stern, D.; Schmidt, A. M., Receptor-mediated endothelial cell dysfunction in diabetic vasculopathy. Soluble receptor for advanced glycation end products blocks hyperpermeability in diabetic rats. *The Journal of Clinical Investigation* **1996,** *97* (1), 238-243.
15. Park, L.; Raman, K. G.; Lee, K. J.; Lu, Y.; Ferran Jr, L. J.; Chow, W. S.; Stern, D.; Schmidt, A. M., Suppression of accelerated diabetic atherosclerosis by the soluble receptor for advanced glycation endproducts. *Nature Medicine* **1998,** *4*, 1025.
16. Kalea, A. Z.; See, F.; Harja, E.; Arriero, M.; Schmidt, A. M.; Hudson, B. I., Alternatively Spliced RAGEv1 Inhibits Tumorigenesis through Suppression of JNK Signaling. *Cancer Research* **2010,** *70* (13), 5628-5638.
17. vTv Therapeutics to Present on Azeliragon at the 10th Clinical Trials on Alzheimer's Disease (CTAD). *Business Wire* **2017**.
18. Tekabe, Y.; Kollaros, M.; Li, C.; Zhang, G.; Schmidt, A. M.; Johnson, L., Imaging receptor for advanced glycation end product expression in mouse model of hind limb ischemia. *EJNMMI Research* **2013,** *3* (1), 37.

19. Wolf, S.; Haase-Kohn, C.; Lenk, J.; Hoppmann, S.; Bergmann, R.; Steinbach, J.; Pietzsch, J., Expression, purification and fluorine-18 radiolabeling of recombinant S100A4: a potential probe for molecular imaging of receptor for advanced glycation endproducts in vivo? *Amino Acids* **2011,** *41* (4), 809-820.
20. Konopka, C. J.; Wozniak, M.; Hedhli, J.; Ploska, A.; Schwartz-Duval, A.; Siekierzycka, A.; Pan, D.; Munirathinam, G.; Dobrucki, I. T.; Kalinowski, L., Multimodal imaging of the receptor for advanced glycation end-products with molecularly targeted nanoparticles. *Theranostics* **2018,** *8* (18), 5012.
21. Deane, R.; Singh, I.; Sagare, A. P.; Bell, R. D.; Ross, N. T.; LaRue, B.; Love, R.; Perry, S.; Paquette, N.; Deane, R. J.; Thiyagarajan, M.; Zarcone, T.; Fritz, G.; Friedman, A. E.; Miller, B. L.; Zlokovic, B. V., A multimodal RAGE-specific inhibitor reduces amyloid β–mediated brain disorder in a mouse model of Alzheimer disease. *The Journal of Clinical Investigation* **2012,** *122* (4), 1377-1392.
22. Ross, N. T.; Deane, R.; Perry, S.; Miller, B. L., Structure–activity relationships of small molecule inhibitors of RAGE-Aβ binding. *Tetrahedron* **2013,** *69* (36), 7653-7658.
23. Lue, L.-F.; Walker, D. G.; Brachova, L.; Beach, T. G.; Rogers, J.; Schmidt, A. M.; Stern, D. M.; Yan, S. D., Involvement of Microglial Receptor for Advanced Glycation Endproducts (RAGE) in Alzheimer's Disease: Identification of a Cellular Activation Mechanism. *Experimental Neurology* **2001,** *171* (1), 29-45.
24. Miller, M. C.; Tavares, R.; Johanson, C. E.; Hovanesian, V.; Donahue, J. E.; Gonzalez, L.; Silverberg, G. D.; Stopa, E. G., Hippocampal RAGE Immunoreactivity in Early and Advanced Alzheimer's Disease. *Brain research* **2008,** *1230*, 273-280.
25. Buckley, S. T.; Ehrhardt, C., The receptor for advanced glycation end products (RAGE) and the lung. *J Biomed Biotechnol* **2010,** *2010*, 917108.
26. Wager, T. T.; Hou, X.; Verhoest, P. R.; Villalobos, A., Central Nervous System Multiparameter Optimization Desirability: Application in Drug Discovery. *ACS Chemical Neuroscience* **2016**.
27. Farde, L.; Pauli, S.; Hall, H.; Eriksson, L.; Halldin, C.; Hogberg, T.; Nilsson, L.; Sjogren, I.; Stone-Elander, S., Stereoselective binding of 11C-raclopride in living human brain--a search for extrastriatal central D2-dopamine receptors by PET. *Psychopharmacology (Berl)* **1988,** *94* (4), 471-8.
28. Debruyne, D.; Abadie, P.; Barre, L.; Albessard, F.; Moulin, M.; Zarifian, E.; Baron, J. C., Plasma pharmacokinetics and metabolism of the benzodiazepine antagonist [11C]Ro 15-1788 (flumazenil) in baboon and human during positron emission tomography studies. *Eur. J. Drug Metab. Pharmacokinet.* **1991,** *16* (2), 141-52.
29. Kong, Y.; Hua, F.; Guan, Y.; Zhao, B., RAGE-specific probe 18F -FPS-ZM1 may be a promising biomarker for early detection of Diabetes with Alzheimer's disease. *Journal of Nuclear Medicine* **2016,** *57* (supplement 2), 1049.
30. Bongarzone, S.; Luzi, F.; Savickas, V.; Singh, N.; Turkheimer, F.; Gee, A. D., Development of a carbon-11 PET tracer for imaging the Receptor for Advanced GLycation Endproducts (RAGE) in Alzheimer's disease. *Journal of Labelled Compounds and Radiopharmaceuticals* **2017,** *60* (S1), 140.
31. Jockers, R.; Maurice, P.; Boutin, J. A.; Delagrange, P., Melatonin receptors, heterodimerization, signal transduction and binding sites: what's new? *British Journal of Pharmacology* **2008,** *154* (6), 1182-1195.
32. Savaskan, E.; Olivieri, G.; Meier, F.; Brydon, L.; Jockers, R.; Ravid, R.; Wirz-Justice, A.; Müller-Spahn, F., Increased melatonin 1a-receptor immunoreactivity in the hippocampus of Alzheimer's disease patients. *Journal of Pineal Research* **2002,** *32* (1), 59-62.
33. Megwalu, U. C.; Finnell, J. E.; Piccirillo, J. F., The Effects of Melatonin on Tinnitus and Sleep. *Otolaryngology - Head and Neck Surgery* **2006,** *134* (2), 210-213.
34. Jules, J.; Maiguel, D.; Hudson, B. I., Alternative splicing of the RAGE cytoplasmic domain regulates cell signaling and function. *PLoS One* **2013,** *8* (11), e78267.
35. Manigrasso, M. B.; Pan, J.; Rai, V.; Zhang, J.; Reverdatto, S.; Quadri, N.; DeVita, R. J.; Ramasamy, R.; Shekhtman, A.; Schmidt, A. M., Small Molecule Inhibition of Ligand-Stimulated RAGE-DIAPH1 Signal Transduction. *Sci. Rep.* **2016,** *6*, 22450.

36. Kabalka, G. W.; Mereddy, A. R., Microwave promoted synthesis of functionalized 2-aminothiazoles. *Tetrahedron Letters* **2006,** *47* (29), 5171-5172.
37. Mossine, A. V.; Brooks, A. F.; Makaravage, K. J.; Miller, J. M.; Ichiishi, N.; Sanford, M. S.; Scott, P. J. H., Synthesis of [^{18}F]Arenes via the Copper-Mediated [^{18}F]Fluorination of Boronic Acids. *Organic Letters* **2015,** *17* (23), 5780-5783.
38. Makaravage, K. J.; Brooks, A. F.; Mossine, A. V.; Sanford, M. S.; Scott, P. J. H., Copper-Mediated Radiofluorination of Arylstannanes with [^{18}F]KF. *Org. Lett.* **2016,** *18* (20), 5440-5443.

CHAPTER 6
Investigation into RAGE as a Neuroinflammatory Biomarker

After our efforts to develop small molecule radioligands to use as molecular probes in the study of RAGE biology, we decided to focus on more biological techniques because the small molecule's behavior *in vivo* was not selective enough. In order to optimize these RAGE ligands, we needed to understand how RAGE is involved in neuroinflammation. We decided to evaluate RAGE in the widely used animal model of lipopolysaccharide (LPS) induced inflammation. If this model shows increased RAGE activity, it could be further used for ligand optimization.

1. Introduction

The receptor for advanced glycation end-products (RAGE) was isolated and characterized in the early 1990's by researchers focused on vascular dysfunction. Schmidt and coworkers described the receptor based on its first recognized ligands, advanced glycation end-products (AGEs).[1] AGEs are non-enzymatically glycated macromolecules such as proteins, peptides, DNA, lipids, and etc. These modifications occur in oxidative environments in the presence of glucose, which provides a logical explanation for this receptor's involvement in diabetes and related neuropathy.[2] The isolated gene contained three putative binding sites for nuclear factor kappa-light-chain-enhancer of activated B cells (NF-κB), a transcription factor well known for its pro-inflammatory nature. After cellular experiments using both endothelial and smooth muscle cells with lipopolysaccharide (LPS) stimulation, NF-κB binding sites were confirmed and it was also discovered that the *RAGE* gene itself is regulated by NF-κB.[3] Ligand binding and transcriptional activation increases the expression of RAGE, and thus the cell's

sensitivity to other ligands in the extracellular environment. This positive feedback loop has been confirmed in other studies along with a variety of other ligands including amyloid-beta (Aβ) peptide.[3]

The involvement of RAGE in Alzheimer's disease (AD) has been attributed to the fact Aβ is a ligand for RAGE signaling.[4-5] It was claimed that RAGE mediates the interaction between Aβ and neuronal cells, resulting in oxidative stress.[4] Experimentally, ^{125}I-labelled Aβ peptide was shown to generate thiobarbituric acid reactive substances (TBARS), and this effect was not dependent on apolipoproteins; ApoE is known to bind Aβ peptide and was expected to have an effect on the binding to endothelial cells. Aβ binding proteins were identified from a pull down assay;[4] however, this assay was performed in bovine lung. The authors claimed to use this tissue because it is an endothelial-cell rich, and plentiful in comparison to human brain tissue. The protein found from this experiment was bovine RAGE; the experiment was repeated in human brain homogenates and confirmed RAGE as a significant binding partner.[4] In 1996, this was an exciting discovery in regards to the possible mechanism of action of Aβ peptide's neurotoxicity and gave support to the budding neuroinflammatory hypothesis. Soon after, it was found that RAGE bound and internalized ^{125}I-labelled Aβ peptide in a time and temperature dependent manner, partially sensitive to anti-RAGE blockade.[5] Combined, this body of work indicated a role for RAGE in neuroinflammation as two-fold: 1) Aβ peptide ligand binding promotes NF-κB transcription and proinflammatory signals and 2) RAGE can internalize Aβ peptide and thus prevent clearing it from the CNS.

These claims were supported by thoughtful experiments; however, the claims rely entirely on the experimental choice to use bovine lung tissue in the preliminary Aβ peptide pull-down assay.[4] Although the reasoning was explained to be entirely rooted in the availability of the

tissue type and because it is easier work with (lipids in brain tissue were challenging to work around), the choice could possibly have influenced the results. The same group isolated and characterized RAGE in bovine lung tissue in 1992 based on identifying proteins that bind advanced glycation end-products.[6-7] Transcytosis of Aβ peptide being time and temperature dependent are classic signs of a transporter-like process; however, blocking the RAGE binding site with excess antibody only prevented 36% of internalization.[5] Internalization of Aβ requires RAGE expression on the apical side of the blood-brain barrier endothelial cells; however, RAGE expression has been evaluated in astrocytes, microglia, and neurons as well.[8] The real interest with RAGE as a neuroinflammatory biomarker relies on its presence in the hippocampus- an area identified by amyloid PET scanning to be involved with the earlier deposition of Aβ plaques.[9] The earliest sites of brain atrophy are the medial temporal lobe, this study suggested that atrophy in the hippocampus occurs preferentially with Aβ plaque accumulation.[9] Increased immunoreactivity in hippocampal neurons of AD brains sections have supported the theory of RAGE's involvement in Aβ accumulation.[8, 10]

In the classic LPS model of neuroinflammation, RAGE has been shown to be increased modestly in male mice and rats. LPS has long been used to induce peripheral inflammation, it is a known toll-like receptor 4 (TLR4) ligand. It has been previously demonstrated that relatively low doses, 5 mg/kg, given i.p can cause chronic neuroinflammation up to 10 months post induction; this experiment in particular followed TNFα, MCP-1, IL-1β, and NF-κB p65 expression in wild-type mice.[11] Male C57BL/6 J mice, which received 0.3 mg/kg doses of LPS by i.p injections, demonstrated a ~2 fold increase in normalized RAGE abundance after 1 day.[12] A study using Wistar rats (5 mg/kg LPS, i.p) also found increases in RAGE levels in the prefrontal cortex (~3 fold), cerebellum (~2 fold), and substantia nigra (SN: ~1.5 fold) compared

to vehicle control.[13] The highest region of expression was the SN, and RAGE was found to be co-localized with tyrosine hydroxylase (a marker of dopaminergic neurons). Interestingly, no difference was found in the hippocampus- the region suggested by human immunohistochemistry (IHC) to be a region of high RAGE expression. Furthermore, the IHC analysis showed that in all brain structures, the cell site of RAGE expression had changed from endothelial-like structures to neuronal cells.[13]

The goal of this chapter, and to close the RAGE project, was to confirm if RAGE is a neuroinflammation biomarker by utilizing LPS induction in mice. We have chosen to follow this experimental model[11] using the same wild type strain of mice and LPS dose; however, our time points are only 1 day and 14 days. Another important difference in our study compared to the literature is that we use of both male and female mice. Despite the literature precedent for only using male mice, there is no documented explanation for this choice. Our hypothesis consisted of the simple principle, if RAGE is a sensitive biomarker, then abundance changes will be evident at 1 day and increase 14 days in both sexes, in a similar manner to the other NF-κB transcribed genes: IL-1β and TNFα. Furthermore, we aimed to evaluate the selectivity of small molecule radioligands by performing autoradiography in this mouse brain tissue. The tissue binding studies should correspond to the immunoreactivity observed, assuming the small molecule ligands are selective and specific for RAGE.

2. Results

Establishing the Model

The mortality rate for this study was 0%; every individual survived the duration of the study. There was no significant change in weight/ alertness score during the 14 day LPS

induction (figure 6.1). Based on the dosage used, 5 mg/kg, and utilizing intraperitoneal injection, mortality was not considered a high risk.

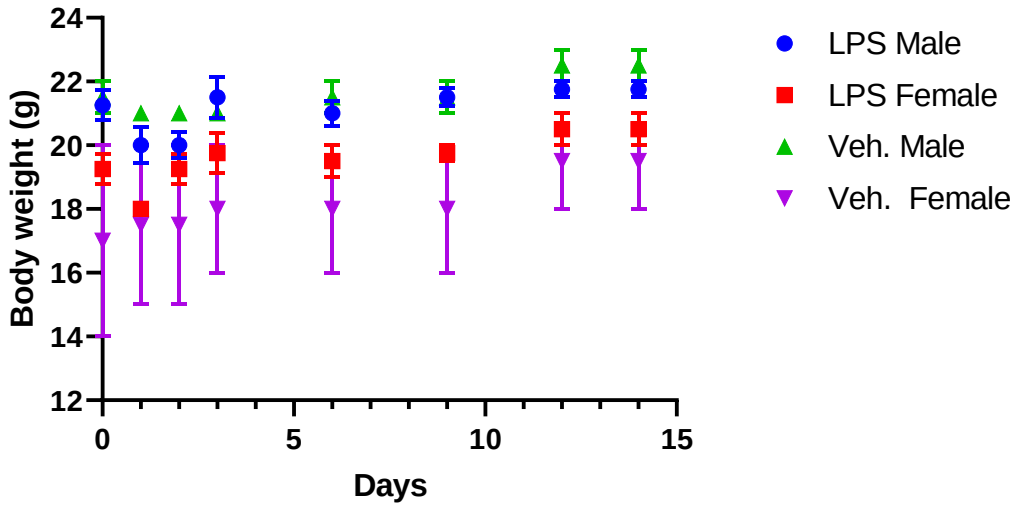

Figure 6.1 Body weight changes over time in 14 day cohorts. Not shown: body score description did not change over the course of the experiment. The mean body weight of males did not statistically differ. There is a significant difference between mean body weight in females, due to one individual mouse beginning at 14g. At the day of sacrifice, there was no significant difference in body weight between the female LPS and female vehicle groups.

Immunohistochemistry of the known biomarkers confirmed the induction of neuroinflammation in all of the experimental cohorts (figure 6.2). Males exhibited significantly higher levels of IL-1β (1.5-10 fold) and TNFα (10-20 fold) in both the experimental cohorts. Although lower in abundance, the female cohorts also demonstrated a significant increase in both known biomarkers at 24 hour and 14 days compared to vehicle control.

RAGE immunoreactivity

RAGE abundance increased in the male experimental cohorts only, not in the female cohorts. The increase, approximately 2.5 fold, was statistically significant (figure 6.2). The magnitude of change in RAGE abundance does not change between 1 day and 14 days, unlike the known biomarkers of this model TNFα and IL-1β.

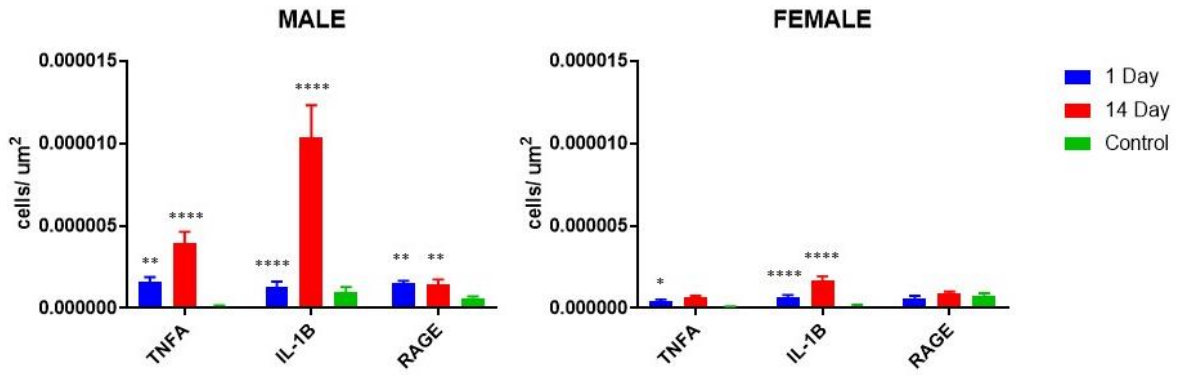

Figure 6.2. Immunoreactivity of Inflammatory Biomarkers. TNFα and IL-1β immunoreactivity were compared for both sexes at 1 day and 14 day post LPS induction. Tukey's multiple comparison test was used to evaluate the mean values. Bars show mean ± standard error of the mean; * p< 0.05, ** p< 0.01, *** p< 0.001.

Autoradiography with [^{3}H]RAGE ligands

Binding studies were performed on frozen tissue with three ligands for the extracellular domain of RAGE (figure 6.3). [^{3}H]RAGER, based on [^{3}H]FPS-ZM1, are both previously characterized for their binding to RAGE, with [^{3}H]RAGER experimentally calculated K_d= 15 nM. [^{3}H]azeliragon (TTP-488) is not well documented for its binding properties and thus, we attempted to determine the K_d and B_{max} on rat brain tissue before using the experimental LPS mouse tissue. Unfortunately on rat brain tissue, the exact K_d and B_{max} could not be determined based on concentration range limitations. It was assumed the K_d for [^{3}H]azeliragon on tissue was greater than 150 nM. Binding assays were performed at 1 nM of [^{3}H]ligand, below K_d for each ligand. Total binding and nonspecific binding were determined experimentally and specific binding was calculated as the difference (figure 6.4).

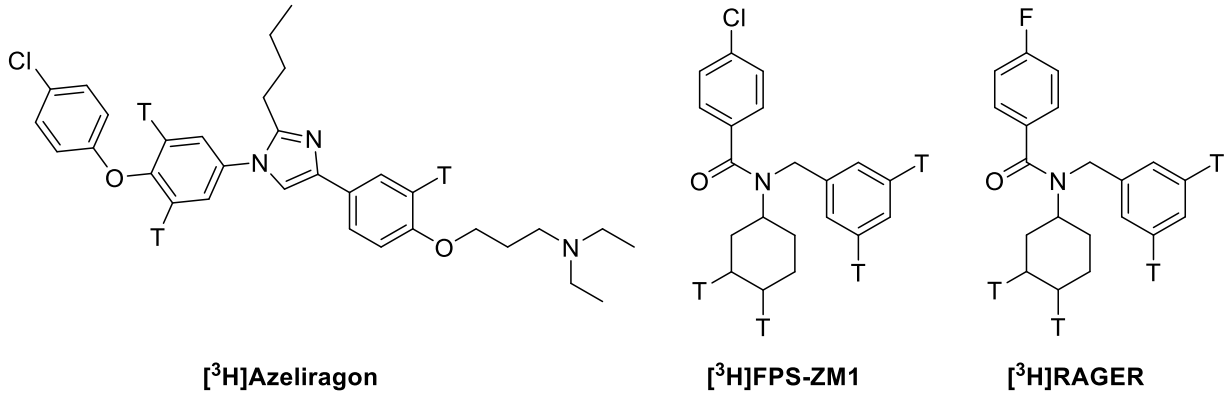

Figure 6.3.RAGE Ligands. Radioligands provided by Marc Skadden at Abbvie.

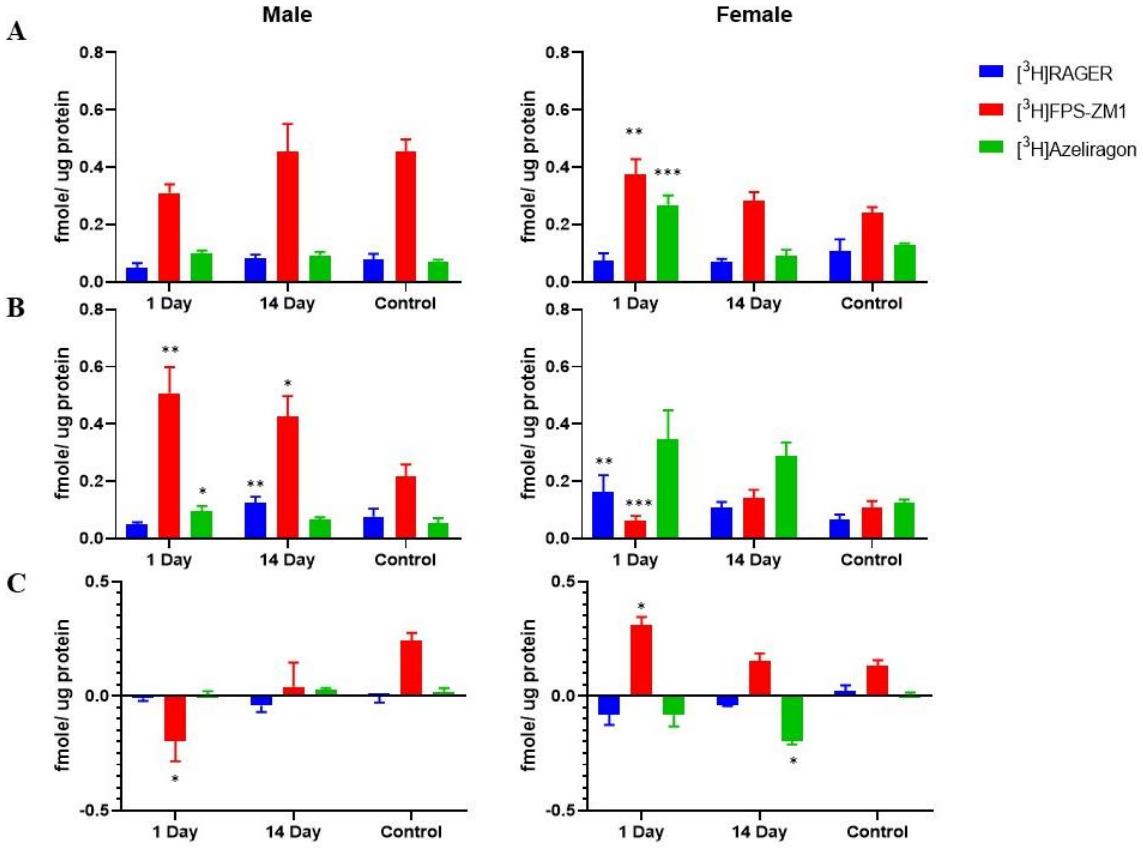

Figure 6.4. Autoradiography Summary. *In vitro* binding studies (4 tissue sections/ animal) were performed to evaluate A) total binding, B) nonspecific binding, and to determine C) specific binding of three RAGE ligands. Tukey's multiple comparison test was used to evaluate the mean values. Bars show mean ± standard error of the mean; * $p< 0.05$, ** $p< 0.01$, *** $p< 0.001$.

RAGE immunoreactivity of the mouse brain tissue suggested there should only be an observable change in RAGE binding in the male cohorts. Total binding (figure 6.4A) of the [^{3}H]RAGE ligands did not differ significantly in the male and female cohorts in either time point

versus vehicle control. However, there was an increase in nonspecific binding (figure 6.4B) in the 1 day female cohort and 14 day male cohort ($p= 0.0015$, $p= 0.0058$). Nonspecific binding refers to the so called off-target, or nondisplaceable binding of this radioligand. It could be relating to a difference in white matter, or unidentified off-target binding partner in the tissue. Calculating the specific binding from subtracting nonspecific from total (figure 6.4C) for [^{3}H]RAGER reveals no significant differences across the groups.

The structurally related compound [^{3}H]FPS-ZM1 also didn't contain differences in total binding the male cohorts. Though, there was a significant increase in [^{3}H]FPS-ZM1 total binding in the female 1 day cohort over vehicle control ($p= 0.0126$). [^{3}H]FPS-ZM1 nonspecific binding was increased in the 1 day and 14 day male cohorts ($p= 0.0026$, $p= 0.035$); however, it was decreased in the 1 day female cohort ($p< 0.0001$). It is very interesting to observe a decrease in NSB in this female cohort, while in the [^{3}H]FPS-ZM1 total binding of the same cohort there was an increase. Calculating the specific binding from subtracting nonspecific from total (figure 6.4C) still reveals a significant increase in the 1 day female cohort [^{3}H]FPS-ZM1 binding over control ($p= 0.0253$). The [^{3}H]FPS-ZM1 specific binding in the 1 day male group was determined to be negative; a phenomenon which highlights an impracticality of this measurement. The nonspecific binding being increased, and higher than total binding, results in the perceived "negative" specific binding being significantly lower than vehicle control ($p=0.0260$).

[^{3}H]Azeliragon total binding was also increased in the female 1 day cohort ($p= 0.0003$). However, the large variation in nonspecific binding did not show significance against the vehicle control in females. The 1 day male cohort had a small increase in nonspecific binding ($p= 0.0337$); however, there was no detected difference in specific binding in the male groups. The

[^{3}H]azeliragon specific binding in females was determined to be significantly lower in the 14 day cohort to control ($p= 0.0083$).

3. Discussion

RAGE immunoreactivity of the mouse brain sections indicate that RAGE is not a sensitive biomarker of neuroinflammation in the murine LPS model. Unlike the known biomarkers IL-1β and TNFα, the change in RAGE expression did not continue to increase over time (figure 6.2). The documented effects of the LPS model indicate measurable changes in inflammatory biomarkers up to ten months after induction, with continuous increase in certain biomarkers.[11] An increase was only measurable in the male cohorts; there are no previously identified sex differences in RAGE brain expression. Male mice are almost exclusively used for the LPS induced neuroinflammation because of the proposed protective effects of estrogen. A compelling investigation into these differences in the inhaled LPS model of the lung-bone inflammatory responsive confirmed these differences.[14] LPS exposure in male mice, and ovarectomized female mice, lead to bone quality deterioration on the measures of bone mineral density and ratio of bone volume/ tissue volume. Control female mice did not have bone deterioration. Furthermore, estradiol supplementation of ovarectomized female mice and males protected against bone deterioration. There has not been a similar study involving the protective effect of estradiol against neuroinflammation, to my knowledge.

The hypothesis for this work stated that RAGE should be increased in both sexes; as the overall goal of the project is to develop a radioligand for PET imaging neuroinflammation in AD patients- and two-thirds of AD patients are female.[15] While the work surrounding estradiol and estrogen as having protective effects is compelling, we don't believe this translates to human disease in the case of neuroinflammation. If the majority of patients are female, it is appropriate

to utilize female animals in models of disease precisely because of the sex differences. Developing a radioligand for RAGE based on the LPS model would not be apt based on these findings because RAGE levels are not increased in female mouse brain.

The secondary evaluation of RAGE ligands for their selectivity and specificity in this tissue must be evaluated in the light that the female brain tissue has no change in RAGE abundance, and the male cohorts' change is small. The observed changes in the female cohorts' total, nonspecific, and specific binding strongly indicates the lack of specificity amongst these radioligands (figure 6.4).

However, there are significant differences between fixed and frozen tissue, used for immunohistochemistry and autoradiography respectively. Fixed tissue has been washed repeatedly and many soluble factors native to live tissue have been removed. Being that RAGE has a significant soluble splice-isoform, it is possible that the fixed tissue used for immunohistochemistry does not include count of this soluble factor. Fresh frozen tissue, however, could still contain this isoform as it has been treated with fewer and less harsh conditions. This could show a difference between ligand binding and immunoreactivity. Though, one would expect this phenomenon to be observed in both the male and female brain sections.

Another curiosity concerning this data set is the differing magnitudes of binding of the ligands. [^{3}H]RAGER and [^{3}H]azeliragon seem to be binding to the same degree in both male and female cohorts (figure 6.4A), despite the lower K_d of [^{3}H]RAGER. [^{3}H]FPS-ZM1, however, very structurally similar to [^{3}H]RAGER, is nearly 4 fold higher in total binding. In nonspecific binding, this trend is only true for the male cohorts while unexpectedly [^{3}H]azeliragon increases greatly.

The differences in nonspecific binding, in particular the increases over total binding, were expected with [^{3}H]RAGER based on previous experience with [^{18}F]RAGER.[16] On human tissue, we observed higher nonspecific binding than total binding on white matter. The cause of nonspecific binding was never identified (see chapter 5), and it was also suspected to be a physiochemical effect associated with logP. Excess cold mass falling out of solution, with the radioligand, and not being removed through washes of the tissue. These effects could be at play with these [^{3}H]RAGE ligands; however, like the previous discussion about sRAGE, it would be expected that this phenomenon would affect all groups equally.

4. Conclusion

Overall this work argues that while small increases in RAGE were observed in males, it is not a sensitive or appropriate biomarker of neuroinflammation in the LPS murine model. Future evaluation of RAGE and its role in neuroinflammation should be performed in alternative animal models or strictly using human tissue. The RAGE ligands: FPS-ZM1, RAGER, and azeliragon, do not show appear to show specificity or selectivity to RAGE as measured by autoradiography on mouse tissue but any small change in RAGE expression could be masked by very high nonspecific binding. Further optimization of RAGE ligands is recommended before clinical translation, particularly to ensure specific adequate binding.

5. Methods

LPS Model

Normal black mice (C57Bl/6J) were divided into experimental and vehicle control cohorts. Experimental cohorts were divided by sex (n=8/ each) into time groups (n=4/ each) for either 24 hour or 14 day induction. Vehicle control cohorts were divided by gender (n=4/ each) and time (n=2/ each) for the same time points. Experimental cohorts received 5 mg/kg LPS (from

Escherichia coli O111:B4) in saline intraperitoneally. Weight and body score description was monitored in the 14 day cohort approximately every 3 days. Sacrifice was performed by cervical ligation and brain removal; brains were immediately sectioned on the sagittal plane and flash frozen in dry ice. Sections were stored at -80 °C until further use.

Tissue Preparation

Half of the brain sections were cut using a microtome to 20 µm sections and thaw-mounted onto poly-lysine coated glass slides. Slides utilized for immunohistochemistry were fixed in Davidson's fixative (8.1% formaldehyde, 33.3% ethanol, 11.1% acetic acid, Eosin Y stain) for 24 hours and then rinsed with 70% ethanol to remove residual formaldehyde before use. Slides utilized for autoradiography were stored at -80 °C until the day of experiment. The corresponding halves of brain sections were grouped by cohort and homogenized together in 1X PBS (7.4). Homogenized solutions were utilized for scintillation proximity assay experiments on the same day as homogenization in order to limit the influence of freeze/ thaw cycles.

Immunohistochemistry

Fixed tissue sections were incubated in phosphate buffer saline (PBS) with 1% SDS for 5 min. Sections were then washed 3 x 5 min in PBS before quenching in 70% methanol with 0.3% hydrogen peroxide for 15 min. All slides were washed 3 x 5 min in PBS-T (PBS, 0.4% Triton-X-100, pH 7.4) and blocked for 30 min with PBS-TBA (PBS, 0.4% Triton-X-100, 1% BSA, 0.025% sodium azide, pH 7.4) before incubating in a 1:200 dilution of primary antibody (anti-IL-1β, Fisher (AF401NA), anti-TNFα, Fisher (PIPA546945), or anti-RAGE, Fisher, (NBP242913)) in PBS-TBA overnight. Finally, brain sections were washed 3 x 5 minutes in PBS-T to remove unbound antibody. Tissue sections were incubated in a 1:200 dilution of secondary antibody (anti-goat-IgG, Vector Laboratories BA-5000, anti-rabbit-IgG, Vector

Laboratories BA-1000) in PBS-TBA for 2 hr and washed 3 x 5 min with PBS-T. All incubations were carried out at room temperature. Slides were developed as instructed using the VECTASTAIN Elite ABC Kit (Standard) (Vector Laboratories PK-6100). Tissue sections were then washed 3 x 5 min in PBS-T before incubating for 4 min in a 0.5% w/v solution of diaminobenzidine in PBS-T (filtered) with 0.001% hydrogen peroxide. Giemsa counterstaining was utilized to visualize nucleus and cytoplasm in cells. Tissue sections were washed for 5 min in dH_2O prior to overnight incubation in a 1:50 solution of Giemsa in dH_2O. Slides were then rinsed for 30 sec in dH_2O, 2 x 4 min in n-butanol, and 1 min in xylene. Permount was applied to the fixed tissue to attach coverslips to the polylysine-coated glass slides and allowed to set for 45 min prior to quantification. All incubations were carried out at room temperature.

Four tissue sections from each animal (2 sections/ slide) were used for each primary antibody and counted. Immunoreactivity was quantified using StereoInvestigator. A region was drawn around the entire tissue section and using the serial section manager, 5% of the section was counted and picked using a randomized rotation. Immunoreactivity is presented as cells/ μm^2. Statistical analyses were performed in GraphPad Prism (8.01).

Autoradiography

Brain sections on slides were removed from -80°C freezer and thawed at room temperature for 5 min before rehydration in PBS (pH 7.4) for another 5 min. Then, brain sections were incubated with a range of concentrations of tritiated ligands and unlabeled ligands ([^{3}H]RAGER, [^{3}H]FPS-ZM1, or [^{3}H]azeliragon). Incubation times were determined by equilibrium experiments; 30 minute incubations were used for [^{3}H]RAGER and [^{3}H]FPS-ZM1, 60 minutes for [^{3}H]azeliragon at room temperature. All sections were washed 3 x 2 min with PBS at 4 °C and then rinsed in dH_2O for 30 sec at 4 °C to remove unbound radioactivity. Finally,

slides were dried under the continuous airflow for 30 min before exposure to a high-resolution phosphoimaging plate for 2 weeks. The exposed plate was scanned using a GE Typhoon FLA 7000 phosphoimager. Image analysis was performed using ImageQuant (Molecular Dynamics) software. Regions of interest were drawn and converted to DPM/ μg protein using the Amersham standards, and then using the individual ligand's specific molar activity converted to nmole/ μg protein.

6. References

1. Brett, J.; Schmidt, A. M.; Du Yan, S.; Zou, Y. S.; Weidman, E.; Pinsky, D.; Nowygrod, R.; Neeper, M.; Przysiecki, C.; Shaw, A., Survey of the distribution of a newly characterized receptor for advanced glycation end products in tissues. *The American journal of pathology* **1993,** *143* (6), 1699.
2. Bongarzone, S.; Savickas, V.; Luzi, F.; Gee, A. D., Targeting the Receptor for Advanced Glycation Endproducts (RAGE): A Medicinal Chemistry Perspective. *Journal of Medicinal Chemistry* **2017**.
3. Li, J.; Schmidt, A. M., Characterization and functional analysis of the promoter of RAGE, the receptor for advanced glycation end products. *Journal of Biological Chemistry* **1997,** *272* (26), 16498-16506.
4. Yan, S. D.; Chen, X.; Fu, J.; Chen, M.; Zhu, H.; Roher, A.; Slattery, T.; Zhao, L.; Nagashima, M.; Morser, J.; Migheli, A.; Nawroth, P.; Stern, D.; Schmidt, A. M., RAGE and amyloid-[beta] peptide neurotoxicity in Alzheimer's disease. *Nature* **1996,** *382* (6593), 685-691.
5. Mackic, J. B.; Stins, M.; McComb, J. G.; Calero, M.; Ghiso, J.; Kim, K. S.; Yan, S. D.; Stern, D.; Schmidt, A. M.; Frangione, B.; Zlokovic, B. V., Human blood-brain barrier receptors for Alzheimer's amyloid-beta 1- 40. Asymmetrical binding, endocytosis, and transcytosis at the apical side of brain microvascular endothelial cell monolayer. *Journal of Clinical Investigation* **1998,** *102* (4), 734-743.
6. Schmidt, A. M.; Vianna, M.; Gerlach, M.; Brett, J.; Ryan, J.; Kao, J.; Esposito, C.; Hegarty, H.; Hurley, W.; Clauss, M., Isolation and characterization of two binding proteins for advanced glycosylation end products from bovine lung which are present on the endothelial cell surface. *Journal of Biological Chemistry* **1992,** *267* (21), 14987-97.
7. Neeper, M.; Schmidt, A. M.; Brett, J.; Yan, S. D.; Wang, F.; Pan, Y. C.; Elliston, K.; Stern, D.; Shaw, A., Cloning and expression of a cell surface receptor for advanced glycosylation end products of proteins. *Journal of Biological Chemistry* **1992,** *267* (21), 14998-5004.
8. Miller, M. C.; Tavares, R.; Johanson, C. E.; Hovanesian, V.; Donahue, J. E.; Gonzalez, L.; Silverberg, G. D.; Stopa, E. G., Hippocampal RAGE Immunoreactivity in Early and Advanced Alzheimer's Disease. *Brain research* **2008,** *1230*, 273-280.
9. Hsu, P. J.; Shou, H.; Benzinger, T.; Marcus, D.; Durbin, T.; Morris, J. C.; Sheline, Y. I., Amyloid Burden in Cognitively Normal Elderly is Associated with Preferential Hippocampal Subfield Volume Loss. *J. Alzheimer's Dis.* **2015,** *45* (1), 27-33.
10. Lue, L.-F.; Walker, D. G.; Brachova, L.; Beach, T. G.; Rogers, J.; Schmidt, A. M.; Stern, D. M.; Yan, S. D., Involvement of Microglial Receptor for Advanced Glycation Endproducts (RAGE) in Alzheimer's Disease: Identification of a Cellular Activation Mechanism. *Experimental Neurology* **2001,** *171* (1), 29-45.
11. Qin, L.; Wu, X.; Block, M. L.; Liu, Y.; Breese, G. R.; Hong, J.-S.; Knapp, D. J.; Crews, F. T., Systemic LPS causes chronic neuroinflammation and progressive neurodegeneration. *Glia* **2007,** *55* (5), 453-462.
12. Liu, L.; Zhao, Z.; Lu, L.; Liu, J.; Sun, J.; Wu, X.; Dong, J., Icariin and icaritin ameliorated hippocampus neuroinflammation via inhibiting HMGB1-related pro-inflammatory signals in lipopolysaccharide-induced inflammation model in C57BL/6 J mice. *International Immunopharmacology* **2019,** *68*, 95-105.
13. Gasparotto, J.; Ribeiro, C. T.; da Rosa-Silva, H. T.; Bortolin, R. C.; Rabelo, T. K.; Peixoto, D. O.; Moreira, J. C. F.; Gelain, D. P., Systemic Inflammation Changes the Site of RAGE Expression from Endothelial Cells to Neurons in Different Brain Areas. *Molecular Neurobiology* **2018**.
14. Nelson, A. J.; Roy, S. K.; Warren, K.; Janike, K.; Thiele, G. M.; Mikuls, T. R.; Romberger, D. J.; Wang, D.; Swanson, B.; Poole, J. A., Sex differences impact the lung-bone inflammatory response to repetitive inhalant lipopolysaccharide exposures in mice. *J. Immunotoxicol.* **2018,** *15* (1), 73-81.
15. Gaugler, J.; James, B.; Johnson, T.; Marin, A.; Weuve, J. Alzheimer's Disease Facts and Figures. https://www.alz.org/media/HomeOffice/Facts%20and%20Figures/facts-and-figures.pdf.

16. Cary, B. P.; Brooks, A. F.; Fawaz, M. V.; Drake, L. R.; Desmond, T. J.; Sherman, P.; Quesada, C. A.; Scott, P. J. H., Synthesis and Evaluation of [^{18}F]RAGER: A First Generation Small-Molecule PET Radioligand Targeting the Receptor for Advanced Glycation Endproducts. *ACS Chemical Neuroscience* **2016,** *7* (3), 391-398.

CHAPTER 7
Conclusions & Future Directions

"I never look back, darling! It distracts from the *now*." – Edna Mode, *The Incredibles*

1. Overall Conclusions

The number of individuals with neurodegenerative disorders, particularly Alzheimer's disease (AD), is growing and is projected to continue increasing.[1] Despite this reality, there are no available treatments for AD.[2] Positron emission tomography (PET) imaging has been a valuable tool in this drug discovery and development process, and has been used to advance pathological research of AD. PET imaging strategies in AD have followed the biomarkers used in the drug discovery pipeline, with an early focus on amyloid-β (Aβ)[3] and tau neurofibrillary tangles (NFTs), neurotransmitter systems, and neuroinflammation.[4] The focus of this thesis has been on using PET imaging to investigate AD pathology, and research projects have bridged bench to bedside. Firstly, the tau ligand [^{18}F]AV-1451, that is routinely employed for clinical tau PET scans in our PET center, was investigated for its off-target binding effects to monoamine oxidase (MAO). Secondly, MAO is a marker of microgliosis, the activation of microglia, and we considered to use it as a biomarker for PET imaging neuroinflammation. We developed substrates for imaging MAO-B activity, using a trapped metabolite approach.[5] Inspired by this principle, we used an MAO substrate, [^{11}C]AZ to demonstrate that it would be possible to use an enzyme substrate for dual PET-magnetic resonance (MR) imaging. PET-MR with a single agent was typically considered impossible because PET imaging would not work at the high mass (low specific activity) generally required for PET imaging. We demonstrated that MAO was not saturable *in vivo* at the necessary MR concentration, and that PET scans could be acquired with

no detriment to signal quantification.[6] Lastly, we evaluated ligands for a new biomarker of neuroinflammation, the receptor for advanced glycation end-products (RAGE), using an extracellular[7] and intracellular approach. We evaluated RAGE as a biomarker using the standard lipopolysaccharide (LPS) murine model of neuroinflammation. We found 2 fold increases in male mouse brain, consistent with literature;[8] however, no significant change in female mouse brain. Given the small changes in RAGE expression and the pronounced sex difference in rodent, we recommend that this model not be used in the future to evaluate or optimize new RAGE ligands.

This body of work has made progress in the field of AD research, with particular focus toward investigating MAO and RAGE as suitable neuroinflammatory biomarkers. Despite this progress, many questions remain. In the subsequent sections, ideas for future steps are outlined for each chapter.

2. Monoamine Oxidase as an Off-Target of [^{18}F]AV-1451

In summary, we confirmed that AV-1451 is an inhibitor of monoamine oxidase (MAO) activity through the *in vitro* assay we had previously developed.[5] We demonstrated that [^{18}F]AV-1451 binding on tissue can be displaced with MAO inhibitors, and that total [^{18}F]AV-1451 binding correlates positively to MAO-B immunoreactivity in human, diseased substantia nigra tissue. Using mature, female rhesus macaques, we showed that pretreatment with an MAO inhibitor changed the equilibrium binding in various brain regions, including in the cerebellum (the reference region). The combined results suggest that MAO is playing a role in human [^{18}F]AV-1451 PET imaging and that a prospective clinical trial investigating this issue in human tau PET is worth performing.

The eventual goal of this work was to demonstrate preclinical proof of concept to justify a clinical trial. This trial would recruit MAO inhibitor (MAO-I) naïve patients and have them undergo a baseline [^{18}F]AV-1451 PET scan and a second scan following pretreatment with a low dose of deprenyl 1 hour before. Standard uptake value ratio (SUVR) is a measure can often underestimate the effect of off-target binding, and as such it would be ideal to do dynamic scanning in these patients. Though this is not always appropriate in patient populations because dynamic scans require the individual to stay in the PET scanner for nearly two hours, it is still possible. It would also, ideally, include arterial blood sampling- a process that is uncomfortable and invasive to the patient, but which is essential for understanding subtle changes that might stem from MAO inhibition.

It is worth considering, before undertaking such a clinical trial, what the impact might be on the field. Off-target binding to MAO has been known (but not necessarily accepted) by the community since 2012; however, this has not really affected the use of [^{18}F]AV-1451. With the development of [^{18}F]MK-6240, which in some accounts appears to be a better tracer due to its higher overall signal. We would predict that [^{18}F]AV-1415 scans will become less widely used in the next five years. Realistically speaking, after 6 months to a year (the time required to conduct such a clinical trial), this information might not be able to impact how tau PET is conducted.

3. Trapped Metabolite PET Imaging of MAO-B

MAO-B is an incredibly well characterized enzyme, and yet there is still debate over how substrates are oxidized. In a small way, this work contributed to the discussion over this *in vivo* enzymatic mechanism. We developed an assay using human MAO supersomes and a fluorogenic substrate to evaluate the kinetic isotope effect (KIE) from deuterium substitution. The *in vitro* assay predicted no observable change in turnover; which was confirmed *in vivo* using PET

imaging. The basis for the expected KIE was rooted in the hydrogen abstraction (HAT) mechanism and oxidation being the rate limiting step in the mechanism. Our results indicate that for this substrate, either HAT is not the mechanism experienced or other steps are partially rate limiting and mask the expected KIE.[5] The next step for the [^{11}C]Cou project would be clinical translation. Arterial blood sampling during the PET scan would allow for kinetic modeling. It is possible that with input function correction, this radiotracer is better behaved than assumed in nonhuman primate brain with no input function.

4. Monoamine Oxidase: Dual PET-MR Imaging

This study served as a proof of concept for using one agent for both detection by PET and MRS. The feasibility was proven in our rodent studies showing no change in the time activity curves of [^{11}C]PMP and [^{11}C]AZ at high and low specific activity.[6] The obvious next step for this project would be to acquire an MR scan using our AZ substrate; however, our lab does not have a small animal MR and so we are setting up a collaboration with Joan Greve's MR laboratory in Biomedical Engineering to conduct this work. Furthermore, before using AZ as a PET-MR agent in the clinic, a toxicity study would need to be performed. In order to use the high mass of compound necessary for MR, a toxicity study is necessary. This project is a proof of concept and is not intended to sell [^{11}C]AZ as a good MAO dual PET-MR tracer for clinical imaging, but instead serve as an example for future dual imaging strategies.

5. Imaging the receptor for advanced glycation end-products

5.1 Intracellular

Small molecule inhibitors of RAGE were not discovered until high throughput screening, also performed by the Schmidt group, discovered FPS-ZM1.[9] This hit compound was validated as a RAGE-Aβ peptide inhibitor *in vitro*, and showed decreased Aβ fibril accumulation in an AD

mouse model. Independently, FPS-ZM1 has been used as an inhibitor and shown to reduce AGE-induced oxidative stress in primary microglia.[10] Despite this hit compound never being optimized after a structure-activity relationship study revealed flat SAR,[11] this compound is cited in six separate patents for various use in chronic obstructive pulmonary disease (COPD),[12] cachexia,[13-14] AD,[15-16] and renal failure.[17]

In chapter 5, the RAGE project focused on the development of radioligands for the extracellular and (to a lesser extent) intracellular domains of RAGE. The original proposal for this project, as outlined in my candidacy document, was to synthesize a small library of RAGER analogues with the goal of improving specific binding (retention of radioligand) *in vivo*. FPS-ZM1 was always a hit compound, not a lead, and we aimed to do some hit optimization for the purpose of radioligand development. However, as the evaluation of [^{18}F]RAGER progressed, and nonspecific binding became an inescapable issue, the analogue side of this project was put on hold in order to better understand the basic biology of RAGE as an imaging biomarker. The details of the proposed experiments, as well as the progress made, will be described in the following sections.

A direct binding assay using surface plasmon resonance (SPR) was proposed to evaluate the RAGER analogue library. Assay development required the overexpression and purification of RAGE-VC1 domains, condition optimization, and positive controls (known RAGE-VC1 ligand S100A had been selected for this). The RAGE-VC1 with 6xHis tag was gifted to me by Dr Laure Yatime; the crystallographer responsible for proposing a dimer structure for these domains (figure 7.1).[18-19] A small library of 13 RAGER analogues were synthesized (figure 7.2).

5.2 RAGE-VC1 protein purification

Transformation. 2uL of pETM11-RAGEVC1 to Shuffle T7 *E.coli* cells. Incubate on ice for 30 min. Cells were heat shocked at 42 °C for 30 s before 625 μL of fresh 2XYT media was added. Cells were allowed to shake at 37 °C for 1 h, then a 50 μL sample was spread onto a warm kanamycin-agar plate. The plate was incubated overnight at 37 °C.

Culture + Overexpression. A single, isolated colony was picked from the plate with a sterile toothpick. The toothpick was dropped into a plastic tube containing fresh 2XYT media (10 mL) and kanamycin. The culture was incubated overnight at 37 °C. Next, the starter culture was diluted into 1 L of 2XYT media with kanamycin. A 1 mL sample was removed to serve as a "blank" to read OD_{600}. The culture was incubated at 37 °C until OD_{600} = 0.7 (about 3 hours). Overexpression was induced with 1 mM IPTG. The culture was incubated and shaken overnight at 18 °C.

Purification. Cells were harvested by centrifugation (9000 g for 20 min at 4 °C). Cell pellet was resuspended in 25 mL of buffer A (50 mM HEPES, 300 mM NaCl, 30 mM imidazole, 1 mM PMSF, pH 7.4). Cells were sonicated (required multiple rounds). Solution was clarified by centrifugation (31,000 g for 20 min at 4 °C) and the supernatant was filtered. Supernatant was applied to 5 mL Ni-column (HisTrap FF column) and begin program "Histrap FF RAGE", 4% B and then 40%B). Fractions were collected and concentrated before dilution with 50mM HEPES (pH 7.5) to reach a final salt concentration of 250 mM. These were then applied to 9-mL Source 15S cation exchange. Elution performed with a 100-ml linear gradient from 250-650 mM NaCl for VC1, elute as single peak around 440 mM NaCl. Fractions were collected and analyzed by SDSPAGE (figure 7.2).

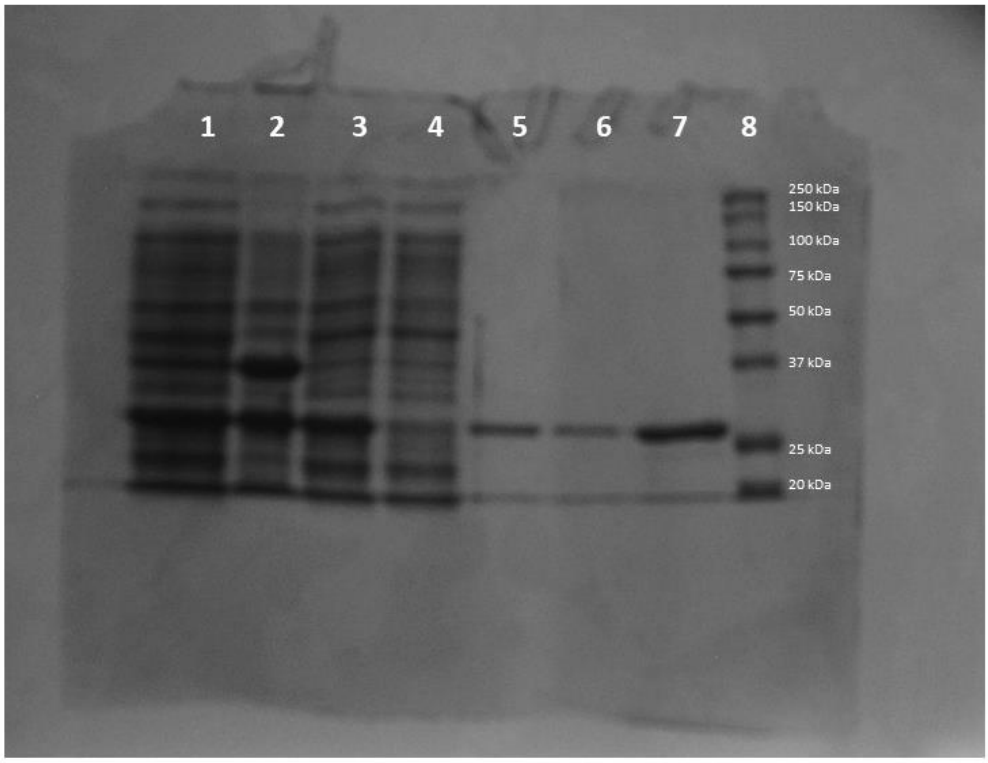

Figure 7.1. SDS-PAGE analysis of RAGE-VC1 purification. Lane 1. Crude, post-sonification. 2. Cell pellet. 3. Lysate. 4. HisTrap FF column flow through. 5. CIEX flow through. 6. Fractions (4-6). 7. Fractions (8-9). 8. Ladder. His Trap elutate (not shown) was used immediately into the CIEX column.

5.3 Synthesis of RAGE Analogue reference standards

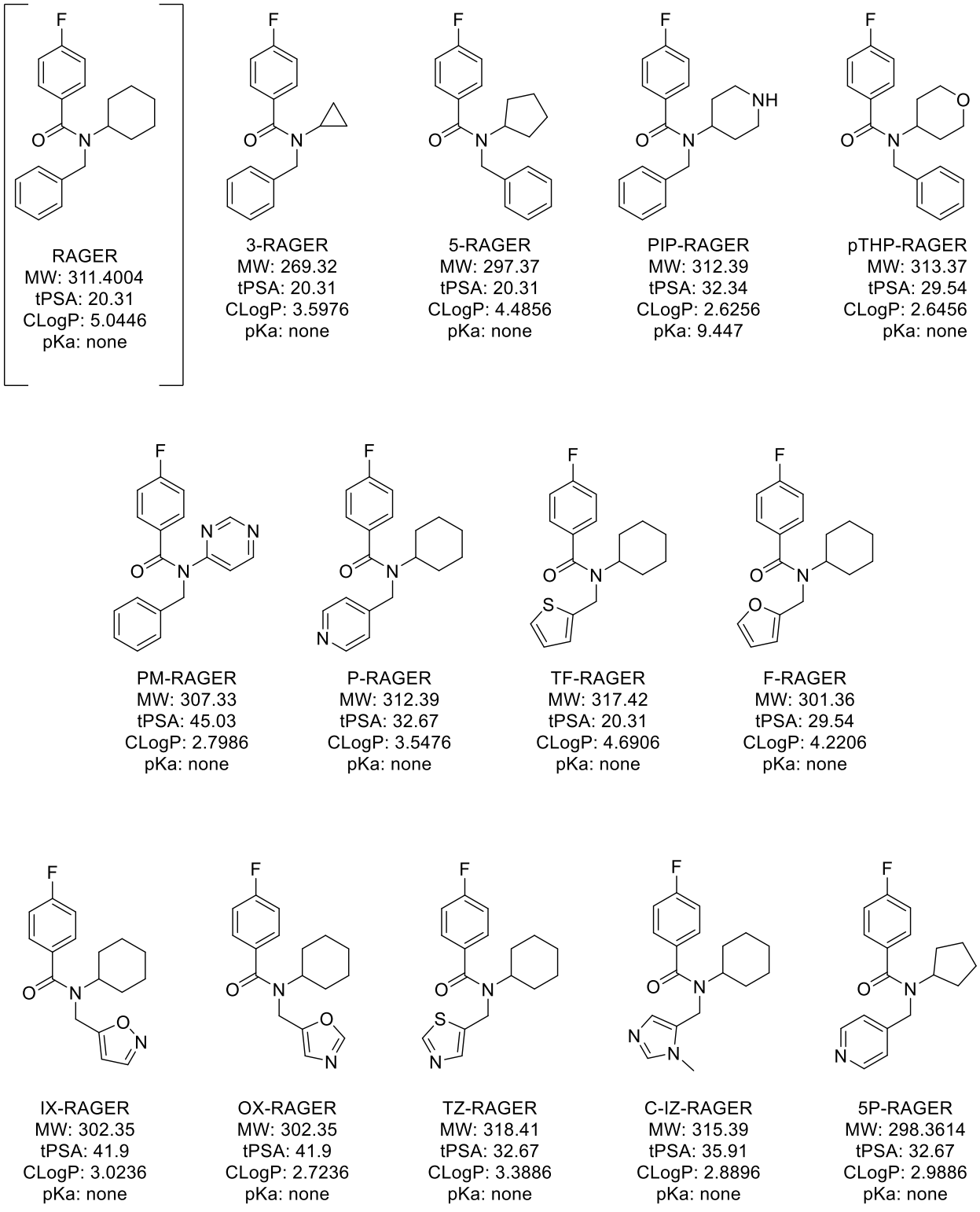

Figure 7.2. RAGER Analogues

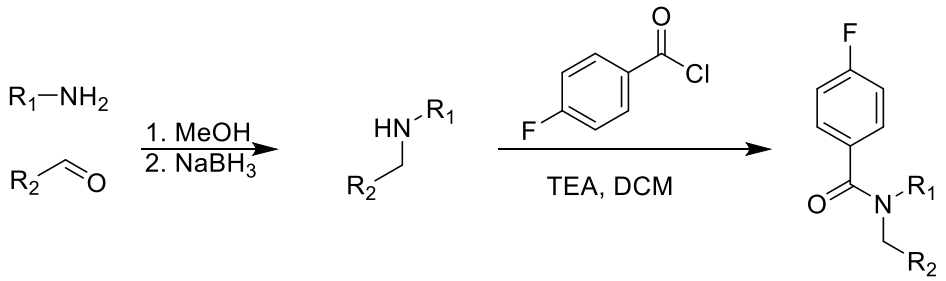

Scheme 7.1. Generic Synthesis for RAGER analogues.

*Preparation of N-benzyl-N-cyclopropyl-4-fluorobenzamide (***3-RAGER**). Cyclopropylamine (2.52 mmol, 143 mg) and benzaldehyde (2.52 mmol, 267 mg) were dissolved in methanol (5ml). Sodium sulfate was added and the mixture stirred at 50 °C overnight. After filtration, the filtrate was concentrated *in vacuo* to remove unreacted benzaldehyde. The resultant semisolid was redissolved in methanol (5ml), cooled to 0°C; sodium borohydride was slowly added. The reaction stirred for 4 hours and then was quenched with saturated ammonium chloride solution. The intermediate was extracted in dichloromethane and did not require purification. Triethylamine (3.02 mmol, 306 mg) was added to the intermediate dissolved in dichloromethane, mixture was cooled to 0°C and 4-fluorobenzoyl chloride (2.772 mmol, 439.5 mg) was added. The solution was stirred overnight under argon. The reaction was quenched with H_2O and the product extracted in dichloromethane. Product was purified by flash chromatography. ^{1}H NMR (400 MHz; $CDCl_3$/ δ (ppm) 7.52 (d, 2H), 7.34 (m, 3H), 7.09 (m, 2H), 4.74 (s, 2H), 2.59 (m, 1H), 0.58 (s, 2H), 0.48 (s, 2H)). ^{19}F NMR (347 MHz; $CDCl_3$/δ (ppm) -110.53 (s, 1F). HRMS calculated for [M+H]+ (M= $C_{17}H_{16}FNO$) 270.1289, found 270.1282.

Preparation of N-benzyl-N-cyclopentyl-4-fluorobenzamide (**5-RAGER**) Cyclopentylamine (2.52 mmol, 214.6 mg) and benzaldehyde (2.52 mmol, 267 mg) were dissolved in methanol (5ml). Sodium sulfate was added and the mixture stirred at 50 °C overnight. After filtration, the filtrate was concentrated *in vacuo* to remove unreacted benzaldehyde. The resultant semisolid was redissolved in methanol (5 ml), cooled to 0 °C; sodium borohydride was slowly added. The

reaction stirred for 4 hours and then was quenched with saturated ammonium chloride solution. The intermediate was extracted in dichloromethane and did not require purification. Triethylamine (3.02 mmol, 306 mg) was added to the intermediate dissolved in dichloromethane, mixture was cooled to 0°C and 4-fluorobenzoyl chloride (2.772 mmol, 439.5 mg) was added. The solution was stirred overnight under argon. The reaction was quenched with H_2O and the product extracted in dichloromethane. Product was purified by flash chromatography. ^{1}H NMR (400 MHz; MeOD/ δ (ppm) 7.429 (s, 1H), 7.324 (m, 2H), 7.238 (m, 2H), 7.066 (m, 2H), 4.612 (s, 2H), 1.642 (m, 5H). ^{19}F NMR (347 MHz; MeOD/δ (ppm) -111.060 (s, 1F); HRMS calculated for [M+H]+ (M= $C_{19}H_{20}FNO$) 298.1602, found 298.1611.

Preparation of N-cyclopently-4-fluoro-N-(pyridine-4-ylmethyl)benzamide (**5P-RAGER**)

Cylcopentlyamine (2.52 mmol, 214.6 mg) and isonicotinaldehyde (2.52 mmol, 270 mg) were dissolved in methanol (5ml). Sodium sulfate was added and the mixture stirred at 50 °C overnight. After filtration, the filtrate was concentrated *in vacuo* to remove unreacted isonicotinaldehyde. The resultant semisolid was redissolved in methanol (5ml), cooled to 0°C; sodium borohydride was slowly added. The reaction stirred for 4 hours and then was quenched with saturated ammonium chloride solution. The intermediate was extracted in dichloromethane and was purified by flash chromatography (gradient, DCM to 10% MeOH: R_f= 0.4). ^{1}H NMR (400 MHz; $CDCl_3$/ δ (ppm) 8.54 (d; 2H), 7.30 (d; 2H), 3.81 (s; 2H), 3.11 (s; 1H), 1.85 (m; 1H), 1.71 (m; 2H), 1.54 (m; 2H), 1.53 (m; 2H), 1.41 (m; 2H). HRMS calculated for [M+H]+ (M= $C_{11}H_{16}N_2$) 176.13, found 177.1386. Triethylamine (3.02 mmol, 306 mg) was added to the intermediate dissolved in dichloromethane, mixture was cooled to 0°C and 4-fluorobenzoyl chloride (2.772 mmol, 439.5 mg) was added. The solution was stirred overnight under argon. The reaction was quenched with H_2O and the product extracted in dichloromethane. Product was

purified by flash chromatography. ^{1}H NMR (400 MHz; MeOD/ δ (ppm) 8.711 (s, 2H), 8.139 (m, 2H), 7.421 (m, 2H), 7.257 (m, 2H), 5.402 (s, 2H), 1.23 (m, 5H). ^{19}F NMR (347 MHz; MeOD/δ (ppm)-104.54 (s, 1F); HRMS calculated for $[M+H]^{+}$ (M= $C_{18}H_{19}FN_2O$) 299.1554, found 299.1565.

Preparation of N-cyclohexyl-N-((1-methyl-1H-imidazol-5-yl)methyl)-4-fluorobenzamide. (**C-IZ RAGER**) Cyclohexylamine (2.52 mmol, 250 mg) and 1-methyl-1H-imidazole-5-carbaldehyde (2.52 mmol, 277 mg) were dissolved in methanol (5ml). Sodium sulfate was added and the mixture stirred at 50 °C overnight. After filtration, the filtrate was concentrated *in vacuo* to remove unreacted 1-methyl-1H-imidazole-5-carbaldehyde. The resultant semisolid was redissolved in methanol (5ml), cooled to 0°C; sodium borohydride was slowly added. The reaction stirred for 4 hours and then was quenched with saturated ammonium chloride solution. The intermediate was extracted in dichloromethane and did not require purification. Triethylamine (3.02 mmol, 306 mg) was added to the intermediate dissolved in dichloromethane, mixture was cooled to 0°C and 4-fluorobenzoyl chloride (2.772 mmol, 439.5 mg) was added. The solution was stirred overnight under argon. The reaction was quenched with H_2O and the product extracted in dichloromethane. Product was purified by flash chromatography. ^{1}H NMR (400 MHz; MeOD/ δ (ppm) 7.55 (s, 1H), 7.44 (d, 2H), 7.20 (m, 2H), 6.90 (d, 1H), 5.49 (s, 1H), 4.64 (s, 1H), 3.71 (s, 3H), 1.77 (s, 3H), 1.58 (m, 3H), 1.09 (s, 2H)). ^{19}F NMR (347 MHz; MeOD/δ (ppm) -112.52 (s, 1F). HRMS calculated for [M+H]+ (M= $C_{18}H_{22}FN_3O$) 315.1747, found 316.1827.

Preparation of N-cyclohexyl-4-fluoro-N-(furan-2-ylmethyl)benzamide. (**F-RAGER**) Cyclohexylamine (2.52 mmol, 250mg) and furfural (2.52 mmol, 242 mg) were dissolved in methanol (5ml). Sodium sulfate was added and the mixture stirred at 50 °C overnight. After

filtration, the filtrate was concentrated *in vacuo* to remove unreacted furfural. The resultant semisolid was redissolved in methanol (5 ml), cooled to 0°C; sodium borohydride was slowly added. The reaction stirred for 4 hours and then was quenched with saturated ammonium chloride solution. The intermediate was extracted in dichloromethane and did not require purification. Triethylamine (3.02 mmol, 306 mg) was added to the intermediate dissolved in dichloromethane, mixture was cooled to 0 °C and 4-fluorobenzoyl chloride (2.772 mmol, 439.5 mg) was added. The solution was stirred overnight under argon. The reaction was quenched with H_2O and the product extracted in dichloromethane. Product was purified by flash chromatography. ^{1}H NMR (400 MHz; MeOD/ δ (ppm) 7.77 (m 4H), 7.10 (m, 3H), 5.87 (s, 2H), 2.05- 1.74 (m, 11H). HRMS calculated for $[M+H]^+$ (M= $C_{18}H_{20}FNO_2$) 302.1551, found 302.1558.

*Preparation of N-cyclohexyl-4-fluoro-N-(isoxazol-5-ylmethyl)benzamide (***IX-RAGER***).* Cyclohexylamine (2.52 mmol, 250mg) and isoxazole-5-carbaldehyde (2.52 mmol, 244 mg) were dissolved in methanol (5ml). Sodium sulfate was added and the mixture stirred at 50 °C overnight. After filtration, the filtrate was concentrated *in vacuo* to remove unreacted isoxazole-5-carbaldehyde. The resultant semisolid was redissolved in methanol (5 ml), cooled to 0 °C; sodium borohydride was slowly added. The reaction stirred for 4 hours and then was quenched with saturated ammonium chloride solution. The intermediate was extracted in dichloromethane and did not require purification. Triethylamine (3.02 mmol, 306 mg) was added to the intermediate dissolved in dichloromethane, mixture was cooled to 0°C and 4-fluorobenzoyl chloride (2.772 mmol, 439.5 mg) was added. The solution was stirred overnight under argon. The reaction was quenched with H_2O and the product extracted in dichloromethane. Product was purified by flash chromatography (10g SiO_2, 2% MeOH/ DCM – 10% MeOH/DCM). ^{1}H NMR

(400 MHz; MeOD/ δ (ppm) 8.189 (m, 2H), 8.123 (m, 2H), 7.38 (m, 1H), 7.19 (m, 1H), 4.78 (s, 2H), 1.88-1.25 (m, 11H). ^{19}F NMR (347 MHz; MeOD/δ (ppm)-104.23 (s, 1F); HRMS calculated for $[M+H]^+$ (M= $C_{17}H_{19}FN_2O_2$) 303.1503, found 303.1508.

*Preparation of N-cyclohexyl-4-fluoro-N-(oxazol-5-ylmethyl)benzamide (***OX-RAGER***)*. Cyclohexylamine (2.52 mmol, 250mg) and oxazole-5-carbaldehyde (2.52 mmol, 244 mg) were dissolved in methanol (5ml). Sodium sulfate was added and the mixture stirred at 50 °C overnight. After filtration, the filtrate was concentrated *in vacuo* to remove unreacted oxazole-5-carbaldehyde. The resultant semisolid was redissolved in methanol (5 ml), cooled to 0 °C; sodium borohydride was slowly added. The reaction stirred for 4 hours and then was quenched with saturated ammonium chloride solution. The intermediate was extracted in dichloromethane and did not require purification. Triethylamine (3.02 mmol, 306 mg) was added to the intermediate dissolved in dichloromethane, mixture was cooled to 0°C and 4-fluorobenzoyl chloride (2.772 mmol, 439.5 mg) was added. The solution was stirred overnight under argon. The reaction was quenched with H_2O and the product extracted in dichloromethane. Product was purified by flash chromatography. ^{1}H NMR (400 MHz; MeOD/ δ (ppm)8.14 (s, 1H), 7.43 (d, 2H), 7.20 (d, 2H), 7.10 (s, 1H), 4.71 (s, 2H), 3.57 (s, 1H), 3.30 (solvent), 1.77 (m, 4H), 1.64 (m, 3H), 1.12 (m, 3H)). ^{19}F NMR (347 MHz; MeOD/δ (ppm) -112.50 (s, 1F)); HRMS calculated for [M+H]+ (M= $C_{17}H_{19}FN_2O_2$) 302.1431, found 303.1510.

Preparation of N-benzyl-4-fluoro-N-(piperidin-4-yl)benzamide.(**PIP-RAGER**) 4-aminopiperidine (3 mmol, 300.5mg) and benzaldehyde (3mmol, 321.3mg) were dissolved in methanol (5ml). Sodium sulfate was added and the mixture stirred at 50 °C overnight. After filtration, the filtrate was concentrated *in vacuo* to remove unreacted benzaldehyde. The resultant semisolid was redissolved in methanol (5 ml), cooled to 0 °C; sodium borohydride was slowly

added. The reaction stirred for 4 hours and then was quenched with saturated ammonium chloride solution. The intermediate was extracted in dichloromethane and did not require purification. Triethylamine (3.02 mmol, 306 mg) was added to the intermediate dissolved in dichloromethane, mixture was cooled to 0°C and 4-fluorobenzoyl chloride (2.772 mmol, 439.5 mg) was added. The solution was stirred overnight under argon. The reaction was quenched with H_2O and the product extracted in dichloromethane. Product was purified by flash chromatography. ^{1}H NMR (400 MHz; MeOD/ δ (ppm) 7.74 (m, 2H), 7.32 (m, 4H), 7.11 (m, 3H), 5.88 (s, 2H), 2.04-1.25 (m, 9H). ^{19}F NMR (347 MHz; MeOD/δ (ppm) -108.08 (s, 1F); HRMS calculated for [M+H]+ (M= $C_{19}H_{21}FN_2O$) 313.1711, found 313.1716.

Preparation of N-benzyl-4-fluoro-N-(pyrimidin-4-yl)benzamide. (**PM-RAGER**) 4-aminopyrimidine (3 mmol, 285.3mg) and benzaldehyde (3mmol, 321.3mg) were dissolved in methanol (5ml). Sodium sulfate was added and the mixture stirred at 50 °C overnight. After filtration, the filtrate was concentrated *in vacuo* to remove unreacted benzaldehyde. The resultant semisolid was redissolved in methanol (5 ml), cooled to 0 °C; sodium borohydride was slowly added. The reaction stirred for 4 hours and then was quenched with saturated ammonium chloride solution. The intermediate was extracted in dichloromethane and was purified by column chromatography (gradient, DCM to 10% MeOH, R_f= 0.3125). Triethylamine (3.02 mmol, 306 mg) was added to the intermediate dissolved in dichloromethane, mixture was cooled to 0°C and 4-fluorobenzoyl chloride (2.772 mmol, 439.5 mg) was added. The solution was stirred overnight under argon. The reaction was quenched with H_2O and the product extracted in dichloromethane. Product was purified by flash chromatography. ^{1}H NMR (400 MHz; MeOD/ δ (ppm) 8.19 (m, 4H), 8.116 (m, 2H), 7.434 (m, 2H), 7.12 (m, 4H), 5.34 (s, 2H)). ^{19}F NMR (347

MHz; MeOD/δ (ppm) -104.5 (s, 1F); HRMS calculated for [M+H]+ (M= $C_{18}H_{14}FN_3O$) 313.1711, found 313.1711.

*Preparation of N-cyclohexyl-4-fluoro-N-(pyridine-4-ylmethyl)benzamide (***P-RAGER***).* Cyclohexylamine (2.52 mmol, 250mg) and isonicotinaldehyde (2.52 mmol, 270 mg) were dissolved in methanol (5ml). Sodium sulfate was added and the mixture stirred at 50 °C overnight. After filtration, the filtrate was concentrated *in vacuo* to remove unreacted isonicotinaldehyde. The resultant semisolid was redissolved in methanol (5 ml), cooled to 0 °C; sodium borohydride was slowly added. The reaction stirred for 4 hours and then was quenched with saturated ammonium chloride solution. The intermediate was extracted in dichloromethane and purified by flash chromatography (gradient, DCM to 10% MeOH, R_f= 0.3125). ^{1}H NMR (400 MHz; $CDCl_3$/ δ (ppm) 8.54 (d; 2H), 7.29 (d; 2H), 3.84 (s, 2H), 2.47 (s, 1H), 1.90 (m, 1H), 1.82 (m, 3H), 1.72 (m, 1H), 1.20 (m, 5H). HRMS calculated for [M+H]+ (M= $C_{12}H_{18}N_2$) 190.15, found 191.1543. Triethylamine (3.02 mmol, 306 mg) was added to the intermediate dissolved in dichloromethane, mixture was cooled to 0°C and 4-fluorobenzoyl chloride (2.772 mmol, 439.5 mg) was added. The solution was stirred overnight under argon. The reaction was quenched with H_2O and the product extracted in dichloromethane. Product was purified by flash chromatography. ^{1}H NMR (400 MHz; MeOD/ δ (ppm) 8.537 (m, 4H), 7.287 (m, 4H), 3.84 (s, 2H), 2.47-1.199 (m, 11H)).HRMS calculated for [M+H]+ (M= $C_{19}H_{21}FN_2O$) 312.16, found 313.1722.

Preparation of N-benzyl-4-fluoro-N-(tetrahydro-2H-pyran-4-yl)benzamide. (**p-THP-RAGER**) Tetrahydro-2*H*-pyran-amine (2.52 mmol, 255 mg) and benzaldehyde (2.52 mmol, 267 mg) were dissolved in methanol (5ml). Sodium sulfate was added and the mixture stirred at 50 °C overnight. After filtration, the filtrate was concentrated *in vacuo* to remove unreacted

benzaldehyde. The resultant semisolid was redissolved in methanol (5 ml), cooled to 0 °C; sodium borohydride was slowly added. The reaction stirred for 4 hours and then was quenched with saturated ammonium chloride solution. The intermediate was extracted in dichloromethane and did not require purification. Triethylamine (3.02 mmol, 306 mg) was added to the intermediate dissolved in dichloromethane, mixture was cooled to 0 °C and 4-fluorobenzoyl chloride (2.772 mmol, 439.5 mg) was added. The solution was stirred overnight under argon. The reaction was quenched with H_2O and the product extracted in dichloromethane. Product was purified by flash chromatography. ^{1}H NMR (400 MHz; MeOD/ δ (ppm) 7.87 (m, 1H), 7.49 (s, 2H), 7.32 (m, 2H), 7.23 (m, 1H), 7.16 (d, 2H), 3.89 (s, 2H), 3.51 (m, 2H), 1.87 (m, 4H), 1.62 (m, 4H)). ^{19}F NMR (347 MHz; MeOD/δ (ppm) -110.85 (d, 2F), -112.64 (s, 1F); HRMS calculated for [M+H]+ (M= $C_{19}H_{20}FNO_2$) 313.1478, found 314.1561.

Preparation of N-cyclohexyl-4-fluoro-N-(thiophen-2-ylmethyl)benzamide.(**TF-RAGER**) Cyclohexylamine (2.52 mmol, 250mg) and thiophene-3-carbaldehyde (2.52 mmol, 282 mg) were dissolved in methanol (5ml). Sodium sulfate was added and the mixture stirred at 50 °C overnight. After filtration, the filtrate was concentrated *in vacuo* to remove unreacted thiophene-3-carbaldehyde. The resultant semisolid was redissolved in methanol (5 ml), cooled to 0 °C; sodium borohydride was slowly added. The reaction stirred for 4 hours and then was quenched with saturated ammonium chloride solution. The intermediate was extracted in dichloromethane and did not require purification. Triethylamine (3.02 mmol, 306 mg) was added to the intermediate dissolved in dichloromethane, mixture was cooled to 0 °C and 4-fluorobenzoyl chloride (2.772 mmol, 439.5 mg) was added. The solution was stirred overnight under argon. The reaction was quenched with H_2O and the product extracted in dichloromethane. Product was purified by flash chromatography. ^{1}H NMR (400 MHz; MeOD/ δ (ppm) 8.07 (m, 3H), 7.85 (d,1

H), 7.15 (m, 3H), 4.88 (s, 2H), 3.84 (m, 1H), 1.96 (m, 2H), 1.79 (m, 2H), 1.36 (m, 2H), 1.33 (d, 2H), 1.23 (d, 2H)). ^{19}F NMR (347 MHz; MeOD/δ (ppm) -108.68 (s, 1F), -111.18 (s, 1F); HRMS calculated for [M+H]+ (M= $C_{18}H_{20}FNOS$) 318.1322, found 318.1311.

*Preparation of N-cyclohexyl-4-fluoro-N-(thiazol-5-ylmethyl)benzamide (***TZ-RAGER***).* Cyclohexylamine (3 mmol, 297.5mg) and 5-thiazolecarboxaldehyde (3 mmol, 339.4 mg) were dissolved in methanol (5ml). Sodium sulfate was added and the mixture stirred at 50 °C overnight. After filtration, the filtrate was concentrated *in vacuo* to remove unreacted 5-thaizaolecarboxaldehyde. The resultant semisolid was redissolved in methanol (5 ml), cooled to 0 °C; sodium borohydride was slowly added. The reaction stirred for 4 hours and then was quenched with saturated ammonium chloride solution. The intermediate was extracted in dichloromethane and did not require purification. Triethylamine (3.02 mmol, 306 mg) was added to the intermediate dissolved in dichloromethane, mixture was cooled to 0 °C and 4-fluorobenzoyl chloride (2.772 mmol, 439.5 mg) was added. The solution was stirred overnight under argon. The reaction was quenched with H_2O and the product extracted in dichloromethane. Product was purified by flash chromatography. ^{1}H NMR (400 MHz; MeOD/ δ (ppm) 8.90 (s, 1H), 8.00 (m, 1H), 7.42 (m, 2H), 7.42 (m, 2H), 7.22 (m, 2H), 3.55 (s, 2H), 3.48 (m, 1H), 1.56 (m, 6H), 1.14 (m,1H), 1.11 (m, 4H)). ^{19}F NMR (347 MHz; MeOD/δ (ppm) -109.05 (s, 1F), -112.42 (s, 1F); HRMS calculated for [M+H]+ (M= $C_{17}H_{19}FN_2OS$) 319.1275, found 319.1283.

5.4 [^{11}C]InRAGER2

From chapter 5, InRAGER2 appeared to be less promiscuous than InRAGER based on the receptor screening results. The precursor was never made due to time constraints but below is a proposed route (scheme 7.2). The starting material is a chlorinated derivative of salicylic acid, so it is very cheap. The next steps for this project are relatively straight forward: 1) synthesize

the precursor, 2) optimize the radiosynthesis, 3) evaluate ligand binding on tissue and 4) in healthy animal.

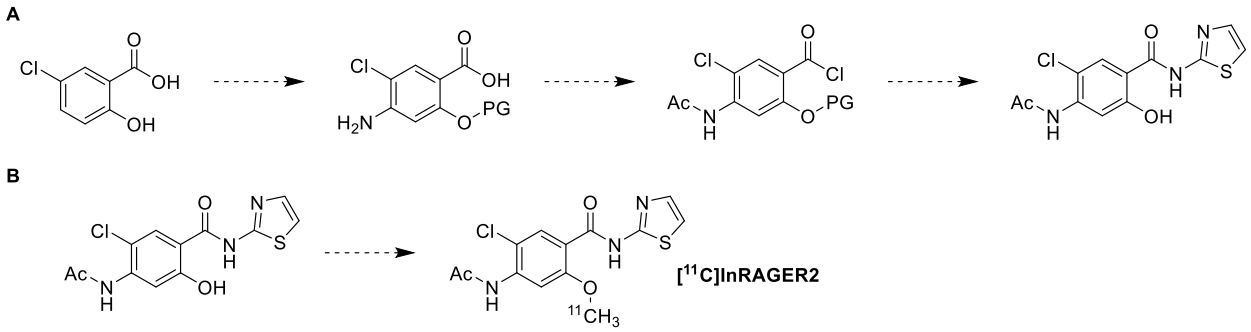

Scheme 7.2. Proposed synthesis of InRAGER2 precursor and proposed radiosynthesis.

6. Investigation into RAGE as an inflammatory biomarker

The lipopolysaccharide (LPS) induced model of neuroinflammation in chapter 6 indicated that RAGE is not a robust biomarker in this model. Moving forward, it is recommended to not use this model to evaluate RAGE ligand binding. It would be very valuable, however, to perform similar quantitative immunohistochemistry on human AD tissue sections. This was originally a goal of the project, and human AD brain sections (with age matched controls) were requested in July. To date, the Ann Arbor Brain Bank has not approved this request and this has delayed progress of this part of the project. If it were to be approved and fulfilled, the human antibodies would need to be purchased and the project could continue as planned.

7. References

1. Gaugler, J.; James, B.; Johnson, T.; Marin, A.; Weuve, J. Alzheimer's Disease Facts and Figures. https://www.alz.org/media/HomeOffice/Facts%20and%20Figures/facts-and-figures.pdf.
2. Matthews, P. M.; Rabiner, E. A.; Passchier, J.; Gunn, R. N., Positron emission tomography molecular imaging for drug development. *British Journal of Clinical Pharmacology* **2012,** *73* (2), 175-186.
3. Okamura, N., Molecular imaging of amyloid in dementia. *Annu. Rev. Shinkei* **2012**, 50-58.
4. Lindsley, C. W.; Hooker, J. M., Beyond the amyloid hypothesis of Alzheimer's disease: Tau pathology takes center stage. *ACS Chem. Neurosci.* **2018,** *9* (11), 2519.
5. Drake, L. R.; Brooks, A. F.; Mufarreh, A. J.; Pham, J. M.; Koeppe, R. A.; Shao, X.; Scott, P. J. H.; Kilbourn, M. R., Deuterium Kinetic Isotope Effect Studies of a Potential in Vivo Metabolic Trapping Agent for Monoamine Oxidase B. *ACS Chemical Neuroscience* **2018**.
6. Brooks, A. F.; Drake, L. R.; Shao, X.; Zhao, A.; Scott, P. J. H.; Kilbourn, M. R., Evaluation of Enzyme Substrate Radiotracers as PET/MRS Hybrid Imaging Agents. *ACS Med. Chem. Lett.* **2018,** *9* (11), 1140-1143.
7. Cary, B. P.; Brooks, A. F.; Fawaz, M. V.; Drake, L. R.; Desmond, T. J.; Sherman, P.; Quesada, C. A.; Scott, P. J. H., Synthesis and Evaluation of [^{18}F]RAGER: A First Generation Small-Molecule PET Radioligand Targeting the Receptor for Advanced Glycation Endproducts. *ACS Chemical Neuroscience* **2016,** *7* (3), 391-398.
8. Gasparotto, J.; Ribeiro, C. T.; da Rosa-Silva, H. T.; Bortolin, R. C.; Rabelo, T. K.; Peixoto, D. O.; Moreira, J. C. F.; Gelain, D. P., Systemic Inflammation Changes the Site of RAGE Expression from Endothelial Cells to Neurons in Different Brain Areas. *Molecular Neurobiology* **2018**.
9. Deane, R.; Singh, I.; Sagare, A. P.; Bell, R. D.; Ross, N. T.; LaRue, B.; Love, R.; Perry, S.; Paquette, N.; Deane, R. J.; Thiyagarajan, M.; Zarcone, T.; Fritz, G.; Friedman, A. E.; Miller, B. L.; Zlokovic, B. V., A multimodal RAGE-specific inhibitor reduces amyloid β–mediated brain disorder in a mouse model of Alzheimer disease. *The Journal of Clinical Investigation* **2012,** *122* (4), 1377-1392.
10. Shen, C.; Ma, Y.; Zeng, Z.; Yin, Q.; Hong, Y.; Hou, X.; Liu, X., RAGE-Specific Inhibitor FPS-ZM1 Attenuates AGEs-Induced Neuroinflammation and Oxidative Stress in Rat Primary Microglia. *Neurochemical Research* **2017**.
11. Ross, N. T.; Deane, R.; Perry, S.; Miller, B. L., Structure–activity relationships of small molecule inhibitors of RAGE-Aβ binding. *Tetrahedron* **2013,** *69* (36), 7653-7658.
12. Yang, S. R.; Lee, H. B. Pharmaceutical composition comprising FPS-ZM1 or pharmaceutically acceptable salt for preventing or treating chronic obstructive pulmonary disease. KR1901062B1, 2018.
13. Thomas, D. K.; Golub, T. R. RAGE receptor antibodies, compounds and screens for identifying and treating cachexia or pre-cachexia. WO2016201319A1, 2016.
14. Thomas, D. K.; Golub, T. R. RAGE antibodies and receptor antagonists for identifying and treating cachexia or pre-cachexia. WO2016201368A1, 2016.
15. Zlokovic, B. V.; Deane, R.; Miller, B. L. Inhibiting amyloid-beta peptide/rage interaction at the blood-brain barrier. US8778985B2, 2014.
16. Zlokovic, B. V.; Deane, R.; Miller, B. L. Tertiary amide inhibition of amyloid-β peptide/RAGE receptor interaction at the blood-brain barrier, and therapeutic uses. WO2007089616A2, 2007.
17. Axelsson, J. Mechanism, diagnostic, and treatments for complications of renal failure using a filter body with immobilized either a CD36 receptor or a SCARB1 receptor. WO2013182905A2, 2013.
18. Yatime, L.; Andersen, G. R., Structural insights into the oligomerization mode of the human receptor for advanced glycation end-products. *FEBS J.* **2013,** *280* (24), 6556-6568.
19. Yatime, L.; Andersen, G. R., The specificity of DNA recognition by the RAGE receptor. *J. Exp. Med.* **2014,** *211* (5), 749-750.

APPENDIX A

Complete data sets

Table A.1 Complete list of inhibition data from LeadProfilingScreen for RAGER

Assay Name	Species	% Inhibition
Adenosine A_1	Human	8
Adenosine A_{2A}	Human	5
Adenosine A_3	Human	4
Adrenergic α_{1A}	Rat	-1
Adrenergic α_{1B}	Rat	4
Adrenergic α_{1D}	Human	7
Adrenergic α_{2A}	Human	13
Adrenergic β_1	Human	4
Adrenergic β_2	Human	7
Androgen (Testosterone)	Human	59
Bradykinin B_1	Human	-7
Bradykinin B_2	Human	-3
Calcium Channel L-Type, benzothiazepine	Rat	13
Calcium Channel L-Type, dihydropyridine	Rat	25
Calcium Channel N-Type	Rat	5
Cannabinoid CB_1	Human	18
Dopamine D_1	Human	4
Dopamine D_{2S}	Human	-1
Dopamine D_3	Human	8
Dopamine $D_{4.2}$	Human	1
Endothelin ET_A	Human	0
Endothelin ET_B	Human	3
Epidermal Growth Factor (EGF)	Human	-8
Estrogen ERα	Human	32
$GABA_A$, flunitrazepam, central	Rat	55
$GABA_A$, muscimol, central	Rat	-6
$GABA_{B1A}$	Human	-5
Glucocorticoid	Human	9
Glutamate, Kainate	Rat	1
Glutamate, NMDA, Agonism	Rat	11
Glutamate, NMDA, Glycine	Rat	4
Glutamate, NMDA, Phencyclidine	Rat	-5
Histamine H_1	Human	23
Histamine H_2	Human	-3
Histamine H_3	Human	15
Imidazole I_2, central	Rat	13
Interleukin IL-1	Human	14

Leukotriene, Cysteinyl $CysLT_1$	Human	-7
Melatonin MT_1	Human	96
Muscarinic M_1	Human	-1
Muscarinic M_2	Human	16
Muscarinic M_3	Human	17
Neuropeptide Y Y_1	Human	-9
Neuropeptide Y Y_2	Human	-14
Nicotinic Acetylcholine	Human	-16
Nicotinic Acetylcholine α1, bungarotoxin	Human	-3
Opiate δ_1 (OP1, DOP)	Human	0
Opiate κ(OP1, KOP)	Human	33
Opiate μ (OP1, MOP)	Human	6
Phorbol Ester	Mouse	5
Platelet Activating Factor	Human	6
Potassium Channel [K_{ATP}]	Human	22
Potassium Channel hERG	Human	24
Prostanoid EP_4	Human	6
Purinergic P2X	Rabbit	24
Purinergic P2Y	Rat	2
Rolipram	Rat	8
Serotonin (5-Hydroxytryptamine) $5\text{-}HT_{1A}$	Human	2
Serotonin (5-Hydroxytryptamine) $5\text{-}HT_{2B}$	Human	20
Serotonin (5-Hydroxytryptamine) $5\text{-}HT_3$	Human	-1
Sigma σ_1	Human	9
Sodium Channel, site 2	Rat	1
Tachykinin NK_1	Human	20
Thyroid Hormone	Rat	5
Transporter, Dopamine (DAT)	Human	52
Transporter, GABA	Rat	4
Transporter, Norepinephrine (NET)	Human	24
Transporter, Serotonin (5-Hydroxytryptamine) (SERT)	Human	3

Table A.2. Complete list of inhibition data from LeadProfilingScreen for InRAGER

Assay Name	Species	% Inhibition
Adenosine A_1	Human	46.5
Adenosine A_{2A}	Human	75.7
Adenosine A_{2B}	Human	-11.9
Adenosine A_3	Human	98.8
Adrenergic α_{1A}	Human	35.2
Adrenergic α_{1B}	Human	16.4
Adrenergic α_{2A}	Human	-22.5
Adrenergic α_{2B}	Human	-29.7
Adrenergic β_1	Human	-36.5
Adrenergic β_2	Human	4.0
AT_1	Human	-7.2
AT_2	Human	-5.6
BZD (central)	Rat	-3.7
BZD (peripheral)	Rat	63.2
B_2	Human	-68.2
CGRP	Human	3.0
CB_1	Human	5.9
CB_2	Human	35.3
CCK_1 (CCK_A)	Human	76.4
Dopamine D_1	Human	21.2
Dopamine D_{2S}	Human	-5.7
Endothelin ET_A	Human	-11.2
Endothelin ET_B	Human	-4.3
$GABA_{A1}$	Human	-27.3
NMDA	Rat	4.5
TNF-α	Human	-6.3
H_1	Human	-19.9
H_2	Human	-33.9
MT_2	Human	15.9
MAO-A	Human	14.4
Motilin	Human	6.5
M_1	Human	-66
M_2	Human	-43.3
M_3	Human	-16.6
M_4	Human	-2.9
M_5	Human	-24.9
NK_1	Human	30.0
NK_2	Human	31.5
Y_1	Human	-16.2
δ (DOP)	Human	46.7
κ (KOP)	Human	83.1
μ (MOP)	Human	14.2
PPARγ	Human	86.5
PCP	Rat	-0.4
EP_2	Human	73.6
P2X	Rat	-8.2

5-HT_{1A}	Human	31.5
5-HT_{1B}	Human	-7.1
5-HT_{2A}	Human	67.3
5-HT_{2B}	Human	97.1
5-HT_{2C}	Human	17.4
5-HT_{3}	Human	0.9
5-HT_{4e}	Human	14.4
5-HT_{7}	Human	-31.9
sigma (non-selective)	Human	20.8
GR	Human	21.6
Estrogen ER alpha	Human	11.2
AR	Human	26.5
UT	Human	77.7
VPAC $_1$ (VIP_1)	Human	-0.5
$V_{1\,a}$	Human	1.2
Ca^{2+} channel (L, dihydropyridine site)	Rat	45.2
Ca^{2+} channel (L, diltiazem site)	Rat	21.4
K_{ATP} channel	Rat	-15.6
SK_{Ca} channel	Rat	4.2
Na^{+} channel (site 2)	Rat	9.7
Cl^{-} channel (GABA gated	Rat	21.3
norepinephrine transporter	Human	94.6
dopamine transporter	Human	49.8
GABA transporter	Rat	-11.9
5-HT transporter	Human	-7.7

Table A3. Complete list of inhibition data from LeadProfilingScreen for InRAGER2

Assay Name	Species	% Inhibition
Adenosine A_1	Human	25.2
Adenosine A_{2A}	Human	39.7
Adenosine A_{2B}	Human	-34.6
Adenosine A_3	Human	74.6
Adrenergic $_{\alpha 1A}$	Human	13.9
Adrenergic $_{\alpha 1B}$	Human	4.3
Adrenergic $_{\alpha 2A}$	Human	-7.0
Adrenergic $_{\alpha 2B}$	Human	-12.7
Adrenergic $_{\beta 1}$	Human	2.5
Adrenergic $_{\beta 2}$	Human	-8.3
AT_1	Human	4.5
AT_2	Human	2.7
BZD (central)	Rat	1.7
BZD (peripheral)	Rat	81.2
B_2	Human	-21.3
CGRP	Human	-1.3
CB_1	Human	11.8
CB_2	Human	25.0
CCK_1 (CCK_A)	Human	-9.3

Dopamine D_1	Human	-7.2
Dopamine D_{2S}	Human	-2.3
Endothelin ET_A	Human	-1.4
Endothelin ET_B	Human	-13.1
$GABA_{A1}$	Human	-34.8
NMDA	Rat	-16.2
TNF-α	Human	2.7
H_1	Human	-2.0
H_2	Human	-21.7
MT_2	Human	28.8
MAO-A	Human	14.4
Motilin	Human	21.6
M_1	Human	2.6
M_2	Human	-25.3
M_3	Human	-22.1
M_4	Human	16.7
M_5	Human	-6.1
NK_1	Human	-2.9
NK_2	Human	20
Y_1	Human	6.0
δ (DOP)	Human	20.9
κ (KOP)	Human	42.5
μ (MOP)	Human	-5.3
PPARγ	Human	31.6
PCP	Rat	-3.4
EP_2	Human	36.3
P2X	Rat	-1.7
$5\text{-}HT_{1A}$	Human	23.8
$5\text{-}HT_{1B}$	Human	-0.8
$5\text{-}HT_{2A}$	Human	8.7
$5\text{-}HT_{2B}$	Human	95.1
$5\text{-}HT_{2C}$	Human	48.8
$5\text{-}HT_3$	Human	15.9
$5\text{-}HT_{4e}$	Human	14.1
$5\text{-}HT_7$	Human	-7.7
sigma (non-selective)	Human	11.1
GR	Human	11.0
Estrogen ER alpha	Human	1.4
AR	Human	-19.5
UT	Human	84.9
$VPAC_1$ (VIP_1)	Human	-13.5
V_{1a}	Human	-0.8
Ca^{2+} channel (L, dihydropyridine site)	Rat	-10.3
Ca^{2+} channel (L, diltiazem site)	Rat	-20.5
K_{ATP} channel	Rat	-1.6
SK_{Ca} channel	Rat	-3.7
Na^+ channel (site 2)	Rat	24.9
Cl^- channel (GABA gated	Rat	18.2
norepinephrine transporter	Human	1.8

dopamine transporter	Human	5.5
GABA transporter	Rat	3.0
5-HT transporter	Human	-12.3

Figure A.1. Details from AV-1451 Autoradiography Optimization

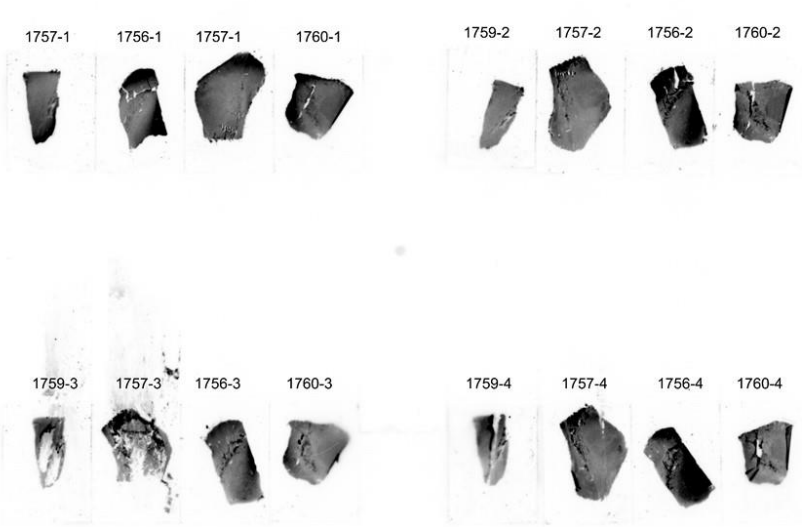

09 May 2018
[18F]AV1451
Human tissue
Control SN.
Inc time: 30 min
*Washes: (on ice)
1) Buffer, 2 min
2) buffer, 2 min
3) buffer, 2 min
4) Water, 30 s
Block time:
1) 0 min
2) 15 min
3) 30 min
4) 45 min

yes the order is Different

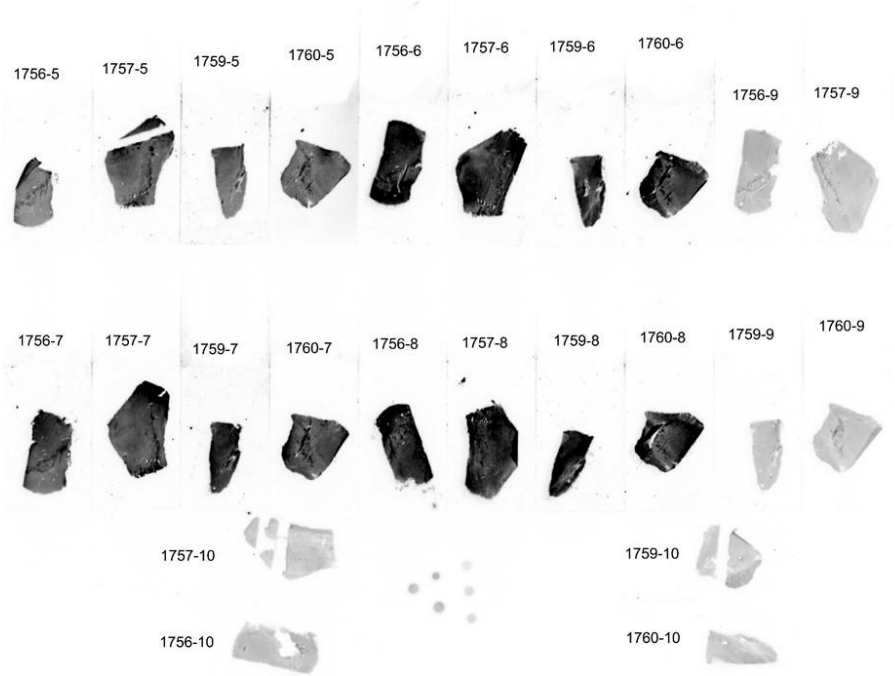

10 May 2018
[^{18}F]AV1451
Human tissue
Control SN.
Odds= total
Evens= NSB
5/6: PBS + 0.1% BSA
7/8: PBS + 1.0% BSA
9/10: PBS + 0.5% Tween-20
Inc time: 45 min
Temp: on ice

Washes: (on ice)
1) Buffer, 2 min
2) buffer, 2 min
3) buffer, 2 min
4) Water, 30 s

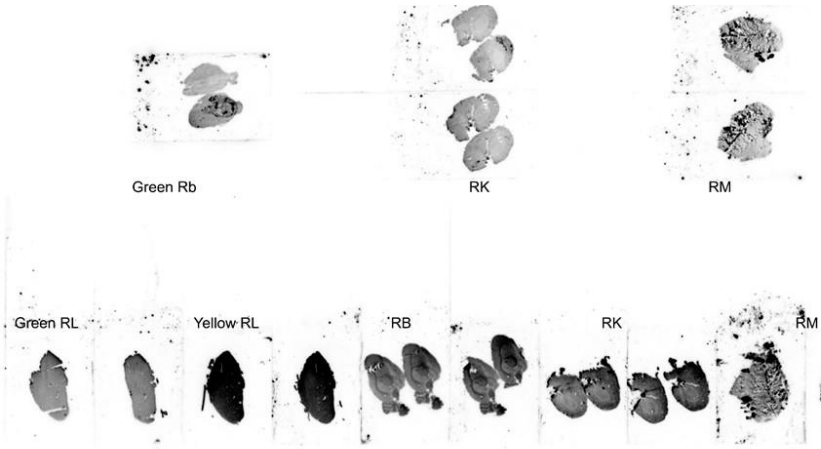

23 May 2018
[^{18}F]AV1451
Rat tissue
B= brain
K= kidney
L= liver
M= muscle
Buffer: PBS + 0.1% BSA
Inc time: 45 min
Temp: on ice

Washes: (on ice)
1) Buffer, 2 min
2) buffer, 2 min
3) buffer, 2 min
4) Water, 30 s

Green= total binding
Yellow= 2 uM cold AV1451 (NSB)
Red= 2 uM Deprenyl

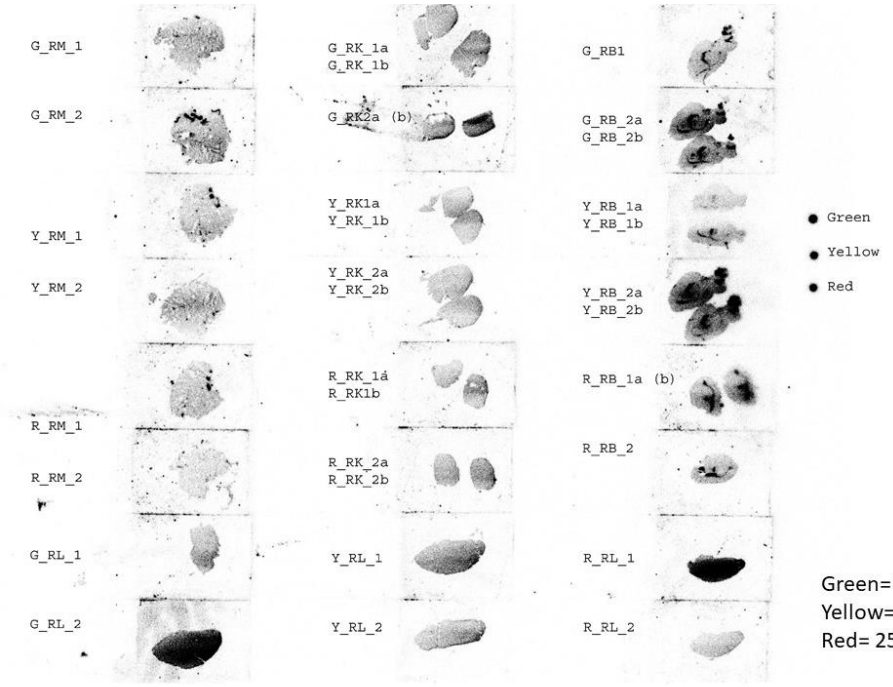

30 May 2018
[18F]AV1451
Rat tissue
B= brain
K= kidney
L= liver
M= muscle

Buffer: PBS + 0.1% BSA
Inc time: 45 min
Temp: on ice

Washes: (on ice)
1) Buffer, 1 min
2) 70% EtOH, 2 min
3) 30% EtOH, 1 min
4) Water, 1 min

Green= total binding
Yellow= 25 uM cold AV1451 (NSB)
Red= 25 uM Deprenyl

Rat Brain

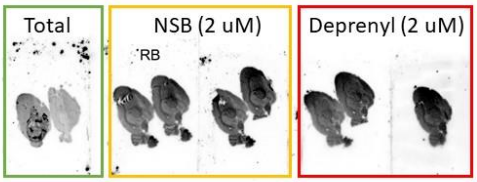

05/23/18

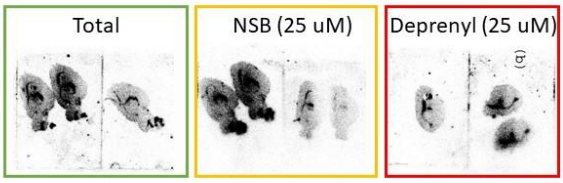

05/30/18: ethanol washing lowers overall binding

APPENDIX B
Protocols

1. Generic Immunohistochemistry Protocol- Fixed Tissue

Stock Solutions:

- Davidson's Fixative
- Vectastain elite ABC kit (be sure to match species of 1° antibody)
- 70% Ethanol (in water)
- 70% Methanol (in water)
- 30% Peroxide (H_2O_2 in water)
- Phosphate buffered saline, pH 7.4, 0.4% Triton-X-100, 1% BSA, 0.025% NaN_3 (**PBS-TBA**)
- Phosphate buffered saline, pH 7.4, 0.4% Triton-X-100 (**PBS-T**)
- Phosphate buffered saline, pH 7.4, 1 mM EDTA (**PBS-EDTA**)
- Diaminobenzidine 0.05% + 0.01% H_2O_2 in PBS-T (**DAB**)
- 100% n-Butanol
- Xylene
- Permount

Procedure:

Fixing the fresh-frozen, thaw-mounted slides

(use ~10 mL volumes in cytomailers)

1.	Rehydration	PBS-EDTA, pH 7.4, 30 s
2.	Fixation	Davidson's fixative, 24 hr @ RT
3.	Rinse	70% EtOH (to remove formaldehyde)

Primary Antibody

4.	1% SDS/PBS	5 minutes
5.	PBS	3 x 5 min at RT (to remove SDS)
6.	Quenching	10 mL (70% MeOH, 100 µl 30% H_2O_2), 15 min, RT
7.	Wash PBS-T	3 x 5 min at RT
8.	Blocking	PBS-TBA, 30 min, RT
9.	1° Antibody	(specific dilution) in PBS-TBA overnight at RT
10.	Wash PBS-T	3 x 5 min, RT

Secondary Antibody

11.	2° Antibody	50 µL in 10 mL PBS-TBA, 2+ hr, RT
12.	Wash PBS-T	3 x 5 min, RT

Visualization

13. ABC Solution RT	ABC reagent diluted per Vectastain instructions in PBS-T, 30 min,
14. Wash PBS-T	3 x 5 min, RT
15. DAB Solution 3.33	~4 min, RT (5 mg DAB + 10 mL PBS-T, dissolve, filter, then add
	µL 30% H_2O_2)
16. Rinse	dH_2O, 1 min, RT

Counterstain- Giemsa

17. Wash	dH_2O, 5 min, RT
18. Giemsa	1:50 (Giemsa in dH_2O), overnight, RT
19. Rinse	dH_2O, 30 s, RT
20. Rinse	2 x 4 min, 100% n-Butanol
21. Fix	Xylene, 1 min
22. Coverslip	Permount (let set for ~45 min before using microscope)

2. Example Hot Metabolism Protocol

Materials:
glass culture tubes, Eppendorf tubes, HPLC vials, filters

#1. Monkey liver microsome w/o UDPA, incubation time: (20, 45, 90, 150 min)

Glycine/NaOH, pH 9.2	1M (2X)	125 ul
(mw. 75.07. Glycine 15.01 g/ 200 ml)		
$MgCl_2$. $6H_2O$	50mM (10X)	50 ul
(mw 203.30. 2.33g/ 200 ml)		
DTT	30mM (10X)	50 ul
(Dithiothreitol, mw 154.25. 2.32g/0.5ml)		
Microsome	0.5 mg(20 ug/ul)	25 ul
½ final volume		250 ul

#2. Monkey liver microsome w/o UDPA, incubation time: (20, 45, 90, 150 min)

Glycine/NaOH, pH 9.2	1M (2X)	75 ul
(mw. 75.07. Glycine 15.01 g/ 200 ml)		
$MgCl_2$. $6H_2O$	50mM (10X)	50 ul
(mw 203.30. 2.33g/ 200 ml)		
DTT	30mM (10X)	50 ul
(Dithiothreitol, mw 154.25. 2.32g/0.5ml)		
UDP-glucuronic acid	20mM (10X)	50 ul
(UDPGA, mw 631.38. 6.32 mg/ 0.5 ml)		

Microsome	0.5 mg(20 ug/ul)	25 ul
½ final volume		250 ul
Add Substrate to each tube:		
RAGER	2.5mM (10X)	50 ul
(mw 311.4004. 0.7785/ml)		
ddH_2O		200 ul
Total volume		500 ul

Sample Preparation:
Reaction was terminated by removing 250 ul aliquot (of 1000 ul total) and addition of ice cold methanol 500 ul. Vortex for 1 min, centrifuge 5 mins. Supernatant was filtered for HPLC. Conditions: 10 mM ammonium acetate 60% Acetonitrile pH 9.

3. Example MAO-B Supersome Assay

Monaomine Oxidase Activity Assays													
February 19th, 2016			[enzyme]	80	ug/ml		*edit protocol to be 100 minutes long (20 reads)					
			addition	10	uL							
Name	MW (Da)		stock enzyme	1.2	mg/ml							
7-hydroxy-4-methyl-coumarin	115.08		make stock	247	ul buffer							
Coumarin-D3	274.14		78 uL aliquot in -80! A and B									
Coumarin	271.31											
Fluorescent Standard		total vol (uL)	150	DF	5		10	mM	0.00002	mol	2.3016	mg
	ROWS	stock volume (uL)	Stock (uM)	buffer (uL)	Final (uM)				2	mL		
Make dilutions outside of well.	A	50	-----	200	300							
Add 150uL to well.	B	50	300	200	60		Making first stock:					
	C	50	60	200	12							
	D	50	12	200	2.4		10	mM	stock			
*Duplicate	E	50	2.4	200	0.48		30	uL	stock			
	F	50	0.48	200	0.096		970	uL	buffer			
	G	50	0.096	200	0.0192		1000	uL	total vol			
	H	50	0.0192	200	0.00384							
LRD.II.60B		total vol (ul)	150	DF	1.5		10	mM	0.00002	mol	5.4828	mg
D3 Compound range	ROWS	stock volume (uL)	Stock (uM)	enzyme (uL)	buffer (uL)	Final (uM)			2	mL		
	A	20	1500	10	120	200						
MAO-A	B	20	1000	10	120	133.33	Making first stock:					
	C	20	667	10	120	88.89	1 ml each				300 ul	buffer
*Duplicate	D	20	444	10	120	59.26	10	mM	stock		600 ul	stock
	E	20	296	10	120	39.51	60	uL	stock			
	F	20	198	10	120	26.34	340	uL	buffer			
	G	20	132	10	120	17.56	400	uL	total vol			
	H	20	88	10	120	11.71						
AFB. VII.99		total vol (ul)	150	DF	1.5		10	mM	0.00002	mol	5.4262	mg
Compound range	ROWS	stock volume (uL)	Stock (uM)	enzyme (uL)	buffer (uL)	Final (uM)			2	mL		
	A	20	1500	10	120	200						
MAO-A	B	20	1000	10	120	133.33	Making first stock:					
	C	20	667	10	120	88.89	1 ml each				300 ul	buffer
*Duplicate	D	20	444	10	120	59.26	10	mM	stock		600 ul	stock
	E	20	296	10	120	39.51	60	uL	stock			
	F	20	198	10	120	26.34	340	uL	buffer			
	G	20	132	10	120	17.56	400	uL	total vol			
	H	20	88	10	120	11.71						

LRD.II.60B		total vol (ul)	150	DF	5		10	mM	0.00002	mol	0	mg
D3 Compound range	ROWS	stock volume (uL)	Stock (uM)	enzyme (uL)	buffer (uL)	Final (uM)			2	mL		
	A	20	375	10	120	50						
MAO-B	B	20	75	10	120	10.00	Making first stock:					
	C	20	15	10	120	2.00	1 ml each				200 ul	buffer
*Duplicate	D	20	3	10	120	0.40000	10	mM	stock		50 ul	stock
	E	20	1	10	120	0.08000	37.5	uL	stock			
	F	20	0	10	120	0.01600	962.5	uL	buffer			
	G	20	0	10	120	0.00320	1000	uL	total vol			
	H	0	0	10	140	0.00064						

AFB. VII.99		total vol (ul)	150	DF	5		10	mM	0.00002	mol	0	mg
Compound range	ROWS	stock volume (uL)	Stock (uM)	enzyme (uL)	buffer (uL)	Final (uM)			2	mL		
	A	20	375	10	120	50						
MAO-B	B	20	75	10	120	10.00	Making first stock:					
	C	20	15	10	120	2.00	1 ml each				200 ul	buffer
*Duplicate	D	20	3	10	120	0.40000	10	mM	stock		50 ul	stock
	E	20	1	10	120	0.08000	37.5	uL	stock			
	F	20	0	10	120	0.01600	962.5	uL	buffer			
	G	20	0	10	120	0.00320	1000	uL	total vol			
	H	0	0	10	140	0.00064						

	1	2	3	4	5	6	7	8	9	10	11	12
A		F	E	A	A	B	B	A	A	B	B	
B		L	N	A	A	B	B	A	A	B	B	
C		U	T	A	A	B	B	A	A	B	B	
D		O		A	A	B	B	A	A	B	B	
E		R	S	A	A	B	B	A	A	B	B	
F		E	T	A	A	B	B	A	A	B	B	
G		S	D	A	A	B	B	A	A	B	B	
H		C		A	A	B	B	A	A	B	B	
BORATE				D-3				COU				

Prepping the assay:

1. Make standard curve dilutions from fresh powder stock (10mm in DMSO) using borate buffer
2. Make MAO-A substrate dilutions (denote vials as: AA, AB, AC…). Keep in separate bag!
3. Make MAO-B substrate dilutions (denote vials as: BA, BB, BC…). Keep in separate bag!
4. Transport supersomes in dry ice.
5. Bring a new plate and buffer!

Prepping the plate:

1. Fill columns 2-3 with fluorescent standard (140 ul)
2. Fill columns 4-5 with MAO-A D3 substrate (20 ul)
3. Fill columns 6-7 with MAO-B D3 substrate (20 ul)
4. Fill columns 8-9 with MAO-A coumarin substrate (20 ul)
5. Fill columns 10-11 with MAO-B coumarin substrate (20 ul)
6. Use multichannel to fill columns 1 + 12 with buffer (150 ul)

7. Use multichannel to fill columns 4-11 with buffer (120 ul)
8. Check to see if plate reader is at 37!
9. Thaw supersomes in 37 water bath (~3 min)
10. Dilute supersomes by addition of 247 ul borate buffer
11. Initiate reaction by addition of enzyme 4-5 A, 6-7 B, 8-9 A, 10-11, B (10 ul)
12. READ PLATE.

4. Drake & Desmond Autoradiography Protocol

Follow basic flowchart with experiment-specific changes

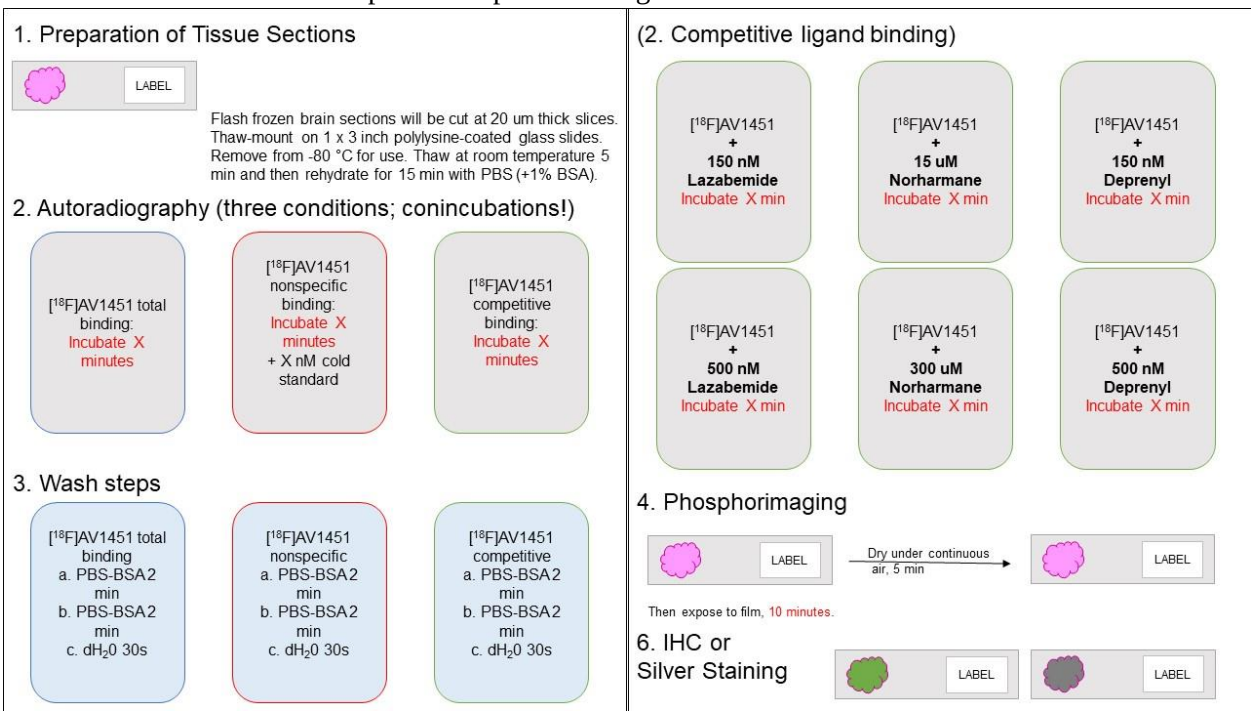

1) Thaw tissues at room temperature for 5 minutes; rehydrate in experiment buffer for ~15 minutes (approximately, no more than 30 minutes).

2a) Use spreadsheet to calculate the volume to be added for the experiment: (example)

Calculating autoradiography dose		
Tracer	[18F]	AV1451
Specific Activity	1178	Ci/ mmol
Dose Activity	0.104	Ci
Dose Volume	10	mL
Final conc	0.0000004	mmol
Add	0.045307692	ml
	45.30769231	ul

2b) Add the requisite concentration of radioligand to your buffer; similarly for competitive or nonspecific binding add that ligand as well. In the "total binding" well add the same volume of vehicle.

2c) Incubate/ co-incubate, recommended between 30-45 minutes. TIME SENSITIVE
3) Wash tissues. 2 minutes (experimental buffer x 2), 30 s of water. TIME SENSITIVE
4) Dry completely before exposing to plate, recommended 5 minutes of drying and 10 min exposure. Don't forget to add your TLC plate with "experimental activity" spotted on it.
5) Fix the slides if you are going to move onto step 6, which for some reason is not on this flowchart.

5. Buffer Recipes

Phosphate Buffered Saline (PBS: 1X)

NaCl	32.03g
KCl	0.89 g
Na_2HPO_4	4.54 g
KH_2PO_4	1.22 g

Total Volume: 4 L
Adjust pH to: 7.4

Phosphate Buffered Saline + EDTA (PBS- EDTA)

NaCl	32.03g
KCl	0.89 g
Na_2HPO_4	4.54 g
KH_2PO_4	1.22 g
EDTA	1.17 g

Total Volume: 4 L
Adjust pH to: 7.4

Borate Buffer (100 mM)

Boric Acid	6.185 g
NaCl	4.385 g
Sodium Tetraborate	9.535 g

Total Volume: 1 L
Adjust pH to: 8.4

*This does not go into solution easily and will need to be heated while stirring.

6. Code for the RAGER Analogues in the freezer

ANALOGUE CODE

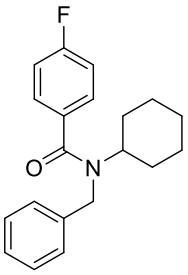

RAGER
MW: 311.4004
tPSA: 20.31
CLogP: 5.0446
pKa: none
alpha

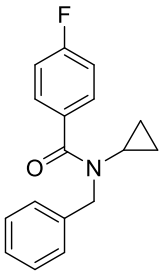

3-RAGER
III.95
MW: 269.32
tPSA: 20.31
CLogP: 3.5976
pKa: none
beta

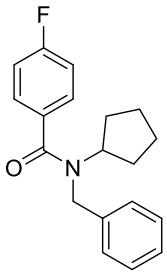

5-RAGER
VI.13
MW: 297.37
tPSA: 20.31
CLogP: 4.4856
pKa: none
gamma

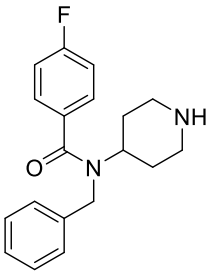

PIP-RAGER
V.71
MW: 312.39
tPSA: 32.34
CLogP: 2.6256
pKa: 9.447
delta

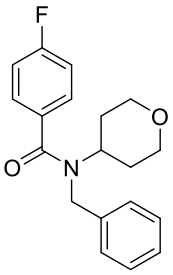

pTHP-RAGER
VI.1
MW: 313.37
tPSA: 29.54
CLogP: 2.6456
pKa: none
epsilon

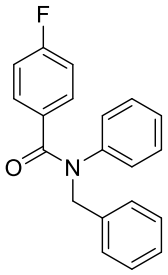

2B-RAGER
VI.31
MW: 305.3524
tPSA: 20.31
CLogP: 5.2526
pKa: none
zeta

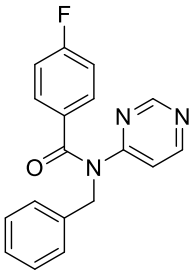

PM-RAGER
V.61
MW: 307.33
tPSA: 45.03
CLogP: 2.7986
pKa: none
eta

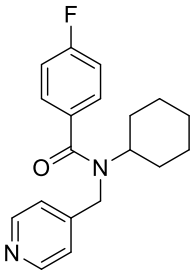

P-RAGER
III.65
MW: 312.39
tPSA: 32.67
CLogP: 3.5476
pKa: none
theta

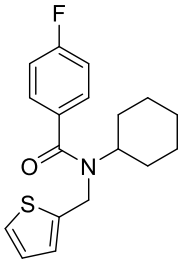

TF-RAGER
III.92
MW: 317.42
tPSA: 20.31
CLogP: 4.6906
pKa: none
iota

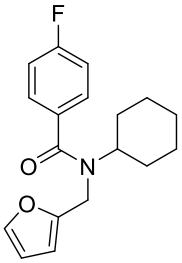

F-RAGER
III.97
MW: 301.36
tPSA: 29.54
CLogP: 4.2206
pKa: none
kappa

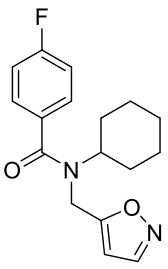

IX-RAGER
VI.23
MW: 302.35
tPSA: 41.9
CLogP: 3.0236
pKa: none
lambda

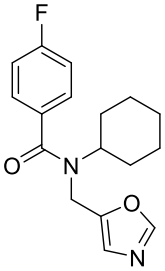

OX-RAGER
VI.27
MW: 302.35
tPSA: 41.9
CLogP: 2.7236
pKa: none
mu

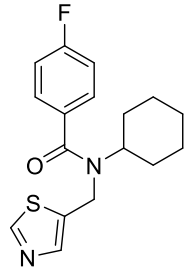

TZ-RAGER
V.65
MW: 318.41
tPSA: 32.67
CLogP: 3.3886
pKa: none
nu

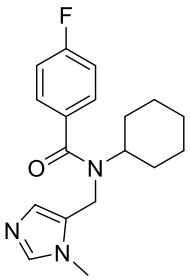

C-IZ-RAGER
V.73
MW: 315.39
tPSA: 35.91
CLogP: 2.8896
pKa: none
xi

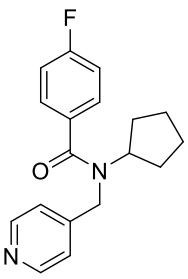

5P-RAGER
VI.33
MW: 298.3614
tPSA: 32.67
CLogP: 2.9886
pKa: none
omicron

Table B.1. Inventory of freezer boxes.

Box #	Cut Date	Species	Brain Tissue	Disease State	Notes
1	Sept 2018	Human	substantia nigra/ cerebellum	AD/ DLB	
2	Oct 2018	Mouse	sagittal half	LPS – 1 day	male animals 1 +2
3	Oct 2018	Mouse	sagittal half	LPS – 1 day	male animals 3 + 4
4	Aug 2018	Mouse	sagittal half	normal	male and female
5	Oct 2018	Mouse	sagittal half	LPS – 1 day	female animals 1 +2
6	Oct 2018	Mouse	sagittal half	LPS – 1 day	female animals 3 + 4
7	Aug 2018	Rat	sagittal half	normal	
8	Oct 2018	Human	cerebellum	Normal	
9	Nov 2018	Mouse	sagittal half	Normal	male + female
10	Nov 2018	Mouse	sagittal half	Normal	14 day vehicles
11	Nov 2018	Mouse	sagittal half	LPS- 14 day	male animals 1 -4
12	Nov 2018	Mouse	sagittal half	LPS- 14 day	female animals 1- 4